Light-matter interaction is a powerful tool for unravelling the properties of novel materials. In this work, we study the electron dynamics induced in effective Dirac systems, such as graphene and topological insulator surface states, by time-periodic driving and ultrashort laser pulses. We propose that so-called Floquet oscillations arise when a static electric field drives electrons through the Floquet bandstructure established by time-periodic driving. This phenomenon is an analogue of Bloch oscillations in spatially periodic lattices. Moreover, we explore the high-order harmonic radiation emitted by topological insulator surface states interacting with ultrashort, strong laser pulses. We develop a novel simulation method based on the propagation of wave packets, that takes the Fermi sea into account. Our results show how the Berry curvature imprints on the emitted spectrum and we find a susceptibility of the spectra to external magnetic fields.

Universität Regensburg
UNIVERSITÄTSBIBLIOTHEK

ISBN 978-3-88246-501-3

Vanessa Junk

Dynamics of electrons in strongly driven Dirac systems:
From Floquet oscillations to high-harmonic generation

Vanessa Junk

Dynamics of electrons in strongly driven Dirac systems:
From Floquet oscillations to high-harmonic generation

Eine Publikation der
Universitätsbibliothek Regensburg

Dynamics of electrons in strongly driven Dirac systems: From Floquet oscillations to high-harmonic generation

dissertation zur erlangung des doktorgrades der naturwissenschaften (dr. rer. nat.) der fakultät für physik

der universität regensburg

vorgelegt von

Vanessa Junk aus

Schrobenhausen

im Jahr 2023

Promotionsgesuch eingereicht am: 26.06.2023

Das Promotionskolloquium fand statt am: 11.01.2024

Die Arbeit wurde angeleitet von: Prof. Dr. Klaus Richter

Prüfungsausschuss

Vorsitzender: Prof. Dr. Rupert Huber
1. Gutachter: Prof. Dr. Klaus Richter
2. Gutachter: Prof. Dr. John Schliemann
Weiterer Prüfer: Prof. Dr. Christoph Lehner

Bibliografische Information der Deutschen Nationalbibliothek

Die Deutsche Nationalbibliothek verzeichnet diese Publikation in der Deutschen Nationalbibliografie. Detaillierte bibliografische Daten sind im Internet unter `http://dnb.dnb.de` abrufbar.

ISBN (Print): 978-3-88246-501-3

ISBN (PDF): 978-3-88246-502-0

DOI: 10.5283/epub.55413

Link zur Online-Version: `https://epub.uni-regensburg.de/55413`

Satz und Layout: Vanessa Junk

Titelbild: Vanessa Junk

Umschlaggestaltung: Peter Brünsteiner

Herstellung: Universitätsbibliothek Regensburg

Erscheinungsort: Regensburg, 2024

Druck und Bindung: Digital Print Group o. Schimek GmbH, Nürnberg

Abstract

The interaction of matter with strong laser fields is a powerful tool for studying and even manipulating a material's properties. Investigating the light-induced electron dynamics in novel, Dirac-like quantum materials, such as graphene and three dimensional topological insulators, is an important step towards unraveling the full potential of such exotic matter for technological applications. In this dissertation, we explore the electron dynamics in effective Dirac systems induced by both time-periodic driving and ultrashort laser pulses.

In the first part, we propose so-called *Floquet oscillations* in periodically driven systems as an analogue of the well-known Bloch oscillations in spatially periodic lattices. The time-periodic driving leads to the formation of Floquet bands, that describe the dynamics of electrons similar to the usual Bloch bands. By applying an additional static electric field, electrons are driven through this Floquet bandstructure and thereby undergo an oscillatory motion governed by the profile of the Floquet bands, allowing for an imaging of the latter. Alternatively, Floquet oscillations can be understood as consecutive transitions of the electron at (multi-)photon resonances of the driving field with the static system's bandstructure. Accordingly, the frequency of the Floquet oscillations does not follow the driving frequency, but is inversely proportional to it. We demonstrate Floquet oscillations and their properties by propagating wave packets in effective Dirac systems for two types of driving, and confirm their potential experimental realization in graphene. We do so both in a time-dependent framework and by applying Floquet theory. Therefore, our studies bridge the gap between the Floquet picture and the straightforward time-dependent analysis.

In the second part, we consider the nonlinear interaction of electrons in topological insulator surface states with ultrashort laser pulses. These surface states are also governed by the Dirac equation, and are extremely robust against perturbations due to their topological protection. The suppression of backscattering, caused by spin-momentum locking, gives rise to long electron scattering times and allows for the imprint of coherent transport effects on the high-order harmonics emitted by the strongly driven electrons. After performing detailed studies of the single-electron dynamics induced by the laser pulse, we develop a novel method for simulating high-harmonic generation from a Fermi sea by propagating wave packets. This method complements the oftentimes applied semiconductor Bloch equations, and offers a more intuitive insight into the effective Fermi sea dynamics. Additionally, our

approach allows for the inclusion of spatially dependent potentials and thus for studying orbital effects of a magnetic field. Our results highlight, how the Berry curvature imprints on the emitted spectrum. On top of that, we find evidence for the influence of different momentum-space regions on the emitted harmonics and a susceptibility of the spectra to external magnetic fields.

List of used acronyms:

1D	one-dimensional/one dimension
2D	two-dimensional/two dimensions
3D	three-dimensional/three dimensions
ARPES	angle-resolved photoemission spectroscopy
BZ	Brillouin zone
COM	center of mass
DFT	density functional theory
FBZ	Floquet Brillouin zone
HH	high(er) harmonic
HHG	high-harmonic generation
PHS	particle-hole symmetry
SOC	spin-orbit coupling
TRS	time-reversal symmetry
TI	topological insulator
TQT	Time-dependent Quantum Transport

List of important constants/symbols:

$\mathbb{1}$	unit matrix
c	speed of light
E_F	Fermi energy
$\mathbf{E}_\mathrm{el}$	electric field
e	positive elementary charge
$\mathbf{e}_{x/y/z}$	unit vector in $x/y/z$ direction
ε_0	vacuum permittivity
g_eff	effective g factor
$\hat{\mathcal{H}}$	Hamiltonian
h	Planck constant
$\hbar$	reduced Planck constant $h/2\pi$
i	imaginary unit, $\mathrm{i}^2 = -1$
k_B	Boltzmann constant
μ_B	Bohr magneton
$\mathbf{\Omega}$	Berry curvature
P	power spectrum
$\sigma_{x/y/z}$	Pauli matrices
v_F	Fermi velocity

Contents

1. Introduction

The fascination with colorful phenomena, such as rainbows, runs through the entire human history, as recounted e.g. in the book "The rainbow: from myth to mathematics" by Boyer [1]. Closely related to this fascination is the search for an understanding of the nature of light itself. Already in the era of the Roman empire, the natural philosopher Seneca observed the similarity of the colors created by a conically shaped glass rod and a rainbow. One of the first actual drawings of such a spectral decomposition based on systematic experiments was found in the notebooks of da Vinci. The famous polymath studied the rainbow colors projected onto the floor by light transmitted through air bubbles in a transparent glass of water, thus excluding his own eyes as origin of the phenomenon. The term *spectrum*, however, was only introduced by Newton about 200 years later, in 1672, in order to describe the colorful image the sun created in a prism. During the 19^{th} century, the discovery of dark lines in the solar spectrum, first by Wollaston and then, in refined resolution, by Fraunhofer, as well as of the dependence of a flame's color on the burned material by Brewster and Herschel, among others, revealed the relation between spectral lines and the matter with which the light interacts [2]. In 1859, Kirchhoff and Bunsen determined that the so-called Frauhofer lines in the solar spectrum allow conclusions about the elements that sunlight passes through on its way to earth [3]. Shortly after, in 1865, Maxwell published his famous differential equations, and thus established the classical understanding of light as an electromagnetic wave [4].

Nowadays, we additionally have a quantum mechanical interpretation of light, based on the introduction of energy quantization by Planck in 1901 [5] and the explanation of the photoelectric effect by Einstein in 1905 [6]. In this picture, light consists of photons, a massless particle with energy $E = h\nu$ depending on the light's frequency ν and quantized with Planck's constant $h = 4.135\ldots \cdot 10^{-15}\,\text{eV}\,\text{s}$. When interacting with atoms, molecules, or solids, photons with energy matching the energy difference between two electronic states of the material can be absorbed and excite an electron to a higher energy level. Equivalently, a photon of the same energy is emitted when the electron

relaxes back to its original state. Furthermore, this electronic relaxation can be triggered by the passing of another photon of the same energy. This process is called *stimulated emission* and was predicted by Einstein in 1917 [7]. It is the basic working principle of the laser, which was first developed in the middle of the twentieth century [8, 9]. Laser radiation is characterized by its long coherence length and a narrow beam width. It can be used to achieve high intensities of radiation and nearly monochromatic light, as well as to create ultrashort pulses which in turn contain a broader spectral window. Today, the application of lasers ranges from every-day life (e.g. DVD players or laser pointers), over industry (cutting tools) and medicine (corrective eye surgery), to fundamental research in the natural sciences. The significance of the laser and related scientific achievements is reflected in the award of more than 30 Nobel Prizes [10].

Just this year (2023), Agostini, Krausz, and L'Huillier were granted the Nobel Prize for their contributions to the development of "experimental methods that generate attosecond pulses of light for the study of electron dynamics in matter" [11]. The first step on the long road towards creating such pulses was the observation of high-harmonic generation (HHG) from noble gases by L'Huillier and coworkers in 1988 [12]. In short, this phenomenon arises when atoms, molecules, or solids interact with high-intensity laser fields. The laser field drives strongly nonlinear processes in the material, which in turn generate radiation at frequencies that are integer multiples of the incoming laser frequency. Even though L'Huillier et al. were not the first to measure HHG, their experiment was the first to reveal a very clear plateau, and to thus show what is nowadays considered the typical shape of a high-harmonics (HHs) spectrum: an intensity fall-off at the lowest-order harmonics, followed by a plateau over multiple frequencies, and then finally a cutoff with again decreasing intensity. It is the plateau, that was considered to provide the bandwidth necessary for the creation of very short pulses [13–15]. However, for an actual realization, first the mechanisms behind HHG from gases had to be understood. A first intuition was provided by L'Huillier et al. by solving the time-dependent Schrödinger equation for single electrons [16]. Soon after, the rescattering model [17] and the three-step model [18] were presented by Schafer et al. and Corkum, respectively. Both models are based on the idea that the laser field first ionizes the atom it interacts with. Then, the field accelerates the electron away from the ion. Since the field reverses in the next half-cycle, the electron is moved back towards the ion and may recombine with it. In this recombination process, the excess kinetic energy of the electron is emitted as a photon, and thus a higher harmonic of the original laser frequency is created. In 1994, these semiclassical interpretations were confirmed by a full quantum

theory [19]. Then, further experimental verification [20] and the development of techniques for measuring the duration of ultrashort pulses followed [21]. Finally, in 2001, the research groups of both Krausz and Agostini produced the first attosecond pulses. Krausz achieved isolated pulses of a duration of 650 as [22], whereas Agostini demonstrated a train of pulses with a duration of 250 as each [23]. By unlocking these ultrashort timescales, the ground for observing the dynamics of electrons in atoms, molecules, and solids was set.

In this work, we focus on theoretically investigating the dynamics of electrons in strongly driven Dirac systems. We propose the concept of *Floquet oscillations* induced by periodic driving and an additional constant bias, and study HHG from topological insulator (TI) surface states. Therefore, in the following we introduce the research field of *Floquet engineering* and the surge of topological concepts in condensed matter physics.

The creation of attosecond pulses is one of many technical advancements in the field of nonlinear light-matter interaction. Since the early days of laser physics, numerous scientists have worked on improving experimental methods and theoretical approaches to study nonlinear effects. One branch of research that emerged from these efforts is *Floquet engineering*. The goal of such engineering is to create new, exotic states of matter by modifying a system's properties with a time-periodic external potential, typically in form of a laser field. The influence of the applied potential is described by Floquet's theorem, a mathematical framework for the solution of linear differential equations with periodic coefficients [24]. The first publications using this theorem to solve the Schrödinger equation for time-periodic Hamiltonians, date from shortly after the invention of the laser [25–27]. They motivated the development of various formalisms to compute atomic and molecular multiphoton processes in intense laser fields based on Floquet's theorem, as summarized in the review article [28] by Chu and Telnov. Concerning crystalline solids, already in 1975, Tzoar and Gersten predicted that intense radiation can induce band-gap openings in the bandstructure. For their calculations, they combined Bloch and Floquet theory in order to treat the Schrödinger equation of a spatially and time-periodic Hamiltonian [29]. Even though this demonstrates that the concept of Floquet engineering is almost as old as the laser itself, new interest in this field arose with the discovery of novel quantum materials such as TIs [30, 31], Dirac and Weyl semimetals [32–34], as well as strongly correlated systems [35]. Floquet engineering is a tool for studying and creating such novel materials, as reviewed e.g. by Oka and Kitamura in Ref. [36]. In the following, we focus on TIs and the Dirac semimetal graphene.

The first experimentally observed fingerprints of topology in condensed matter physics were the integer and fractional quantum Hall effects in the 1980s, measured by von Klitzing, and Tsui and Störmer, respectively, and honored by Nobel Prizes in later years [37, 38]. The effects can be observed in two-dimensional (2D) electron gases at low temperatures under the influence of strong magnetic fields, and denote the integer/fractional quantization of the Hall resistance with the so-called Klitzing constant $R_{\mathrm{K}} = h/e^2$, where h is Planck's constant and e the elementary charge. The unusual robustness of the two effects against imperfections like disorder is a typical characteristic of a topologically protected system. The discovery of the quantum spin Hall effect in 2005 revealed, that there also exist material systems which have intrinsic topological properties [39]. Such TIs can be found in 2D and 3D structures. They are characterized by hosting 1D edge channels and 2D surface states, respectively, which are topologically protected by the presence of time-reversal symmetry (TRS). Up to now, only a few representatives of this new material class have been found, namely HgTe/CdTe quantum wells [40, 41] in 2D and Bi_2Se_3, [42], Bi_2Te_3 [43], and Sb_2Te_3 [44], as well as strained bulk HgTe [45] in 3D. Within this work, we focus on the 3D TI Bi_2Te_3. In lowest-order momentum approximation, the surface states of 3D TIs are described by a 2D Dirac cone. The surface states have a helical spin texture and feature spin-momentum locking, which means that the spin orientation is fixed by the momentum state and vice versa. Accordingly, scattering, i.e. a change of momentum, also requires a change of spin. This leads to a strong suppression of backscattering, since then the spin would also have to be flipped by 180°. The special properties of their surface states make TIs interesting candidates for applications ranging from spintronics to quantum computation [30]. Nevertheless, fundamental research is still working on uncovering their full potential.

Already in 1988, Haldane devised a theoretical model based on a 2D honeycomb lattice with nearest- and second-nearest-neighbor hopping, that exhibits a Hall effect without the presence of a magnetic field, if the hoppings are chosen such that TRS is broken [46]. Nowadays, this effect is denoted as the *anomalous Hall effect* and the corresponding topological phase as *Chern insulator* [47–49]. However, with the underlying 2D honeycomb lattice, Haldane's concept was considered a mere toy model for a long time, since the existence of a 2D structure was deemed as thermodynamically unstable [50, 51]. This changed, when Novoselov and Geim created 2D graphene sheets by exfoliation in 2004 [52], and it turned out that slight crumbling leads to stabilizing effects [53]. By breaking TRS of a graphene sheet with circularly polarized light, i.e. using Floquet engineering, an anomalous Hall phase is induced [54, 55], just as

predicted by the Haldane model [46]. Accordingly, Floquet engineering can be applied to introduce topological phases in matter. These *Floquet TIs*, as they were denoted by Lindner et al. [56], can mimic originally undriven topological phases, such as the Haldane model, but are also able to host a topological phase that does not have a counterpart in non-driven systems [57–64]. Due to the energy periodicity within the Floquet picture, edge states cannot only connect bands inside the first energy Brillouin zone (BZ), but also wrap around it, leading to peculiar consequences for the classifying topological invariant [65–69]. Good knowledge and understanding of the Floquet bandstructure is necessary to study this novel topological phase. The Floquet oscillations we propose in **Chap. 4** offer one possibility to map out Floquet bands and to gain deeper insights into the relation between the Floquet picture and a fully time-dependent description of a system. The concept behind Floquet oscillations is analogous to that of Bloch oscillations [70–72]. By applying a constant electric field, electrons are driven through the effective Floquet bandstructure. Since the electron velocity is determined by the quasi-energy dispersion, their motion in real space is proportional to the Floquet bands, thus effectively drawing a picture of them [73]. From the perspective of the time-dependent system, Floquet oscillations can be interpreted as consecutive jumps between valence and conduction band whenever the periodic driving is in resonance with the local energy gap. The opposite slopes of the two bands lead to a reversal of the electron's motion with every jump, thus explaining the oscillatory behavior [74]. We demonstrate these Floquet oscillations based on an effective Dirac Hamiltonian with two different time-periodic driving protocols and explore the experimental feasibility in graphene.

In **Chaps. 5**, **6**, and **7**, we leave the Floquet picture and time-periodic driving behind, and consider short laser pulses instead. We continue studying effective Dirac models, but focus on the surface states of the 3D TI Bi_2Te_3 rather than graphene. Our research aims at a better understanding of the interaction of the surface electrons with strong light fields and the resulting emission of high-order harmonics, as motivated in the following.

Experimental studies of TI surface states are often complicated by the need to separate the contributions of bulk and surface to the measured signal. For transport experiments, this issue can be circumvented by studying nanowires instead of bulk crystals, thereby reducing the ratio of bulk to surface area [75–77]. An alternative option is to use techniques that are only sensitive to the surface, such as angle-resolved photoemission spectroscopy (ARPES), which allows for the direct measurement of the surface bandstructure [42–44, 78, 79]. In 2018, a group of scientists around Huber achieved to take snapshots

of the charge currents induced in Bi_2Te_3 surface states by an intense THz laser pulse with subcycle time resolution using a time-resolved ARPES setup [80]. Their experiment demonstrated, that the scattering times of the surface currents are larger than 1 ps, making topological surface states a suitable platform for all-coherent lightwave-driven electronic devices. Additionally, the time-resolved observation of light-induced currents offers fascinating insights into how the electrons interact with the strong laser pulse. Another signature of strong-field light-matter interaction is the generation of HHs of the incoming pulse frequency. Within a collaboration of several experimental and theoretical groups, we contributed to the follow-up experiment of Huber et al., where the observation of HHG from Bi_2Te_3 surface states was achieved [81]. In this experiment, the bulk contribution to the emitted radiation was suppressed by tuning the laser pulse frequency below the bulk band gap. Then, no resonant transitions can occur in the bulk crystal, resulting in no free charge carriers to generate HH emission from the bulk. Due to the gapless spectrum of the surface states, however, no strong-field interband transitions are needed to obtain free charge carriers in these states, giving rise to efficient HHG even at relatively weak driving fields. Such efficient HHG from Dirac states has also been reported for graphene [82, 83] and the Dirac semimetal Cd_3As_2 [84]. The aforementioned long scattering times of the surface states additionally lead to the imprint of coherent transport effects in the HHs spectrum. For Bi_2Te_3 this gives rise to an alternating polarization of odd and even harmonics originating from the threefold symmetric Berry curvature of the surface states [85], which in turn is a consequence of the hexagonal warping term entering higher-order momentum expansions of the corresponding surface Hamiltonian [86–88]. Similar effects, as well as an anomalous laser-ellipticity dependence of the emitted harmonics, were observed for Bi_2Se_3 [89, 90]. Recent experiments even suggest that this ellipticity dependence can be used to distinguish between topologically trivial and non-trivial phases in Bi_2Se_3 [91], even though the existence of universal signatures of topological phases in HHG is still under debate [92].

For theoretical investigations of HHG in solids [93, 94], the most commonly used numerical methods are the semiconductor Bloch equations [95], time-dependent density functional theory (DFT) [96, 97] and methods based on solving the time-dependent Schrödinger equation [98]. Despite these various theoretical approaches, there still remain open questions about the interplay of the different quantum processes occurring during the highly nonlinear interaction of the laser field and the sample. In **Chap. 5**, we present our theoretical studies on the processes that take place when electrons in effective Dirac systems are accelerated by a strong THz pulse. We compare the

results of four different Dirac-based models with focus on the Bi_2Te_3 surface states. Our findings highlight, how the Berry curvature imprints on the dynamics with orientation perpendicular to the laser polarization, and thus also determines whether only odd or also even order harmonics are emitted from the system. We consider single test charges that are narrow in momentum space in order to disentangle contributions from different transition regimes. For the actual computation of HHs spectra, however, methods considering only single active electrons [99–101] have proven to be rather limited. They neglect the interference of the emission from different states, which results in the emergence of peak structures that vanish when computing the spectrum for an actual Fermi sea [102]. Therefore, approaches calculating HHG in solids typically integrate over the full BZ [98, 103–105]. This is not possible for effective models, since they have no periodic structure in momentum space and are only valid within a certain energy range [106]. In simulations using the semiconductor Bloch equations for effective Dirac and semiconductor models, a filled band is approximated by including finite dephasing times and converging the resulting HHs spectra with respect to the included momentum space [107, 108]. In **Chap. 6**, we develop a complementary approach based on solving the time-dependent Schrödinger equation without dephasing for wave packets that cover a vast momentum-space area. Instead of converging the full spectra, we limit the included momentum states by approximately converging the intraband contribution only, thus assuming strong dephasing for all states outside of the considered area. Our new method delivers clean HHs spectra and reproduces the polarization rotation experimentally observed for the Bi_2Te_3 surface. Additionally, restricting the evaluated momentum space reveals a plateau in the HH spectrum that does not emerge without choosing a fixed boundary for the evaluation. Another advantage of our presented method is that it can treat Hamiltonians that depend both on position and momentum, without facing issues like fermion doubling [109–111]. This allows for including orbital magnetic field effects, which are typically neglected in studies of HHG. In **Chap. 7**, we give a first perspective on how magnetic fields affect HHG in effective Dirac systems, aiming at including light as an electro*magnetic* wave instead of approximating it as an electric field only. Still, within this thesis, we focus on static magnetic fields in addition to the electric laser pulse. We find that external, out-of-plane magnetic fields are particularly promising candidates for tuning the frequencies of the emitted harmonics with polarization perpendicular to the driving field. The gap opened by the Zeeman coupling competes with the hexagonal warping of the Bi_2Te_3 surface states and gives rise to additional emission at odd orders. Moreover, the circular electron motion induced by the orbital coupling potentially amplifies the perpendicular emission due to Berry phase effects.

Before we present a detailed discussion of the results already touched upon in the previous paragraphs, we introduce the basic concepts relevant for our work in **Chaps. 2** and **3**. We conclude this thesis with a summary and a brief overview of interesting questions for future research in **Chap. 8**.

2. Basic concepts

2.1. Effective Dirac Hamiltonians

Throughout this thesis, we focus on systems with description based on effective Dirac Hamiltonians. Two prominent examples of Dirac systems in condensed matter are graphene [32, 52] and the surface states of TIs [30, 31, 40, 41]. However, it is also possible to achieve systems with Dirac dispersion for cold atoms in artificial honeycomb lattices [112], for plasmons [113] and polaritons [114], among others.

In this work, we first study Floquet oscillations in effective Dirac systems and consider graphene as a candidate for the experimental realization. Afterwards, we focus on TIs and their surface states. From a physical viewpoint, their effective Dirac Hamiltonians have different origins. For graphene, the spinor structure stems from the pseudospin, related to the sublattices A and B. In TI surfaces, on the other hand, the spinor is directly related to the real electron spin. These material-dependent properties influence e.g. the coupling of the system to magnetic fields. Mathematically however, the effective Dirac Hamiltonians of graphene and TI surface states are similar up to first-order approximation. For higher-order approximations graphene and TI surface states become different. In this section we introduce the most important aspects of both systems, concentrating on the 3D TIs Bi_2Se_3, Bi_2Te_3 and Sb_2Te_3, highlighting the differences and similarities relevant for our work.

2.1.1. Graphene

The first theoretical description of graphene dates back to 1947 when Wallace studied graphite. He considered it as many monolayers of hexagonal carbon lattices, i.e. graphene sheets, stacked on top of each other and bound together by van der Waals forces [115]. Even though for a long time it was believed that

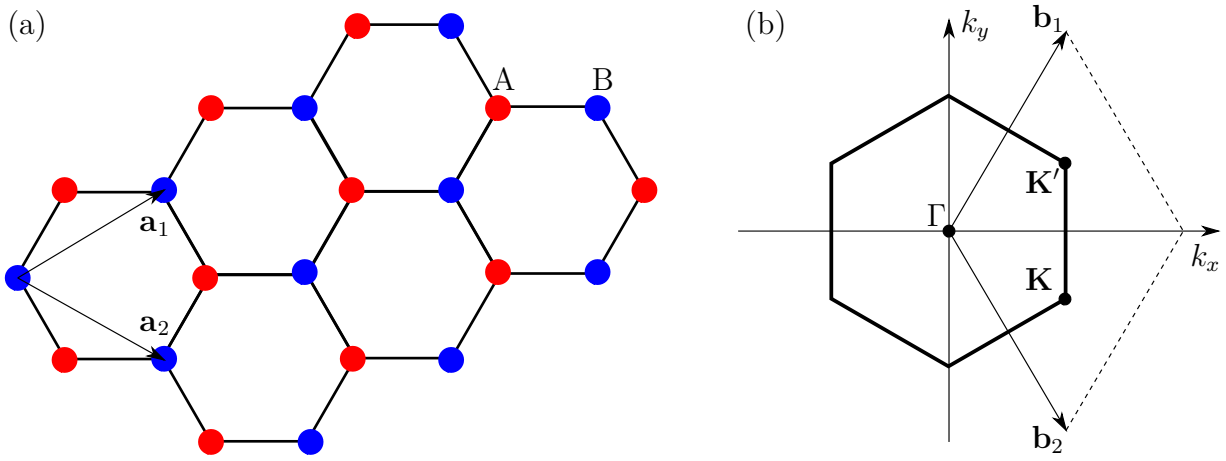

Fig. 2.1: (a) Crystal structure of graphene. The arrows indicate the lattice vectors $\mathbf{a}_1 = \frac{a}{2}\left(3, \sqrt{3}\right)$ and $\mathbf{a}_2 = \frac{a}{2}\left(3, -\sqrt{3}\right)$ and the red and blue dots mark the two sublattices A and B, respectively. (b) Reciprocal lattice of graphene. $\mathbf{K}$ and $\mathbf{K}'$ are the high symmetry points where the Dirac cones are located. $\mathbf{b}_1 = \frac{2\pi}{3a}\left(1, \sqrt{3}\right)$ and $\mathbf{b}_2 = \frac{2\pi}{3a}\left(1, -\sqrt{3}\right)$ are the reciprocal lattice vectors.*

* Figure taken from [123].

fabricating such strictly two dimensional (2D) structures is impossible since they should be thermodynamically unstable [50, 51], graphene sheets became of theoretical interest due to their relation to quantum electrodynamics [116]. Graphene as quantum system governed by the Dirac equation could offer a playground for studying quantum relativistic effects.

In 2004 Novoselov and Geim discovered that in fact graphene sheets could be produced by exfoliation [52] thanks to the stabilizing effect of slight crumbling [53]. Finally, the stage for accessible experiments on such systems was set. Shortly after the first demonstration, they observed various characteristics of massless Dirac fermions in graphene [117], including an anomaly of the integer quantum Hall effect [118] and the relation $E = m_c c*^2$ for the cyclotron mass m_c and the Fermi velocity $v_F = c* = 10^6\,\mathrm{m\,s^{-1}}$. Even the famous Klein paradox [119], predicted already in 1929, was eventually experimentally confirmed in graphene [120, 121]. Their contribution to these advancements in science earned Novoselov and Geim the Nobel prize in 2010.

In the following, we summarize the derivation of the Dirac Hamiltonian as low-energy approximation from the tight-binding description of graphene based on the publication of Sasaki and Saito [122]. Note that this summary is partially adapted from my master's thesis [123]. For a very detailed overview of graphene and its properties we recommend Katsnelson's book [124], which was also used for writing part of this section.

Graphene is a 2D sheet of carbon atoms forming a honeycomb crystal lattice. Its crystal structure, described by the lattice vectors

$$\mathbf{a}_1 = \frac{a}{2}\left(3, \sqrt{3}\right), \ \mathbf{a}_2 = \frac{a}{2}\left(3, -\sqrt{3}\right), \tag{2.1}$$

with nearest-neighbor distance $a \approx 1.4\,\text{Å}$, is depicted in Fig. 2.1(a). It is made up of two sublattices A and B, and the elementary cell consists of two atoms. As shown in Fig. 2.1(b), the corresponding reciprocal lattice, defined by the lattice vectors

$$\mathbf{b}_1 = \frac{2\pi}{3a}\left(1, \sqrt{3}\right), \ \mathbf{b}_2 = \frac{2\pi}{3a}\left(1, -\sqrt{3}\right), \tag{2.2}$$

is again hexagonal but rotated by 90° against the lattice in real space. The marked high-symmetry points $\mathbf{K}$ and $\mathbf{K}'$ have the coordinates

$$\mathbf{K} = \left(\frac{2\pi}{3a}, \frac{2\pi}{3\sqrt{3}a}\right) \ , \quad \mathbf{K}' = \left(\frac{2\pi}{3a}, -\frac{2\pi}{3\sqrt{3}a}\right). \tag{2.3}$$

Around these points, the bandstructure can be approximated by the Dirac Hamiltonian for low energies, giving rise to graphene's relativistic properties. For the derivation, one starts with the tight-binding model

$$\hat{\mathcal{H}}_0 = -\gamma_0 \sum_{i\in \mathrm{A}} \sum_{a=1,2,3} \left(\left(c^{\mathrm{B}}_{i+a}\right)^\dagger c^{\mathrm{A}}_i + \left(c^{\mathrm{A}}_i\right)^\dagger c^{\mathrm{B}}_{i+a} \right), \tag{2.4}$$

with nearest-neighbor hopping $\gamma_0 = 2.7\,\text{eV}$ and the annihilation (creation) operators c^{A}_i ($(c^{\mathrm{A}}_i)^\dagger$) for sublattice A at position $\mathbf{r}_i$ and c^{B}_{i+a} ($(c^{\mathrm{B}}_{i+a})^\dagger$) for sublattice B at position $\mathbf{r}_{i+a} = \mathbf{r}_i + \mathbf{R}_a$. Here, $\mathbf{R}_a$, with $a = 1, 2, 3$, points to the three nearest-neighbor atoms in sublattice B as seen from an atom in sublattice A.

To find the eigenenergies of Eq. (2.4), one applies Bloch's theorem and by choosing the basis states

$$\begin{aligned} |\Psi^{\mathbf{k}}_{\mathrm{A}}\rangle &= \frac{1}{\sqrt{N_u}} \sum_{i\in \mathrm{A}} \mathrm{e}^{\mathrm{i}\mathbf{k}\cdot\mathbf{r}_i} (c^{\mathrm{A}}_i)^\dagger |0\rangle, \\ |\Psi^{\mathbf{k}}_{\mathrm{B}}\rangle &= \frac{1}{\sqrt{N_u}} \sum_{i\in \mathrm{B}} \mathrm{e}^{\mathrm{i}\mathbf{k}\cdot\mathbf{r}_i} (c^{\mathrm{A}}_i)^\dagger |0\rangle, \end{aligned} \tag{2.5}$$

with N_u being the number of hexagonal cells, $|0\rangle$ the vacuum state and $\mathbf{k} = (k_x, k_y)$, obtains the eigenequation in (2×2) matrix form as

$$E(\mathbf{k}) \begin{pmatrix} |\Psi^{\mathbf{k}}_{\mathrm{A}}\rangle \\ |\Psi^{\mathbf{k}}_{\mathrm{B}}\rangle \end{pmatrix} = -\gamma_0 \begin{pmatrix} 0 & f(\mathbf{k}) \\ f(\mathbf{k})^* & 0 \end{pmatrix} \begin{pmatrix} |\Psi^{\mathbf{k}}_{\mathrm{A}}\rangle \\ |\Psi^{\mathbf{k}}_{\mathrm{B}}\rangle \end{pmatrix}. \tag{2.6}$$

Diagonalization of (2.6) gives the eigenenergies

$$E(\mathbf{k}) = \pm\gamma_0|f(\mathbf{k})|, \text{ with } f(\mathbf{k}) = \sum_{a=1}^{3} f_a(\mathbf{k}) = \sum_{a=1}^{3} \mathrm{e}^{\mathrm{i}\mathbf{k}\cdot\mathbf{R}_a}, \tag{2.7}$$

where $(+)$ is the conduction and $(-)$ the valence band. At the $\mathbf{K}$ ($\mathbf{K}'$) point, where $\mathbf{k} = \mathbf{k}_F$ ($\mathbf{k} = -\mathbf{k}_F$), $|f(\mathbf{k})| = 0$. Thus, conduction and valence band touch in these points and one obtains the low-energy Hamiltonian by expanding $f_a(\mathbf{k})$ around them. Up to first order in $\mathbf{k}$, at the $\mathbf{K}$ point Eq. (2.6) gives

$$E(\mathbf{k}_\mathrm{F}+\mathbf{k}) \begin{pmatrix} |\Psi_\mathrm{A}^{\mathbf{k}_\mathrm{F}+\mathbf{k}}\rangle \\ |\Psi_\mathrm{B}^{\mathbf{k}_\mathrm{F}+\mathbf{k}}\rangle \end{pmatrix} = \frac{3\gamma_0 a_\mathrm{CC}}{2} \begin{pmatrix} 0 & k_x - \mathrm{i}k_y \\ k_x + \mathrm{i}k_y & 0 \end{pmatrix} \begin{pmatrix} |\Psi_\mathrm{A}^{\mathbf{k}_\mathrm{F}+\mathbf{k}}\rangle \\ |\Psi_\mathrm{B}^{\mathbf{k}_\mathrm{F}+\mathbf{k}}\rangle \end{pmatrix}, \tag{2.8}$$

where $a_\mathrm{CC} = a/\sqrt{3}$ is the atom-atom bond length. In short, Eq. (2.8) defines the Dirac Hamiltonian

$$\hat{\mathcal{H}}_0^{\mathbf{K}} = \hbar v_\mathrm{F} \mathbf{k}\cdot\boldsymbol{\sigma}, \tag{2.9}$$

with Fermi velocity $v_\mathrm{F} = \gamma_0 3a_\mathrm{CC}/2\hbar$ ($\sim 10^6\,\mathrm{m\,s^{-1}}$) and the vector of the Pauli matrices $\boldsymbol{\sigma} = (\sigma_x, \sigma_y)$. In graphene, the latter are operators in pseudospin space, originating from the sublattices A and B. The derivation at the $\mathbf{K}'$ point is analogous and gives

$$\hat{\mathcal{H}}_0^{\mathbf{K}'} = \hbar v_\mathrm{F} \mathbf{k}\cdot\boldsymbol{\sigma}', \tag{2.10}$$

with $\boldsymbol{\sigma}' = (-\sigma_x, \sigma_y)$, being the negative complex conjugate of the Hamiltonian at the $\mathbf{K}$ point. Accordingly, the physics at both points are similar. Since for our work we only consider the low-energy approximation and neglect coupling between the $\mathbf{K}$- and $\mathbf{K}'$-valley, we will concentrate on the $\mathbf{K}$ point whenever we consider graphene.

The eigenenergies of the Dirac Hamiltonian Eq. (2.9) are sketched in Fig. 2.2(a) and given by

$$E_\pm(\mathbf{k}) = \pm\hbar v_\mathrm{F}|\mathbf{k}| \equiv \pm\hbar v_\mathrm{F} k, \tag{2.11}$$

with the length $|\mathbf{k}| \equiv k = \sqrt{k_x^2 + k_y^2}$. Up to this order, the spectrum is linear and rotational symmetric. It is also called *Dirac cone* and consists of two branches marked in red and blue. Due to the opposed slopes of these branches [125], their constant group velocity has opposite directions

$$\mathbf{v}_\mathrm{g} = \frac{1}{\hbar}\frac{\mathrm{d}E(\mathbf{k})}{\mathrm{d}\mathbf{k}} = \pm v_\mathrm{F}, \tag{2.12}$$

where $(+)$ is the blue and $(-)$ the red branch. This property will play an important role for the Floquet oscillations introduced in Sec. 4.3. For

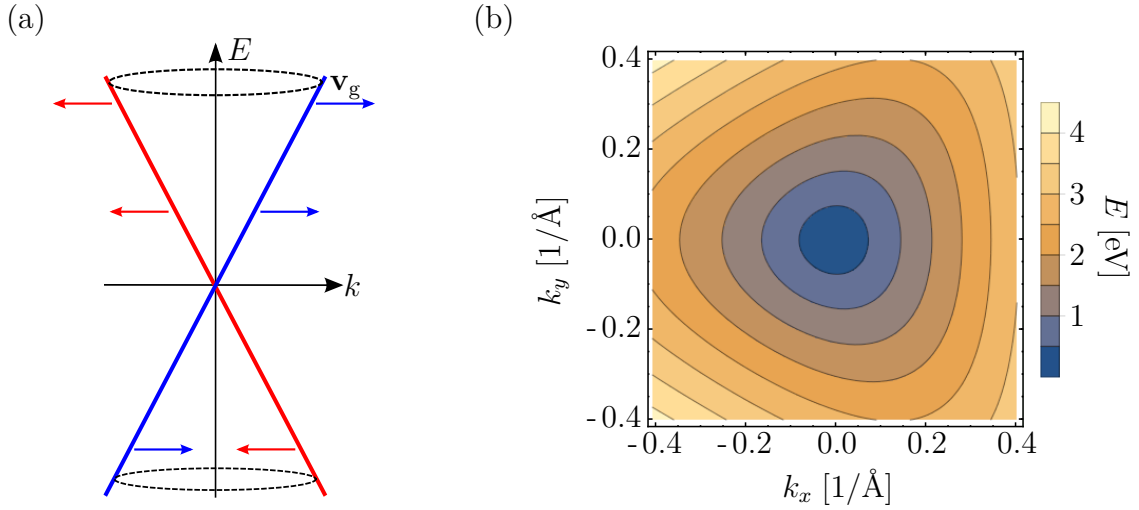

Fig. 2.2: (a) Dirac cone at the **K**-point of graphene.* Its two different branches with opposed group velocities $\mathbf{v}_g$ are shown in red and blue. (b) Energy contour of graphene around the **K**-point in second order approximation (Eq. (2.15)). Between $0.5 - 1\,\mathrm{eV}$ the threefold symmetry of the trigonal warping starts to appear. For lower energies, the Dirac Hamiltonian (Eq. (2.10)) provides a sufficient model.
* Panel (a) adapted from [123, 126].

computing the full velocity of a wave function in a Dirac system, one needs the velocity operator $\hat{\mathbf{v}}$ of the Dirac Hamiltonian (2.9). It reads

$$\hat{\mathbf{v}} = \frac{\mathrm{i}}{\hbar}\left[\hat{\mathcal{H}}_0^{\mathbf{K}}, \hat{\mathbf{r}}\right] = \frac{\mathrm{i}}{\hbar}\left[\hat{\mathcal{H}}_0^{\mathbf{K}}, \mathrm{i}\nabla_{\mathbf{k}}\right] = v_{\mathrm{F}}\boldsymbol{\sigma}, \tag{2.13}$$

with $\hat{\mathbf{r}} = \mathrm{i}\nabla_{\mathbf{k}}$ being the position operator represented in k space.

The eigenstates in k space are spinors of the form

$$\varphi_{\pm}(\mathbf{k}) = \langle \mathbf{k}|\varphi_{\mathbf{k},\pm}\rangle = \frac{1}{\sqrt{2}}\begin{pmatrix} 1 \\ \pm \mathrm{e}^{\mathrm{i}\theta_{\mathbf{k}}} \end{pmatrix}, \tag{2.14}$$

where $\theta_{\mathbf{k}} = \arctan(k_y/k_x)$ defines the polar angle. To achieve the sign convention such that $(+)$ revers to the conduction and $(-)$ to the valence band, we use $\theta_{\mathbf{k}} = \arctan2(k_x, k_y)$ throughout this work.

The Dirac cone approximation in Eq. (2.10) is only valid in the limit $|\mathbf{k}|a \ll 1$ [127]. When investigating the experimental feasibility of Floquet oscillations in graphene in Sec. 4.5.2, we will include the second order in the approximation of $f_a(\mathbf{k})$ from Eq. (2.7) around the **K** point. This adds a trigonal warping term to the Dirac Hamiltonian, modifying it to

$$\hat{\mathcal{H}}_0^{\mathbf{K}} = \hbar v_{\mathrm{F}}\mathbf{k}\cdot\boldsymbol{\sigma} - \mu\left[\left(k_y^2 - k_x^2\right)\sigma_x + 2k_xk_y\sigma_y\right], \tag{2.15}$$

where $\mu = 3a^2\gamma_0/8$ [124]. The trigonal warping breaks the rotational symmetry of the energy dispersion, implementing a threefold symmetry instead. The

transition from one symmetry to the other between $0.5 - 1\,\mathrm{eV}$ is shown in the contour plot of the (positive) eigenenergies

$$E_{\pm}(\mathbf{k}) = \pm\sqrt{(\hbar v_{\mathrm{F}} k_x - \mu(k_y^2 - k_x^2))^2 + (\hbar v_{\mathrm{F}} k_y - 2\mu k_x k_y)^2} \tag{2.16}$$

of Eq. (2.15) in Fig. 2.2(b). As stated e.g. in the review by Goerbig, this second-order expansion is indistinguishable from the full tight-binding model up to energies of 1 eV and still a good approximation for up to 2 eV [127].

2.1.2. Topological insulator surface states

The concept of *topology* plays an important role in condensed matter physics nowadays. Phenomena such as the integer and fractional quantum Hall effect [37, 38] can be explained using the principles of topology. In 2005, with the discovery of the quantum spin Hall effect in HgTe quantum wells, a new class of topological materials was introduced: so-called *topological insulators* (TIs) [39–41]. These materials feature an insulating bulk but host conducting surface states that are defined by an odd number of Dirac cones[1] in lowest-order momentum approximation. The surface states are topologically protected by TRS and robust against any deformation as long as TRS is not broken. As we will discuss in detail later on, these states feature spin-momentum locking. Therefore, electronic backscattering is strongly suppressed. HgTe quantum wells are 2D TIs with one-dimensional (1D) edge channels. Within this work, we focus on three-dimensional (3D) TIs, where the surface states live in 2D and wrap around the entire crystal.

The origin of the surface states lies within the ordering and parity of the bulk bands. By studying which atomic orbitals form valence and conduction band, one can determine whether a material is topologically trivial or non-trivial. In topologically trivial semiconductors and insulators, the valence band has negative parity, whereas the parity of the conduction band is positive around the Γ point of the Brillouin zone (BZ). In TIs, the band ordering is inverted, i.e. the conduction band has negative and the valence band positive parity. Whenever two materials are brought into contact, at the interface their bands have to continuously transform into one another. However, this is not possible for bands with different parity, since their states are orthogonal with respect to each other. Hence, when a material of non-trivial topology is brought into

[1] Note that this does not contradict the Nielsen-Ninomiya theorem [109–111] discussed in the context of fermion doubling in Sec. 3.1, since counted over all surfaces a TI hosts an even number of Dirac cones.

contact with a trivial one, one band has to move down in energy and the other up such that bands of the same parity connect. The inverted band order inevitably leads to a band crossing and thus the formation of a Dirac cone at the interface. Since vacuum states are also of trivial topology, a TI hosts Dirac states at its surface even without being in contact with a semiconductor or trivial insulator.

In 2008, the first observation of the surface states of a 3D TI was achieved in ARPES experiments on the alloy $Bi_{0.9}Sb_{0.1}$ [78, 79]. Shortly after, the prediction [86] and experimental confirmation of the 3D TIs Bi_2Se_3 [42], Bi_2Te_3 [43], and Sb_2Te_3 [44] followed. It was also demonstrated that strain can induce a topological phase in bulk HgTe crystals [128]. In this section, we introduce the model Hamiltonian for the surface states of 3D TIs in the Bi_2Se_3 family, namely Bi_2Se_3, Bi_2Te_3, and Sb_2Te_3, following the derivations of Refs. [86, 87]. These materials host a single Dirac cone on their surface with a spectrum altered by a hexagonal warping term, which is especially significant in Bi_2Te_3 [88]. Among others, the warping is predicted to induce an angle-dependence in the Andreev reflection at a TI - superconductor junction [129] and changes the charge [130], spin [131], thermoelectric [132], and optical [133] conductivity of the surface states.

Bi_2Se_3 (and analogously Bi_2Te_3 and Sb_2Te_3) has a rhombohedral crystal structure with space group D^5_{3d} ($R\bar{3}m$). Its unit cell consists of two Bi and three Se atoms lying on different atomic layers. Hence, five of these layers can be viewed as one unit, also called quintuple layer. Within this layer structure, one can distinguish two types of Se atoms: the one in the center (Se2) and the two at the borders (Se1) of the quintuple layer (see Fig. 2.3(a)). The atomic layers each form a triangular lattice of different positions A, B and C as shown in Fig. 2.3(b) and are stacked along the z axis with ordering A-B-C-A-B-C-... . The crystal has threefold rotation symmetry R_3 along the z direction, twofold rotation symmetry R_2 along the x direction, inversion symmetry with respect to the central Se layer and TRS. To see why Bi_2Se_3 is a 3D TI, a closer look at the atomic orbitals forming its bandstructure is necessary.

The electron configuration of a single Se atom is $4s^24p^4$ and that of a Bi atom $6s^26p^3$. For both elements, the outmost occupied shells are p orbitals, therefore all other orbitals can be neglected when searching for conduction and valence bands of Bi_2Se_3. Since neighboring quintuple layers of Bi_2Se_3 are only coupled by van der Waals force and chemical bonding within one layer is very strong, it is reasonable to start by considering only a single layer. As already discussed, the unit cell within one quintuple layer consists of five

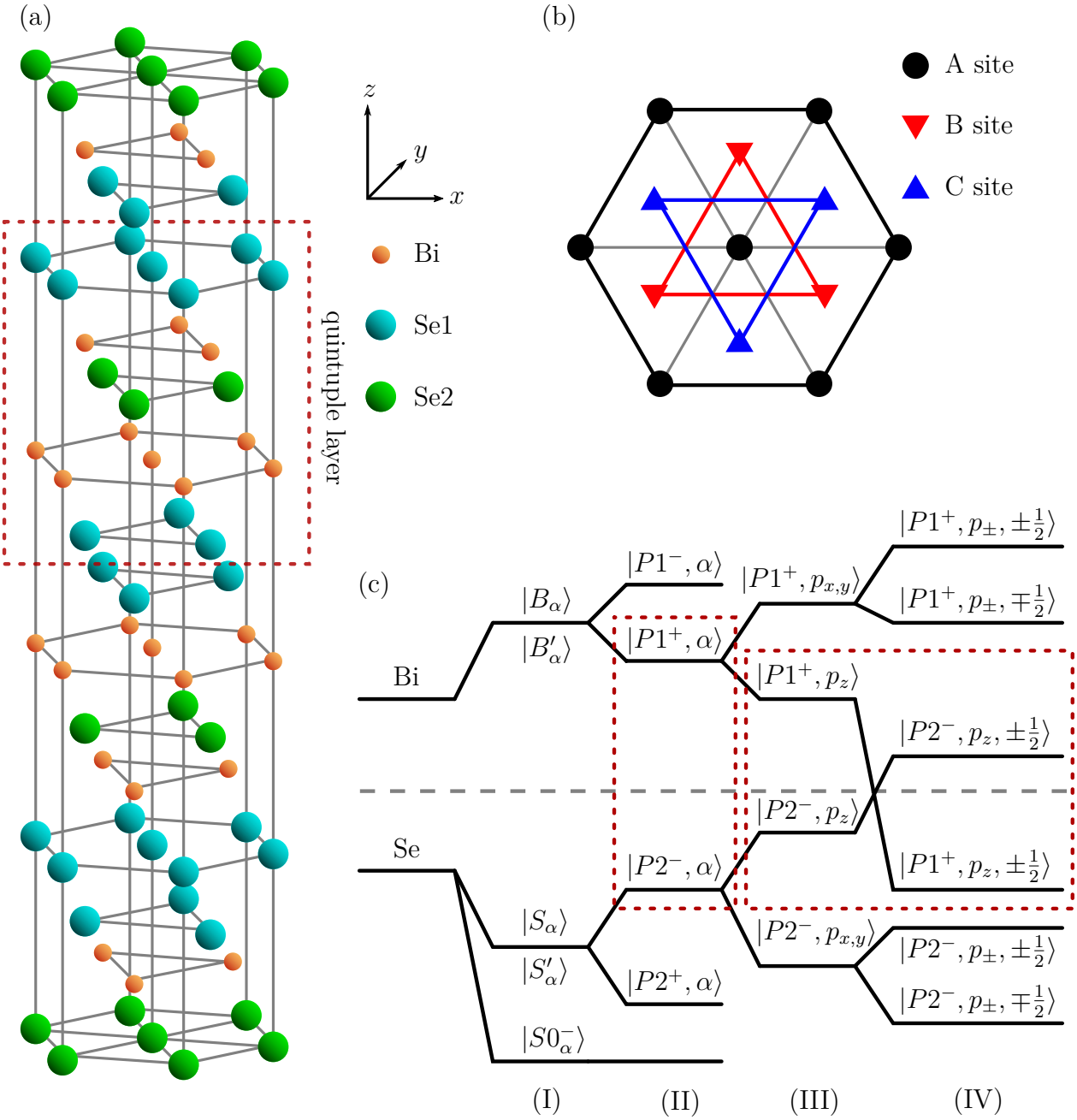

Fig. 2.3: (a) Crystal structure of Bi_2Se_3. The red box marks one quintuple layer consisting of two Bi layers and three Se layers, where the two layers at the border (Se1) are distinguished from the one in the center (Se2). (b) In-plane projection of the different positions A, B, C of the triangular lattices. (c) Sketch of the bandstructure formation out of the atomic orbitals of Bi and Se. It is divided into four steps: (I) hybridization of Bi and Se orbitals, (II) inversion symmetry allowing for the formation of bonding and anti-bonding states with definite parity that split in energy, (III) crystal field splitting lifting the degeneracy between $p_{x,y}$ and p_z orbitals, and (IV) SOC inducing a level repulsion that finally leads to band inversion around the Fermi energy. The red boxes highlight the most important orbitals.*

* Figure adapted from [86, 87].

atoms. Each atom has three orbitals $p_{x,y,z}$, giving a total of 15 orbitals per unit cell, where spin is neglected for now. As displayed in Fig. 2.3(a), Bi and Se layers alternate within one quintuple layer. Thus, the strongest coupling occurs between Bi and Se layers. This results in a level repulsion, increasing (decreasing) the energy levels of Bi (Se) and leading to two (three) hybridized states $|B_\alpha\rangle$ and $|B'_\alpha\rangle$ ($|S_\alpha\rangle$, $|S'_\alpha\rangle$ and $|S0_\alpha\rangle$), where $\alpha = p_{x,y,z}$, see Fig. 2.3(c), step (I). Due to inversion symmetry, these orbitals can be combined to bonding and anti-bonding states with definite parity

$$|P1^\pm, \alpha\rangle = \frac{1}{\sqrt{2}}\left(|B_\alpha\rangle \mp |B'_\alpha\rangle\right) \quad \text{and} \quad |P2^\pm, \alpha\rangle = \frac{1}{\sqrt{2}}\left(|S_\alpha\rangle \mp |S'_\alpha\rangle\right), \tag{2.17}$$

where the upper index ($\pm$) marks the parity. The coupling between $|B_\alpha\rangle$ and $|B'_\alpha\rangle$ ($|S_\alpha\rangle$ and $|S'_\alpha\rangle$) gives rise to an energy splitting of bonding and anti-bonding states, the former being energetically favorable, see Fig. 2.3(c), step (II). As a consequence, $|P1^+, \alpha\rangle$ and $|P2^-, \alpha\rangle$ are the orbitals closest to the Fermi energy and the other states can be neglected when constructing conduction and valence band. The next effect that has to be taken into account is the crystal field splitting. Due to the layered structure, the z direction differs from the atomic planes in x and y direction. As a consequence, the energetic degeneracy between p_z and $p_{x,y}$ orbitals is lifted both for the $P1^+$ and $P2^-$ states. The $|P1^+, p_{x,y}\rangle$ and $|P2^-, p_z\rangle$ orbitals rise in energy, whereas the $|P1^+, p_z\rangle$ and $|P2^-, p_{x,y}\rangle$ orbitals are pushed down, see Fig. 2.3(c), step (III). Thus, so far the valence band mainly consists of $|P2^-, p_z\rangle$ orbitals and the conduction band of $|P1^+, p_z\rangle$. Finally, one has to introduce the spin and consider spin-orbit coupling (SOC). The states get an additional label $\sigma = \pm\frac{1}{2}$, resulting in $|P1^+, \alpha, \sigma\rangle$ and $|P2^-, \alpha, \sigma\rangle$. A transformation of the $p_{x,y}$ orbitals to $p_\pm$ gives states with definite orbital angular momentum

$$|\Lambda, p_\pm, \sigma\rangle = \mp\frac{1}{\sqrt{2}}\left(|\Lambda, p_x, \sigma\rangle \mp \mathrm{i}|\Lambda, p_y, \sigma\rangle\right), \tag{2.18}$$

where $\Lambda = P1^+, P2^-$. A careful analysis of the SOC (see Refs. [86, 87]) shows that it couples the states $|\Lambda, p_z, +\frac{1}{2}\rangle$ ($|\Lambda, p_z, -\frac{1}{2}\rangle$) to $|\Lambda, p_+, -\frac{1}{2}\rangle$ ($|\Lambda, p_-, +\frac{1}{2}\rangle$), inducing a level repulsion between them. This pushes $|P2^-, p_z, \pm\frac{1}{2}\rangle$ up while $|P1^+, p_z, \pm\frac{1}{2}\rangle$ is pushed down, leading to a level crossing of these two pairs of states for sufficiently large SOC, see Fig. 2.3(c), step (IV). In Bi_2Se_3, Bi_2Te_3 and Sb_2Te_3 SOC is large enough and the levels cross. Due to the opposite parity of the crossing states band inversion is achieved, making Bi_2Se_3 (and analogously Bi_2Te_3 and Sb_2Te_3) representatives of the class of 3D TIs.

Up to first order in momentum $\mathbf{k} = (k_x, k_y)$ the surface states of 3D TIs are

described by a Dirac Hamiltonian. For the Bi_2Se_3 family, one finds [86–88]

$$\hat{\mathcal{H}}_0(\mathbf{k}) = A(k_y\sigma_x - k_x\sigma_y), \tag{2.19}$$

where $A = \hbar v_\mathrm{F}$ is the slope determined by the Fermi velocity v_F and $\sigma_{x,y}$ are the Pauli matrices. The eigenstates

$$\varphi_\pm(\mathbf{k}) = \langle \mathbf{k}|\varphi_{\mathbf{k},\pm}\rangle = \frac{1}{\sqrt{2}}\begin{pmatrix} 1 \\ \pm \mathrm{e}^{\mathrm{i}\theta'_\mathbf{k}} \end{pmatrix}, \tag{2.20}$$

of (2.19) take the same form as the spinors of the low-energy approximation of graphene, see Eq. (2.14), but here $\theta'_\mathbf{k} = \arctan(-k_y/k_x)$. One can show that, in contrast to the Dirac Hamiltonian of graphene, see Eq. (2.10), the Pauli matrices $\sigma_{x,y,z}$ act in spin space for 3D TI surface states. Thus, also the spinors (2.20) are linked to the spin states at the respective momentum[2]. This property is called *spin-momentum locking*. Around the Dirac point $|\mathbf{k}| = 0$ the spin texture of TI surface states is helical, similar to a Fermi surface in a trivial 2D electron gas with Rashba SOC. However, the Fermi surface of the latter consists of two closed curves, whereas the Dirac cone consists of only one. Hence, in the TI surface backscattering, i.e. $\mathbf{k} \to -\mathbf{k}$ or vice versa, would also require flipping the spin and therefore is strongly suppressed [134].

As already mentioned, for higher orders in momentum the spectrum of the surface states is altered by a hexagonal warping term. That this term is different from the higher-order expansion of the Dirac Hamiltonian in graphene given in Eq. (2.15) is a consequence of the Pauli matrices representing the pseudospin in graphene but the real electron spin in the 3D TIs, since the time-reversal operator acts differently on these two spaces [88]. Additionally, particle-hole symmetry (PHS) is broken for the TI surface states. Respecting the crystal symmetry and TRS, up to third order in momentum one finds the Hamiltonian [87, 88]

$$\hat{\mathcal{H}}(\mathbf{k}) = C\mathbb{1} + \underbrace{D(k_x^2 + k_y^2)\mathbb{1}}_{\text{PHS breaking}} + \underbrace{A(k_y\sigma_x - k_x\sigma_y)}_{\hat{\mathcal{H}}_0(\mathbf{k})} + \underbrace{2R(k_x^3 - 3k_xk_y^2)\sigma_z}_{\text{hexagonal warping}}, \tag{2.21}$$

with unit matrix $\mathbb{1}$. In this representation k_x points along the $\overline{\Gamma\mathrm{K}}$ and k_y along the $\overline{\Gamma\mathrm{M}}$ direction of the surface's BZ. This corresponds to the x and y direction of the surface in real space, respectively. The prefactors C, D, A and R depend on the material. In this work we focus on Bi_2Te_3, since there the hexagonal warping is strongest. The literature values for the prefactors differ slightly [87, 88]. For concreteness we choose

[2]Note that we do not say that spinor and spin state are equal since in fact the Pauli matrices are only proportional to the actual spin operators. Accordingly, spinor and spin are also linked by this proportionality.

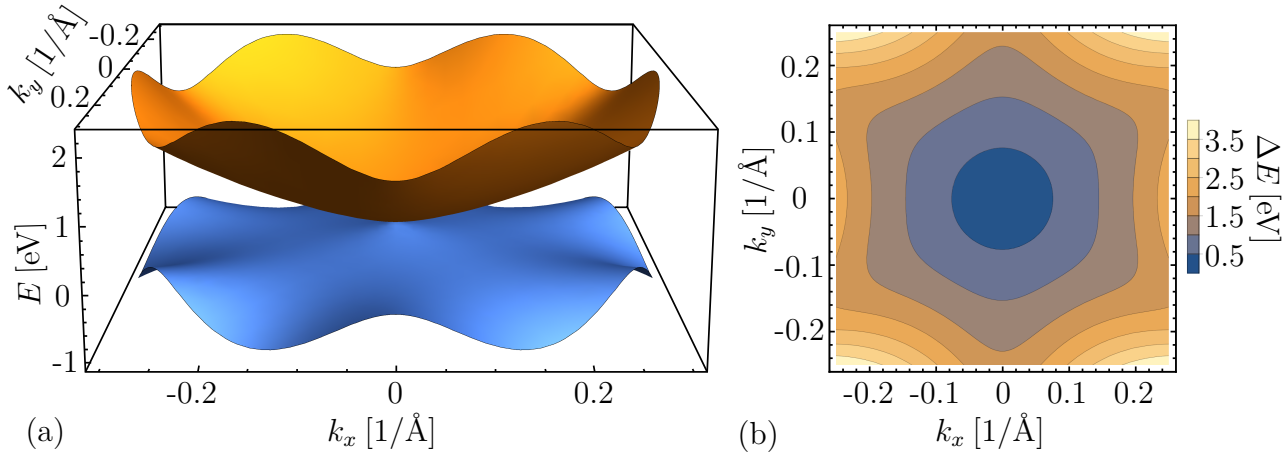

Fig. 2.4: (a) Bandstructure of Bi_2Te_3 for our model system cut at $|\mathbf{k}| = \sqrt{k_x^2 + k_y^2} = 0.3\,\text{Å}^{-1}$. The hexagonal warping and PHS breaking lead to a distortion of the Dirac cone. (b) Energy difference ΔE between both bands. For small $|\mathbf{k}|$, the rotational symmetry of the Dirac cone is visible. Then, the sixfold symmetry due to the hexagonal warping emerges. The PHS breaking does not affect the energy difference between the bands.

C	A	D	R
0 eV	3.2718 eVÅ	8.9402 eV Å^2	25.6614 eV Å^3

from Ref. [87] for our calculations[3]. It is important to mention that with this model only qualitatively correct results are to be expected. Further refinement would be required for quantitative comparison to experiments. One step towards this was done by fitting the Hamiltonian parameters to results from density functional theory, see Sec. 5.2 and Ref. [81].

The eigenenergies of the third-order Hamiltonian (2.21) are given by

$$E_\pm(\mathbf{k}) = C + D(k_x^2 + k_y^2) \pm \sqrt{A^2(k_x^2 + k_y^2) + 4R^2(k_x^3 - 3k_x k_y^2)^2} \tag{2.22}$$

and plotted in Fig. 2.4(a) for $|\mathbf{k}| = \sqrt{k_x^2 + k_y^2} \leq 0.3\,\text{Å}^{-1}$. The hexagonal warping and PHS breaking term clearly distort the original Dirac cone. The sixfold symmetry imposed by the hexagonal warping also appears when looking at the energy difference ΔE between the bands, see Fig. 2.4(b). The PHS breaking however does not affect the energy difference since it only couples to the unit matrix $\mathbb{1}$. For small $|\mathbf{k}|$, the rotational symmetry of the Dirac cone is approximately restored.

The eigenstates of the Hamiltonian (2.21) have a more complex form than those for the simple Dirac Hamiltonian (2.19). The most general way to write

[3]Note that a different value for C is given in Ref. [87]. However, since it only induces a shift of the Dirac point in energy we set it to $C = 0\,\text{eV}$ for simplicity.

down eigenstates of (2×2) Hamiltonians is to write the Hamiltonian in the form

$$\hat{\mathcal{H}}(\mathbf{k}) = h_0(\mathbf{k})\mathbb{1} + h_x(\mathbf{k})\sigma_x + h_y(\mathbf{k})\sigma_y + h_z(\mathbf{k})\sigma_z. \tag{2.23}$$

Then, the normalized eigenstates[4] are

$$\varphi_\pm(\mathbf{k}) = \frac{1}{\sqrt{N}} \begin{pmatrix} h_z(\mathbf{k}) \pm \sqrt{h_x(\mathbf{k})^2 + h_y(\mathbf{k})^2 + h_z(\mathbf{k})^2} \\ h_x(\mathbf{k}) + \mathrm{i}h_y(\mathbf{k}) \end{pmatrix}, \tag{2.24}$$

where $N = h_x(\mathbf{k})^2 + h_y(\mathbf{k})^2 + \left(\mp h_z(\mathbf{k}) - \sqrt{h_x(\mathbf{k})^2 + h_y(\mathbf{k})^2 + h_z(\mathbf{k})^2}\right)^2$. For the Hamiltonian (2.21) one can identify $h_0(\mathbf{k}) = C + D(k_x^2 + k_y^2)$, $h_x(\mathbf{k}) = Ak_y$, $h_y(\mathbf{k}) = -Ak_x$ and $h_z(\mathbf{k}) = 2R(k_x^3 - 3k_xk_y^2)$. Accordingly, the hexagonal warping plays a very important role in the eigenstates, whereas PHS breaking, given by $h_0(\mathbf{k})$, does not affect the eigenstates. The hexagonal warping term also greatly alters the geometrical properties of the Hamiltonian. We will discuss this in more detail in Chap. 5 when studying the influence of Berry curvature effects on electron dynamics and HHG. There, we will also compare the model (2.21) with the aforementioned fitted Hamiltonian. To compute the dynamics, we need the velocity operator $\hat{\mathbf{v}}$ of the Hamiltonian (2.21). It reads

$$\hat{\mathbf{v}} = \frac{\mathrm{i}}{\hbar}\left[\hat{\mathcal{H}}(\mathbf{k}), \hat{\mathbf{r}}\right] = \frac{1}{\hbar}\left[2D\begin{pmatrix} k_x \\ k_y \end{pmatrix}\mathbb{1} + A\begin{pmatrix} -\sigma_y \\ \sigma_x \end{pmatrix} + 6R\begin{pmatrix} k_x^2 - k_y^2 \\ -2k_xk_y \end{pmatrix}\sigma_z\right]. \tag{2.25}$$

For small $\mathbf{k}$ it becomes $\mathbf{k}$ independent as expected for a Dirac cone and is similar to the velocity operator in graphene, see Eq. (2.13). For larger $\mathbf{k}$, it is altered both by PHS breaking and the hexagonal warping.

2.2. Berry phase, connection, and curvature

In 1984, Berry published the paper "Quantal phase factors accompanying adiabatic changes" [135], where he introduced a *geometrical phase* a state acquires when the corresponding Hamiltonian $\hat{\mathcal{H}}(\mathbf{R}(t))$ is adiabatically changed along a closed path $\mathbf{R}(t)$ in its parameter space. This geometrical phase is an addition to the dynamical phase. The latter "register[s] the passage of time" [135]. By now, the geometrical phase is commonly known as *Berry phase*. It is gauge invariant and thus a physical observable. As shown by Berry, it can be computed by integrating a vector field containing the geometric properties

[4] Naturally, the eigenenergies can also be written down in this general fashion, giving $E_\pm(\mathbf{k}) = h_0(\mathbf{k}) \pm \sqrt{h_x(\mathbf{k})^2 + h_y(\mathbf{k})^2 + h_z(\mathbf{k})^2}$.

of the Hamiltonian over the surface enclosed by the loop $\mathbf{R}(t)$. This vector field is nowadays widely known as *Berry curvature*.

While the publication process of Berry's work was still ongoing, Simon showed that the Berry curvature can also be used to calculate the Chern number of a system, which he related to the so-called TKNN invariant in the same publication [136]. The Chern number is a quantity that classifies the topological phase of a certain kind of system with broken TRS introduced by Chern and Simons ten years earlier [137], whereas the TKNN invariant was introduced by Thouless, Kohomoto, Nightingale and den Nijs in 1982 when they explained the robustness of the quantum Hall effect by identifying it as topological [138]. Since then, the concept of the Berry phase and curvature has found many more applications in condensed matter physics. It leads to the anomalous velocity [139], which we discuss in more detail in Sec. 2.3.2, delivers an intrinsic explanation of the anomalous Hall effect [48] and gives rise to additional contributions of the electric polarization [140, 141] and orbital magnetization [142, 143], among others. An overview of the Berry phase's influence on electronic properties is given in Ref. [144] and with special focus on the anomalous Hall effect in Ref. [49].

In the following we introduce and define the Berry phase, connection and curvature based on Ref. [144]. Since in our work the parameter space is usually spanned by the quasimomentum $\mathbf{k}$, we take $\mathbf{R} \equiv \mathbf{k}$. Assume we have a system defined by the Hamiltonian $\hat{\mathcal{H}}(\mathbf{k})$ with eigenstates $|\varphi_{\mathbf{k},n}\rangle$ and eigenenergies $E_n(\mathbf{k})$, where n is the band index. Now, we slowly vary $\mathbf{k} \to \mathbf{k}(t)$ along a path $\mathcal{C}$, where $\mathbf{k}_i = \mathbf{k}(t_0)$ marks the initial $\mathbf{k}$, and study the adiabatic time evolution of a state $|\Psi_{\mathbf{k}_i,n}(t)\rangle$. By choosing a fixed gauge we write the state as

$$|\Psi_{\mathbf{k}_i,n}(t)\rangle = \underbrace{\exp\Big(\mathrm{i}\,\gamma_n(t)\Big)}_{\text{geometrical phase factor}} \underbrace{\exp\left(-\frac{\mathrm{i}}{\hbar}\int_0^t \mathrm{d}t'\; E_n(\mathbf{k}(t'))\right)}_{\text{dynamical phase factor}} |\varphi_{\mathbf{k}(t),n}\rangle, \tag{2.26}$$

containing a dynamical and a geometrical phase. With our gauge choice we require that the phase varies smoothly and is single valued along the path $\mathcal{C}$. By plugging Eq. (2.26) into the time-dependent Schrödinger equation

$$\hat{\mathcal{H}}(\mathbf{k}(t))|\Psi_{\mathbf{k}_i,n}(t)\rangle = \mathrm{i}\hbar\frac{\mathrm{d}}{\mathrm{d}t}|\Psi_{\mathbf{k}_i,n}(t)\rangle \tag{2.27}$$

and multiplying Eq. (2.27) with $\langle\varphi_{\mathbf{k}(t),n}|$ from the left, one finds that the geometrical phase $\gamma_n(t)$ can be written as

$$\gamma_n(t) = \int_{\mathcal{C}} \mathrm{d}\mathbf{k}\cdot\boldsymbol{\mathcal{A}}_{nn}(\mathbf{k}), \tag{2.28}$$

where $\boldsymbol{\mathcal{A}}_{nn}$ is the Berry connection of band n. It is given by

$$\boldsymbol{\mathcal{A}}_{nn}(\mathbf{k}) = \mathrm{i}\left\langle \varphi_{\mathbf{k},n} \left| \nabla_{\mathbf{k}} \right| \varphi_{\mathbf{k},n} \right\rangle . \tag{2.29}$$

Since $\boldsymbol{\mathcal{A}}_{nn}(\mathbf{k})$ is a gauge-dependent quantity, for a long time it was believed that it is always possible to find a gauge transformation $|\varphi_{\mathbf{k},n}\rangle \to \mathrm{e}^{\mathrm{i}\xi(\mathbf{k})}|\varphi_{\mathbf{k},n}\rangle$ such that the geometrical phase $\gamma_n(t)$ accumulated along the path $\mathcal{C}$ vanishes. This changed with the work of Berry [135] who considered a *closed* path $\mathcal{C}$. Then, initial and final point $\mathbf{k}(t_0) = \mathbf{k}(t_{\mathrm{fin}})$ are equivalent and since we required a single-valued phase, the gauge transformation $\mathrm{e}^{\mathrm{i}\xi(\mathbf{k})}$ has to fulfill

$$\xi(\mathbf{k}(t_0)) - \xi(\mathbf{k}(t_{\mathrm{fin}})) = 2\pi \cdot \text{integer}. \tag{2.30}$$

The geometrical phase γ_n cannot be removed anymore and along a closed path $\mathcal{C}$ becomes a gauge-invariant physical quantity,

$$\gamma_n = \oint_{\mathcal{C}} \mathrm{d}\mathbf{k} \cdot \boldsymbol{\mathcal{A}}_{nn}(\mathbf{k}), \tag{2.31}$$

also often called Berry phase nowadays. The time dependence of $\mathbf{k}(t)$ is irrelevant when computing γ_n, only the geometric shape of the closed path $\mathcal{C}$ matters.

In analogy to electrodynamics, one can derive a vector field from the Berry connection $\boldsymbol{\mathcal{A}}_{nn}(\mathbf{k})$. It is called *Berry curvature*. The Berry curvature contains the geometric properties of a system and can be considered as the magnetic field in parameter space. It is gauge invariant and hence observable independently of any path $\mathcal{C}$ a state might take. The anomalous velocity we introduce in Sec. 2.3.2 is one consequence of that. However, the Berry curvature also has a significant impact on the dynamics in the non-adiabatic limit of a system, as we will study in detail in Chaps. 5 and 6. For the 3D quasimomentum $\mathbf{k} = (k_x, k_y, k_z)$, the Berry curvature $\boldsymbol{\Omega}_n(\mathbf{k})$ of band n is the rotation of the Berry connection $\boldsymbol{\mathcal{A}}_{nn}(\mathbf{k})$,

$$\boldsymbol{\Omega}_n(\mathbf{k}) = \nabla_{\mathbf{k}} \times \boldsymbol{\mathcal{A}}_{nn}(\mathbf{k}). \tag{2.32}$$

Using Stokes' theorem, the Berry phase γ_n from Eq. (2.31) can then also be expressed as

$$\gamma_n = \int_{\mathcal{S}} \mathrm{d}\mathbf{S} \cdot \boldsymbol{\Omega}_n(\mathbf{k}), \tag{2.33}$$

where $\mathcal{S}$ is the surface of the Berry curvature enclosed by the path $\mathcal{C}$. If the systems dimensions are unequal to three, one finds the more general tensor form

$$\Omega^n_{\mu\nu}(\mathbf{k}) = \frac{\partial}{\partial k^\mu}\mathcal{A}^{nn}_\nu(\mathbf{k}) - \frac{\partial}{\partial k^\nu}\mathcal{A}^{nn}_\mu(\mathbf{k}) \tag{2.34}$$

of the Berry curvature. It is related to the vector by

$$\Omega^n_{\mu\nu} = \epsilon_{\mu\nu\zeta}(\boldsymbol{\Omega}_n)_\zeta, \tag{2.35}$$

where $\epsilon_{\mu\nu\zeta}$ is the Levi-Cività antisymmetry tensor.

The Berry curvature can not only be related to the Berry connection $\boldsymbol{\mathcal{A}}_{nn}(\mathbf{k})$, but also to the interband (or transition) matrix element

$$\boldsymbol{\mathcal{A}}_{nn'}(\mathbf{k}) = \mathrm{i}\left\langle \varphi_{\mathbf{k},n} \left| \nabla_{\mathbf{k}} \right| \varphi_{\mathbf{k},n'} \right\rangle, \tag{2.36}$$

which describes the coupling between two bands n, n'. It is similar to the Berry connection (2.29), but $n \neq n'$. Its relation to the Berry curvature already indirectly appeared in 1982 in the publication of Thouless et al. [138] before the actual introduction of the latter. It follows from expressing the Berry curvature as a summation over the eigenstates

$$\Omega^n_{\mu\nu}(\mathbf{k}) = \mathrm{i}\sum_{n\neq n'} \frac{\left\langle \varphi_{\mathbf{k},n} \left| \frac{\partial\hat{\mathcal{H}}(\mathbf{k})}{\partial k^\mu} \right| \varphi_{\mathbf{k},n'} \right\rangle \left\langle \varphi_{\mathbf{k},n'} \left| \frac{\partial\hat{\mathcal{H}}(\mathbf{k})}{\partial k^\nu} \right| \varphi_{\mathbf{k},n} \right\rangle - (\nu \leftrightarrow \mu)}{\left[E_n(\mathbf{k}) - E_{n'}(\mathbf{k})\right]^2}. \tag{2.37}$$

As we show in App. A.1, this expression is linked to the interband matrix elements $\boldsymbol{\mathcal{A}}_{nn'}(\mathbf{k})$ and can be rewritten as

$$\Omega^n_{\mu\nu}(\mathbf{k}) = -\mathrm{i}\sum_{n\neq n'} \left[\mathcal{A}^\mu_{nn'}(\mathbf{k})\mathcal{A}^{*\,\nu}_{nn'}(\mathbf{k}) - (\nu \leftrightarrow \mu)\right]. \tag{2.38}$$

For two-band systems in 2D with $(\mu, \nu) = (x, y)$ and $n, n' = \pm$, using relation (2.35) between the Berry curvature tensor and the vector field, one finds that $\Omega^\pm_{xy} = \epsilon_{xy\zeta}(\boldsymbol{\Omega}_\pm)_\zeta$. This expression is zero for $\zeta \neq z$, i.e. for such systems only the z component of the Berry curvature is unequal to zero. Then, Eq. (2.38) simplifies and the z component of the Berry curvature[5] can be computed as [145]

$$(\boldsymbol{\Omega}_\pm(\mathbf{k}))_z = \pm 2\mathrm{Im}\left[\mathcal{A}^x_{+-}(\mathbf{k})\mathcal{A}^{*\,y}_{+-}(\mathbf{k})\right]. \tag{2.39}$$

There also exists another simple and generic way to calculate the Berry curvature in two-band systems, see Ref. [144], which we employ for our studies. We start from the general (2×2) Hamiltonian given in Eq. (2.23) and rewrite $\mathbf{h} = (h_x, h_y, h_z)$ in spherical coordinates

$$\mathbf{h} = h(\sin\theta\cos\phi, \sin\theta\sin\phi, \cos\theta), \tag{2.40}$$

[5]Note that the relation $\Omega^+_{xy} = -\Omega^-_{xy}$ is a direct consequence of the local conservation law for the Berry curvature: $\sum_n \Omega^n_{\mu\nu}(\mathbf{k}) = 0$.

where $h = \sqrt{h_x^2 + h_y^2 + h_z^2}$, $\phi = \arctan(h_y/h_x)$ and $\cos\theta = h_z/h$. Since h_0 does not affect the Berry curvature, it can be neglected here[6]. The eigenstates $|\varphi_\pm\rangle$ of $\mathbf{h}$ in spherical coordinates[7] become

$$|\varphi_-\rangle = \begin{pmatrix} \sin\frac{\theta}{2}\,\mathrm{e}^{-\mathrm{i}\phi} \\ -\cos\frac{\theta}{2} \end{pmatrix}, \qquad |\varphi_+\rangle = \begin{pmatrix} \cos\frac{\theta}{2}\,\mathrm{e}^{-\mathrm{i}\phi} \\ \sin\frac{\theta}{2} \end{pmatrix}, \tag{2.41}$$

with corresponding eigenenergies $\pm h$. For the lower band $(-)$, one obtains the Berry connection

$$\mathcal{A}_\theta^{--} = \left\langle \varphi_- \middle| \mathrm{i}\frac{\partial}{\partial\theta}\,\varphi_- \right\rangle = 0, \qquad \mathcal{A}_\phi^{--} = \left\langle \varphi_- \middle| \mathrm{i}\frac{\partial}{\partial\phi}\,\varphi_- \right\rangle = \sin^2\frac{\theta}{2}, \tag{2.42}$$

and thus the Berry curvature

$$\Omega_{\theta\phi}^{-} = \frac{\partial}{\partial\theta}\mathcal{A}_\phi^{--} - \frac{\partial}{\partial\phi}\mathcal{A}_\theta^{--} = \frac{1}{2}\sin\theta. \tag{2.43}$$

Up to now, we dropped the parameter dependence of $\mathbf{h}(\mathbf{k})$ on $\mathbf{k}$. For $\mathbf{k} = (k_x, k_y)$ as for the systems discussed in this work, see Sec. 2.1, the Berry curvature (2.43) transforms back into Cartesian coordinates as

$$\Omega_{xy}^{\pm}(\mathbf{k}) = \mp\frac{1}{2}\left[\left(\frac{\partial\cos(\theta(\mathbf{k}))}{\partial k_x}\right)\left(\frac{\partial\phi(\mathbf{k})}{\partial k_y}\right) - \left(\frac{\partial\cos(\theta(\mathbf{k}))}{\partial k_y}\right)\left(\frac{\partial\phi(\mathbf{k})}{\partial k_x}\right)\right], \tag{2.44}$$

which is a simple and general formula for the Berry curvature in two-level systems.

2.3. Velocity in two-band systems

The velocity expectation value of (time-dependent) states in two-band quantum systems is a crucial observable throughout this work. We use it to study Floquet oscillations in Chap. 4 and HHG in Chaps. 5, 6 and 7. Therefore in this section we will thoroughly introduce all properties of the velocity expectation value both in time-independent and time-dependent systems relevant for our work. Note that all the observations made in the following for two-band systems can easily be extended to systems with more bands.

[6] In Sec. 2.1.2, Eq. (2.24), we already saw that h_0 does not appear in the eigenstates. Thus, by definition (see Eqs. (2.29), (2.32)), it also does not affect the Berry curvature.

[7] See equation (2.24) for the eigenstates in Cartesian coordinates.

We start with time-independent two-band systems with Hamiltonian $\hat{\mathcal{H}}(\mathbf{k})$ and consider single $\mathbf{k}$ states for simplicity. In the most general case, a state $|\Psi_{\mathbf{k}}(t)\rangle$ in such a system can be written as

$$|\Psi_{\mathbf{k}}(t)\rangle = \exp\left(-\frac{\mathrm{i}}{\hbar}E_+(\mathbf{k})t\right) c_{\mathbf{k},+}|\varphi_{\mathbf{k},+}\rangle + \exp\left(-\frac{\mathrm{i}}{\hbar}E_-(\mathbf{k})t\right) c_{\mathbf{k},-}|\varphi_{\mathbf{k},-}\rangle, \quad (2.45)$$

where $|\varphi_{\mathbf{k},\pm}\rangle$ are the eigenstates and $E_\pm(\mathbf{k})$ the eigenengergies of upper $(+)$ and lower $(-)$ band, $c_{\mathbf{k},\pm}$ the respective amplitudes of $|\Psi_{\mathbf{k}}(t)\rangle$ in the eigenstates and $\exp\left(-\frac{\mathrm{i}}{\hbar}E_\pm(\mathbf{k})t\right)$ is the dynamical phase describing the time evolution of the state[8]. Generally, the velocity expectation value $\mathbf{v}_{\mathbf{k}}(t)$ can be computed using Ehrenfest's theorem,

$$\begin{aligned}\mathbf{v}_{\mathbf{k}}(t) &= \langle\Psi_{\mathbf{k}}(t)|\hat{\mathbf{v}}|\Psi_{\mathbf{k}}(t)\rangle \\ &= \frac{\mathrm{i}}{\hbar}\left\langle\Psi_{\mathbf{k}}(t)\left|\left[\hat{\mathcal{H}}(\mathbf{k}),\hat{\mathbf{r}}\right]\right|\Psi_{\mathbf{k}}(t)\right\rangle = \frac{1}{\hbar}\left\langle\Psi_{\mathbf{k}}(t)\left|\nabla_{\mathbf{k}}\hat{\mathcal{H}}(\mathbf{k})\right|\Psi_{\mathbf{k}}(t)\right\rangle,\end{aligned} \quad (2.46)$$

where $\hat{\mathbf{r}} = \mathrm{i}\nabla_{\mathbf{k}}$ is the position operator and $\hat{\mathbf{v}} = \frac{\mathrm{i}}{\hbar}\left[\hat{\mathcal{H}}(\mathbf{k}),\hat{\mathbf{r}}\right] = \frac{1}{\hbar}\nabla_{\mathbf{k}}\hat{\mathcal{H}}(\mathbf{k})$ the velocity operator. For the state (2.45) one obtains

$$\begin{aligned}\mathbf{v}_{\mathbf{k}}(t) = &\underbrace{|c_{\mathbf{k},+}|^2\langle\varphi_{\mathbf{k},+}|\hat{\mathbf{v}}|\varphi_{\mathbf{k},+}\rangle + |c_{\mathbf{k},-}|^2\langle\varphi_{\mathbf{k},-}|\hat{\mathbf{v}}|\varphi_{\mathbf{k},-}\rangle}_{\text{diagonal}} \\ &+ \underbrace{2\mathrm{Re}\left[c^*_{\mathbf{k},+}c_{\mathbf{k},-}\exp\left(-\frac{\mathrm{i}}{\hbar}\left[E_-(\mathbf{k})-E_+(\mathbf{k})\right]t\right)\langle\varphi_{\mathbf{k},+}|\hat{\mathbf{v}}|\varphi_{\mathbf{k},-}\rangle\right]}_{\text{off diagonal}}.\end{aligned} \quad (2.47)$$

We can separate the resulting velocity $\mathbf{v}_{\mathbf{k}}(t)$ in a diagonal and an off-diagonal contribution, associated with the matrix elements of $\hat{\mathbf{v}}$ in the basis of the eigenstates $|\varphi_{\mathbf{k},\pm}\rangle$. As derived in App. A.1, they read

$$\mathbf{v}_{\mathbf{k}}^{++} = \langle\varphi_{\mathbf{k},+}|\hat{\mathbf{v}}|\varphi_{\mathbf{k},+}\rangle = \frac{1}{\hbar}\nabla_{\mathbf{k}}E_+(\mathbf{k}), \quad (2.48)$$

$$\mathbf{v}_{\mathbf{k}}^{+-} = \langle\varphi_{\mathbf{k},+}|\hat{\mathbf{v}}|\varphi_{\mathbf{k},-}\rangle = \frac{\mathrm{i}}{\hbar}\left[E_+(\mathbf{k})-E_-(\mathbf{k})\right]\boldsymbol{\mathcal{A}}_{+-}(\mathbf{k}), \quad (2.49)$$

and $\mathbf{v}_{\mathbf{k}}^{--}$ and $\mathbf{v}_{\mathbf{k}}^{-+}$ analogously. $\boldsymbol{\mathcal{A}}_{+-}(\mathbf{k})$ is the interband or transition matrix element defined in Eq. (2.36). The diagonal contribution is also called *intraband* or *group velocity* and combining Eqs. (2.47) and (2.48) can be written as

$$\mathbf{v}_{\mathbf{k},\mathrm{intra}}(t) = \mathbf{v}_{\mathbf{k},\mathrm{g}}(t) = \frac{1}{\hbar}|c_{\mathbf{k},+}|^2\nabla_{\mathbf{k}}E_+(\mathbf{k}) + \frac{1}{\hbar}|c_{\mathbf{k},-}|^2\nabla_{\mathbf{k}}E_-(\mathbf{k}), \quad (2.50)$$

[8]Note that since the Hamiltonian $\hat{\mathcal{H}}(\mathbf{k})$ is time independent, the integral in the dynamical phase is trivial and no Berry phase can be acquired.

i.e. it is defined by the energy dispersion $E_{\pm}(\mathbf{k})$ [125]. The off-diagonal term can be identified as *Zitterbewegung* or *interband velocity*. For both velocity contributions, we are not aware of a general and sharp distinction between the different nomenclatures. However, the term *Zitterbewegung* tends to be used for an intrinsic off-diagonal velocity in undriven systems as discussed in Sec. 2.3.1 and *interband velocity* for off-diagonal velocities in combination with external driving, as discussed in Sec. 2.3.2. In any case, the off-diagonal velocity can also be expressed through the interband matrix element $\boldsymbol{\mathcal{A}}_{+-}(\mathbf{k})$ based on Eqs. (2.47) and (2.49),

$$\begin{aligned}\mathbf{v}_{\mathbf{k}}^{\mathrm{ZB}}(t) &= \mathbf{v}_{\mathbf{k},\mathrm{inter}}(t) \\ &= 2\mathrm{Re}\left[\frac{\mathrm{i}}{\hbar}c_{\mathbf{k},+}^{*}c_{\mathbf{k},-}\exp\left(-\frac{\mathrm{i}}{\hbar}\left[E_{-}(\mathbf{k})-E_{+}(\mathbf{k})\right]t\right)\left[E_{+}(\mathbf{k})-E_{-}(\mathbf{k})\right]\boldsymbol{\mathcal{A}}_{+-}(\mathbf{k})\right].\end{aligned} \tag{2.51}$$

This directly links the off-diagonal velocity and the Berry curvature, see Eqs. (2.37), (2.38), (2.39). We will further elaborate on this link in Secs. 2.3.1 and 2.3.2 and study its consequences in Chaps. 5 and 6.

2.3.1. Zitterbewegung

This section gives a short introduction of the main characteristics of Zitterbewegung in two-band systems. It summarizes part of the PhD thesis of Reck [126], where the interested reader may find a more detailed discussion of the properties of Zitterbewegung in two-band systems and numerical studies on graphene.

Originally, the term *Zitterbewegung* refers to a jittery movement of highly relativistic particles governed by the Dirac equation. It was predicted by Schrödinger in 1930 [146] and arises since the velocity operator does not commute with the Dirac Hamiltonian and thus is no constant of motion. In fact, it is an interference term between particle- and antiparticle-like solution of the Dirac equation. However, for free particles Zitterbewegung occurs on such short time and length scales that its experimental observation is still pending [147].

In principle, the requirement of the Hamiltonian not commuting with the velocity operator can be met in any two- or more band system as demonstrated in Ref. [148]. The Zitterbewegung appears as off-diagonal terms of the velocity operator and “is a general real effect for a nonrelativistic particle

moving in a crystal, as a consequence of interband transitions" [148], see Eqs. (2.49) and (2.51). There, the off-diagonal matrix element of the velocity operator is related to the interband or transition matrix element $\boldsymbol{\mathcal{A}}_{+-}(\mathbf{k})$. In multi-band systems, the interference of particle- and antiparticle-like solution is replaced by a state that occupies more than one band interfering with itself, see Eqs. (2.47) and (2.51). The first theoretical proposal to observe Zitterbewegung in solid state systems was made by Schliemann et al. in III-V semiconductor quantum wells with SOC [149], which exhibit an energy spectrum similar to the Dirac Hamiltonian. Now, theoretical studies also exist for carbon nanotubes [150], graphene [151–153] and TIs [154], among others. Experimentally, Zitterbewegung has been demonstrated for single $^{40}Ca^{+}$-ions [155], in Bose-Einstein condensates [156, 157] and in InGaAs [158]. For a more detailed review of Zitterbewegung in semiconductors and an overview of the historical background we recommend Ref. [159].

In equation (2.47) we derived the general representation of the velocity expectation value $\mathbf{v}_{\mathbf{k}}(t)$ of a $\mathbf{k}$ mode $|\Psi_{\mathbf{k}}(t)\rangle$, see Eq. (2.45), in a time-independent two-band system. It contains an off-diagonal term which in undriven systems is identified as *Zitterbewegung*[9]. Additionally, we showed that this term can be rewritten in terms of the interband matrix element $\boldsymbol{\mathcal{A}}_{+-}(\mathbf{k})$, see Eq. (2.51). From equations (2.47) and (2.51) one can deduce that Zitterbewegung only appears if the $\mathbf{k}$ state has a non-zero amplitude $c_{\mathbf{k},\pm} \neq 0$ in both bands. Moreover, if the velocity operator $\hat{\mathbf{v}}$ commutes with the Hamiltonian $\hat{\mathcal{H}}(\mathbf{k})$, the eigenstates $|\varphi_{\mathbf{k},\pm}\rangle$ of $\hat{\mathcal{H}}(\mathbf{k})$ also are eigenstates of $\hat{\mathbf{v}}$ and the Zitterbewegung vanishes. The link between the off-diagonal velocity and the Berry curvature implies that a two-band system with non-vanishing Zitterbewegung in both velocity components $v^{\mathrm{ZB}}_{x/y,\mathbf{k}} \neq 0$ also has a non-zero Berry curvature $\boldsymbol{\Omega}_{\pm}(\mathbf{k})$. This also means that in this system either TRS or spatial inversion symmetry is broken[10] and emphasizes that the Zitterbewegung is an intrinsic effect.

That Zitterbewegung is equivalent to an oscillating velocity becomes even more apparent when rewriting the off-diagonal part of Eq. (2.47) componentwise as

$$v^{\mathrm{ZB}}_{i,\mathbf{k}}(t) = A_{i,\mathbf{k}} \cos\left(\omega^{\mathrm{ZB}}_{\mathbf{k}} t + \phi_{i,\mathbf{k}}\right), \tag{2.52}$$

[9] We emphasize the condition of an undriven system here because as we will discuss in Sec. 2.3.2 the term *interband velocity* is generally preferred when including driving by electric fields into the system.

[10] As shown in review [144] the Berry curvature vanishes in systems that have both TRS and spatial inversion symmetry.

where $i \in \{x, y\}$ and

$$\begin{aligned} \text{amplitude:} \quad & A_{i,\mathbf{k}} = 2|c_{\mathbf{k},+}||c_{\mathbf{k},-}||\langle\varphi_{\mathbf{k},+}|\hat{\mathbf{v}}|\varphi_{\mathbf{k},-}\rangle|, \\ \text{frequency:} \quad & \omega_{\mathbf{k}}^{\mathrm{ZB}} = \frac{1}{\hbar}\left(E_-\left(\mathbf{k}\right) - E_+\left(\mathbf{k}\right)\right), \\ \text{phase:} \quad & \phi_{i,\mathbf{k}} = -\left(\arg(c_{\mathbf{k},+}^* c_{\mathbf{k},-}) + \arg\left(\langle\varphi_{\mathbf{k},+}|\hat{\mathbf{v}}|\varphi_{\mathbf{k},-}\rangle\right)\right). \end{aligned} \tag{2.53}$$

The amplitude encodes the conditions for non-vanishing Zitterbewegung of a single $\mathbf{k}$ mode. The frequency is independent of the velocity component i and given by the energy difference of the two bands. The phase is not important when considering a single $\mathbf{k}$ mode but for instance determines whether the Zitterbewegung of two modes $\pm\mathbf{k}$ interferes constructively or destructively.

When considering the Zitterbewegung of wave packets, one will find that it decays over time. This decay can be explained in a rather intuitive fashion. As we already stated, Zitterbewegung is an interference effect of states distributing over two or more bands. In the case of single $\mathbf{k}$ modes, i.e. plane waves, the state spreads over the complete real space and thus both band contributions overlap for all times. A wave packet made up of more $\mathbf{k}$ modes however is localized in space. Since commonly the contributions of the two bands have velocities of different signs, eventually the wave packet splits into two parts, the two band contributions do not interfere anymore and no Zitterbewegung can be observed. For a mathematical derivation of the decay of Zitterbewegung we refer to Reck [126, 153] who extensively studied how to prevent or at least slow down the decaying process.

2.3.2. Influence of electric fields

Electric fields – mostly representing time-dependent laser pulses – play a major role in the systems studied throughout this work. A homogeneous electric field $\mathbf{E}_{\mathrm{el}}(t)$ can be introduced into a Hamiltonian $\hat{\mathcal{H}}_0(\mathbf{k})$ in two ways. It can either be expressed by the vector potential $\mathbf{A}(t)$, where $\mathbf{E}_{\mathrm{el}}(t) = -\frac{\partial}{\partial t}\mathbf{A}(t)$, which is included into the Hamiltonian by minimal coupling

$$\hat{\mathcal{H}}(\mathbf{k}, t) = \hat{\mathcal{H}}_0\left(\mathbf{k} + \frac{e}{\hbar}\mathbf{A}(t)\right), \tag{2.54}$$

or by the scalar potential $\phi_{\mathrm{el}}(\mathbf{r}, t)$, with $\mathbf{E}_{\mathrm{el}}(t) = -\nabla_{\mathbf{r}}\phi_{\mathrm{el}}(\mathbf{r}, t)$, that is added to the Hamiltonian,

$$\hat{\mathcal{H}}(\mathbf{k}, \mathbf{r}, t) = \hat{\mathcal{H}}_0(\mathbf{k}) + e\phi_{\mathrm{el}}(\mathbf{r}, t). \tag{2.55}$$

Accordingly, choosing one of the options is equivalent to choosing the gauge of the electric field $\mathbf{E}_{\mathrm{el}}(t)$. In the literature concerning light-driven systems, the first method based on the vector potential $\mathbf{A}(t)$ is also called *velocity gauge*, whereas the second option based on the scalar potential is called *length gauge*. As we will discuss in Chap. 3, our numerical tool can handle the Hamiltonian in mixed position-momentum-space representation. Thus we can use both length and velocity gauge in our studies. In principle, due to gauge invariance both gauges should give the same results. However, we found several publications discussing the stability of the gauges with respect to approximations of the system [160–162]. Based on a comparison of both gauges for a reduced density matrix approach, Ventura et al. [162] argue that one has to be careful when applying the velocity gauge in effective Hamiltonians. It also gives rise to additional terms in the velocity operator $\hat{\mathbf{v}} = \frac{1}{\hbar}\nabla_{\mathbf{k}}\hat{\mathcal{H}}(\mathbf{k}, t)$ for Hamiltonians that are not linear in momentum $\mathbf{k}$ [160, 162]. Hence, in our work we mainly apply the length gauge.

In equation (2.45) we show the time evolution of a state $|\Psi_{\mathbf{k}}(t)\rangle$ under the time-independent Hamiltonian[11] $\hat{\mathcal{H}}_0(\mathbf{k})$. Applying an additional electric field $\mathbf{E}_{\mathrm{el}}(t)$ effectively induces a shift in the momentum $\mathbf{k}$ of the state. This shift is described by the acceleration theorem [70]

$$\hbar\frac{\mathrm{d}\mathbf{k}}{\mathrm{d}t} = e\left[\frac{\partial\mathbf{A}(t)}{\partial t} + \nabla_{\mathbf{r}}\phi_{\mathrm{el}}(\mathbf{r}, t)\right] \equiv -e\mathbf{E}_{\mathrm{el}}(t). \tag{2.56}$$

Note that the last term holds for any gauge of $\mathbf{E}_{\mathrm{el}}(t)$. The shift has to be taken into account as time dependence of the momentum $\mathbf{k} \to \mathbf{k}(t)$. In the following we discuss how this time dependence affects the time evolution and velocity of a state. Our statements apply to any system with momentum shift and are independent of the cause of the shift. Nevertheless, we focus on electric fields in our discussion.

To clearly label a state with time-dependent momentum $\mathbf{k}(t)$, its initial momentum $\mathbf{k}_i = \mathbf{k}(t_0)$ at starting time t_0 has to be known. Since the state is moving through momentum space, Berry curvature effects can appear in its dynamics. Furthermore, sufficiently strong electric fields can drive transitions between the energy bands[12], leading to a time dependence of the amplitudes $c_{\mathbf{k},\pm} \to c_{\mathbf{k}_i,\pm}(t)$. Altogether, we can now write the time-dependent state in the

[11] Note that we introduce the subscript 0 to distinguish the original Hamiltonian from the one including the electric field.

[12] A more detailed overview of relevant transition mechanisms is given in Sec. 2.4.

eigenbasis of $\hat{\mathcal{H}}_0(\mathbf{k})$ as

$$\begin{aligned}|\Psi_{\mathbf{k}_i}(t)\rangle =& \exp\left(-\frac{\mathrm{i}}{\hbar}\int_{t_0}^{t} E_+(\mathbf{k}(t'))\,\mathrm{d}t'\right) c_{\mathbf{k}_i,+}(t)|\varphi_{\mathbf{k}(t),+}\rangle \\ &+ \exp\left(-\frac{\mathrm{i}}{\hbar}\int_{t_0}^{t} E_-(\mathbf{k}(t'))\,\mathrm{d}t'\right) c_{\mathbf{k}_i,-}(t)|\varphi_{\mathbf{k}(t),-}\rangle,\end{aligned} \tag{2.57}$$

where $|\varphi_{\mathbf{k}(t),-}\rangle$ are the eigenstates of $\hat{\mathcal{H}}_0(\mathbf{k})$ at the respective momentum $\mathbf{k}(t)$. In this notation, a potentially arising geometric phase is absorbed in the amplitudes $c_{\mathbf{k}_i,\pm}(t)$, see Eq. (2.26) for comparison. The corresponding velocity expectation value then reads

$$\begin{aligned}\mathbf{v}_{\mathbf{k}_i}(t) = &\underbrace{|c_{\mathbf{k}_i,+}(t)|^2\langle\varphi_{\mathbf{k}(t),+}|\hat{\mathbf{v}}|\varphi_{\mathbf{k}(t),+}\rangle + |c_{\mathbf{k}_i,-}(t)|^2\langle\varphi_{\mathbf{k}(t),-}|\hat{\mathbf{v}}|\varphi_{\mathbf{k}(t),-}\rangle}_{\text{intraband}} + \\ &\underbrace{2\mathrm{Re}\left[c^*_{\mathbf{k}_i,+}(t)c_{\mathbf{k}_i,-}(t)\exp\left(-\frac{\mathrm{i}}{\hbar}\int_{t_0}^{t}\mathrm{d}t'\left[E_-(\mathbf{k}(t'))-E_+(\mathbf{k}(t'))\right]\right)\langle\varphi_{\mathbf{k}(t),+}|\hat{\mathbf{v}}|\varphi_{\mathbf{k}(t),-}\rangle\right]}_{\text{interband}}.\end{aligned} \tag{2.58}$$

We now label the two velocity contributions as *intraband* and *interband velocity* since this is the most common nomenclature within the context of light-driven systems. In principle, the velocity (2.58) is very similar to the velocity of a state in a system without electric field, see Eq. (2.47). Still, the dynamics introduced by the electric field can give rise to a much more complex time dependence and nonlinear effects. As for undriven systems, the intraband velocity is defined by the band dispersion, see Eq. (2.50). Analogously, all displayed representations for the off-diagonal velocity, namely Eqs. (2.47), (2.51) and (2.52), also hold for the interband velocity. The only difference is that now a time dependence has to be introduced in all parameters. Naturally, this modifies the quantities related to Zitterbewegung in Eq. (2.53). The movement of the electron through momentum space leads to a time dependence of the Zitterbewegung frequency $\omega^{\mathrm{ZB}}_{\mathbf{k}}$ and transitions modulate its amplitude. The resulting velocity has a more complex time profile and is better known as *interband velocity*. This name might originate from the relation between off-diagonal velocity and the interband or transition matrix element $\boldsymbol{\mathcal{A}}_{+-}(\mathbf{k})$, see Eq. (2.51). In the context of electric fields, this formulation is more intuitive since the transition matrix also describes how the different states are coupled by the driving[13].

In the limit of weak electric fields, i.e. the adiabatic regime where no transitions between bands occur, the link between velocity, transition matrix element and

[13] We do not want to elaborate further on how the transition matrix describes the coupling of states here but refer to the master's thesis of Ebner for more details on the significance of $\boldsymbol{\mathcal{A}}_{+-}(\mathbf{k})$ with focus on Dirac systems under electric ratiation [163].

ultimately the Berry curvature, see Eq. (2.51), is even more apparent. Already in 1954 Karplus and Luttinger showed that the coupling of the bands due to an electric field within first-order perturbation theory in the field strength gives rise to an additional term in the velocity expectation value [164]. After the introduction of the concept of Berry curvature, Chang and Niu demonstrated that this *anomalous velocity* is directly related to the latter [139]. They found that up to first order, the velocity of a state that adiabatically evolves within band n is given by

$$\mathbf{v}_{\mathbf{k}_i}(t) = \underbrace{\frac{1}{\hbar}\nabla_{\mathbf{k}} E_n(\mathbf{k}(t))}_{\text{intraband velocity}} \underbrace{-\frac{\mathrm{e}}{\hbar}\mathbf{E}_{\mathrm{el}}(t) \times \boldsymbol{\Omega}_n(\mathbf{k}(t))}_{\text{anomalous velocity}}, \tag{2.59}$$

where $\boldsymbol{\Omega}_n(\mathbf{k}(t))$ is the Berry curvature of band n. For a more detailed derivation, we recommend the review [144]. As extensively studied in [165], by applying a constant electric field $\mathbf{E}_{\mathrm{el}}(t) = \mathbf{E}_{\mathrm{el}}$ tuned such that the test state evolves adiabatically, one can use the anomalous velocity to map the Berry curvature of a system. We will demonstrate this in Chap. 5 and use the velocity approximation (2.59) to crosscheck our fully quantum mechanical simulations in the adiabatic limit.

2.3.3. High-harmonic generation

Throughout this section, we have explored how system properties such as the bandstructure and the Berry curvature are related to the velocity expectation value of a single $\mathbf{k}$ state. Additionally, we have seen, how introducing a (time-dependent) electric field can lead to a more complicated time profile of the velocity, especially when the field strength is large enough to drive transitions between the bands. In experiments, such electric fields are applied to a system in terms of an intense laser pulse, where the pulsing is necessary to avoid sample destruction. The electronic response of the system is then measured as the power spectrum emitted by the sample and contains the spectral information of the induced electron dynamics. In the nonlinear regime, these spectra show HHs of the incoming laser pulse's frequency.

Such *high-harmonic generation* (HHG) is used to study atoms, molecules, and solids. The origin of the field dates back to Goeppert-Mayer, who first suggested frequency doubling in 1931. In her PhD thesis, she theoretically predicted that an atom can be excited to a higher energy state by simultaneously absorbing two photons, if the combined energy of the photons matches

the energy difference of the atomic states. In the subsequent relaxation, only one photon is emitted, which correspondingly has twice the frequency of the originally absorbed photons [166]. However, experimental observation of such a nonlinear process was not possible until the invention of the laser, since a high density of photons is necessary to achieve enough events for actual detection. In 1961, Franken et al. were able to measure the generation of a second harmonic of the original laser frequency by illuminating crystalline quartz with an intense ruby laser [167]. In subsequent years, the field evolved towards the study of higher-order harmonic generation, aiming at the creation of coherent radiation in the ultraviolet regime and beyond. Nowadays, HHG is also employed as a spectroscopic tool for gaining insights into a materials properties. Measurements of HHs can e.g. be used to detect Bloch oscillations [168] and interference effects of electrons in a crystal [169], to study the Berry curvature of a system [81, 170], or to observe heating of Dirac gases [83]. A summary about recent developments of HHG in condensed matter is given e.g. in Ref. [94]. In our work, we investigate HHG in effective Dirac systems with focus on TI surface states, see Chaps[14]. 5, 6 and 7. In such systems, the topological protection entails large scattering times of at least 1 ps [80], and thus a fully quantum mechanical description without dephasing is valid. For the two-band model introduced in Sec. 2.1.2, Eq. (2.21), the emitted HH spectra are directly linked to the velocity given in Eq. (2.58), as we show below.

Generally, the acceleration $\dot{\mathbf{v}}(t)$ of an electron due to the laser pulse generates a power $P(t)$ which is given by Lamor's formula [171]

$$P(t) = \frac{2}{3}\frac{e^2}{4\pi\varepsilon_0 c^3}\,|\dot{\mathbf{v}}(t)|^2, \tag{2.60}$$

where ε_0 is the vacuum permittivity and c the speed of light. The corresponding HH spectra are defined by the Fourier transform $P(\omega)$. In the frequency domain, $\dot{\mathbf{v}}(\omega) = \mathrm{i}\omega\mathbf{v}(\omega)$, and thus the power spectrum $P(\omega)$ is directly related to the electron velocity $\mathbf{v}(\omega)$,

$$P(\omega) = \frac{2}{3}\frac{e^2}{4\pi\varepsilon_0 c^3}\,|\omega\mathbf{v}(\omega)|^2. \tag{2.61}$$

Naturally, the power $P(\omega)$ can be split in the vector components of the velocity $\mathbf{v}(\omega)$ and we can write

$$P(\omega) = \frac{2}{3}\frac{e^2\omega^2}{4\pi\varepsilon_0 c^3}\left(v_x(\omega)^2 + v_y(\omega)^2\right) = P_x(\omega) + P_y(\omega) \tag{2.62}$$

[14]We redirect the reader to these chapters for a more detailed motivation of the respective research.

for a 2D system. As shown in Eqs. (2.47) and (2.58) the velocity can be decomposed in intra- and interband contribution as well. Due to the linearity of the Fourier transform, this also holds in the frequency domain,

$$\mathbf{v}(\omega) = \mathbf{v}_{\mathrm{intra}}(\omega) + \mathbf{v}_{\mathrm{inter}}(\omega). \tag{2.63}$$

Plugging Eq. (2.63) in (2.61) gives

$$P(\omega) = \frac{2}{3}\frac{e^2}{4\pi\varepsilon_0 c^3}\,\omega^2 \left|\mathbf{v}^2_{\mathrm{intra}}(\omega) + \mathbf{v}^2_{\mathrm{inter}}(\omega) + 2\mathrm{Re}\left[\mathbf{v}^*_{\mathrm{intra}}(\omega)\mathbf{v}_{\mathrm{inter}}(\omega)\right]\right|. \tag{2.64}$$

Hence, both velocity contributions and their interference influence the resulting HH spectrum.

Within this work, we calculate HHs spectra from numerically computed velocity data. Since this data has a limited amount of data points, we take several steps to improve the quality of the spectra. First of all, we interpolate the velocities in order to increase the density of points in time. Then, we damp the second half of the signal with a Gaussian-shaped decay such that the final velocity is constant and equal to the initial velocity. This damping acts as dephasing on the simplest possible level as it does not distinguish between intra- and interband contributions. Third, we pad the numerical velocity with zeroes before and after the actual dynamics. These measures are similar to multiplying the data with a window function, which is a typical procedure when computing HHs spectra from numerical results [172]. We show the details and an exemplary study of the effects of our data processing in App. A.9.

2.4. Transition mechanisms in laser-driven two-level systems

In Sec. 2.3.2 we have discussed how electric fields influence the velocity of an electron. Now, we want to go into more details on the different regimes of light-induced electron transitions between bands. In Fig. 2.5 we sketch the main processes occurring when an electron is driven by an intense laser field. Therein, the field is indicated by the purple wave and resembles the laser pulse applied in Chap. 5 and following. Initially, the electron we consider occupies only the valence band. In panel (a), only intraband dynamics occur while the electron moves through momentum space. At points of minimal band gap or when the local gap is in resonance with the driving frequency,

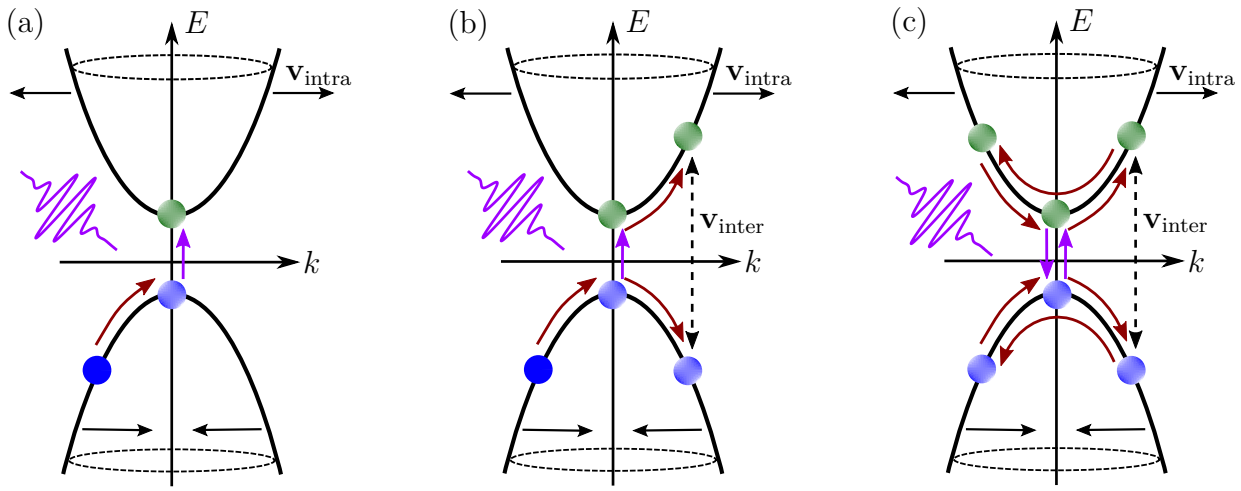

Fig. 2.5: Electron dynamics in a two-band system driven by an intense laser field sketched in 1D. (a) Initially, the electron (blue dot) is shifted through momentum space (red arrow). It only has an intraband velocity. When it reaches a resonance or point of minimal band gap, it (shaded blue and shaded green dot) is partially excited into the other band (purple arrow). (b) The two electron parts move within their respective band. Both parts contribute to the intraband velocity. Their interference additionally gives rise to an interband velocity (dashed arrow). (c) Due to the oscillation of the light field, the electron parts move back and forth in momentum space and transitions occur repeatedly.

part of the electron is excited to the conduction band. After such a transition, both amplitudes $c_{\mathbf{k}_i,\pm} \neq 0$ of the electron wave function are non-zero, compare Eq. (2.57), and the occupation is distributed over valence and conduction band. The electron amplitudes continue moving within their respective band and contributing to the intraband velocity. Additionally, their interference generates an interband velocity, see panel (b). Since a laser pulse is described by an oscillating electric field[15], after one optical half-cycle the electron's direction of motion in momentum space is reversed. Its two amplitudes return to the point of minimal gap or resonance condition and another transition occurs. Then, their reshuffled amplitudes continue the intraband motion until their direction in momentum space is reversed again. These processes are repeated throughout the pulse duration, as indicated in panel (c). The probability of finding the electron in the valence or conduction band after the pulse depends on the type of transitions that dominate the process.

The simple sketch in Fig. 2.5 implies that intraband motion and interband transitions are two connected processes that depend on various system parameters, such as the energy dispersion and the driving field. One attempt to disentangle and categorize different transition mechanisms in light-driven two-band systems was made by Heide et al. [173]. Their analysis is based on a

[15]Note that we neglect the variation of the fields amplitude throughout the pulse here.

massive Dirac model in 1D[16], where the electron is driven around the minimal band gap by a linearly polarized laser pulse, as sketched in Fig. 2.5. Dephasing and dissipation effects are neglected. They distinguish five different categories. The first one is simply the *adiabatic regime* where no transitions happen. The other four describe different transition mechanisms. The *Keldysh* or *adiabaticity parameter* γ determines, whether the system's driving is within the perturbative limit or has entered the strong-field regime [174]. The parameter is defined as

$$\gamma = \frac{2\pi\nu_{\mathrm{el}}\sqrt{m^*\Delta E}}{eE_{\mathrm{el}}} = \frac{\Delta E h\nu_{\mathrm{el}}}{\sqrt{2}\hbar v_{\mathrm{F}} eE_{\mathrm{el}}} = \frac{\Delta E}{\sqrt{2}\hbar\Omega_{\mathrm{R}}}, \tag{2.65}$$

where m^* is the effective electron mass, ΔE the minimal band gap, $E_{\mathrm{el}} = |\mathbf{E}_{\mathrm{el}}|$ the electric field strength, and ν_{el} the driving frequency. The first expression is the original definition by Keldysh [174], the second and third expression are obtained for the model system in Ref. [173][17] with Rabi frequency $\Omega_{\mathrm{R}} = v_{\mathrm{F}} eE_{\mathrm{el}}/(h\nu_{\mathrm{el}})$.

As long as $\gamma > 1$, i.e. in the perturbative limit, only *resonant transitions* are possible. They require a photon energy $nh\nu_{\mathrm{el}} \approx \Delta E$, where n is an integer. Due to the relatively low field strength compared to the band gap ΔE and driving frequency ν_{el}, only the single-photon process $n = 1$ plays a role. In this regime, an occupation builds up in the conduction band and for sufficiently long pulses, Rabi oscillations appear. By adequate tuning of the parameters, the occupation can be completely transferred from valence to conduction band and remains there[18].

For $\gamma < 1$ the light-matter interaction exceeds the perturbative limit and enters the strong-field regime. Then, the intraband motion of the electron also becomes relevant and one has to consider the time-dependence of its instantaneous eigenergy. This leads to a more complicated resonance condition. Besides resonant transitions, Heide et al. [173] use the Landau-Zener formalism [175–180] to classify three more mechanisms. Within this formalism, non-resonant transitions that occur when an electron passes a point of minimal band gap as in Fig. 2.5 are approximated. The transition probability P_{LZ} is estimated as

$$P_{\mathrm{LZ}} = \exp\left(-2\pi\delta_{\mathrm{LZ}}\right), \quad \text{with} \quad \delta_{\mathrm{LZ}} = \frac{(\Delta E/2)^2}{2\hbar v_{\mathrm{F}} eE_{\mathrm{el}}}, \tag{2.66}$$

[16] They add a mass term $M\sigma_z$ to the Dirac Hamiltonian (2.9) and set $k_y = 0$. The mass term opens a gap $\Delta E = 2M$ in the spectrum and the bands look like those sketched in Fig. 2.5.

[17] Note that in Ref. [173] they mistakenly put a factor of 2 in the denominator instead of the $\sqrt{2}$ given here.

[18] A more detailed analysis of this mechanism in a gapped Dirac cone is given in the master's thesis of Ebner [163].

see Ref. [173] for details. Hence, the transition probability decreases with increasing gap ΔE or decreasing field strength E_{el}.

For $\delta_{\mathrm{LZ}} \ll 1$, one finds the *impulsive Landau-Zener regime*. There, $P_{\mathrm{LZ}} \approx 1$ and the electron undergoes an (almost) complete transition from one band to the other whenever it passes the minimal band gap. As a consequence, during the pulse the population repeatedly jumps from valence to conduction band and back and for a symmetric pulse and an even number of transitions ends up in the valence band afterwards. Thus, no population build-up occurs.

A similar behavior is found in the *nonimpulsive Landau-Zener regime*. The only difference in this regime is that the population transfer is smoother and only part of the electron switches band. This can be understood by comparing the transition time τ_{t} to the period of the driving. The transition time $\tau_{\mathrm{t}} = \pi/\Omega_{\mathrm{R}}$ is defined by the Rabi frequency Ω_{R} and can be understood as the time over which the transition process stretches. If $\tau_{\mathrm{t}} > 1/\nu_{\mathrm{el}}$, the transition takes longer than the one half cycle of the pulse. Thus, the occupation change appears smoother than in the impulsive Landau-Zener regime and classifies as nonimpulsive.

The last category is the *adiabatic-impulsive Landau-Zener(-Stückelberg) regime*. There, $P_{\mathrm{LZ}} \approx 0.5$ and thus one half of the electron's wave function stays in its original band whereas the other half is transferred to the other band. During the pulse, the wave-function parts repeatedly meet at the band gap and interfere with each other during transitions. This interference is taken into account via the Stückelberg phase [175, 178, 181] and modifies the actual transition such that population build-up can occur and appears rather effective.

These different categories smoothly transform from one to another when varying the system parameters. For 2D systems, different regimes can be accessed for the same laser pulse. By changing the initial position of the electron in momentum space, one can tune the band-structure cut it moves through during the pulse. Then, the minimal band gap ΔE the electron crosses changes, modifying the resonance frequency, the Keldysh parameter γ, the Rabi frequency Ω_{R}, and the Landau-Zener transition probability P_{LZ}. In Sec. 5.4 we demonstrate this tunability for four different Dirac models.

3. Simulating wave-packet dynamics in time-dependent quantum systems

Throughout this thesis we study electron dynamics in quantum systems with time-dependent driving. For the numerical simulation of these dynamics we mainly rely on the C++ library TQT (*Time-dependent Quantum Transport*) which was developed by Krückl in the scope of his PhD thesis [182]. Its central objective is to study time-dependent 1D or 2D systems based on wave-packet approaches, solving the time-dependent Schrödinger equation

$$\hat{\mathcal{H}}\Psi(\mathbf{r},t) = \mathrm{i}\hbar\frac{\mathrm{d}}{\mathrm{d}t}\Psi(\mathbf{r},t) \tag{3.1}$$

for a wave packet $\Psi(\mathbf{r},t)$ in discrete time steps. The Hamiltonian $\hat{\mathcal{H}}$ can be represented as atomic tight-binding or effective continuum model. In the latter case, it usually originates from the low-energy approximation of a solid's bandstructure at special k points and is a good description of the electronic properties within a certain energy window [106].

In this chapter, we want to introduce the relevant principles and algorithms implemented in TQT related to wave-packet propagation in quantum systems without leads. We focus on continuum Hamiltonians, tight-binding models have not been used for the work presented here. For a more detailed and full-fledged description of TQT, especially concerning the usage of tight-binding Hamiltonians and quantum transport calculations with leads, we redirect the reader to Krückl's thesis [182]. Additionally, we will present new algorithms we implemented for our studies and give an overview of the TQT-internal observables used throughout this thesis.

3.1. Avoiding fermion doubling in effective Dirac Hamiltonians

One major strength of TQT lies in treating effective continuum models for Dirac fermions without the fermion-doubling problem. The latter arises whenever effective Dirac Hamiltonians are discretized and solved on a spatial grid. These issues are quite well-known in the context of high-energy physics [183, 184] and generally defined by the Nielsen-Ninomiya theorem published in 1981 [109–111]. Within the field of condensed matter physics, people became more and more aware of the problem since the rise of graphene in 2004 [52]. In the context of solids, the Nielsen-Ninomiya theorem does not only have consequences for the mathematical treatment but also explains why only an even number of Dirac cones can exist in the bandstructure of a crystal. Nowadays, Dirac systems play a significant role within the community as they can be found not only in graphene but also in surface states of TIs. Since these are the systems we will be working on throughout this thesis, TQT is the ideal numerical tool for our studies. In order to demonstrate how TQT avoids fermion doubling, we shortly want to sketch the origin of the latter. For a detailed and pedagogical introduction of the phenomenon we refer to the PhD thesis of Kozlovsky [185].

As already mentioned, fermion doubling naturally appears whenever an effective Dirac Hamiltonian is discretized and solved on a real-space numerical grid. Such a scheme is e.g. applied in the widely used python package Kwant [186], which is quite powerful for solving transport problems, and its extension Tkwant [187], that can treat transport problems for time-dependent Hamiltonians. Just like in a crystal lattice, the spatial periodicity will introduce an artificial BZ. This imposes a periodicity in k on the corresponding energy dispersion $E(k)$, requiring $E(-\pi/a) = E(\pi/a)$, where a is the grid spacing. For concreteness, let us consider a simple Dirac Hamiltonian in 1D

$$\hat{\mathcal{H}}(k) = \hbar v_{\mathrm{F}} k \sigma_x, \tag{3.2}$$

with Fermi velocity v_{F}, Planck's constant $\hbar$ and Pauli matrix σ_x. When transforming to real space, $k \to -\mathrm{i}\partial_x$. Taking the plane-wave ansatz $\Psi(x) = \frac{1}{\sqrt{L}} \mathrm{e}^{\mathrm{i}kx} \varphi$ with spinor φ and length L, the continuous problem can easily be solved by diagonalizing the (2×2) Hamiltonian, giving the spectrum

$$E_{\mathrm{cont}}(k) = \pm \hbar v_{\mathrm{F}} |k|. \tag{3.3}$$

Now, we discretize x on a numerical grid with N lattice points labeled by j. To obtain periodic boundary conditions, $j = 1$ is equivalent to $j = N + 1$.

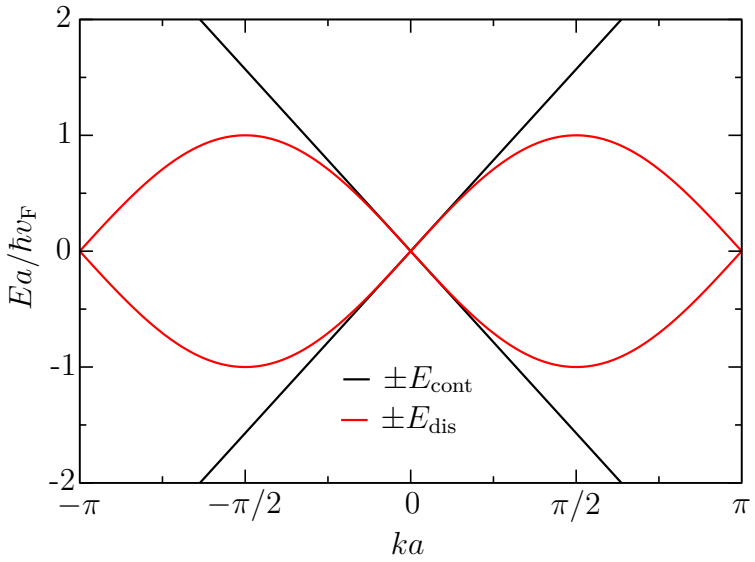

Fig. 3.1: Energy dispersion of the continuous (black) and the discretized (red) Dirac Hamiltonian. The discretization of the Hamiltonian on a spatial lattice leads to the formation of an additional Dirac point at the artificially imposed BZ boundaries $k/a = \pm\pi$. This phenomenon is called *fermion doubling*.

Then, $x \to ja$, $\Psi(x) \to \Psi(ja) \equiv \Psi_j$, and the derivative ∂_x is approximated by difference quotients on the grid, i.e.

$$\hat{\mathcal{H}}\Psi_j = -i\hbar v_\mathrm{F}\sigma_x\partial_x\Psi_j = -\mathrm{i}\hbar v_\mathrm{F}\sigma_x\frac{1}{2a}\left(\Psi_{j+1} - \Psi_{j-1}\right) = E\Psi_j. \tag{3.4}$$

Plugging in $\Psi_j = \frac{1}{\sqrt{L}}\mathrm{e}^{\mathrm{i}kja}\varphi$ gives the spectrum

$$E_\mathrm{dis}(k) = \pm\hbar v_\mathrm{F}\frac{1}{a}\left|\sin(ka)\right|. \tag{3.5}$$

As depicted in Fig. 3.1, this periodicity leads to the formation of a spurious Dirac point at the boundaries of the artificial BZ, giving rise to the name *fermion doubling*. Depending on what kind of physics one intends to study, the additional Dirac cone can completely change the numerical results. Additionally, the discretized spectrum is only a good approximation within a limited range of k around the original Dirac point. Even though there are options to circumvent the fermion doubling [188], one has to be careful when applying them since they again can alter the modeled physics. For the studies presented here, we apply (strong) electric fields to the system. Especially when studying HHG, the energy dispersion and geometrical properties of the model Hamiltonian are crucial for the results, as we will demonstrate in Chap. 5. Therefore, using a numerical method where we circumvent fermion doubling is very beneficial.

TQT works with Hamiltonians in a mixed real- and momentum-space repre-

sentation. The most general form these Hamiltonians can take is

$$\hat{\mathcal{H}} = \sum_{m_x,m_y} c_{m_x m_y}(\mathbf{r})\ \hat{k}_x^{m_x}\hat{k}_y^{m_y}, \tag{3.6}$$

where $c_{m_x m_y}(\mathbf{r})$ are position-dependent matrices and $\hat{k}_x^{m_x}$, $\hat{k}_y^{m_y}$ are powers m_x, m_y of the momentum operators[1]. To avoid transforming $\hat{k}_x$, $\hat{k}_y$ to real space, TQT performs several basis transformations, modifying the Hamiltonian to

$$\hat{\mathcal{H}} = \sum_{m_x,m_y} c_{m_x m_y}(\mathbf{r})\ \mathcal{F}_x^{-1}k_x^{m_x}\mathcal{F}_x^1\ \mathcal{F}_y^{-1}k_y^{m_y}\mathcal{F}_y^1, \tag{3.7}$$

with the Fourier transforms

$$\mathcal{F}_x^{\pm1}\Psi(\mathbf{r},t) = \frac{1}{\sqrt{2\pi}}\int \mathrm{d}x \mathrm{e}^{\mp \mathrm{i}k_x x}\Psi(\mathbf{r},t) \text{ and } \mathcal{F}_y^{\pm1}\Psi(\mathbf{r},t) = \frac{1}{\sqrt{2\pi}}\int \mathrm{d}y \mathrm{e}^{\mp \mathrm{i}k_y y}\Psi(\mathbf{r},t). \tag{3.8}$$

The propagated wave packet $\Psi(\mathbf{r},t)$ is converted between real and momentum space such that the operators k_x, k_y, and $\mathbf{r}$ can be applied in their respective scalar representation. Hence, even though the system is discretized on a numerical grid, fermion doubling is avoided.

TQT uses the algorithm of *Fast Fourier transforms* [189] for conversions between the two spaces. For the highest numerical efficiency, the rectangular grid $N_x \times N_y$, on which the wave packet $\Psi(\mathbf{r},t)$ is cast, should have a number of $N_x = 2^n$ ($N_y = 2^m$), $n, m \in \mathbb{N}$, grid points in x (y) direction. When choosing the optimal grid size $N_x \times N_y$ and grid spacing δx (δy) for one's calculations, one has to keep in mind that the momentum-space grid by definition is $k_x \in [-\pi/\delta x, \pi/\delta x]$ ($k_y \in [-\pi/\delta y, \pi/\delta y]$) with spacing $\delta k_x = 2\pi/(N_x \delta x)$ ($\delta k_y = 2\pi/(N_y \delta y)$). The center of the real-space grid can be chosen freely by the user. By default it is set to the origin, such that $x \in [-\delta x N_x/2, \delta x N_x/2]$ ($y \in [-\delta y N_y/2, \delta y N_y/2]$).

3.2. Discrete time evolution of wave packets

We have discussed how TQT treats the position and momentum dependencies of Hamiltonians $\hat{\mathcal{H}}$ in Sec. 3.1. Now we want to focus on the actual wave-packet propagation for explicitly time-dependent Hamiltonians[2] $\hat{\mathcal{H}}(t)$. In general,

[1] Note that TQT can only treat continuum Hamiltonians that are polynomials in $\hat{k}_x$, $\hat{k}_y$. More complicated functional dependencies have to be expanded into polynomials beforehand.

[2] TQT can also treat time-independent Hamiltonians. But this is not needed throughout this thesis and therefore not explicitly considered here.

the time evolution is obtained by solving the time-dependent Schrödinger equation (3.1) for the Hamiltonian $\hat{\mathcal{H}}(t)$ [190]. For an initial state $\Psi(\mathbf{r}, t_0)$, the propagation can be written as

$$\Psi(\mathbf{r}, t) = \hat{\mathcal{U}}(t, t_0)\Psi(\mathbf{r}, t_0) \tag{3.9}$$

with the time-evolution operator

$$\hat{\mathcal{U}}(t, t_0) = \hat{\mathcal{T}} \exp\left(-\frac{\mathrm{i}}{\hbar}\int_{t_0}^{t} \hat{\mathcal{H}}(\tau)\,\mathrm{d}\tau\right), \tag{3.10}$$

where $\hat{\mathcal{T}}$ is the time-ordering operator. For time-independent Hamiltonians, $\hat{\mathcal{U}}(t, t_0)$ simplifies to

$$\hat{\mathcal{U}}(t, t_0) = \exp\left(-\frac{\mathrm{i}}{\hbar}\hat{\mathcal{H}}\,(t - t_0)\right). \tag{3.11}$$

One can exploit expression (3.11) by discretizing the time t into N_t small steps. The duration δt of these steps has to be chosen sufficiently small such that the Hamiltonian is approximately constant and the dynamics adiabatic during each time step. The TQT timeline sets $t_0 = 0$ by definition, so we will adopt this from now on. Then, one can write

$$\hat{\mathcal{U}}(t = N_t\delta t, 0) \approx \prod_{n=1}^{N_t} \exp\left(-\frac{\mathrm{i}}{\hbar}\hat{\mathcal{H}}(n\delta t)\delta t\right) \tag{3.12}$$

for the time evolution operator from $t = 0$ to $t = N_t\delta t$ and the time evolution of the wave packet in Eq. (3.9) reduces to an easy multiplication instead of a time-ordered product. To efficiently treat the exponential function, different expansion methods can be used. So far, Chebychev [191], Faber [192, 193], Lanczos [194, 195], and Arnoldi [196] propagators are implemented in TQT. The optimal choice depends on the properties of the Hamiltonian $\hat{\mathcal{H}}(t)$. For the work presented here, we only used the Lanczos method, so we again redirect the interested reader to Krückl's work [182] for more details on the other propagators.

The Lanczos method is most suitable for explicitly time-dependent Hamiltonians $\hat{\mathcal{H}}(t)$ in closed systems. In this context, *closed* means that the wave packet cannot leave the system, i.e. we consider periodic boundaries. When a wave packet hits the boundary of either real- or momentum-space grid, it reenters on the other side of the grid. Note however, that the Hamiltonian $\hat{\mathcal{H}}(t)$ does not have to be periodic within either of the spaces. Thus, if the wave packet exceeds the limits of one of the grids within the propagation, this might affect the numerical results and lead to unphysical signatures in the computed

observables. This also has to be taken into consideration when defining the initial wave packet $\Psi(\mathbf{r}, 0)$ that is handed over to the propagator. In principle, the choice of the wave packet's shape is arbitrary but it's dimensions in real and momentum space are linked by the Fourier transforms (3.8) and thus must be chosen to fit both grids.

For single-particle physics, these limitations are usually not an issue. In Chaps. 6 and 7 however, we want to explore the role of the Fermi sea and spatial dependence of the pulse on HHG. For the latter, we implemented an extended version of the Lanczos propagator in TQT which we will introduce in Sec. 3.3. This *Lanczos Source propagator* in certain limits reduces to the Lanczos propagator and since we give a detailed description of the Lanczos method there, we omit any further mathematical details at this point.

3.3. Plane waves in spatially localized time-dependent potentials

So far, it was only possible to study the dynamics of wave packets, that by definition are localized both in position and momentum space, in TQT. This is not an issue as long as the applied time-dependent potentials are homogeneous and non-local in real space and the system's geometry is trivial[3], since then the initial central position of the wave packet does not play any role for the outcome of the simulation. If the applied fields become localized and maybe even inhomogeneous, such as the laser pulses introduced in Chap. 7.4, the question of where to initialize the wave packet and how to sample the full field profile arises.

One intuitive approach to this question would be to run several calculations with different starting positions to eventually sample the complete relevant real space. Here, we want to pursue a different strategy inspired by the *source-sink algorithm* [197] used in Tkwant [187]. It's advantage is that it offers the possibility to propagate plane waves and a rather straightforward option to include Fermi sea effects in the calculation of observables. As formally demonstrated in App. A.7, one only needs to integrate over all initially occupied states in order to consider a Fermi sea[4]. Note that we do not

[3] We focus on real-space-dependent potentials here since this is what we considered in our work.

[4] How to realize a Fermi sea using wave packets in spatially uniform potentials is discussed and studied in detail in Chap. 6.

want to treat the *sink* part of the algorithm here. Its basic idea is to include non-hermitian terms in the Hamiltonian for damping out the wave function at the boundaries of the system to avoid spurious effects from reflections. This concept has already been included in TQT by Krückl [182] and is not necessary for our work.

We implemented the source algorithm in TQT by introducing a *Lanczos Source propagator*. It is based on the same principles as the other TQT propagators, meaning that it also takes Hamiltonians in mixed position and momentum space representation and uses Fourier transforms to treat the operators in their respective scalar representation (see Sec. 3.1). A test application of the algorithm in a Fabry-Perot setup is shown in App. A.12. In the following we present the theory behind the algorithm and concentrate on the derivation in real space for the sake of simplicity. The Hamiltonian can be written as

$$\hat{\mathcal{H}}(\mathbf{r},t) = \hat{\mathcal{H}}_0(\mathbf{r}) + \hat{\mathcal{V}}(\mathbf{r},t), \tag{3.13}$$

where $\hat{\mathcal{V}}(\mathbf{r},t)$ contains all time-dependent terms and has to be localized in real space. The goal of the source algorithm is to compute the time evolution of a plane wave $\Psi_n(\mathbf{r},t)$. Since plane waves spread over the whole real space, this is quite challenging numerically. If $\Psi_n(\mathbf{r},0) = \varphi_n(\mathbf{r})$ is chosen to be an eigenstate of $\hat{\mathcal{H}}_0(\mathbf{r})$ with eigenenergy E_n, such that

$$\hat{\mathcal{H}}_0(\mathbf{r})\varphi_n(\mathbf{r}) = E_n\varphi_n(\mathbf{r}), \tag{3.14}$$

one can split the time evolved state into two parts

$$\Psi_n(\mathbf{r},t) = \psi_n(\mathbf{r},t) + \exp\left(-\frac{\mathrm{i}}{\hbar}E_n t\right)\varphi_n(\mathbf{r}). \tag{3.15}$$

Here, $\psi_n(\mathbf{r},t)$ contains all parts with non-trivial time evolution caused by $\hat{\mathcal{V}}(\mathbf{r},t)$ and its initial condition is $\psi_n(\mathbf{r},0) = 0$. Plugging this ansatz into the time-dependent Schrödinger equation (3.1) gives

$$\mathrm{i}\hbar\frac{\mathrm{d}}{\mathrm{d}t}\psi_n(\mathbf{r},t) = \hat{\mathcal{H}}(\mathbf{r},t)\psi_n(\mathbf{r},t) + \underbrace{\hat{\mathcal{V}}(\mathbf{r},t)\exp\left(-\frac{\mathrm{i}}{\hbar}E_n t\right)\varphi_n(\mathbf{r})}_{\text{source term}}. \tag{3.16}$$

This is the Schrödinger equation for $\psi_n(\mathbf{r},t)$ with an additional *source term* determined by the plane wave $\varphi_n(\mathbf{r})$. As long as the potential $\hat{\mathcal{V}}(\mathbf{r},t)$ is localized, $\psi_n(\mathbf{r},t)$ is simply a wave packet generated out of the plane wave $\varphi_n(\mathbf{r})$ by the time-dependent potential $\hat{\mathcal{V}}(\mathbf{r},t)$. The reduction of the complicated time evolution of a plane wave to a wave packet is the key idea of Tkwant's source algorithm [197].

For the actual numerical implementation it is favorable to rewrite Eq. (3.15) to

$$\Psi_n(\mathbf{r},t) = \exp\left(-\frac{\mathrm{i}}{\hbar}E_n t\right)(\psi_n(\mathbf{r},t) + \varphi_n(\mathbf{r})), \tag{3.17}$$

such that the modified Schrödinger equation (3.16) becomes

$$\mathrm{i}\hbar\frac{\mathrm{d}}{\mathrm{d}t}\psi_n(\mathbf{r},t) = \left(\hat{\mathcal{H}}(\mathbf{r},t) - E_n\right)\psi_n(\mathbf{r},t) + \hat{\mathcal{V}}(\mathbf{r},t)\varphi_n(\mathbf{r}). \tag{3.18}$$

Thus, the highly oscillatory dynamical phase $\exp\left(-\frac{\mathrm{i}}{\hbar}E_n t\right)$ does not have to be considered in the differential equation, increasing the numerical stability.

Apart from the source term and the shift $\hat{\mathcal{H}}(\mathbf{r},t)\psi_n(\mathbf{r},t) \to (\hat{\mathcal{H}}(\mathbf{r},t) - E_n)\psi_n(\mathbf{r},t)$ due to our redefinition of $\Psi_n(\mathbf{r},t)$ in Eq. (3.17), Eq. (3.18) is the same equation as treated by the other TQT propagators. There, for our type of systems the Lanczos method is most suitable. Generally, the Lanczos method describes how to approximate eigenvalue problems for large matrices by projecting them onto a much smaller subspace [194], thus making them numerically cheap. Park and Light showed how to apply this method to the Schrödinger equation [195], Dunbar and Woodbury described how the Lanczos method can be used on a set of inhomogeneous differential equations [198]. In the following, we combine both methods to solve the modified Schrödinger equation (3.18). Note that if one would include sinks in the Hamiltonian, the Arnoldi method [196] would be needed. In practice, the Arnoldi and Lanczos method are very similar, so everything derived here can easily be adopted for an *Arnoldi Source propagator*.

We start by expanding $\psi_n(\mathbf{r},t)$ and $\varphi_n(\mathbf{r})$ into the N-function basis $\{\phi_i(\mathbf{r})\}_N$

$$\psi_n(\mathbf{r},t) = \sum_{i=1}^{N} a_i(t)\phi_i(\mathbf{r}), \qquad \varphi_n(\mathbf{r}) = \sum_{i=1}^{N} b_i\phi_i(\mathbf{r}). \tag{3.19}$$

In TQT these $\phi_i(\mathbf{r})$ define the grid in real space and $N = N_x N_y$ is the number of grid points. A key requirement for the Lanczos method to work is that the propagation is performed in small time steps. As explained in Sec. 3.2, the step size has to be sufficiently small to assure that all parameters are constant during one step. In the following we therefore drop the time dependency of $\hat{\mathcal{H}}(\mathbf{r},t)$ and $\hat{\mathcal{V}}(\mathbf{r},t)$ and make the derivation for one single time step. Plugging our ansatz Eq. (3.19) into Eq. (3.18) gives

$$\mathrm{i}\hbar\sum_{i=1}^{N}\dot{a}_i(t)\phi_i(\mathbf{r}) = \left(\hat{\mathcal{H}}(\mathbf{r}) - E_n\right)\sum_{i=1}^{N}a_i(t)\phi_i(\mathbf{r}) + \hat{\mathcal{V}}(\mathbf{r})\sum_{i=1}^{N}b_i\phi_i(\mathbf{r}), \tag{3.20}$$

where $\frac{\mathrm{d}}{\mathrm{d}t}a_i(t) = \dot{a}_i(t)$. We can now rewrite this as a matrix equation. Note that the $\{\phi_i(\mathbf{r})\}_N$ basis in general is non-orthogonal but square integrable. Thus, the equations do not decouple and we get

$$\mathrm{i}\hbar\hat{S}\frac{\mathrm{d}\mathbf{a}(t)}{\mathrm{d}t} = \hat{H}\mathbf{a}(t) + \hat{V}\mathbf{b}, \tag{3.21}$$

where $\hat{S}$ is the overlap matrix with $S_{ij} = \langle\phi_i|\phi_j\rangle$, $\hat{H}$ is the Hamiltonian matrix with $H_{ij} = \langle\phi_i|\hat{\mathcal{H}}(\mathbf{r}) - E_n|\phi_j\rangle$ and $\hat{V}$ is the source matrix with $V_{ij} = \langle\phi_i|\hat{\mathcal{V}}(\mathbf{r})|\phi_j\rangle$. In TQT however the $\{\phi_i(\mathbf{r})\}_N$ are orthogonal since two different grid points $\mathbf{r}$ and $\mathbf{r}'$ do not overlap and $\hat{S} = \mathbb{1}$. Nevertheless, we will keep $\hat{S}$ in the following derivation for the sake of generality.

We can now solve Eq. (3.21) for $\dot{\mathbf{a}}(t)$

$$\dot{\mathbf{a}}(t) = -\frac{\mathrm{i}}{\hbar}\hat{S}^{-1}\hat{H}\mathbf{a}(t) - \frac{\mathrm{i}}{\hbar}\hat{S}^{-1}\hat{V}\mathbf{b}. \tag{3.22}$$

At this point, we can use the Lanczos method to reduce the dimension of our problem from N to $p \ll N$. Its recursive algorithm constructs a set of p $\hat{S}$-orthogonal vectors $\{\mathbf{q}\}_p$ spanning a subspace in which the Hamiltonian obtains a tridiagonal form. Note that even though our equation is inhomogeneous the definition of $\{\mathbf{q}\}_p$ is the same as for the standard Schrödinger equation

$$\begin{aligned}\hat{S}^{-1}\hat{H}\mathbf{q}_0 &= \alpha_0\mathbf{q}_0 + \beta_0\mathbf{q}_1,\\ \hat{S}^{-1}\hat{H}\mathbf{q}_k &= \beta_{k-1}\mathbf{q}_{k-1} + \alpha_k\mathbf{q}_k + \beta_k\mathbf{q}_{k+1}.\end{aligned} \tag{3.23}$$

The only thing that changes for the Lanczos Source algorithm so far is the starting vector $\mathbf{q}_0$. In principle, its choice is largely arbitrary, but in Ref. [198] they state that "the process should contain basis states that are the primary components of interest". Usually, the Lanczos propagator in TQT takes $\mathbf{q}_0 = \mathbf{a}(t_0)/\left|\mathbf{a}(t_0)\right|$, where $\mathbf{a}(t_0)$ is the result from the prior time step. However, we have to be careful since $\mathbf{q}_0$ must not be zero. Thus, as long as $\mathbf{a}(t_0) = 0$ in our propagation, we take $\mathbf{q}_0 = \mathbf{b}/\left|\mathbf{b}\right|$. As soon as a finite value $\mathbf{a}(t_0)$ has been generated by the source term, we start with $\mathbf{q}_0 = \mathbf{a}(t_0)/\left|\mathbf{a}(t_0)\right|$ instead[5].

The transformation from the basis $\{\phi_i(\mathbf{r})\}_N$ to the subspace $\{\mathbf{q}\}_p$ is given by the $(N \times p)$-matrix $\hat{A}_p$

$$\hat{A}_p = [\mathbf{q_0}\ \ \mathbf{q_1}\ \ \mathbf{q_2}\ \ \ldots\ \ \mathbf{q_{p-1}}] \tag{3.24}$$

[5]Note that finite for numerics means sufficiently large to avoid issues with numerical precision. Currently, we demand $|\mathbf{a}(t_0)|^2 > 10^{-10}$ in order to use it as starting vector.

and the Hamiltonian matrix $\hat{H}_p$ in this subspace reads

$$\hat{H}_p = \begin{pmatrix} \alpha_0 & \beta_0 & 0 & \cdots & 0 & 0 \\ \beta_0 & \alpha_1 & \beta_1 & \cdots & 0 & 0 \\ 0 & \beta_1 & \alpha_2 & \cdots & 0 & 0 \\ \vdots & \vdots & \vdots & \ddots & \vdots & \vdots \\ 0 & 0 & 0 & \cdots & \alpha_{p-2} & \beta_{p-2} \\ 0 & 0 & 0 & \cdots & \beta_{p-2} & \alpha_{p-1} \end{pmatrix}. \tag{3.25}$$

Accordingly, we can write $\mathbf{a}(t) = \hat{A}_p \mathbf{c}(t)$. Note that $\hat{A}_p$ is not quadratic and therefore not invertible. However, since the $\{\mathbf{q}\}_p$ are orthonormal by definition, $\hat{A}_p^\dagger \hat{A}_p = \mathbb{1}$. We get

$$\dot{\mathbf{c}}(t) = -\frac{\mathrm{i}}{\hbar} \hat{A}_p^\dagger \hat{S}^{-1} \hat{H} \hat{A}_p \mathbf{c}(t) - \frac{\mathrm{i}}{\hbar} \hat{A}_p^\dagger \hat{S}^{-1} \hat{V} \mathbf{b}. \tag{3.26}$$

Due to the $\hat{S}$-orthogonality of our new basis $\{\mathbf{q}\}_p$, $\hat{A}_p^\dagger \hat{S}^{-1} \hat{H} \hat{A}_p = \hat{H}_p$. Thus, the differential equation (3.26) only consists of p components instead of N which makes finding its solution numerically by diagonalization much faster than for the original Eq. (3.22).

Let $\{\mathbf{h}\}_p$ be the eigenbasis of $\hat{H}_p$ with eigenvalues λ_i. Then

$$\hat{T}_p = [\mathbf{h_0} \;\; \mathbf{h_1} \;\; \mathbf{h_2} \;\; \ldots \;\; \mathbf{h_{p-1}}] \tag{3.27}$$

is the transformation from $\{\mathbf{q}\}_p$ to $\{\mathbf{h}\}_p$. Since the eigenvectors $\{\mathbf{h}\}_p$ are orthonormal, $\hat{T}_p^{-1} = \hat{T}_p^\dagger$. We can write the diagonalized form of Eq. (3.26) as

$$\dot{\mathbf{d}}(t) = -\frac{\mathrm{i}}{\hbar} \hat{T}_p \hat{H}_p \hat{T}_p^\dagger \mathbf{d}(t) - \frac{\mathrm{i}}{\hbar} \underbrace{\hat{T}_p \hat{A}_p^\dagger \hat{S}^{-1} \hat{V} \mathbf{b}}_{\mathbf{g}}, \tag{3.28}$$

where[6] $\mathbf{c}(t) = \hat{T}_p^\dagger \mathbf{d}(t)$. Equation (3.28) finally decouples and can be solved analytically for each component,

$$d_i(t) = d_i(t_0) \exp\left(-\frac{\mathrm{i}}{\hbar} \lambda_i t\right) - \frac{g_i}{\lambda_i} \left[1 - \exp\left(-\frac{\mathrm{i}}{\hbar} \lambda_i t\right)\right]. \tag{3.29}$$

This solution is exact as long as $\mathbf{b}$ is constant in the considered time step. We can calculate the initial condition as $\mathbf{d}(t_0) = \hat{T}_p \mathbf{c}(t_0) = \hat{T}_p \hat{A}_p^\dagger \mathbf{a}(t_0)$. For the

[6] Note that the transformation is different from the one before since the eigenvectors that build $\hat{T}_p$ are those of $\hat{H}_p$ and not of the diagonalized matrix.

first time steps, $\mathbf{d}(t_0) = 0$, but as soon as the source term has generated a finite $\mathbf{a}(t_0)$, $\mathbf{d}(t_0) = \mathbf{h}_0 \, |\mathbf{a}(t_0)|$.

At last, we can transform the solution back to our original space $\{\phi_i(\mathbf{r})\}_N$ using $\mathbf{a}(t) = \hat{A}_p \mathbf{c}(t) = \hat{A}_p \hat{T}_p^\dagger \mathbf{d}(t)$ and obtain the time evolved wave packet $\psi_n(\mathbf{r}, t) = \sum_{i=1}^{N} a_i(t) \phi_i(\mathbf{r})$. To calculate physical observables, the propagator in the end adds up both contributions $\psi_n(\mathbf{r}, t)$ and $\varphi_n(\mathbf{r})$ to construct the full time dependent state (3.17). The TQT-internal observables relevant for this work are introduced in Sec. 3.5.

3.4. Including orbital magnetic fields

In Sec. 2.3.2 we thoroughly discussed how electric fields $\mathbf{E}_{\text{el}}(t)$ are introduced in effective model Hamiltonians using either a vector potential $\mathbf{A}(t)$ or a scalar potential $\phi_{\text{el}}(\mathbf{r}, t)$. In this section, we focus on how to treat the orbital coupling of a magnetic field perpendicular to the investigated 2D system, i.e. $\mathbf{B} \parallel \mathbf{e}_z$. This magnetic field can either be static, compare Sec. 7.3.2, or time-dependent, e.g. as the magnetic component of a light field, see Sec. 7.4. In the following, we start with the static case and then extend it to time-dependent magnetic fields.

Generally, the orbital magnetic field $\mathbf{B}$ is included in the effective model by minimal coupling of the vector potential $\mathbf{A}(\mathbf{r})$, see Eq. (2.54). Here, the spatial dependence of the vector potential is crucial since the magnetic field is defined as

$$\mathbf{B} = \nabla_{\mathbf{r}} \times \mathbf{A}(\mathbf{r}). \tag{3.30}$$

The minimal coupling modifies the general polynomial Hamiltonian (3.6) to

$$\hat{\mathcal{H}} = \sum_{m_x, m_y} c_{m_x m_y}(\mathbf{r}) \, \left(\hat{k}_x + \frac{e}{\hbar} A_x(\hat{\mathbf{r}}) \right)^{m_x} \left(\hat{k}_y + \frac{e}{\hbar} A_y(\hat{\mathbf{r}}) \right)^{m_y}, \tag{3.31}$$

where the vector potential in the 2D plane of the simulation is written as $\mathbf{A}(\hat{\mathbf{r}}) = (A_x(\hat{\mathbf{r}}), A_y(\hat{\mathbf{r}}))$. Thus, especially for polynomial Hamiltonians with higher-order momentum terms, including this orbital coupling requires caution due to commutators of the position and momentum operators. Additionally, the newly arising terms make the computation with TQT more costly. Therefore, Krückl developed a TQT-internal routine that efficiently implements the orbital effect using gauge transformations of the vector potential $\mathbf{A}(\mathbf{r})$ [182].

Due to the gauge invariance, the magnetic field $\mathbf{B} = B_z \mathbf{e}_z$ can be expressed either in the symmetric gauge

$$\mathbf{A}^{[0]}(\mathbf{r}) = \frac{1}{2} \begin{pmatrix} -a_x(\mathbf{r}) \\ a_y(\mathbf{r}) \end{pmatrix} \tag{3.32}$$

or in the Landau gauge in x or y direction,

$$\mathbf{A}^{[-1]}(\mathbf{r}) = \begin{pmatrix} -a_x(\mathbf{r}) \\ 0 \end{pmatrix} \quad \text{or} \quad \mathbf{A}^{[1]}(\mathbf{r}) = \begin{pmatrix} 0 \\ a_y(\mathbf{r}) \end{pmatrix}. \tag{3.33}$$

For all three gauges, the vector-field components are given by

$$a_x(\mathbf{r}) = \int_{y_0}^{y} B_z(x, y') \, \mathrm{d}y' \quad \text{and} \quad a_y(\mathbf{r}) = \int_{x_0}^{x} B_z(x', y) \, \mathrm{d}x' \tag{3.34}$$

with $\mathbf{r} = (x, y)$ in the 2D plane. The transformation between different gauges is described by the scalar potential

$$\Lambda_{f \leftarrow i}(\mathbf{r}) = \frac{i - f}{2} \int_{x_0}^{x} \int_{y_0}^{y} B_z(x', y') \, \mathrm{d}y' \, \mathrm{d}x', \tag{3.35}$$

where $f, i \in [-1, 0, 1]$ denote the final (f) and initial (i) gauge. This transformation (3.35) also describes how the propagated wave function $\Psi(\mathbf{r}, t)$ changes with the gauge,

$$\Psi_f(\mathbf{r}, t) = \underbrace{\exp\left(-\frac{\mathrm{i}e}{\hbar} \Lambda_{f \leftarrow i}(\mathbf{r})\right)}_{\mathcal{G}_{f \leftarrow i}} \Psi_i(\mathbf{r}, t). \tag{3.36}$$

By subsequent gauge transformations $\mathcal{G}_{f \leftarrow i}$ one can achieve that $A_x(\mathbf{r}) = 0$ ($A_y(\mathbf{r}) = 0$) when the terms with k_x (k_y) are applied to $\Psi(\mathbf{r}, t)$. Since, conventionally, the vector potential is represented in the symmetric gauge (3.32) to equally distribute numerical errors into k_x and k_y, Krückl chose this gauge as initial and final condition. In combination with the TQT-internal Fourier transforms (3.7), the Hamiltonian (3.31) thus becomes

$$\hat{\mathcal{H}} = \sum_{m_x, m_y} c_{m_x m_y}(\mathbf{r}) \, \mathcal{G}_{0 \leftarrow +1} \left[\mathcal{F}_x^{-1} k_x^{m_x} \mathcal{F}_x^{1}\right] \mathcal{G}_{+1 \leftarrow -1} \left[\mathcal{F}_y^{-1} k_y^{m_y} \mathcal{F}_y^{1}\right] \mathcal{G}_{-1 \leftarrow 0}, \tag{3.37}$$

treating the orbital coupling in a numerically efficient way. When using this routine for a spatially independent magnetic field, TQT only needs the field strength B_z and computes the gauge transformation automatically based on Eq. (3.35) before starting the propagation. When the magnetic field represents a light wave however, it depends on position and time, i.e. $\mathbf{B} \to \mathbf{B}(\mathbf{r}, t)$, compare Sec. 7.4. Then, determining the gauge transformation $\Lambda_{f \leftarrow i}(\mathbf{r}, t)$ with

Eq. (3.35) requires an actual integration, that has to be calculated anew for every time step. We implemented this procedure in an extra routine that takes the vector potential $\mathbf{A}(\mathbf{r}, t)$ instead of the magnetic field as an input. Moreover, to allow for a freedom of gauge in this input, we added an option for specifying the original gauge of $\mathbf{A}(\mathbf{r}, t)$ that is used for defining the gauge transformation (3.35) accordingly.

3.5. Overview of relevant observables

In order to study the properties of a system, one usually wants to calculate physical observables. When using TQT, one can either extract the resulting wave packet $\Psi(\mathbf{r}, t)$ or the Fourier transformed state $\Psi(\mathbf{k}, t)$ for further processing[7] or directly compute observables during the propagation. To simplify the latter, a large variety of observables is already included in the TQT library. In this section we want to introduce the TQT-internal observables used throughout this thesis. Note that the Fourier transformation necessary for the observables evaluated in momentum space is always implemented in the respective observable and will not be explicitly mentioned in the following.

Center of mass motion (COM)

As the name suggests, the *Center of Mass* (COM) observable tracks the center of mass motion of the wave packet $\Psi(\mathbf{r}, t)$ in position space or of the wave packet $\Psi(\mathbf{k}, t)$ in momentum space. It calculates the position expectation value in x and y direction as

$$x(t) = \langle \hat{x}(t) \rangle = \iint |\Psi(\mathbf{r}, t)|^2 x \, \mathrm{d}x \, \mathrm{d}y, \qquad y(t) = \langle \hat{y}(t) \rangle = \iint |\Psi(\mathbf{r}, t)|^2 y \, \mathrm{d}y \, \mathrm{d}x, \tag{3.38}$$

where the integrals run over the full numerical grid. Additionally, the observable provides the corresponding velocities via derivation, $v_x(t) = \mathrm{d}x(t)/\mathrm{d}t$, $v_y(t) = \mathrm{d}y(t)/\mathrm{d}t$. In momentum space, the expectation values $\langle k_x(t) \rangle$ and $\langle k_y(t) \rangle$ are defined analogously as

$$\langle k_x(t) \rangle = \iint |\Psi(\mathbf{k}, t)|^2 k_x \, \mathrm{d}k_x \, \mathrm{d}k_y, \qquad \langle k_y(t) \rangle = \iint |\Psi(\mathbf{k}, t)|^2 k_y \, \mathrm{d}k_y \, \mathrm{d}k_x. \tag{3.39}$$

[7] However, one has to be careful since the files containing the full wave function $\Psi(\mathbf{r}, t)$ ($\Psi(\mathbf{k}, t)$) can need rather large amounts of storage.

Here, it is possible to include a k-mask $f(\mathbf{k})$ and thus to evaluate the observable in a limited region in momentum space, see Sec. 6.2 for a detailed introduction. The cut expectation values $\langle k_x(t)\rangle_{\mathrm{cut}}$ and $\langle k_y(t)\rangle_{\mathrm{cut}}$ are given by

$$\begin{aligned}\langle k_x(t)\rangle_{\mathrm{cut}} &= \iint f(\mathbf{k})|\Psi(\mathbf{k},t)|^2 k_x \,\mathrm{d}k_x \,\mathrm{d}k_y,\\ \langle k_y(t)\rangle_{\mathrm{cut}} &= \iint f(\mathbf{k})|\Psi(\mathbf{k},t)|^2 k_y \,\mathrm{d}k_y \,\mathrm{d}k_x.\end{aligned} \tag{3.40}$$

Velocity in momentum space

In Chap. 6 we present a method for including Fermi sea effects in the propagation of wave packets that cover a wide range in momentum space. In this context, we introduce the aforementioned k-mask. In order to use the k-mask when computing velocities, we implemented a new observable in TQT that extracts the velocity from the Fourier transformed wave packet $\Psi(\mathbf{k},t)$. This velocity observable requires the velocity operator $\hat{\mathbf{v}}_{\mathbf{k}}$ in addition to the wave packet and is defined as

$$\mathbf{v}(t) = \iint \Psi^*(\mathbf{k},t)\ \hat{\mathbf{v}}_{\mathbf{k}}\ \Psi(\mathbf{k},t)\ \mathrm{d}k_x\ \mathrm{d}k_y. \tag{3.41}$$

Accordingly, the velocity $\mathbf{v}_{\mathrm{cut}}(t)$ cut in momentum space by the k-mask $f(\mathbf{k})$ reads

$$\mathbf{v}_{\mathrm{cut}}(t) = \iint f(\mathbf{k})\ \Psi^*(\mathbf{k},t)\ \hat{\mathbf{v}}_{\mathbf{k}}\ \Psi(\mathbf{k},t)\ \mathrm{d}k_x\ \mathrm{d}k_y. \tag{3.42}$$

Note that currently this observable can only be applied as long as the system's velocity operator $\hat{\mathbf{v}}_{\mathbf{k}}$ is independent of time.

Intra- and interband velocity

As discussed in Sec. 2.3, the velocity can be decomposed in an intra- and an interband contribution. For their computation, we introduced the *velocity-split* observable in collaboration with Wolfgang Hogger. It is an hereditary class of the velocity observable in momentum space and also requires the time-independent velocity operator $\hat{\mathbf{v}}_{\mathbf{k}}$ as an input. The full velocity $\mathbf{v}(t)$ is automatically computed when using the velocity-split observable. Additionally, one has to hand over the eigenstates $\varphi_n(\mathbf{k}) = \langle\mathbf{k}|\varphi_{\mathbf{k},n}\rangle$ of the time-independent Hamiltonian[8] $\hat{\mathcal{H}}_0(\mathbf{k})$. The observable then computes the diagonal components

[8] This means, one has to express the system's Hamiltonian in momentum space $\hat{\mathcal{H}}(\mathbf{r},t) \to \hat{\mathcal{H}}(\mathbf{k},t)$ and separate it into the time-independent part $\hat{\mathcal{H}}_0(\mathbf{k})$ and the time-dependent potential $\hat{\mathcal{V}}(\mathbf{k},t)$. Then, the eigenstates $|\varphi_{\mathbf{k},n}\rangle$ fulfill $\hat{\mathcal{H}}_0(\mathbf{k})|\varphi_{\mathbf{k},n}\rangle = E_n(\mathbf{k})|\varphi_{\mathbf{k},n}\rangle$, where $E_n(\mathbf{k})$ is the respective eigenenergy.

$\mathbf{v}_{\mathbf{k}}^{nn}$ of the velocity matrix, i.e.

$$\mathbf{v}_{\mathbf{k}}^{nn} = \langle \varphi_{\mathbf{k},n} | \hat{\mathbf{v}}_{\mathbf{k}} | \varphi_{\mathbf{k},n} \rangle, \tag{3.43}$$

for each energy band n. During the propagation, the wave packet $\Psi(\mathbf{k}, t)$ is projected onto the different energy bands, giving the occupation

$$|c_{\mathbf{k},n}(t)|^2 = \varphi_n^*(\mathbf{k}) \Psi(\mathbf{k}, t). \tag{3.44}$$

At last, the intraband contribution of band n to the velocity of the wave packet is evaluated as

$$\mathbf{v}_{\text{intra}}(n, t) = \iint |c_{\mathbf{k},n}(t)|^2 \, \mathbf{v}_{\mathbf{k}}^{nn} \, \mathrm{d}k_x \, \mathrm{d}k_y. \tag{3.45}$$

Like for the total velocity (3.42), the introduction of a k-mask $f(\mathbf{k})$ is possible and gives the cut velocity

$$\mathbf{v}_{\text{intra,cut}}(n, t) = \iint f(\mathbf{k}) \, |c_{\mathbf{k},n}(t)|^2 \, \mathbf{v}_{\mathbf{k}}^{nn} \, \mathrm{d}k_x \, \mathrm{d}k_y. \tag{3.46}$$

Since the wave packet $\Psi(\mathbf{k}, t)$ acquires random phases at each time step during propagation in TQT, the interband velocity cannot be calculated similarly to the intraband velocity. We can only compute $\mathbf{v}_{\text{inter}}(t)$ as the difference between the total velocity $\mathbf{v}(t)$ and the sum over all intraband velocities $\mathbf{v}_{\text{intra}}(n, t)$,

$$\mathbf{v}_{\text{inter}}(t) = \mathbf{v}(t) - \sum_n \mathbf{v}_{\text{intra}}(n, t). \tag{3.47}$$

Accordingly, distinguishing the interband contributions between different bands is not possible for systems with more than two bands. By subtracting the cut velocities, the effect of a k-mask $f(\mathbf{k})$ is included,

$$\mathbf{v}_{\text{inter,cut}}(t) = \mathbf{v}_{\text{cut}}(t) - \sum_n \mathbf{v}_{\text{intra,cut}}(n, t). \tag{3.48}$$

4. Floquet oscillations in periodically driven Dirac sytems

4.1. Introduction

Modifying a systems properties by applying a time-periodic external potential has become a powerful tool for creating new, exotic states of matter in the last years. One of the first proposals for so-called Floquet engineering came from Lindner et al. [56]. They found that the spectrum of a topologically trivial semiconductor quantum well can become non trivial under illumination with circularly polarized light. Further studies of such Floquet TIs revealed that they can host a new topological phase that does not have a counterpart in non-driven systems [65–68]. This anomalous Floquet topological phase has already been observed in photonic [57–61] and phononic [62] systems as well as experimentally characterized in ultracold atom systems [63, 64].

For studying these new states of matter, good knowledge and understanding of the Floquet quasi bandstructure is crucial. For example, Wintersperger et al. [63] used Stückelberg interferometry [199, 200] to identify how the gap closings of the Floquet quasi bandstructure and the emergence of topological phases relate to each other. The Floquet oscillations we demonstrate in this chapter offer another option to map out the quasi bandstructure of a Floquet system.

From a mathematical perspective, Floquet theory and Bloch's theorem are equivalent. Both theories treat linear differential equations with periodic coefficients as described by the French mathematician Floquet in his work in 1883 [24]. In Bloch's analysis of the quantum mechanics of electrons in crystal lattices in 1929 [70], these coefficients were periodic in space. Floquet theory is its analogue for time-periodic systems [25–27]. For Bloch bands, already in

the beginning of the 20th century Bloch and Zener [70, 71] predicted that an electron accelerated by a constant external electric field will undergo a time-periodic motion. This phenomenon, by now well known as Bloch oscillations [72], was observed for the first time about 60 years after its prediction in biased semiconductor superlattices [201–203]. Later on, Bloch oscillations and analogues of them have been realized in a wide range of systems, e.g. cold atom gases [204, 205] and classical optical [206, 207] and acoustic waves [208]. Finally, in 2014, Bloch oscillations were measured in a biased bulk semiconductor [168]. Recently, it has been demonstrated that by adding Floquet engineering, Bloch oscillations can be switched on and off [209] or their amplitude increased immensely, leading to "super" Bloch oscillations [73, 210–212].

Here, we focus on the opposite limit: a system under time-periodic driving. We will show that a particle can undergo spatially periodic motion when driven through an oscillating Floquet quasi bandstructure by a static electric field. We call this motion *Floquet oscillation* since it can be considered as Bloch-type oscillation within the Floquet quasi bandstructure. As we will demonstrate, a suitable quasi bandstructure can be generated from a system with effective Dirac Hamiltonian by applying different time-periodic drivings. Hence, spatial periodicity is only necessary to create a bandstructure that can be described by an effective Dirac Hamiltonian within a certain energy window but does not influence the spatial oscillations otherwise.

There are only a few other works considering Bloch-type oscillations not dominated by an underlying spatial lattice. However, the mechanisms leading to Bloch-type oscillations in these studies are of a completely different nature than what we want to present here. For example, in interacting 1D spinor gases it is predicted that one can find Bloch-type oscillations due to the dynamical formation of periodic structures caused by interactions [213]. Experimentally, this has been observed in an atomic Bose liquid [214]. Another interesting prediction are Bloch oscillations of light, which should appear as frequency oscillations of photons [215].

Most of the results presented in this chapter have been published in Ref. [74]. Part of this work (mainly in Secs. 4.3, 4.4.1, 4.4.2) has already been done in my master's thesis [123] under the supervision of Phillipp Reck. For the sake of completeness, we repeat what is necessary and expand on some aspects.

4.2. Basic concepts of Floquet theory

There exists a large variety of review articles offering introductions to Floquet theory, e.g. [36, 216–220]. Based on Ref. [217], here we will shortly present the most important aspects for our work.

We consider a periodically-driven quantum system described by the Hamiltonian $\hat{\mathcal{H}}(t)$ which fulfills

$$\hat{\mathcal{H}}(t) = \hat{\mathcal{H}}(t+T), \tag{4.1}$$

with the driving period T. Generally, to obtain the time evolution of a state $|\Psi(t)\rangle$ one has to solve the time-dependent Schrödinger equation

$$\mathrm{i}\hbar\frac{\mathrm{d}}{\mathrm{d}t}|\Psi(t)\rangle = \hat{\mathcal{H}}(t)|\Psi(t)\rangle. \tag{4.2}$$

According to Floquet's theorem, for a time-periodic Hamiltonian $\hat{\mathcal{H}}(t)$ a complete, orthonormal basis set is given by the *Floquet states*

$$|\Psi_\alpha(t)\rangle = \exp\left(-\frac{\mathrm{i}}{\hbar}\epsilon_\alpha t\right)|\Phi_\alpha(t)\rangle, \tag{4.3}$$

where ϵ_α is the corresponding *quasienergy* and $|\Phi_\alpha(t)\rangle = |\Phi_\alpha(t+T)\rangle$ a time-periodic function, also called *Floquet mode*[1]. Since these Floquet modes $|\Phi_\alpha(t)\rangle$ have the same periodicity T as the driving, they can be expanded into a discrete Fourier series in terms of the driving frequency $\omega = 2\pi/T$,

$$|\Phi_\alpha(t)\rangle = \sum_n \exp\left(-\mathrm{i}n\omega t\right)|\phi_\alpha^n\rangle. \tag{4.4}$$

Analogously, the time-periodic Hamiltonian can be decomposed to

$$\hat{\mathcal{H}}(t) = \sum_m \exp\left(-\mathrm{i}m\omega t\right)H^m. \tag{4.5}$$

Plugging the ansatz (4.3) and the Fourier series (4.4) and (4.5) into the Schrödinger equation (4.2) eventually yields

$$\left(\epsilon_\alpha + n\hbar\omega\right)|\phi_\alpha^n\rangle = \sum_m H^{(n-m)}|\phi_\alpha^m\rangle. \tag{4.6}$$

To compute the Fourier coefficients $|\phi_\alpha^n\rangle$ and the quasienergies ϵ_α, we rearrange Eq. (4.6) to an eigenvalue equation in Fourier space

$$\hat{H}\varphi_\alpha = \epsilon_\alpha\varphi_\alpha, \tag{4.7}$$

[1]Note that in this decomposition the analogy to Bloch's theorem becomes apparent. The eigenstates of an electron in a spatially periodic crystal are decomposed into a plane wave with *quasimomentum* k and a lattice-periodic function.

where

$$\hat{H} = \begin{pmatrix} \ddots & H^{(-1)} & H^{(-2)} & \iddots \\ H^{(1)} & H^{(0)} - n\hbar\omega & H^{(-1)} & H^{(-2)} \\ H^{(2)} & H^{(1)} & H^{(0)} - (n+1)\hbar\omega & H^{(-1)} \\ \iddots & H^{(2)} & H^{(1)} & \ddots \end{pmatrix}, \; \varphi_\alpha = \begin{pmatrix} \vdots \\ |\phi_\alpha^n\rangle \\ |\phi_\alpha^{(n+1)}\rangle \\ \vdots \end{pmatrix}, \tag{4.8}$$

and $H^{(0)} = \frac{1}{T}\int_0^T \hat{\mathcal{H}}(t)\,\mathrm{d}t$ is the dc part of the Hamiltonian. Note that the matrix $\hat{H}$ has a block structure, where each Fourier component $H^{(n-m)} = \frac{1}{T}\int_0^T \hat{\mathcal{H}}(t)\mathrm{e}^{\mathrm{i}(n-m)\omega t}\,\mathrm{d}t$ has the size $(d \times d)$ with d being the dimension of the Hilbert space spanned by the original Hamiltonian $\hat{\mathcal{H}}(t)$. Accordingly, the $|\phi_\alpha^n\rangle$ are vectors with d components. In principle, $\hat{H}$ is an infinitely large matrix due to the Fourier expansion it is based on. Nevertheless, one can find a finite value N to truncate the matrix, reducing the Fourier expansion to $(2N+1)$ coefficients, and still get converged quasienergies and Floquet modes.

This truncation becomes plausible when taking a closer look at the physical interpretation. Mathematically, the transformation into Fourier space leads to an overcompleteness of solutions. One can get the same Floquet state (4.3) for the quasienergy ϵ_α and all shifted energies $\tilde{\epsilon}_\alpha = \epsilon_\alpha + n\hbar\omega$ when using the Fourier expansion (4.4), all these $\{\epsilon_\alpha\}$ being eigenvalues of the infinite matrix $\hat{H}$. Due to their redundancy however, one can reduce this infinite number of copies of the spectrum to a *first Floquet Brillouin zone* (FBZ) $\epsilon_{\min} \leq \epsilon \leq \epsilon_{\min} + \hbar\omega$. A common choice is $\epsilon_{\min} = -\hbar\omega/2$. The number of bands in the FBZ is equal to the number of bands of the undriven Hamiltonian $\hat{\mathcal{H}}(0)$. To determine the physical energy scale of the system, one can compute the time-averaged spectral function

$$A_\alpha(E) = \sum_n \langle\phi_\alpha^n|\phi_\alpha^n\rangle\; \delta\left(\epsilon_\alpha + n\hbar\omega - E\right), \tag{4.9}$$

giving a spectral weight to the copies of the Floquet bands indicating how the Floquet states would couple to external degrees of freedom (e.g. leads) at energy E. In this notation, $n = 0$ usually labels the bands emerging from the bands of the undriven system, the copies shifted up (down) by $n\hbar\omega$ can be interpreted as those arising from absorption (emission) of n photons of the driving field[2]. Thus, the spectral weight rapidly decreases with increasing n and eventually goes to zero, determining the range $-N \leq n \leq N$ of Fourier components necessary to capture the full physical properties of the system[3].

[2]Note that depending on the driving this could also be phonons or other (quasi)particles with energy $\hbar\omega$.

[3]One has to keep in mind that the truncation of $\hat{H}$ distorts the bands of the outer copies. Thus, N has to be large enough for all physically relevant copies to be fully converged.

Since the Floquet states (4.3) form a complete, orthonormal basis set, one can write down the time evolution $|\Psi(t)\rangle$ of any initial state $|\Psi(0)\rangle$ by projection on the Floquet states $|\Psi_\alpha(t)\rangle$,

$$\begin{aligned} |\Psi(t)\rangle &= \sum_\alpha c_\alpha |\Psi_\alpha(t)\rangle = \sum_\alpha c_\alpha \exp\left(-\frac{\mathrm{i}}{\hbar}\epsilon_\alpha t\right)|\Phi_\alpha(t)\rangle \\ &= \sum_\alpha \langle\Phi_\alpha(0)|\Psi(0)\rangle \exp\left(-\frac{\mathrm{i}}{\hbar}\epsilon_\alpha t\right)|\Phi_\alpha(t)\rangle, \end{aligned} \tag{4.10}$$

$|c_\alpha|^2 = |\langle\Phi_\alpha(0)|\Psi(0)\rangle|^2$ being the occupation of the Floquet band ϵ_α. For a perfect Floquet system, the amplitudes c_α are independent of time. Since the quasienergies ϵ_α are a static quantity, they only capture the stroboscopic dynamics of the system. The dynamics between two periods T of the driving are encoded into the Floquet modes $|\Phi_\alpha(t)\rangle$. The time evolution (4.10) is very similar to the the one for a state in a time-independent system as in Eq. (2.45), Sec. 2.3. This close analogy emphasizes that by changing to the Floquet basis one maps a time-periodic Hamiltonian onto a time-independent one.

In Sec. 4.4.2, we will employ the time evolution of $|\Psi(t)\rangle$ within the Floquet framework, see Eq. (4.10), to compute velocity expectation values. As for the static system in Sec. 2.3 we use Ehrenfest's theorem (2.46) to define the velocity operator[4]. For the Floquet state (4.10) the velocity expectation value is

$$\begin{aligned} \mathbf{v}(t) = \langle\hat{\mathbf{v}}(t)\rangle = &\underbrace{\sum_\alpha |c_\alpha|^2 \langle\Phi_\alpha(t)|\hat{\mathbf{v}}|\Phi_\alpha(t)\rangle}_{\text{diagonal}} \\ &+ \underbrace{\sum_{\alpha\neq\beta} c_\alpha^* c_\beta \exp\left(-\frac{\mathrm{i}}{\hbar}\left(\epsilon_\beta - \epsilon_\alpha\right)t\right)\langle\Phi_\alpha(t)|\hat{\mathbf{v}}|\Phi_\beta(t)\rangle}_{\text{off diagonal}}. \end{aligned} \tag{4.11}$$

Similarly to the velocity of static two-band systems derived in Sec. 2.3, Eq. (2.47), we can divide the velocity into a diagonal and an off-diagonal contribution in the Floquet basis. Note that due to the basis dependency of this distinction, only the total velocity $\mathbf{v}(t)$ is a physical observable. The off-diagonal term contains an oscillation of frequency $\omega_{\mathrm{ZB}} = (\epsilon_\beta - \epsilon_\alpha)/\hbar$. It resembles the Zitterbewegung introduced for undriven systems in Sec. 2.3.1. We will discuss this *Floquet Zitterbewegung* in more detail in Sec. 4.4.3. As discussed in Sec. 2.3, one could also identify the velocity contributions as intraband and interband velocity, respectively, but now within a Floquet

[4]Note that we drop the index $\mathbf{k}$ here.

bandstructure instead of the static bands[5]. Since in the Floquet basis the Hamiltonian of the originally periodically driven system is time independent, we prefer the term *Zitterbewegung* instead of *interband velocity* in this context.

Note that for the sake of simplicity so far the derivation has been performed for a purely time-dependent Hamiltonian. The Hamiltonians we will later on treat in the framework of Floquet formalism will also depend on the quasimomentum $\mathbf{k}$. Therefore, we have to project the Floquet states $|\Psi_\alpha(t)\rangle$ and modes $|\Phi_\alpha(t)\rangle$ into $\mathbf{k}$ space, $\langle\mathbf{k}|\Psi_\alpha(t)\rangle = \Psi_\alpha(\mathbf{k},t)$ and $\langle\mathbf{k}|\Phi_\alpha(t)\rangle = \Phi_\alpha(\mathbf{k},t)$, and the quasienergies ϵ_α and coefficients c_α become $\mathbf{k}$ dependent, i.e. $\epsilon_\alpha(\mathbf{k})$ and $c_{\mathbf{k},\alpha}$. This also modifies the velocity to $\mathbf{v}_\mathbf{k}(t)$.

4.3. General idea behind Floquet oscillations

For introducing the concept of Floquet oscillations, let us first briefly recap the key points of Bloch oscillations [70, 71]. These oscillations arise when an electron is driven through the bands of a lattice-periodic system by a constant electric field. For simplicity, we will discuss a 1D system here but all concepts can trivially be adapted to higher dimensions. Due to the spatial periodicity with lattice constant a, the resulting bandstructure is periodic in quasimomentum k and can be reduced to the first BZ with $k \in [-\pi/a, \pi/a]$. The relation between the applied electric field E_el and the quasimomentum k of the electron is described by the acceleration theorem, see Sec. 2.3.2, Eq. (2.56). For a constant electric field E_el, this will simply lead to a linear movement of the electron through the bandstructure,

$$k(t) = k(0) - \frac{eE_\mathrm{el}}{\hbar}t, \tag{4.12}$$

where $k(0)$ is the inital quasimomentum of the electron and e the elementary charge. The group velocity $v_\mathrm{g}(t)$ of an electron in a band with dispersion $E(k)$ is given by

$$v_\mathrm{g}(t) = \frac{1}{\hbar}\frac{\mathrm{d}E(k)}{\mathrm{d}k}\bigg|_{k(t)}, \tag{4.13}$$

as discussed in Sec. 2.3, Eq. (2.50). Since for the constant electric field k shifts linearly with t and for the lattice periodic system $E(k)$ is periodic with k, the

[5]For more details on the relation between intraband and interband velocity in the Floquet basis and the basis of the time-dependent Hamiltonian, we refer to the bachelor's thesis of Michael Laumer [221], which we supervised. He compares both velocities for a Dirac system driven by circularly polarized light.

electron's group velocity $v_{\mathrm{g}}(t)$ will also be an oscillating quantity. Thus, the electron performs an oscillatory motion in real space which is well known as Bloch oscillation nowadays. The period T_{B} of this motion is determined by the periodicity of the bandstructure, which is equivalent to the width $2\pi/a$ of the first BZ, and the changing rate of k, see Eq. (2.56), resulting in [71]

$$T_{\mathrm{B}} = \frac{2\pi/a}{|eE_{\mathrm{el}}|/\hbar} = \frac{2\pi\hbar}{a|eE_{\mathrm{el}}|}. \tag{4.14}$$

Note that all this only applies as long as scattering is negligible. For the observation of Bloch oscillations it is thus necessary that the mean scattering time $\tau_{\mathrm{s}} > T_{\mathrm{B}}$.

To define Floquet oscillations, we have to transfer the ingredients for Bloch oscillations from Bloch to Floquet bands. First and foremost, we need a system without k-periodic dispersion that under the application of a time-periodic driving develops a (quasi)periodic Floquet bandstructure in k space. Remember that Floquet bands by definition are periodic in energy with multiples $n\hbar\omega$ of the driving frequency ω. For oscillations à la Bloch however, periodicity in quasimomentum k is crucial. This can be achieved quite nicely in effective Dirac systems. Therefore, from now on we will focus on the Hamiltonian

$$\hat{\mathcal{H}}(\mathbf{k}, t) = \hbar v_{\mathrm{F}} \mathbf{k} \cdot \boldsymbol{\sigma} + V(t), \tag{4.15}$$

introduced in Sec. 2.1.1 with some additional time-periodic driving $V(t)$ with frequency ω. For $V(t) = 0$, we recover the Dirac cone with energy branches $E_{\pm} = \pm\hbar v_{\mathrm{F}} k$ with $k = |\mathbf{k}|$. Due to the rotational symmetry of the cone, without loss of generality we from now on set $k_y = 0$ and thus $k = k_x$.

When treating the Hamiltonian (4.15) within Floquet theory, replica of the original Dirac cone emerge. In Fig. 4.1(a) we schematically show the original cone in black and the replica in gray for $V(t) \to 0$. We see that due to the linearity of the energy dispersion the distance Δk_{osc} between the crossings of different replica within the FBZ is independent of k. Since the replica are always shifted by $\hbar\omega$ with respect to each other, their crossing points in k are resonance points of the original Dirac cone with the driving field, i.e. $\Delta E = n\hbar\omega$. Increasing the driving strength $V(t)$ couples the different replica, leading to the opening of band gaps at crossing points. The resulting bands are sketched by the red dashed lines in Fig. 4.1(a). This rather simple scheme already demonstrates the suitability of periodically driven Dirac systems for achieving at least approximately k periodic quasi bandstructures. In Sec. 4.4 and 4.5 we will show this quantitatively for two different driving protocols $V(t)$.

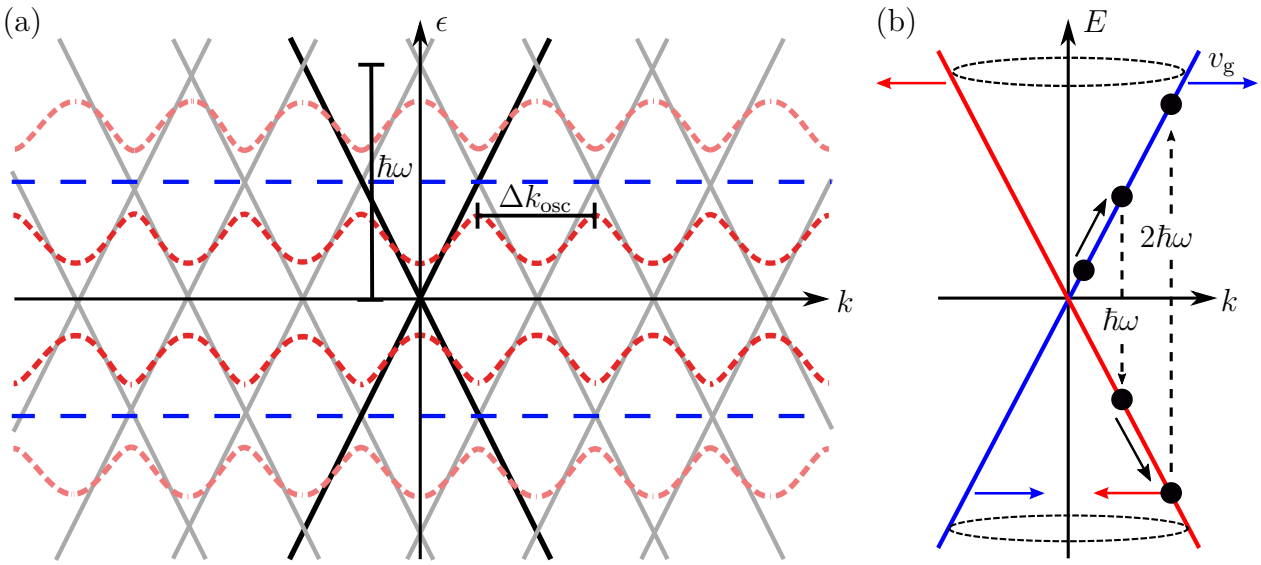

Fig. 4.1: (a) Sketch of the formation of (approximately) k periodic Floquet bands in effective Dirac systems.* When treating the original Dirac cone (black) within Floquet theory, replica of it emerge (gray). For a finite driving $V(t) \neq 0$, the different replica couple and band gaps are formed. This results in an oscillating Floquet bandstructure as shown by the red dashed lines. The maxima of the bands are separated by Δk_{osc}. The blue dashed lines indicate the FBZ. (b) Mechanism behind Floquet oscillations from the perspective of the static Dirac bandstructure. The electron (black dot) travels along one branch in k due to the electric field E_{el} until the local band gap $\Delta E = \hbar\omega$. Then, it transitions to the other branch. This process is repeated whenever $\Delta E = n\hbar\omega$ is in resonance with the driving $V(t)$. Due to the opposing velocities v_{g} of the branches, the electron performs oscillations in real space.

* Reprinted figure from [74]. Copyright (2020) by the American Physical Society.

In Ref. [73] they derive that both Eqs. (2.56) and (4.13) also hold for Floquet systems, the latter now being the cycle averaged group velocity

$$\bar{v}_{\mathrm{g}} = \int_0^T \mathrm{d}t\, v_{\mathrm{g}}(t) = \frac{1}{\hbar}\frac{\mathrm{d}\epsilon_\alpha(k)}{\mathrm{d}k}\bigg|_{k_0}, \tag{4.16}$$

where ϵ_α is the quasienergy of the state and k_0 its k value. Accordingly, as for the Bloch oscillations, by applying an additional static electric field E_{el} we can drive an electron through the Floquet band and if $\epsilon_\alpha(k)$ is oscillating with k, the electron's (cycle averaged) velocity $\bar{v}_{\mathrm{g}}(t)$ will also be oscillating. The resulting oscillatory movement of the electron in real space is what we call *Floquet oscillations*. In general, the period of these oscillations is defined by the k spacing Δk_{osc} between two adjacent maxima/minima of the quasienergy $\epsilon_\alpha(k)$ (as shown in Fig. 4.1) and the velocity $\frac{\mathrm{d}k}{\mathrm{d}t}$ of the electron in k space (as defined in Eq. (2.56)), i.e. $T_{\mathrm{F}} = \frac{\Delta k_{\mathrm{osc}}}{|\mathrm{d}k/\mathrm{d}t|}$. For the Dirac system this leads to

$$T_{\mathrm{F}} = \frac{\omega/v_{\mathrm{F}}}{|-eE_{\mathrm{el}}/\hbar|} = \frac{\hbar\omega}{v_{\mathrm{F}}|eE_{\mathrm{el}}|}. \tag{4.17}$$

The period T_{F} of the Floquet oscillations is inversely proportional to the period

$T = \frac{2\pi}{\omega}$ of the driving generating the Floquet bandstructure. This becomes more plausible when looking at Floquet oscillations without actually treating the Hamiltonian within the Floquet framework, as sketched in Fig. 4.1(b). From the perspective of the Dirac cone, the static electric field drives the electron along one branch. Whenever the energy difference ΔE between both branches is in resonance with the periodic driving's energy $\hbar\omega$, i.e. $\Delta E = n\hbar\omega$ with $n \in \mathbb{N}$, the electron switches branch by absorbing/emitting n quanta of the periodic driving field. Since both branches have opposite slopes, the electron's velocity will change sign whenever it changes from one branch to the other. This is the process behind Floquet oscillations from the viewpoint of the static system's basis (see Sec. 2.1.1). The larger the driving frequency ω, the longer the distance in k between two points $E(k)$ meeting the resonance condition $\Delta E = n\hbar\omega$ and thus the larger the Floquet period T_F.

For realistic systems the gaps opening in the Floquet bandstructure will become smaller with increasing k instead of being constant as depicted in our idealized sketch in Fig. 4.1(a). This accounts for the fact that absorbing/emitting an increasing number of quanta n of the driving field becomes less and less likely, decreasing the probability of the electron switching between both branches of the Dirac cone. For the observability of Floquet oscillations this is a limiting factor. To understand this limit within the Floquet framework, we first have to recognize that the static electric field breaks the perfectly time periodic character of our system. However, as long as the field is not strong enough to drive transitions between different Floquet bands, it is sufficient to include its effect based on the acceleration theorem, see Eq. (2.56), within the Floquet formalism. This approximation breaks down for smaller gaps between the Floquet bands or larger static electric fields. Then, considering the adiabatic time evolution of the electron is not sufficient and one needs to take Landau-Zener transitions [175–180] between the Floquet bands [222, 223] into account, which eventually lead to the disappearance of the Floquet oscillations also in the Floquet picture. This has been studied in my master's thesis [123] and will not be repeated here.

4.4. Proof of principle: Periodically opened mass gap

For a first demonstration of Floquet oscillations, we choose a driving protocol suitable to achieve a large number of Floquet oscillation cycles. Previous

research by Reck on the Dirac quantum time mirror [126, 224] includes the study of single-wave-packet dynamics in a Dirac system where one abruptly opens and closes a mass gap[6]. Here, we will periodically repeat this protocol, giving us the model Hamiltonian

$$\hat{\mathcal{H}}(\mathbf{k},t) = \hbar v_\mathrm{F}\mathbf{k}\cdot\boldsymbol{\sigma} + \sum_{l=0}^{\infty}\Theta\left(t-(lT-\Delta t)\right)\Theta(lT-t)M\sigma_z, \tag{4.18}$$

where Θ is the Heaviside function, M the strength of the mass term, Δt the duration of the gap opening and T the period of the driving. A sketch of one cycle of this pulsing is given in the lower inset in Fig. 4.2(b).

4.4.1. Floquet bandstructure

To compute the Floquet bandstructure, we have to construct and diagonalize the Floquet matrix from the Hamiltonian (4.18) as described in Sec. 4.2. For the dc part we get

$$H^{(0)}(\mathbf{k}) = \frac{1}{T}\int_0^T \hat{\mathcal{H}}(\mathbf{k},t)\,\mathrm{d}t = \hbar v_\mathrm{F}\mathbf{k}\cdot\boldsymbol{\sigma} + \frac{\Delta t}{T}M\sigma_z \tag{4.19}$$

and for the other components

$$H^{(n-m)}(\mathbf{k}) = \frac{1}{T}\int_0^T \hat{\mathcal{H}}(\mathbf{k},t)\,\mathrm{e}^{\mathrm{i}(n-m)\omega t}\,\mathrm{d}t = \frac{M}{2\pi\mathrm{i}(n-m)}\left(1-\mathrm{e}^{-2\pi\mathrm{i}(n-m)\frac{\Delta t}{T}}\right), \tag{4.20}$$

where $\omega = \frac{2\pi}{T}$. For the analysis of the bandstructure we again consider an effective 1D model with $\mathbf{k} = (k_x, 0)$ without loss of generality, so in the following $k_x \equiv k$. Since the mass gap is of rectangular shape, finding good convergence especially of the Floquet modes is challenging. For the data shown here, we found sufficient convergence going up to $n, m = \pm 100$ for the truncation of the Floquet matrix. In App. A.2 we shortly discuss this choice and show data for different values of n, m.

[6] As already stated by Reck, experimental realization of a quickly switched mass gap in graphene, which we use as origin for the Dirac Hamiltonian employed here (see Sec. 2.1.1), is currently not feasible. However, a mathematically similar Dirac Hamiltonian arises in TI surface states (see Sec. 2.1.2). There, the Pauli matrices refer to the electron spin and a mass gap can easily be opened via Zeeman coupling of a perpendicular magnetic field. The orbital effects related to this magnetic field do not destroy the concept of the quantum time mirror, but will change the resulting Floquet bandstructure and electron dynamics. Thus, this mechanism would require further studies. Here, the periodically gapped Dirac Hamiltonian serves as a toy model and proof of principle of Floquet oscillations. For experimental realizations, we study gap openings via circularly polarized light in Sec. 4.5.

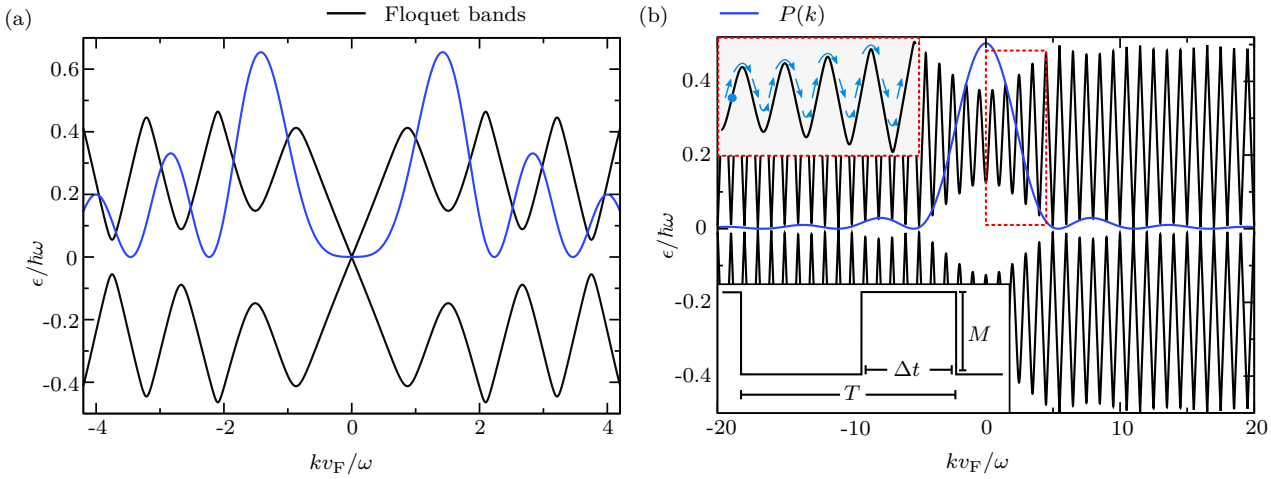

Fig. 4.2: Floquet bandstructure (black) of a periodically gapped Dirac cone with (a) $M\Delta t/\hbar = 6.3$, $\Delta t/T = 0.5$ and (b) $M\Delta t/\hbar = 0.4$, $\Delta t/T = 0.09$ and corresponding transition probability $P(k)$ (blue). Whenever $P(k)$ goes to zero, the gap between the Floquet bands closes. One can even tune the system such that the original Dirac cone is preserved. The lower inset in panel (b) shows the pulse shape for one cycle of the driving. The upper inset sketches the path of an electron (light blue) through part of the bandstructure driven by a constant electric field E_{el}. The band gap in this region is sufficiently large to allow for Floquet oscillations.*

* Reprinted figure from [74]. Copyright (2020) by the American Physical Society.

We focus on two exemplary parameter sets to demonstrate the large tunability of this driving protocol. In Fig. 4.2 we show the Floquet bandstructures for (a) $M\Delta t/\hbar = 6.3$, $\Delta t/T = 0.5$ and (b) $M\Delta t/\hbar = 0.4$, $\Delta t/T = 0.09$. In panel (a) the parameters are chosen such that the original Dirac cone is preserved. In panel (b) we show a set with a large area around $kv_{\mathrm{F}}/\omega = 0$ where the Floquet spectrum is gapped, making this set a good choice for demonstrating Floquet oscillations. A sketch of how an electron moves through part of the suitable bandstructure driven by a static electric field E_{el} is given in the upper inset.

In Sec. 4.3 we stated that the gaps in the Floquet spectrum are directly related to the probability of an electron at kv_{F}/ω switching from one branch of the Dirac cone to the other due to the applied driving. For a single cycle of our driving this probability has been derived in detail in Ref. [224], reading

$$\begin{aligned} P(k) &= \left| \left\langle \varphi_{\mathbf{k},\pm} \left| \mathrm{e}^{-\mathrm{i}\hat{\mathcal{H}}_{\mathrm{M}}\Delta t} \right| \varphi_{\mathbf{k},\mp} \right\rangle \right|^2 \\ &= \left| -\frac{\mathrm{i}}{\sqrt{1+(\hbar v_{\mathrm{F}} k/M)^2}} \sin\left(\frac{M\Delta t}{\hbar} \sqrt{1+(\hbar v_{\mathrm{F}} k/M)^2} \right) \right|^2 , \end{aligned} \tag{4.21}$$

where $\hat{\mathcal{H}}_M = \hbar v_{\mathrm{F}} \mathbf{k}\cdot\boldsymbol{\sigma} + M\sigma_z$ is the Hamiltonian while the mass gap is open and $|\varphi_{\mathbf{k},\pm}\rangle$ is the eigenstate of the Dirac cone without mass (Eq. (2.14), Sec. 2.1.1).

Plotting $P(k)$ together with the Floquet bands in Fig. 4.2 confirms the relation between transition probability $P(k)$ and gap opening in the Floquet spectrum. Accordingly, one can also use the simple formula for $P(k)$ when searching for suitable parameters to achieve a certain kind of Floquet bandstructure in this setup.

4.4.2. Analysis of Floquet oscillations

Having analyzed the Floquet bandstructure of our model system in Sec. 4.4.1, we now want to demonstrate and study Floquet oscillations in this setup. For concreteness, we choose the parameters $M\Delta t/\hbar = 0.4$ and $\Delta t/T = 0.09$, resulting in the Floquet spectrum depicted in Fig. 4.2(b). To numerically compute the Floquet oscillations of an electron moving through the bands as sketched in the upper inset of Fig. 4.2(b), we apply a negative static electric field $E_{\mathrm{el}} < 0$ tuned such that the Floquet period $T_{\mathrm{F}}/T = \frac{\hbar\omega}{v_{\mathrm{F}}|eE_{\mathrm{el}}|T} \simeq 20.8\pi$ (see Eq. (4.17)). We set the field to point along the x direction to be able to continue considering the effective 1D model as in Sec. 4.4.1. We describe the electron as a Gaussian wave packet

$$\Psi(k_i, 0) = \sqrt{\frac{1}{\Delta k\sqrt{\pi}}} \exp\left(-\frac{1}{2\Delta k^2}\left(k_i - k_c\right)^2\right) \begin{pmatrix} 1 \\ 1 \end{pmatrix}, \tag{4.22}$$

where the center k_c is given by $k_c v_{\mathrm{F}}/\omega = 0.35$ and the width $\Delta k/k_c = 1/18$. We choose $t = 0$ for the initial time and define all states depending on their initial momentum k_i. Note that the spinor $\frac{1}{\sqrt{2}}\begin{pmatrix} 1 \\ 1 \end{pmatrix}$ is the eigenstate of the upper band of the unperturbed Dirac Hamiltonian for $k_y = 0$ and $k_x > 0$ (see Eq. (2.14)).

We use two complementary approaches to calculate the time-dependent velocity and position expectation value of the electron in this setup. First, we do a straightforward calculation within the framework of the time-dependent Hamiltonian (4.18). We numerically calculate the time evolution of the initial wave packet (4.22) by solving the time-dependent Schrödinger equation using TQT (see Chap. 3). For these simulations in 1D we set the grid to 8192×4 data points[7] with spacing $\delta x/v_{\mathrm{F}}(T - \Delta t) = 0.025$ and $\delta y/v_{\mathrm{F}}(T - \Delta t) = 0.25$. The calculations converge for a time step $\delta t/(T - \Delta t) = 0.0025$. By directly including the electric field in the Hamiltonian via the scalar potential

[7] Since TQT is designed for simulations in 2D, we need a small amount of data points in the y direction in order to achieve stable results.

$\phi_{\mathrm{el}}(x) = -E_{\mathrm{el}}x$, we obtain the exact, quantum mechanical dynamics of the wave packet. The total Hamiltonian then reads

$$\hat{\mathcal{H}}(\mathbf{k}, x, t) = \hbar v_{\mathrm{F}} \mathbf{k} \cdot \boldsymbol{\sigma} + \sum_{l=0}^{\infty} \Theta\left(t - (lT - \Delta t)\right) \Theta(lT - t) M \sigma_z + e\phi_{\mathrm{el}}(x), \quad (4.23)$$

where e is the elementary charge. Due to the orientation of the electric field along x, studying the dynamics in x direction is sufficient to observe Floquet oscillations. We compute the position $x(t)$ and the corresponding velocity $v_x(t)$ of the wave packet using the COM observable introduced in Sec. 3.5. The results are plotted in Fig. 4.3(a). We see that both $x(t)$ and $v_x(t)$ are oscillating quantities, their period matching the prediction $T_{\mathrm{F}}/T \simeq 20.8\pi$ for the expected Floquet oscillations. Moreover, $x(t)$ contains all characteristic features of the corresponding Floquet bandstructure depicted in the upper inset of Fig. 4.2(b), namely the increasing amplitude of the oscillations and the sharpening of the turning points. This is a direct consequence of Eq. (4.16), relating the average group velocity to the Floquet bandstructure, since $x(t) = \int_0^t v_x(t')\, \mathrm{d}t'$. Especially the velocity $v_x(t)$ exhibits additional fast oscillations on top of the slower Floquet oscillation. They can be attributed to Zitterbewegung and will be discussed in more detail in Sec. 4.4.3. In Fig. 4.3(b) we show snapshots of the wave packet's spatial distribution $|\Psi(x,t)|^2$ taken at the times marked with crosses in panel (a). They illustrate how the electron's center of mass oscillates in real space.

Second, to verify that the observed oscillations can really be understood by the movement of electrons through the Floquet quasi bandstructure, we compute our observables x and $v_x(t)$ using Floquet theory. By expanding the initial electron state $\Psi(k_i, 0)$ in the Floquet basis derived in Sec. 4.4.1, we can compute its time evolution $\Psi(k_i, t)$ as described in Eq. (4.10). We include the additional static electric field E_{el} via the acceleration theorem (2.56),

$$k \to k(t) = k_i - \frac{eE_{\mathrm{el}}}{\hbar} t, \quad (4.24)$$

and assume that the time evolution of $\Psi(k_i, t)$ is perfectly adiabatic within the Floquet basis, as discussed in Sec. 4.3. In consequence, the amplitudes $c_{k_i,\alpha} = \Phi_\alpha^\dagger(k_i, 0)\Psi(k_i, 0)$ are only computed for the initial state $\Psi(k_i, 0)$. They encode the Gaussian structure of the wave packet and its distribution over the two Floquet bands. Since we chose an eigenstate of the undriven Dirac cone for $\Psi(k_i, 0)$ (see Eq. (4.22)), the wave packet contains contributions of both Floquet bands $\alpha = \pm$. We move the wave packet through the Floquet basis by plugging Eq. (4.24) in the quasienergies $\epsilon_\alpha(k)$ and the Floquet modes $\Phi_\alpha(k, t)$. Thus, in contrast to Eq. (4.10), we now have to integrate over the

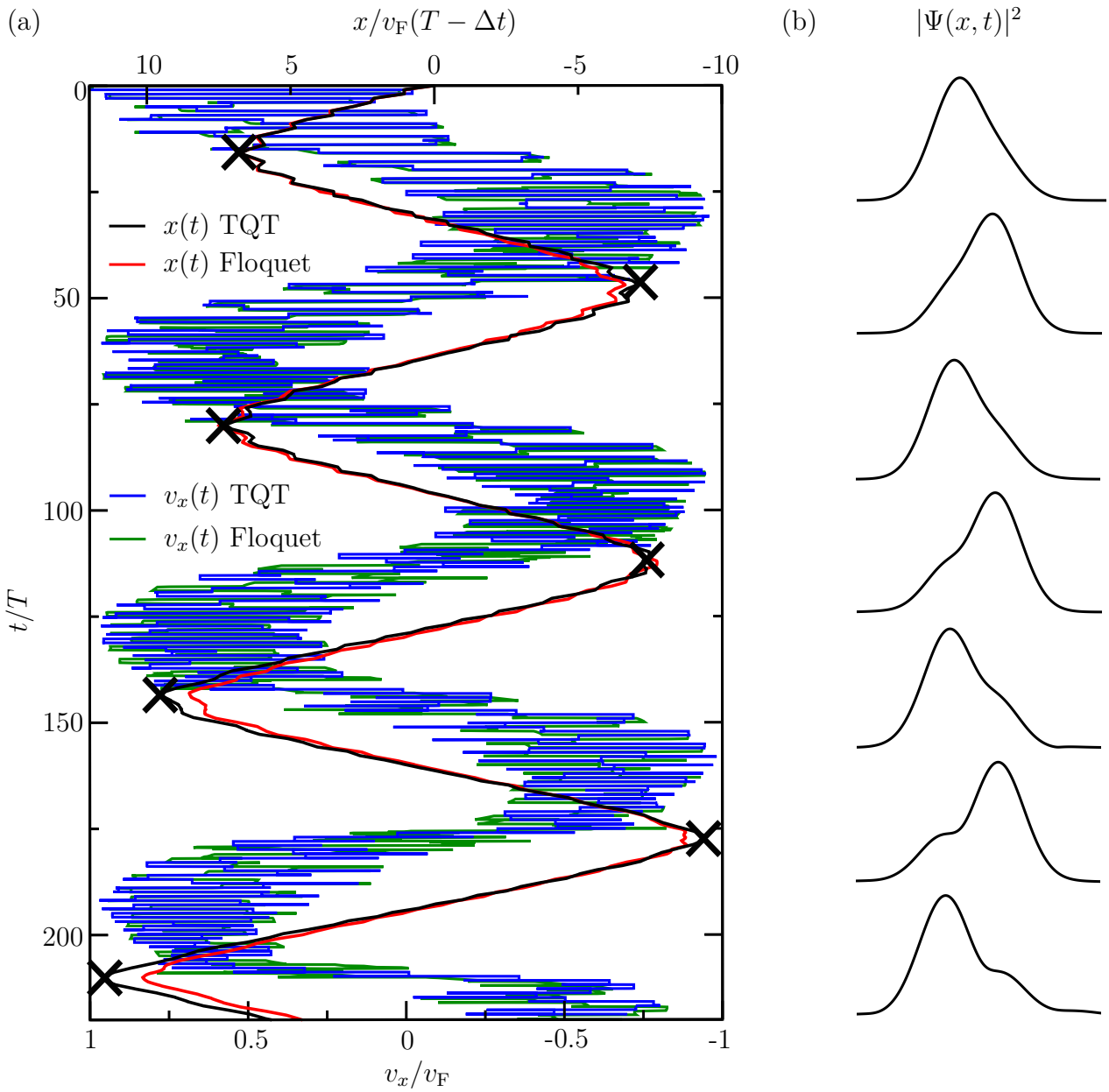

Fig. 4.3: Floquet oscillations in a periodically gapped Dirac cone system. (a) Position and velocity expectation value of $\Psi(k_i, t)$ computed both with TQT and a Floquet approach. Overall, the results of both methods show good agreement. The Floquet oscillations in $x(t)$ mirror the features of the corresponding Floquet bandstructure depicted in Fig. 4.2(b). The velocity $v_x(t)$ exhibits additional fast oscillations that can be attributed to Zitterbewegung. (b) Real-space resolved snapshots of the wave packet $\Psi(x, t)$ taken at times marked by the crosses in panel (a). The wave packet $\Psi(x, t)$ was extracted from the TQT calculation.*

* Reprinted figure from [74] with updated Floquet results. Copyright (2020) by the American Physical Society.

dynamical phase, obtaining

$$\Psi(k_i,t) = \sum_{\alpha=\pm} c_{k_i,\alpha} \exp\left(-\frac{\mathrm{i}}{\hbar}\int_0^t \epsilon_\alpha\left(k\left(t'\right)\right)\mathrm{d}t'\right)\Phi_\alpha(k(t),t), \tag{4.25}$$

where $\alpha = \pm$ labels the respective Floquet band[8]. With $\Psi(k_i,t)$ we can calculate the velocity expectation value $v_x(t)$ following Eq. (4.11). The velocity operator for our Dirac system is $\hat{v}_x = v_\mathrm{F}\sigma_x$, see Eq. (2.13). In total, we obtain

$$\begin{aligned} v_x(t) = v_\mathrm{F}\int_{-\infty}^{\infty}\mathrm{d}k_i \sum_{\alpha,\beta=\pm} c^*_{k_i,\alpha}c_{k_i,\beta}\exp\left[-\frac{\mathrm{i}}{\hbar}\int_0^t\left[\epsilon_\beta\left(k\left(t'\right)\right)-\epsilon_\alpha\left(k\left(t'\right)\right)\right]\mathrm{d}t'\right] \\ \times\,\Phi^\dagger_\alpha(k(t),t)\sigma_x\Phi_\beta(k(t),t), \end{aligned} \tag{4.26}$$

where we average over all initial momenta k_i to take the whole wave packet into account. The corresponding position expectation value $x(t)$ is achieved via simple integration, $x(t) = \int_0^t v_x(t')\,\mathrm{d}t'$. The results are plotted in Fig. 4.3(a). Overall, they show good agreement with those obtained from the TQT simulation. There are only a few details which are not perfectly reproduced. They are especially pronounced in the velocity $v_x(t)$ and mainly integrated out in the position $x(t)$. First of all, the Zitterbewegung is of rectangular shape in the TQT results. In the Floquet approach, these rectangles are not always perfectly resolved, which can be attributed to the truncation of the Floquet matrix at $n,m = \pm 100$. However, taking $n,m = \pm 500$ did not improve the results and the intermediate regime $n,m = \pm 200$, ± 300, ± 400 showed even less agreement. Probably, even larger Floquet matrices are necessary to really reproduce the rectangular Zitterbewegung. Second, for some time windows there seems to be a phase shift of π between the Zitterbewegung in the Floquet and TQT approach. This shift is also observable in the small wiggly motion of the position $x(t)$ and related to the truncation of the Floquet matrix as well. Last, a small shift in time builds up between the TQT and Floquet data. This can be attributed to a slightly different time resolution within the two numerical implementations. Plots for the discussed parameter exploration as well as a zoom into the velocity curve demonstrating the discussed deviations can be found in App. A.2.

In conclusion, in the regime depicted in Fig. 4.3, including the electric field via the acceleration theorem (4.24) and neglecting Landau-Zener transitions between the Floquet bands is a good approximation to evolve the wave packet $\Psi(k_i,t)$ within the Floquet basis, see Eq. (4.25), and to observe Floquet

[8]Note that this is analogous to the time evolution discussed in Sec. 2.3.2 for a state in the basis of a time-independent Hamiltonian with additionally applied homogeneous electric field.

oscillations. If we would consider larger time scales, the electron would enter a k region where the gap between the Floquet bands becomes too small and Landau-Zener transitions would have to be taken into account. Then, the Floquet oscillations are diminished or even vanish completely. The results for $x(t)$ computed with TQT for longer times and thus including the onset of this regime are shown in App. A.2. A more extensive study can be found in Ref. [123].

Note that the data shown here for the Floquet approach is an updated version of the one published in Refs. [74, 123]. When working on the manuscripts of Refs. [74, 123], we were not aware of the fact that we have to integrate over the dynamical phase in Eq. (4.25) in order to correctly include the static electric field E_{el} into the time evolution of $\Psi(k_i, t)$ in the Floquet basis. Since the dynamical phase only enters the off-diagonal terms of the velocity, see Eq.(4.11), we could still reproduce the slow Floquet oscillations with the expansion used in Refs. [74, 123]. Only the fast Zitterbewegung was not computed correctly.

4.4.3. Zitterbewegung in the Floquet basis

The Floquet oscillations studied in Sec. 4.4.2 contain additional fast oscillations that are especially pronounced in the velocity expectation value, see Fig. 4.2(a). We attribute this trembling motion of the electron to Zitterbewegung in the Floquet basis. There already exist extensive studies of Zitterbewegung in Dirac systems with time-dependent mass gap by Reck et al. [126, 153]. They found that Zitterbewegung of wave packets can be revived by abruptly opening and closing a mass gap and that persistent multimodes emerge when the mass term oscillates harmonically. However, they discuss Zitterbewegung in the basis of the undriven Dirac Hamiltonian. Here, we want to focus on Zitterbewegung in the Floquet basis of the periodically gapped Dirac cone as derived in Sec. 4.4.1.

We gave a short introduction to Zitterbewegung in two-band systems in Sec. 2.3.1. Generally, Zitterbewegung is described by the off-diagonal part of the velocity operator and its frequency ω_{ZB} is determined by the energy difference between both bands at the considered k value. When deriving the velocity expectation value in the Floquet basis in Sec. 4.2, we also found an

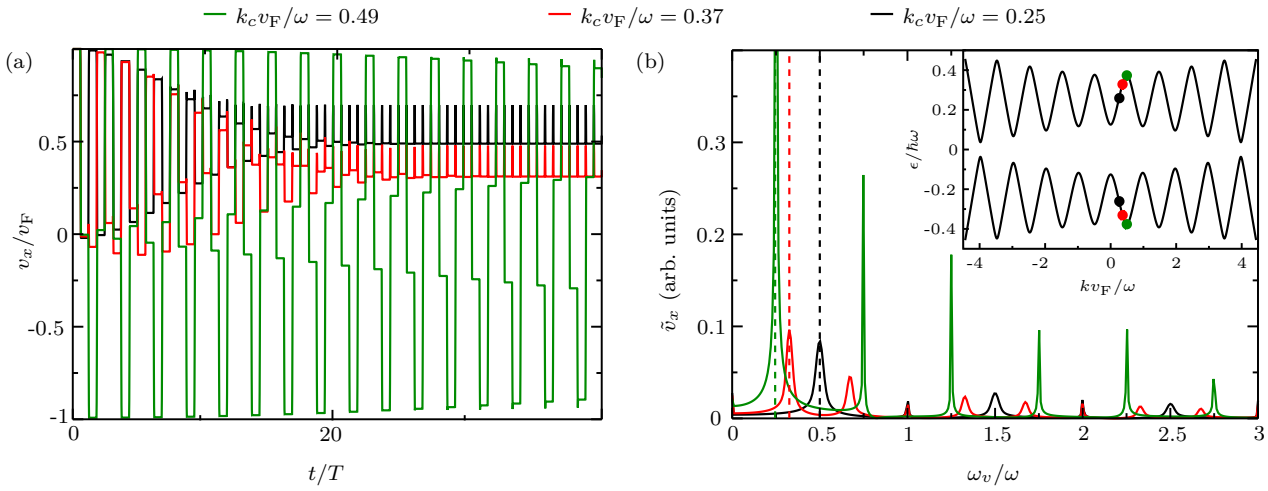

Fig. 4.4: (a) Velocities of wave packets with different k_c in a periodically gapped Dirac cone. They exhibit Zitterbewegung around a constant value determined by the dispersion of the Floquet bands. Here, no static drift field is applied such that k and thus ω_{ZB} are constant. (b) Fourier analysis $\tilde{v}_x(\omega_v)$ of the velocities after subtracting the respective average velocity to avoid a zero-frequency peak. The dashed lines mark the expected Zitterbewegung frequency ω_{ZB}. The inset shows the corresponding Floquet bandstructure with the position of the wave packets marked by dots.*

* Figure adapted from [74]. Copyright (2020) by the American Physical Society.

off-diagonal term containing an oscillation of frequency

$$\omega_{\mathrm{ZB}}(k) = \frac{1}{\hbar}\left[\epsilon_\beta(k) - \epsilon_\alpha(k)\right], \tag{4.27}$$

where $\epsilon_{\beta,\alpha}(k)$ are the Floquet quasienergies, see Eq. (4.11). Using TQT we compute the velocity $v_x(t)$ for a wave packet given by Eq. (4.22) for three different values of k_c in the periodically gapped Dirac system. We employ the same model parameters as in Sec. 4.4.2 but do not apply an additional static field E_{el} such that k and thus ω_{ZB} are independent of time. For the wave packed (4.22) Zitterbewegung in the Floquet basis should arise since it is an eigenstate of the static Dirac Hamiltonian and thus contains contributions of both Floquet bands. Indeed, the results shown in Fig. 4.4(a) exhibit fast oscillations around a constant value, the latter being defined by the slope of the Floquet dispersion according to Eq. (4.16). Additionally, for all three wave packets the amplitude of the Zitterbewegung decays as expected. Following Reck et al. [126, 153] this decay can be understood as the wave packet splitting into two parts, one occupying the upper and one the lower Floquet band, and eventually separating completely in real space. Since Zitterbewegung is an interference effect of contributions from different bands, it can only occur as long as both contributions overlap. Thus, it is clear that the smaller the average velocity of the wave packet, the slower the Zitterbewegung decreases.

In Fig. 4.4(b) we analyze the frequency spectrum ω_v of the velocities. We

subtract the average velocity value from the respective curve before performing the Fourier transform to avoid a zero-frequency peak. The dashed lines mark the Zitterbewegung frequencies ω_{ZB} as expected from Eq. (4.27). The good agreement of both results confirms that the fast oscillations can be understood as Zitterbewegung in the Floquet basis.

The inset of Fig. 4.4(b) shows a zoom into the corresponding Floquet band-structure (a larger k area is plotted in in Fig. 4.2(b)). The k_c positions of the propagated wave packets are marked by dots. To extract the expected Zitterbewegung frequency ω_{ZB} from the Floquet bands, one has to keep in mind their periodicity in energy. For ω_{ZB} the smallest gap has to be considered. For the red and green position, this gap does not lie within the FBZ but between the FBZ and the neighboring replicas. The frequency spectrum ω_v in Fig. 4.4(b) does not only contain ω_{ZB} but also higher harmonics of it. This is caused by the rectangular shape of the velocities, which originates from the underlying Dirac dispersion. The velocity of the wave packet can only change when the mass gap is open and is constant otherwise[9]. For our set of parameters the gap opens only shortly, $\Delta t/T = 0.09$. This short period appears as a jump in the velocity even when the Zitterbewegung has already vanished.

The fast oscillations observed on top of the Floquet oscillations are very similar to those discussed here for the periodically gapped Dirac cone without static electric field. The main difference is that there is no obvious decay of the fast oscillations within the time window studied in Fig. 4.3 even though it is more than five times longer than the time scale considered in Fig. 4.4 without the electric field. The periodic change of sign of the velocity associated with the Floquet oscillations prevents the wave-packet contributions of the two Floquet bands from drifting apart. That the wave packet does not (completely) split is also confirmed by the snapshots shown in Fig. 4.2(b). Thus, one can argue that the static drift field leads to refocusing of the wave packet and its Zitterbewegung does not decay.

[9] One might ask why there is no Zitterbewegung originating from the static Dirac dispersion. As derived e.g. in Ref. [126], the Zitterbewegung in a Dirac cone is always perpendicular to the velocity defined by the band dispersion. Since the wave packet studied here has $k_y = 0$, v_x is governed by the band dispersion and Zitterbewegung appears in v_y, which we do not consider.

4.5. Towards experimental realization: Circularly polarized light

In Sec. 4.4 we have demonstrated that a large number of Floquet oscillation cycles can be achieved in Dirac systems with periodically opened mass gap. For experimental realizations however, using a different driving protocol might be more convenient. There already exists a lot of research concerning the Floquet quasi bandstructure of graphene irradiated by circularly polarized light [54, 225–227], including transport measurements [228] and studies of topological properties [55, 229–232]. Therefore, it is known that circularly polarized light can open a band gap in the central region of a Dirac system's Floquet bandstructure.

In this section we will study Floquet oscillations in Dirac systems illuminated with circularly polarized light of frequency ω described by the vector potential

$$\mathbf{A}(t) = A \begin{pmatrix} \cos(\omega t) \\ \sin(\omega t) \end{pmatrix}. \tag{4.28}$$

First, in Sec. 4.5.1, we will show the tunability of Floquet oscillations in this setup for the simple Dirac Hamiltonian. Then, in Sec. 4.5.2, we will explore Floquet oscillations in graphene for experimentally realistic parameters, also considering the influence of trigonal warping as higher-order approximation of the graphene bandstructure.

4.5.1. Dirac Hamiltonian

We again start with the effective Dirac Hamiltonian derived in Sec. 2.1.1. The vector potential (4.28) is included into the Hamiltonian via minimal coupling, $\mathbf{k} \to \mathbf{k} + \frac{e}{\hbar}\mathbf{A}(t)$, so our total Hamiltonian reads

$$\hat{\mathcal{H}}(\mathbf{k}, t) = \hbar v_\mathrm{F} \mathbf{k} \cdot \boldsymbol{\sigma} + e v_\mathrm{F} \mathbf{A}(t) \cdot \boldsymbol{\sigma} = \hbar v_\mathrm{F} \mathbf{k} \cdot \boldsymbol{\sigma} + e v_\mathrm{F} A \begin{pmatrix} 0 & \mathrm{e}^{-\mathrm{i}\omega t} \\ \mathrm{e}^{\mathrm{i}\omega t} & 0 \end{pmatrix}. \tag{4.29}$$

We construct the Floquet matrix following Sec. 4.2 to then compute the Floquet bandstructure by diagonalization. For the Hamiltonian (4.29) we obtain

$$H^{(0)}(\mathbf{k}) = \frac{1}{T} \int_0^T \hat{\mathcal{H}}(\mathbf{k}, t)\, \mathrm{d}t = \hbar v_\mathrm{F} \mathbf{k} \cdot \boldsymbol{\sigma} \tag{4.30}$$

for the dc part and

$$\begin{aligned} H^{(n-m)}(\mathbf{k}) &= \frac{1}{T}\int_0^T \hat{\mathcal{H}}(\mathbf{k},t)\,\mathrm{e}^{\mathrm{i}(n-m)\omega t}\,\mathrm{d}t \\ &= \frac{ev_\mathrm{F}A}{T}\int_0^T \begin{pmatrix} 0 & \mathrm{e}^{\mathrm{i}(n-m-1)\omega t} \\ \mathrm{e}^{\mathrm{i}(n-m+1)\omega t} & 0 \end{pmatrix}\mathrm{d}t \\ &= ev_\mathrm{F}A \begin{pmatrix} 0 & \delta_{n-m,1} \\ \delta_{n-m,-1} & 0 \end{pmatrix} \end{aligned} \tag{4.31}$$

for the other components, $\delta_{n-m,\pm1} = 0$ for $n-m \neq \pm 1$ being the Dirac delta and $T = 2\pi/\omega$. In Fig. 4.5(a) we show the resulting quasienergy spectra for two different dimensionless driving strengths $\tilde{A} = \frac{ev_\mathrm{F}A}{\hbar\omega}$, namely $\tilde{A} = 0.5$ and $\tilde{A} = 1.1$, cut along $\mathbf{k} = (k_x, 0)$. Again, we can consider this cut without loss of generality. We see that for the larger amplitude $\tilde{A}$ the k_x region in which band gaps between the Floquet bands open increases. This reflects what we discussed in Sec. 4.3: The coupling between different Floquet bands at resonance points[10] is directly related to the probability of absorbing the necessary number n of photons to bridge the energy gap $E = n\hbar\omega$ between the branches of the original Dirac cone. Absorbing a larger amount n of photons becomes more likely for higher amplitudes $\tilde{A}$ of the light field. However, these multiple-photon processes also alter the overall structure of the Floquet bands. For $\tilde{A} = 1.1$ the distance between local minima of the bands is not independent of k_x anymore, which will lead to a non-constant period of the Floquet oscillations.

To observe Floquet oscillations for the above described parameters, we again model the electron as a Gaussian wave packet and propagate it using TQT. Due to some functional limitations of TQT, implementing the Hamiltonian (4.29) is not completely straightforward and requires a different gauge of the circularly polarized light, details are discussed in App. A.3. Now, we explicitly treat the 2D Hamiltonian and consider a rotationally symmetric Gaussian wave packet[11],

$$\Psi(\mathbf{k}_i, 0) = \frac{1}{\Delta k\sqrt{\pi}}\exp\left(-\frac{1}{2\Delta k^2}\left(\mathbf{k}_i - \mathbf{k}_c\right)^2\right)\begin{pmatrix} 1 \\ -\mathrm{e}^{\mathrm{i}\theta_{\mathbf{k}_i}} \end{pmatrix}, \tag{4.32}$$

where the spinor $\frac{1}{\sqrt{2}}\begin{pmatrix} 1 \\ -\mathrm{e}^{\mathrm{i}\theta_{\mathbf{k}_i}} \end{pmatrix}$ is the eigenstate of the lower branch of the undriven Dirac Hamiltonian (see Eq. (2.14)). We choose $\mathbf{k}_c v_\mathrm{F}/\omega = (-1.22, 0)$

[10] As discussed in Sec. 4.3, the Floquet bands form out of replica of the original Dirac cone that are coupled by the applied driving field. By definition, the crossing points of these replica within the FBZ are resonance points of the original Dirac cone with the driving frequency.

[11] Note that this changes the normalization of the wave packet compared to the 1D wave packet in Eq. (4.22).

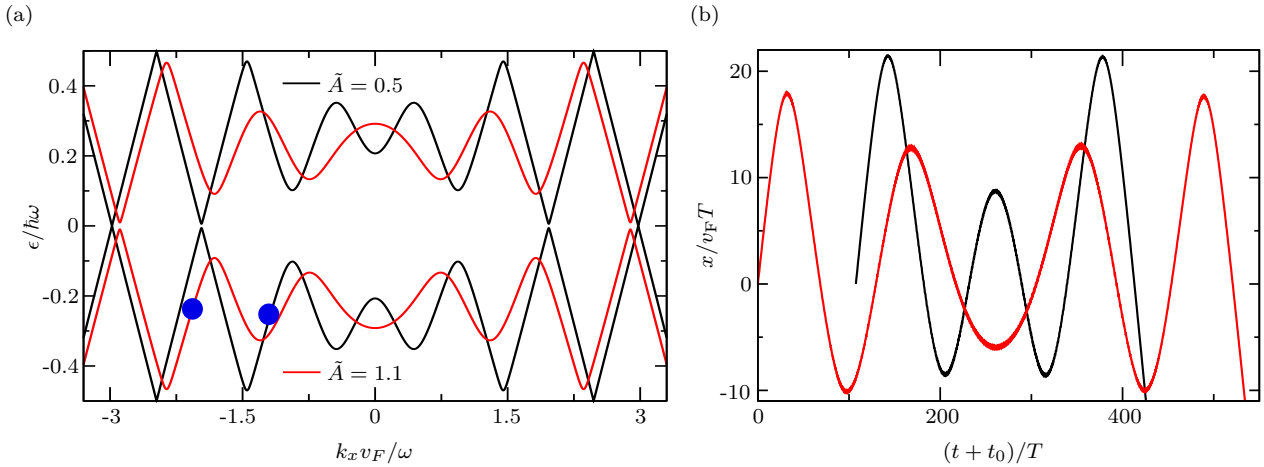

Fig. 4.5: (a) Floquet bandstructure for a Dirac system illuminated with circularly polarized light for two dimensionless driving strengths $\tilde{A} = 0.5$ (black curves) and $\tilde{A} = 1.1$ (red curves). Increasing the amplitude $\tilde{A}$ leads to coupling of the bands at larger k_x values, thus widening the k window in which Floquet oscillations can occur. (b) Position expectation value $x/v_\mathrm{F}T$ of an electron driven through the Floquet bands depicted in panel (a) by a static electric field E_el. The respective initial momenta are marked by the blue dots in panel (a). The movement clearly shows Floquet oscillations and resembles the Floquet bands. To highlight this resemblance, the inital time t_0 of the black curve is shifted to $t_0/T = \frac{\hbar}{|eE_\mathrm{el}|T}(\mathbf{k}_c^{\tilde{A}=1.1} - \mathbf{k}_c^{\tilde{A}=0.5})$. For this electric field strength and resulting Floquet period $T_\mathrm{F}/T \simeq 140$, fast oscillations caused by the circulating electric field of the light are not resolved and only appear as slight broadening of the curves.*

* Reprinted figure from [74]. Copyright (2020) by the American Physical Society.

for $\tilde{A} = 0.5$ and $\mathbf{k}_c v_\mathrm{F}/\omega = (-2.07, 0)$ for $\tilde{A} = 1.1$. For the width Δk we keep $\Delta k/|\mathbf{k}_c| = 1/18$ for both driving amplitudes. The position of $\mathbf{k}_c$ is marked by the blue dots in Fig. 4.5(a). The simulations in 2D are carried out on a grid with 8192×256 data points. The grid spacing and duration of one time step are the same as in Sec. 4.4.

TQT computes the wave-packet dynamics within the framework of the time-dependent Hamiltonian (4.29), where the $\mathbf{k}$ value follows the vector potential $\mathbf{A}(t)$. The initial wave packet is defined using the kinetic momentum[12] $\mathbf{k}(t) = \mathbf{k}^\mathrm{can} + \frac{e}{\hbar}\mathbf{A}(t)$, whereas usually $\mathbf{k} = \mathbf{k}^\mathrm{can}$ is the canonical momentum. Accordingly, we have to shift $\mathbf{k}_c^\mathrm{TQT} = \mathbf{k}_c + \frac{e}{\hbar}\mathbf{A}(0)$ in order to get the correct comparison with the Floquet bands. Generally, the relation between $\mathbf{k}^\mathrm{Floquet}$ in the Floquet framework and $\mathbf{k}^\mathrm{TQT}(t)$ in the time-dependent basis is given by the cycle average

$$\mathbf{k}^\mathrm{Floquet} = \langle \mathbf{k}^\mathrm{TQT}(t) \rangle_t = \frac{1}{T}\int_0^T \mathbf{k}^\mathrm{TQT}(t)\,\mathrm{d}t. \tag{4.33}$$

[12] The gauge-independent form is $\mathbf{k}(t) = \mathbf{k}^\mathrm{can} - \frac{e}{\hbar}\int \mathbf{E}(t')\,\mathrm{d}t'|_t$, which is the integral form of the acceleration theorem (2.56). Thus, the discussed shift is necessary despite the gauge transformation discussed in App. A.3.

As long as no vector potential $\mathbf{A}(t)$ is applied, both values are the same[13]. To simplify the notation, we drop the superscript of $\mathbf{k}^{\text{Floquet}}$ again in the following discussion.

We apply an additional negative, static electric field $\mathbf{E}_{\text{el}} = E_{\text{el}}\mathbf{e}_x$, with $E_{\text{el}} < 0$ and $\mathbf{e}_x$ being the unit vector in x direction, to drive the electron through the band-structure cut shown in Fig. 4.5(a). The field strength E_{el} is set such that $T_{\text{F}}/T = \frac{\hbar\omega}{v_{\text{F}}|eE_{\text{el}}|T} \simeq 140$ (computed for $\tilde{A} = 0.5$). In TQT, E_{el} is included via the scalar potential $\phi_{\text{el}}(x) = -E_{\text{el}}x$. We compute the position expectation value $x(t)$ of the wave packet for both driving amplitudes $\tilde{A}$ using the COM observable of TQT, see Sec. 3.5. The results are shown in Fig. 4.5(b). To highlight the similarity between $x(t)$ and the Floquet bands we shifted the curve corresponding to $\tilde{A} = 0.5$ by $t_0/T = \frac{\hbar}{|eE_{\text{el}}|T}(\mathbf{k}_c^{\tilde{A}=1.1} - \mathbf{k}_c^{\tilde{A}=0.5})$, where $\mathbf{k}_c^{\tilde{A}=1.1}$ and $\mathbf{k}_c^{\tilde{A}=0.5}$ denote the respective initial momenta. Accordingly, t_0/T is the time an electron takes to shift from $\mathbf{k}_c^{\tilde{A}=1.1}$ to $\mathbf{k}_c^{\tilde{A}=0.5}$ driven by the electric field E_{el}. For the circularly polarized light the $\mathbf{k}$ region in which Floquet oscillations are observable is much more limited than for the periodically opened mass gap considered in Sec. 4.4. Still, at least four full oscillation cycles are achievable for the parameters discussed here. Due to the large ratio $T_{\text{F}}/T \simeq 140$ between the Floquet oscillation period T_{F} and the light field period T, the short-time dynamics caused by the circulating vector field only appear as slight broadening of the curves and are not really resolved.

For a better resolution of the short-time dynamics we increase the static field strength E_{el} by a factor of 10, thus reducing the oscillation period to $T_{\text{F}}/T = \frac{\hbar\omega}{v_{\text{F}}|eE_{\text{el}}|T} \simeq 14$. In Fig. 4.6(a) we show the resulting position expectation value $x(t)$ for a wave packet starting at $\mathbf{k}_c v_{\text{F}}/\omega = (-0.64, 0)$ and $\tilde{A} = 0.5$. Since the increase of the static field strength does not change the underlying Floquet bandstructure, the Floquet oscillations of Fig. 4.5(b) for $\tilde{A} = 0.5$ are reproduced qualitatively. Only the change in period and a decrease of the oscillation's amplitude is apparent. Now, tiny oscillations caused by the circulating field of the light are resolved. On the right of Fig. 4.6(a) we depict snapshots of the 2D wave packet's distribution in real space oscillating around $x = 0$. The corresponding points in time are marked by the orange crosses in the $x(t)$ curve. The full trajectory of the wave packet in x-y plane is plotted in Fig. 4.6(b), including a red curve as guide for the eye. Again, the Floquet oscillations in x direction are visible. Additionally, the small oscillations due to the circulating light field are clearly resolved. The trajectory plot reveals that they are not uniform but modulated depending on the position. This

[13]This holds for the periodically gapped Dirac system discussed in Sec. 4.4, for instance.

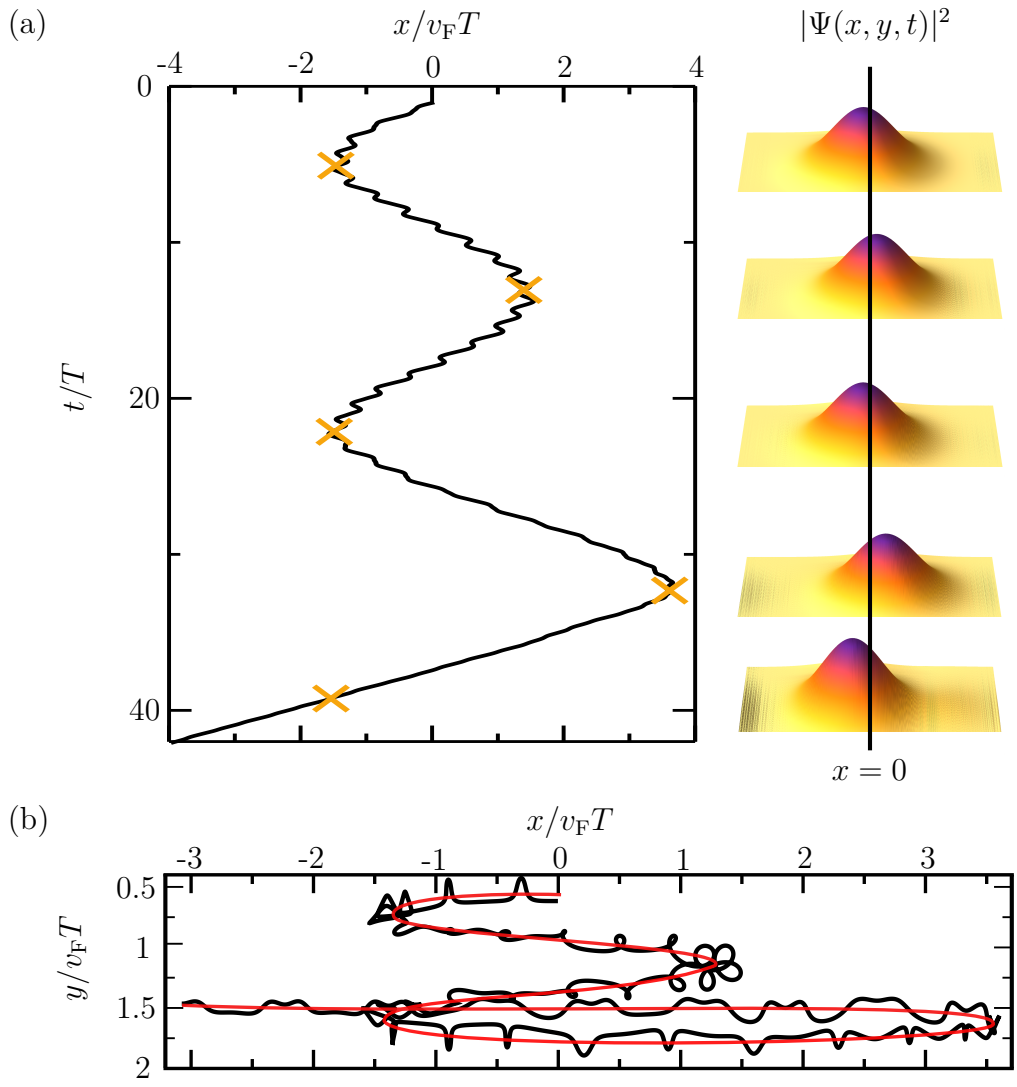

Fig. 4.6: (a) Position expectation value and real-space shape of an electron driven through the Floquet bands for $\tilde{A} = 0.5$ (see Fig. 4.5(a)) starting at $\mathbf{k}_c v_\mathrm{F}/\omega = (-0.64, 0)$. In comparison to the oscillations plotted in Fig. 4.5(b) the strength of E_el is increased by a factor of 10, giving $T_\mathrm{F}/T \simeq 14$. Here, micro motion caused by the circulating light field is resolved. On the right, snapshots of the wave packet in real space taken at times marked by the orange crosses in the position curve are depicted. (b) Trajectory of the wave packet from (a) in x-y plane. It reveals the Floquet oscillations and an additional drift in y direction. The red curve serves as a guide for the eye.*

* Reprinted figure from [74]. Copyright (2020) by the American Physical Society.

modulation is attributable to Zitterbewegung. The drift of the wave packet in y direction is less intuitive. Since it is perpendicular to the electric driving field $\mathbf{E}_{\mathrm{el}}$, we assume that the drift is caused by an anomalous velocity and thus a signature of the Floquet band's Berry curvature $\mathbf{\Omega}(\mathbf{k})$. For time-independent systems with static electric field $\mathbf{E}_{\mathrm{el}}$, the anomalous velocity $\mathbf{v}_{\mathrm{anom}}(\mathbf{k}(t))$ is given by

$$\mathbf{v}_{\mathrm{anom}}(\mathbf{k}(t)) = -\frac{e}{\hbar}\mathbf{E}_{\mathrm{el}} \times \mathbf{\Omega}(\mathbf{k}(t)) \tag{4.34}$$

and has been identified as scattering-independent contribution to the anomalous Hall effect [49, 144], see Sec. 2.3.2. There also exists experimental evidence for such Hall deflection in periodically driven honeycomb lattices realized in cold-atom systems [63] and in graphene illuminated with circularly polarized light [55]. In Sec. 4.5.2 we explore the experimental parameters necessary to observe Floquet oscillations in graphene. When comparing them to the setup used for measuring Hall currents in graphene we see that they are of similar order of magnitude. This fortifies our assumption that the drift is caused by the Floquet band's Berry curvature. Nevertheless, computing the Berry curvature for our Floquet bands and thus proving this assumption could be done in future research.

4.5.2. Including trigonal warping and realistic parameters

In Sec. 4.5.1 we have demonstrated that at least four complete Floquet oscillation cycles can be achieved in Dirac systems irradiated with circularly polarized light. Now, we explore the experimental feasibility. Suitable systems hosting an effective Dirac dispersion are graphene [32], TIs [30, 31, 40, 41], and cold atoms in artificial honeycomb lattices [112]. For the latter, v_{F} and thus the Floquet period can be tuned and relaxation due to disorder or interaction effects can be avoided. However, reaching the necessary time-scales for observing Floquet oscillations is still challenging. In 2020, McIver et al. measured a light-induced anomalous Hall effect in graphene [55]. Their experiment shows which parameters can already be achieved experimentally and serves as a benchmark for our studies. Accordingly, in this section we aim to quantitatively investigate the realizability of Floquet oscillations in real monolayer graphene.

As discussed in Sec. 2.1.1 the Dirac cone is only a valid approximation of the graphene bandstructure within a limited energy range. For a good description of the bands up to 2 eV, one has to include trigonal warping [127]. The

frequency ω of the light field determines the energy window in which Floquet oscillations take place. In Sec. 4.3 we argue that Floquet oscillations can be understood as repeated switching of the electron between the branches of the Dirac cone while being moved through k space by the static field E_{el}. This switching occurs whenever the energy difference $\Delta E = n\hbar\omega$. So by tuning ω one can choose the energy range ΔE corresponding to the absorption/emission of $n = 1, 2, \ldots$ photons. In the Floquet oscillations for $\tilde{A} = 1.1$ up to four-photon processes are involved, which for $\omega/2\pi = 10\,\mathrm{THz}$ corresponds to $\Delta E \simeq 160\,\mathrm{meV}$. In this range of energy, the Dirac approximation should be valid. To verify this, we extend our Hamiltonian to

$$\hat{\mathcal{H}}(\mathbf{k}) = \hbar v_{\mathrm{F}} \mathbf{k} \cdot \boldsymbol{\sigma} - \mu \left[\left(k_y^2 - k_x^2 \right) \sigma_x + 2 k_x k_y \sigma_y \right]. \tag{4.35}$$

For graphene, $v_{\mathrm{F}} = 10^6\,\mathrm{m\,s^{-1}}$ and $\mu = 3a^2\gamma_0/8$ with $a = 1.4\,\text{Å}$ and $\gamma_0 = 2.7\,\mathrm{eV}$, see Sec. 2.1.1. Again, we take the vector potential (4.28) into account via minimal coupling, $\mathbf{k} \to \mathbf{k} + \frac{e}{\hbar}\mathbf{A}(t)$, the trigonal warping term giving rise to non-linear contributions of $\mathbf{A}(t)$. By setting $A = 45\,\mathrm{nV\,s\,m^{-1}}$ and $\omega/2\pi = 10\,\mathrm{THz}$, we reproduce the dimensionless driving $\tilde{A} = 1.1$ from Sec. 4.5.1. We achieve results comparable to those displayed in Fig. 4.5(b) by propagating the wave packet (4.32) with $\mathbf{k}_c = -0.013\,1/\text{Å}$, $\Delta k/|\mathbf{k}_c| = 1/18$ and applying an electric field $E_{\mathrm{el}} = 30\,\mathrm{V\,cm^{-1}}$. The corresponding calculations are again performed using TQT. In Fig. 4.7(a) we compare the Floquet oscillations computed with and without the trigonal warping term and find good qualitative agreement. Thus, we conclude that the Dirac approximation is valid for this set of parameters.

For the experimental observation, it is crucial that the transport relaxation time τ_{s} is larger than the period T_{F} of one Floquet oscillation cycle. For clean, hexagonal boron nitride-encapsulated graphene, typical relaxation times are $\tau_{\mathrm{s}} = 1$–$20\,\mathrm{ps}$ [233, 234]. For $E_{\mathrm{el}} = 30\,\mathrm{V\,cm^{-1}}$, the period $T_{\mathrm{F}} = \frac{\hbar\omega}{v_{\mathrm{F}}|eE_{\mathrm{el}}|} \simeq 13.5\,\mathrm{ps}$ results. Therefore, in good quality samples at least one oscillation cycle should be observable. By increasing the electric field by a factor of ten, so $E_{\mathrm{el}} = 300\,\mathrm{V\,cm^{-1}}$, T_{F} is reduced by a factor of ten to $T_{\mathrm{F}} \simeq 1.3\,\mathrm{ps}$. Then, all four oscillation cycles should be measurable. As depicted in Fig. 4.7(b), also for the higher electric field trigonal warping can be neglected. However, on this short time scale the Floquet oscillations are altered by the momentum change caused by the circulating light field, which is of period $T = 2\pi/\omega = 0.1\,\mathrm{ps}$, and Zitterbewegung.

Finally, we compare the found parameters with those employed in the experimental observation of light-induced Hall currents in graphene [55]. According to estimates, a measurable topological gap opening is expected for fields

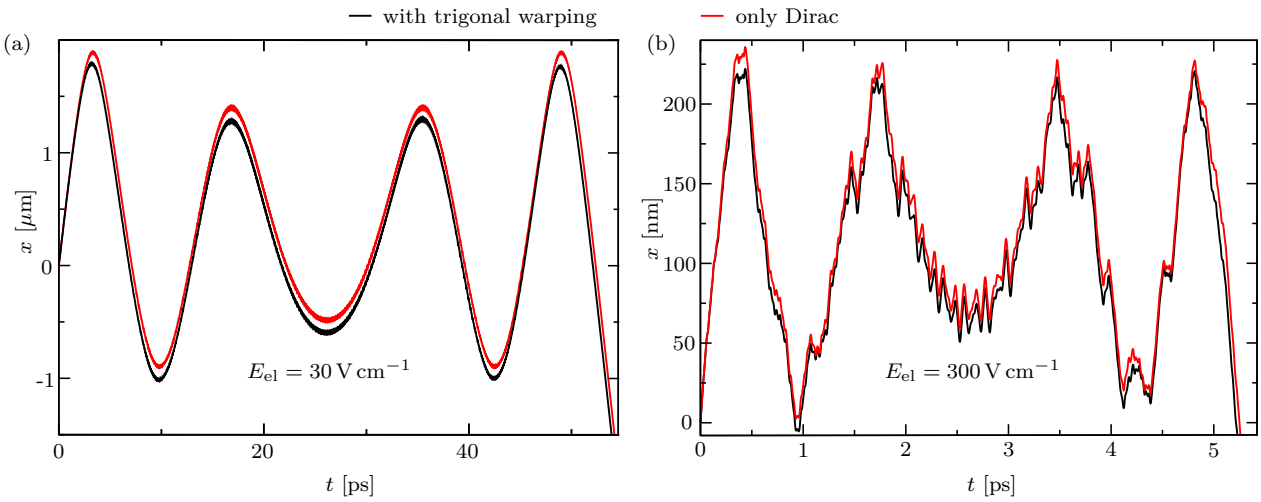

Fig. 4.7: Floquet oscillations for realistic parameters in graphene computed with (black) and without (red) trigonal warping. We choose $A = 45\,\mathrm{nV\,s\,m^{-1}}$ and $\omega/2\pi = 10\,\mathrm{THz}$ for the circularly polarized light, reproducing $\tilde{A} = 1.1$ in Sec. 4.5.1. (a) For a static electric field $E_{\mathrm{el}} = 30\,\mathrm{V\,cm^{-1}}$ Floquet oscillations of period $T_{\mathrm{F}} \simeq 13.5\,\mathrm{ps}$ are achieved. (b) Increasing the field to $E_{\mathrm{el}} = 300\,\mathrm{V\,cm^{-1}}$ reduces the period to $T_{\mathrm{F}} \simeq 1.3\,\mathrm{ps}$. The motion caused by the circulating light field with $T = 2\pi/\omega = 0.1\,\mathrm{ps}$ is clearly resolved on this time scale. In both cases (a) and (b) the Floquet oscillations are not changed qualitatively when including trigonal warping.*

* Reprinted figure from [74]. Copyright (2020) by the American Physical Society.

with strength $E_{\mathrm{THz}} = 10^7$–$10^8\,\mathrm{V\,m^{-1}}$ [54, 235, 236]. In their experiments, McIver et al. apply circularly polarized pulses of frequency $\omega/2\pi = 46\,\mathrm{THz}$, peak field strength $E_{\mathrm{THz}} = 4.0 \cdot 10^7\,\mathrm{V\,m^{-1}}$ and duration of 500 fs. The pulsing is necessary to avoid sample destruction. At peak strength, these parameters correspond to an amplitude $A = 140\,\mathrm{nV\,s\,m^{-1}}$ and intensity $I = \frac{c\varepsilon_0}{2} A^2\omega^2 = 430\,\mathrm{MW\,cm^{-2}}$ (with speed of light c and vacuum permittivity ε_0), which is two orders of magnitude larger than for our proposed parameters, there $I \simeq 1\,\mathrm{MW\,cm^{-2}}$. This discrepancy can be traced back to our lower frequency $\omega/2\pi = 10\,\mathrm{THz}$ and light amplitude $A = 45\,\mathrm{nV\,s\,m^{-1}}$. Still, our parameters result in a field strength $E_{\mathrm{THz}} = A\omega \simeq 0.28 \cdot 10^7\,\mathrm{V\,m^{-1}}$. This is a bit below the estimated lower bound for observable gap openings in graphene but that does not exclude the observability of Floquet oscillations for our parameter set. Additionally, the Floquet bandstructure around the Dirac cone shown in Ref. [55] is also suitable to generate Floquet oscillations. To achieve the same Floquet period $T_F = \frac{\hbar\omega}{v_{\mathrm{F}}|eE_{\mathrm{el}}|}$ as estimated for our parameters, one has to increase the static electric field E_{el} by a factor of 4.6 to $E_{\mathrm{el}} \simeq 1.3\,\mathrm{kV\,cm^{-1}}$. Then, $T_{\mathrm{F}} \simeq 1.3\,\mathrm{ps}$ and thus at the lower bound of typical relaxation times $\tau_{\mathrm{s}} = 1$–$20\,\mathrm{ps}$ in hexagonal boron nitride-encapsulated graphene [233, 234]. In summary, we can conclude that experimentally realizing Floquet oscillations in graphene illuminated with circularly polarized light seems feasible.

4.6. Summary: Extending concepts from Bloch to Floquet systems

In this chapter, we have proposed the concept of Floquet oscillations. This oscillatory electron motion arises, when combining a periodically driven system and a constant, electric bias. The origin of these oscillations can be attributed to consecutive electron transitions at (multi-)photon resonances of the driving field with the bandstructure of the static system, since whenever the electron switches band, its velocity is inverted. However, the phenomenon can also be interpreted based on the Floquet theorem. From this perspective, Floquet oscillations highlight, how concepts, well-established for Bloch bands of spatially periodic systems, can be transferred to time-periodic Floquet systems, as we summarize in the following.

First of all, Floquet oscillations themselves are the analog of Bloch oscillations. Both phenomena arise when electrons are adiabatically driven through their respective bandstructure by a constant, electric field. The motion of the electron follows the band dispersion and becomes oscillatory for bands that are (quasi)periodic in momentum. The most important difference between the two phenomena is the nature of the corresponding bandstructures. The Bloch bands originate from a spatial lattice and the Floquet bands from a lattice in time. As a consequence, the Bloch bands are periodic in momentum space by definition, whereas the Floquet bands are periodic in energy but can be tuned such that (quasi)periodicity in momentum is achieved, at least in a certain range. This limitation in the momentum periodicity of the Floquet bands restricts the realizability of Floquet oscillations. Nevertheless, we could show that up to four oscillation cycles should be observable in graphene illuminated with circularly polarized light, see Sec. 4.5.2 for details.

Moreover, we found signatures of Zitterbewegung in the Floquet oscillations. This jittery movement of electrons was originally predicted for highly relativistic, free particles by Schrödinger [146], but it turned out that the effect can also appear for nonrelativistic particles in solids [148]. In the context of condensed matter physics, Zitterbewegung arises due to a particle's wave function spreading over more than one band. Then, the different band contributions interfere, which results in a trembling motion of the particle. For a two-band system, the frequency of this Zitterbewegung corresponds to the local energy difference between the two bands. In turn, the frequency of the Zitterbewegung we observed in the Floquet oscillations is determined by the local energy difference between the Floquet bands, demonstrating that the

concept of Zitterbewegung also extends to lattices in time.

Lastly, the electron trajectories recorded in Sec. 4.5.1 contain fingerprints of an anomalous velocity. Such velocities are induced by the system's Berry curvature and therefore our observation seems to be a signature of a non-vanishing Berry curvature in the Floquet bands. We did not have the opportunity to pursue this further, but similar observations have already been made in experiments on Floquet TIs. Thereby, anomalous Hall currents have been measured in periodically driven cold-atom systems [63] and in graphene irradiated with circularly polarized light [55]. Exploring whether Floquet oscillations offer a suitable tool for investigating the concept of Berry curvature in the Floquet basis is an interesting task for future research.

5. Dynamics of test charges in driven Dirac systems

5.1. Experimental motivation

In Chap. 4 we have studied how (quasi)periodic electron motion arises in Dirac systems when combining a small, constant electric field and periodic driving. Then, repeated transitions between the two branches of the Dirac cone lead to an alternating sign of the electron's velocity. An even more abrupt velocity reversal can be achieved when driving the electron from one branch to the other close to the Dirac point with an intense electric field. When the electron does not directly move through the Dirac point but on a bandstructure cut parallel to it, the electron experiences a finite band gap and switches branch instead of undergoing a transition to the other band. Then, its velocity immediately switches sign. This process is strongly nonlinear and, as a consequence, efficient HHG is expected from Dirac materials. In graphene, HH measurements have been realized both for mid-infrared [82] and THz [83] light fields. Additionally, third-harmonic generation in the THz regime for light pulses with a peak strength of only $6.5\,\mathrm{kV\,cm^{-1}}$ has been observed in the Dirac semimetal Cd_3As_2 [84]. Another material class hosting Dirac states are TIs. As discussed in Sec. 2.1.2, 3D TIs such as Bi_2Se_3, Bi_2Te_3, and Sb_2Te_3 feature topologically protected 2D Dirac surface states where electronic backscattering is strongly suppressed by spin-momentum locking. First signatures of a highly nonlinear optical response of the surface states of Bi_2Se_3 have been found experimentally in 2016 [237]. However, for the actual measurement of HHG in TI surface states a way of disentangling bulk and surface contribution of the spectrum had to be devised.

Within a collaboration of several experimental and theoretical groups we investigated how to achieve and understand HHG in TI surface states, focusing on Bi_2Te_3. The most important results of these studies are published in Ref. [81] and summarized in the following. The experimental findings were

compared to theoretical studies based on the semiconductor Bloch equations [107] and a first intuition of the processes generating HHs was gained by solving the semiclassical Boltzmann equation. Our contribution was to provide insights into the underlying quantum mechanisms and to discuss all results on that basis. Utilizing TQT, see Chap. 3, we computed the dynamics of wave packets in Bi_2Te_3 surface states under the influence of strong laser pulses. We focused on wave packets that are narrow in momentum space, and thereby represent single test charges, in order to disentangle the various quantum processes occurring in different regimes and parts of momentum space.

For the experiments, a laser pulse with frequency ν_{el} between 25 THz and 42 THz, and peak field strength of about $10\,\mathrm{MV\,cm^{-1}}$ was used. Due to the refractive index $n_{\mathrm{r}} \approx 10$ of Bi_2Te_3 this results in a peak field around $3\,\mathrm{MV\,cm^{-1}}$ in the Bi_2Te_3 crystal. The key discovery enabling the analysis of HHG from the surface states of Bi_2Te_3 was the observation of a drastic change in the HH spectra depending on the driving frequency ν_{el}. For frequencies above $\nu_{\mathrm{el}} \gtrsim 33\,\mathrm{THz}$ only odd-order harmonics were detected. For smaller frequencies, $\nu_{\mathrm{el}} < 33\,\mathrm{THz}$, however, the overall HH intensity dropped and even-order peaks emerged. This characteristic distinguishes bulk and surface dominated spectra [89]. From inversion symmetric media such as the bulk Bi_2Te_3 crystal, only odd orders of the driving frequency ν_{el} are emitted. But the broken inversion symmetry at the surface of the crystal allows for the emergence of both odd and even orders. The drop in intensity of the HHs is due to the fact that naturally the surface hosts less electrons than the bulk. The transition between bulk and surface-dominated HHG lies around $\nu_{\mathrm{el}} = 35\,\mathrm{THz}$, since there the photon energy $h\nu_{\mathrm{el}}$ is comparable to the bulk band gap of Bi_2Te_3. When the photon energies $h\nu_{\mathrm{el}}$ are too small to drive resonant transitions between bulk valence and conduction band in single-photon processes[1], i.e. $h\nu_{\mathrm{el}} < E_{\mathrm{b}}$, where E_{b} is the bulk band gap, the bulk hosts no free charge carriers that could generate HHs. The spectra are dominated by the surface contribution. It was also found that the HH spectra emitted from the surface states can be continuously shifted from integer to non-integer multiples of the driving frequency by changing the carrier-envelope phase, i.e. the phase between laser-pulse envelope and oscillation. A deeper theoretical study of the connection between pulse shape and emitted harmonics revealed that a chirp in the pulse is actually responsible for these frequency shifts [108]. Additionally, the experimentalists analyzed the polarization of odd- and even-order harmonics and observed that the polarization of the even-order harmonics is rotated by a degree of up to 20° with respect to the incoming, linearly polarized, laser field.

[1] Multiple-photon processes and non-resonant transitions are not efficient for the laser amplitudes used in the experiment.

This polarization rotation can be attributed to the Berry curvature of the Bi_2Te_3 surface states, as already predicted in earlier works [85]. Similar effects have also been measured in monolayer MoS_2 [238] and α-quartz [170].

Overall, the experimental findings demonstrate that HHG in TI surface states is governed by the gapless Dirac dispersion, leading to efficient HHG even at relatively weak driving fields. Strong-field interband transitions are not necessary to generate free charge carriers due to the semimetallic spectrum. The suppression of electronic backscattering enables ballistic acceleration of electrons for timescales longer than 1 ps [80] and thus allows for the observation of coherent transport effects such as the imprint of the Berry curvature on the dynamics. In Bi_2Te_3 this reveals the importance of the hexagonal warping for an adequate description of the geometrical properties of the surface states. Nevertheless, many open questions remain. For example, the interplay of intraband and interband effects in the emitted harmonics as well as the influence of different regions in momentum space on the resulting spectrum is still unclear and require further theoretical investigation. In the following, we present an extension of the results published in [81]. We study the influence of the Berry curvature and different types of transitions involved in HHG in Dirac systems by considering single test charges that are narrow in momentum space. In Chap. 6 we introduce a new method that includes Fermi sea effects in our wave-packet approach and allows for the investigation of filled bands. In Chap. 7 we go one step further and apply our methods to explore how magnetic fields affect HHG in Bi_2Te_3 surface states.

5.2. Model systems

For our studies of the quantum processes leading to HHG in TI surface states we want to elaborate on how the dynamics are influenced by the underlying model system. To this end, we compare four different models: a simple Dirac cone $\hat{\mathcal{H}}_\mathrm{c}(\mathbf{k})$, a gapped Dirac cone $\hat{\mathcal{H}}_\mathrm{g}(\mathbf{k})$, the Bi_2Te_3 surface model $\hat{\mathcal{H}}_\mathrm{s}(\mathbf{k})$ introduced in Sec. 2.1.2, and the Bi_2Te_3 surface model $\hat{\mathcal{H}}_\mathrm{f}(\mathbf{k})$ developed in Ref. [81]. The respective Hamiltonians read

$$\begin{aligned}
\hat{\mathcal{H}}_\mathrm{c}(\mathbf{k}) &= A(k_y\sigma_x - k_x\sigma_y),\\
\hat{\mathcal{H}}_\mathrm{g}(\mathbf{k}) &= A(k_y\sigma_x - k_x\sigma_y) + M\sigma_z,\\
\hat{\mathcal{H}}_\mathrm{s}(\mathbf{k}) &= C\mathbb{1} + D(k_x^2+k_y^2)\mathbb{1} + A(k_y\sigma_x - k_x\sigma_y) + 2R(k_x^3 - 3k_xk_y^2)\sigma_z,\\
\hat{\mathcal{H}}_\mathrm{f}(\mathbf{k}) &= C_\mathrm{f}\mathbb{1} + D_\mathrm{f}(\mathbf{k})(k_x^2+k_y^2)\mathbb{1} + A_\mathrm{f}(k_y\sigma_x - k_x\sigma_y) + 2R_\mathrm{f}(\mathbf{k})(k_x^3 - 3k_xk_y^2)\sigma_z.
\end{aligned} \tag{5.1}$$

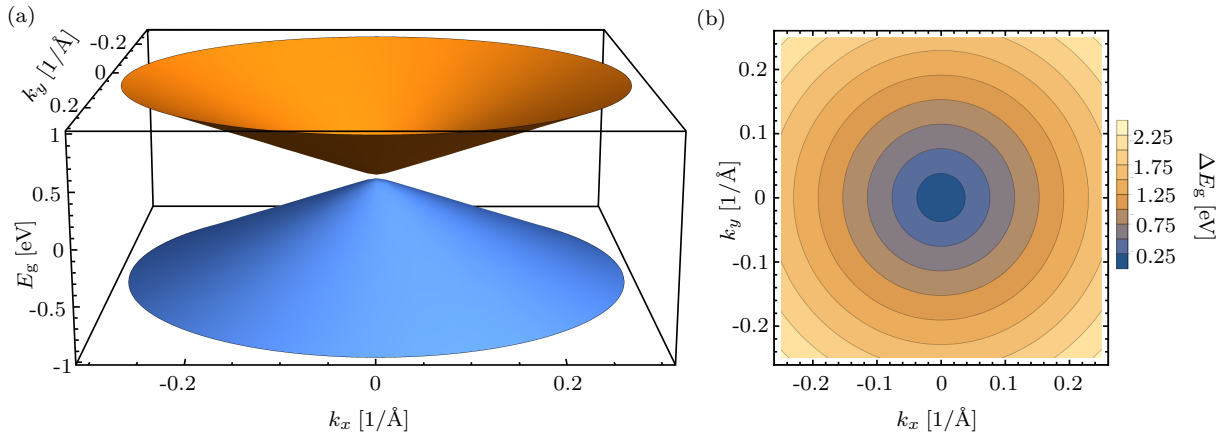

Fig. 5.1: (a) Gapped Dirac cone corresponding to the model Hamiltonian $\hat{\mathcal{H}}_\mathrm{g}(\mathbf{k})$ cut at $|\mathbf{k}| = 0.3\,\text{Å}^{-1}$. (b) Energy difference ΔE_g between both bands. On this scale, the band gap is not resolved and the plot is indistinguishable from the energy difference ΔE_c obtained for the Dirac Hamiltonian $\hat{\mathcal{H}}_\mathrm{c}(\mathbf{k})$.

For the first three models we take the parameters as given in Sec. 2.1.2, for the mass M we choose $M = 0.02\,\text{eV}$. This value is so small that it barely modifies the energy spectrum and only opens a gap of 0.04 eV, see Fig. 5.1. Nevertheless, this gap changes the geometric properties of the system and thus affects the electron dynamics, as we will see in the following sections. The Bi_2Te_3 surface model $\hat{\mathcal{H}}_\mathrm{f}(\mathbf{k})$ from Ref. [81] was derived as a more realistic version of $\hat{\mathcal{H}}_\mathrm{s}(\mathbf{k})$. We will refer to it as *fitted Hamiltonian* $\hat{\mathcal{H}}_\mathrm{f}(\mathbf{k})$. In $\hat{\mathcal{H}}_\mathrm{f}(\mathbf{k})$ a $\mathbf{k}$-dependence of the prefactors $D \to D_\mathrm{f}(\mathbf{k})$ and $R \to R_\mathrm{f}(\mathbf{k})$ was introduced, where

$$D_\mathrm{f}(\mathbf{k}) = \frac{b_2}{k_\mathrm{sym}^2} \frac{1}{1 + \left(\frac{k}{k_\mathrm{sym}}\right)^2}, \quad \text{and} \quad R_\mathrm{f}(\mathbf{k}) = \frac{r_2}{k_\mathrm{asym}^2} \frac{1}{1 + \left(\frac{k}{k_\mathrm{asym}}\right)^4}. \tag{5.2}$$

Since these prefactors only depend on the absolute value $k = |\mathbf{k}| = \sqrt{k_x^2 + k_y^2}$, they do not change the symmetry properties of $\hat{\mathcal{H}}_\mathrm{f}(\mathbf{k})$ compared to $\hat{\mathcal{H}}_\mathrm{s}(\mathbf{k})$ in Eq. (5.1). The model parameters

C_f	A_f	b_2	k_sym	r_2	k_asym
$-0.176\,\text{eV}$	$0.609\,\text{eVÅ}$	$0.32\,\text{eV}$	$0.12\,\text{Å}^{-1}$	$1.57\,\text{eV Å}$	$0.215\,\text{Å}^{-1}$

result from fitting the bandstructure $E_\mathrm{f}(\mathbf{k})$ corresponding to $\hat{\mathcal{H}}_\mathrm{f}(\mathbf{k})$ to bands calculated with DFT. The constant C_f takes the Fermi energy of the crystal used for the experiment in [81] into account. For our calculations with TQT we have to employ another expansion of the Hamiltonian $\hat{\mathcal{H}}_\mathrm{f}(\mathbf{k})$, because TQT can only process Hamiltonians that depend on polynomials of k_x, k_y. We solve

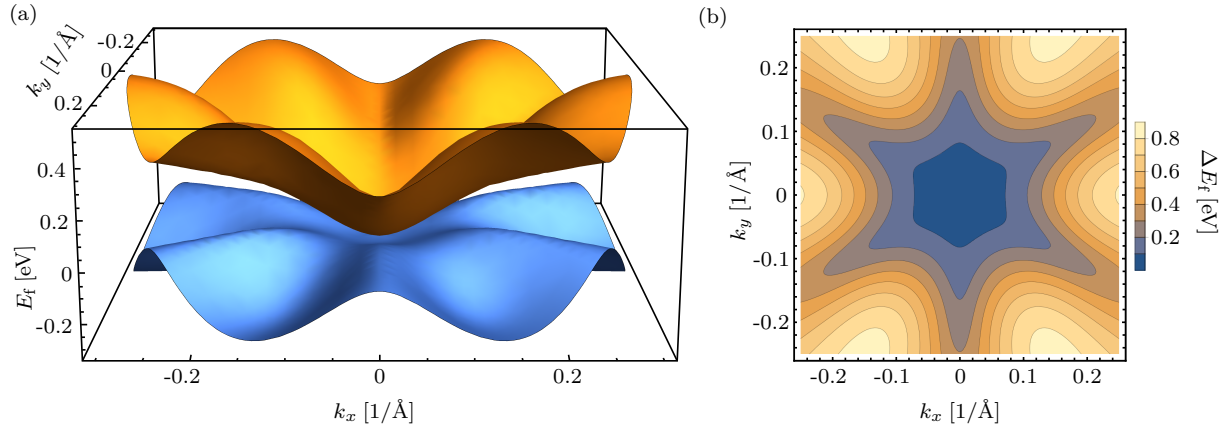

Fig. 5.2: (a) Bandstructure of Bi_2Te_3 for the fitted Hamiltonian $\hat{\mathcal{H}}_f(\mathbf{k})$ from Ref. [81] cut at $|\mathbf{k}| = 0.3\,\text{Å}^{-1}$. The energy scales are smaller and the warping effect stronger than for the model Hamiltonian from Sec. 2.1.2, Fig. 2.4. (b) Energy difference ΔE_f between both bands. The comparably strong warping effect is even more apparent, the retrieval of the rotational symmetry of the Dirac cone around $|\mathbf{k}| = 0$ is not resolved on the shown energy scale.

this issue by expanding the prefactors (5.2) into polynomials and fitting them to the bands $E_f(\mathbf{k})$, see App. A.4 for more details.

The bandstructure and eigenstates of the fitted Hamiltonian $\hat{\mathcal{H}}_f(\mathbf{k})$ are defined analogously to those of $\hat{\mathcal{H}}_s(\mathbf{k})$, see Eqs. (2.22) and (2.24). In Fig. 5.2 we show (a) the eigenenergies E_f for $|\mathbf{k}| \leq 0.3\,\text{Å}^{-1}$ and (b) the local energy difference ΔE_f of the fitted Hamiltonian $\hat{\mathcal{H}}_f(\mathbf{k})$. Like for the surface model $\hat{\mathcal{H}}_s(\mathbf{k})$ from Sec. 2.1.2, PHS is broken and the rotational symmetry of the Dirac cone is reduced to a sixfold symmetry, see Fig. 5.1 of the gapped cone for reference. When directly comparing the spectra of the two surface models, Figs. 5.2 and 2.4, respectively, it is apparent that the warping is stronger in the fitted model. Additionally, the energy scales are different and the local band gaps are more than four times smaller for the fitted Hamiltonian. Hence, the recovery of the rotational symmetry of the Dirac cone is not visible in the scale of Fig. 5.2(b). Whether and how these different energy scales influence the electron dynamics caused by an applied electric field will be investigated in the following sections.

The presented model Hamiltonians all exhibit different Berry curvatures. As discussed in Sec. 2.2, for two-level systems only the z component $[\mathbf{\Omega}_\pm(\mathbf{k})]_z$ is non-vanishing. We compute the latter using Eq. (2.44) and show contour plots for the valence band $(-)$ in Fig. 5.3. For the gapped Dirac cone $\hat{\mathcal{H}}_g(\mathbf{k})$ one obtains

$$[\mathbf{\Omega}_-(\mathbf{k})]_z = \frac{A^2 M}{2\left(A^2|\mathbf{k}|^2) + M^2\right)^{3/2}}. \tag{5.3}$$

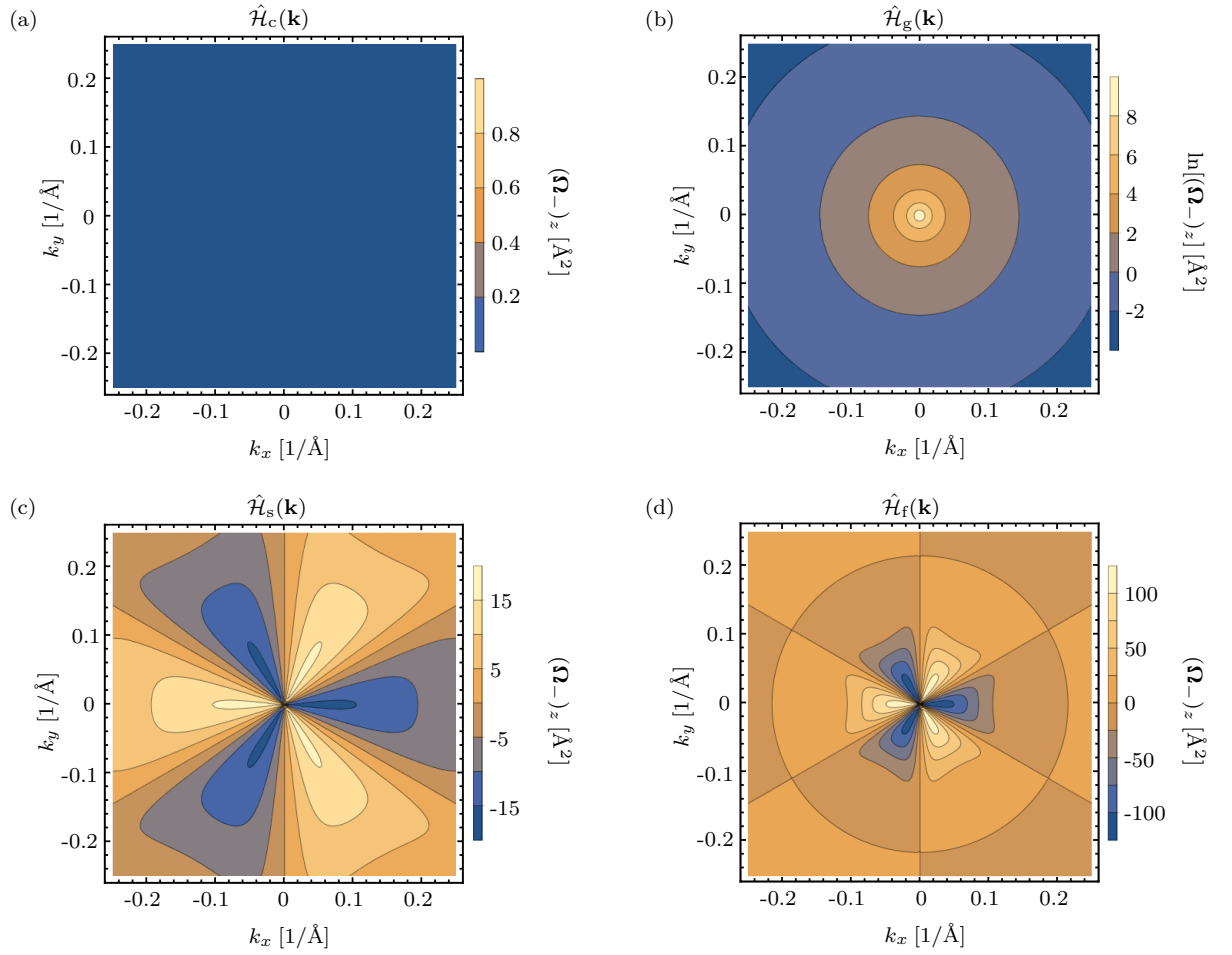

Fig. 5.3: Berry curvature of (a) the Dirac cone $\hat{\mathcal{H}}_c(\mathbf{k})$, (b) the gapped Dirac cone $\hat{\mathcal{H}}_g(\mathbf{k})$, (c) the Bi_2Te_3 surface states $\hat{\mathcal{H}}_s(\mathbf{k})$, and (d) the fitted Hamiltonian $\hat{\mathcal{H}}_f(\mathbf{k})$ for the Bi_2Te_3 surface states. Only the z component of the valence band Berry curvature is shown. It diverges at the Dirac point and is zero for all other $\mathbf{k}$ for the Dirac cone $\hat{\mathcal{H}}_c(\mathbf{k})$. However, the divergence is not resolved here. Opening a gap lifts the divergence and the Berry-curvature peak broadens around the Dirac point, see panel (b). For better resolution, in panel (b) the logarithm of the Berry curvature is shown. The hexagonal warping of the Bi_2Te_3 surface states leads to a more complicated Berry curvature with threefold symmetry. Since the warping is stronger and the energy scales are smaller for the fitted Hamiltonian $\hat{\mathcal{H}}_f(\mathbf{k})$, its Berry curvature is larger than that of the simple surface model $\hat{\mathcal{H}}_s(\mathbf{k})$. Nevertheless, they share the same symmetry.

By taking the limit $M \to 0$, Eq. (5.3) gives the Berry curvature of the Dirac cone $\hat{\mathcal{H}}_\mathrm{c}(\mathbf{k})$. It is zero for all $\mathbf{k}$ except $\mathbf{k} = 0$. At the band touching, the Berry curvature diverges. Note however that this is not resolved in our plot in Fig. 5.3(a). When a gap is opened, i.e. $M \neq 0$, the Berry curvature peak broadens around the Dirac point, its height decreases with increasing mass gap. As given in Eq. (5.3), $[\boldsymbol{\Omega}_-(\mathbf{k})]_z$ is positive since we choose a positive mass M. In panel (c) and (d) we compare the Berry curvatures of the two surface models[2] $\hat{\mathcal{H}}_\mathrm{s}(\mathbf{k})$ and $\hat{\mathcal{H}}_\mathrm{f}(\mathbf{k})$ of Bi_2Te_3. Both Berry curvatures have a threefold symmetry and the same pattern which arises from the hexagonal warping. However, the absolute value of the Berry curvature is larger for the fitted Hamiltonian $\hat{\mathcal{H}}_\mathrm{f}(\mathbf{k})$ because of its smaller energy scale and the larger impact of the warping term. Note that the Berry curvature of $\hat{\mathcal{H}}_\mathrm{f}(\mathbf{k})$ only appears to extend over a smaller area in momentum space in the plot due to the scaling of the color bar.

When analyzing the velocities of test charges in these model systems, in many cases Zitterbewegung arises, see Sec. 2.3.1 for an introduction. For a better understanding of its features, it is instructive to look at the commutator of the velocity operator and Hamiltonian of the respective model. Whenever this commutator is vanishes, no Zitterbewegung is possible. Note that our following considerations are for the Hamiltonians (5.1) and only hold when no additional fields are applied. For $\hat{\mathcal{H}}_\mathrm{c/g}(\mathbf{k})$, the velocity operator $\hat{\mathbf{v}}_\mathrm{c/g}$ is given by

$$\hat{\mathbf{v}}_\mathrm{c/g} = \frac{A}{\hbar} \begin{pmatrix} -\sigma_y \\ \sigma_x \end{pmatrix}, \tag{5.4}$$

its commutator with $\hat{\mathcal{H}}_\mathrm{g}(\mathbf{k})$ reads

$$\left[\hat{\mathbf{v}}_\mathrm{g}, \hat{\mathcal{H}}_\mathrm{g}(\mathbf{k})\right] = \frac{2\mathrm{i}A}{\hbar} \left[A \begin{pmatrix} k_y \\ -k_x \end{pmatrix} \sigma_z - M \begin{pmatrix} \sigma_x \\ \sigma_y \end{pmatrix} \right], \tag{5.5}$$

and by setting $M = 0$ we obtain the commutator $\left[\hat{\mathbf{v}}_\mathrm{c}, \hat{\mathcal{H}}_\mathrm{c}(\mathbf{k})\right]$. Hence, for the Dirac cone $\hat{\mathcal{H}}_\mathrm{c}(\mathbf{k})$ Zitterbewegung in v_x (v_y) is only nonzero, when $k_y \neq 0$ ($k_x \neq 0$), i.e. the Zitterbewegung is always perpendicular to the electron motion. For the gapped cone ($M \neq 0$) also a parallel Zitterbewegung is allowed due to the second, $\mathbf{k}$-independent term. The velocity operator of

[2] Since the expressions become rather long for these Hamiltonians we used the software *Wolfram Mathematica 10.3* [239] for the computation and refrain from showing the full expressions here.

$\hat{\mathcal{H}}_{\mathrm{s}}(\mathbf{k})$ is given in Eq. (2.25). We compute its commutator with $\hat{\mathcal{H}}_{\mathrm{s}}(\mathbf{k})$ as

$$\left[\hat{\mathbf{v}}_{\mathrm{s}}, \hat{\mathcal{H}}_{\mathrm{s}}(\mathbf{k})\right] = \frac{2\mathrm{i}A}{\hbar}\left[A\begin{pmatrix} k_y \\ -k_x \end{pmatrix}\sigma_z - 2R\left(k_x^3 - 3k_x k_y^2\right)\begin{pmatrix}\sigma_x \\ \sigma_y\end{pmatrix} + 6R\left(k_y\sigma_y + k_x\sigma_x\right)\begin{pmatrix} k_x^2 - k_y^2 \\ -2k_x k_y\end{pmatrix}\right]. \tag{5.6}$$

In this case, for $k_x = 0$ no Zitterbewegung in v_y is possible, but there are no restrictions for Zitterbewegung in v_x. As $\hat{\mathcal{H}}_{\mathrm{s}}(\mathbf{k})$ and $\hat{\mathcal{H}}_{\mathrm{f}}(\mathbf{k})$ have the same symmetry, their Zitterbewegung also follows the same rules. The velocity operator $\hat{\mathbf{v}}_{\mathrm{f}}$ contains additional terms due to the momentum-dependent prefactors $D_{\mathrm{f}}(\mathbf{k})$ and $R_{\mathrm{f}}(\mathbf{k})$, but only the latter enters the commutator $\left[\hat{\mathbf{v}}_{\mathrm{f}}, \hat{\mathcal{H}}_{\mathrm{f}}(\mathbf{k})\right]$. Since the prefactors $D_{\mathrm{f}}(\mathbf{k})$ and $R_{\mathrm{f}}(\mathbf{k})$ only depend on the absolute value $k = |\mathbf{k}|$, the possible directions of Zitterbewegung remain unaffected. For completeness we show $\hat{\mathbf{v}}_{\mathrm{f}}$ and $\left[\hat{\mathbf{v}}_{\mathrm{f}}, \hat{\mathcal{H}}_{\mathrm{f}}(\mathbf{k})\right]$ in App. A.5.

5.3. Berry curvature mapping with constant electric fields

As a first step towards understanding the Berry curvature's influence on HHG in TI surface states we want to demonstrate how the Berry curvature $\mathbf{\Omega}_n$, where n is the band index, can be extracted from the anomalous velocity, see Sec. 2.3.2 and Ref. [165]. We focus on our model systems here, which allows for the simplification of considering two bands labeled by $n = \pm$ with Berry curvature $\mathbf{\Omega}_{\pm}(\mathbf{k}) = [\mathbf{\Omega}_{\pm}(\mathbf{k})]_z \mathbf{e}_z$ only along the z direction.

Let us consider two electrons a and b, defined in more detail later, that are driven through momentum space by a constant electric field $\mathbf{E}_{\mathrm{el}}$. The field strength $|\mathbf{E}_{\mathrm{el}}| = E_{\mathrm{el}}$ is tuned such that the electrons evolve adiabatically within one band $E_{\pm}(\mathbf{k})$. For concreteness, we choose the valence band $E_{-}(\mathbf{k})$ in the following. Then, each electron's velocity is given by

$$\mathbf{v}_{\mathbf{k}_i^j}(t) = \frac{1}{\hbar}\nabla_{\mathbf{k}} E_{-}(\mathbf{k}^j(t)) - \frac{\mathrm{e}}{\hbar}\mathbf{E}_{\mathrm{el}} \times \mathbf{\Omega}_{-}(\mathbf{k}^j(t)), \tag{5.7}$$

with $j = \mathrm{a}, \mathrm{b}$ labeling the electron, $\mathbf{k}_i^j$ being the respective initial momentum and $\mathbf{k}^j(t)$ the momentum shifted by the electric field $\mathbf{E}_{\mathrm{el}}$, see Eq. (2.56). The anomalous velocity is perpendicular to both the electric field and the Berry

curvature. Hence, when applying the electric field along x (y) direction, the anomalous velocity is solely contained in the y (x) component of the velocity $\mathbf{v}_{\mathbf{k}_i^j}(t)$. Additionally, as long as the x (y) axis is also a symmetry axis of the dispersion $E_-(\mathbf{k})$, by choosing the initial momenta $\mathbf{k}_i^j$ of the electrons symmetrically around the x (y) axis, the y (x) components of their intraband velocities cancel and only the anomalous velocities remain, i.e.

$$\begin{aligned}\left[\mathbf{v}_{\mathbf{k}_i^{\mathrm{a}}}(t)+\mathbf{v}_{\mathbf{k}_i^{\mathrm{b}}}(t)\right]_y &= +\frac{\mathrm{e}}{\hbar}E_{\mathrm{el}}\left[\boldsymbol{\Omega}_-(\mathbf{k}^{\mathrm{a}}(t))+\boldsymbol{\Omega}_-(\mathbf{k}^{\mathrm{b}}(t))\right]_z, \text{ for } \mathbf{E}_{\mathrm{el}}=E_{\mathrm{el}}\mathbf{e}_x,\\ \left[\mathbf{v}_{\mathbf{k}_i^{\mathrm{a}}}(t)+\mathbf{v}_{\mathbf{k}_i^{\mathrm{b}}}(t)\right]_x &= -\frac{\mathrm{e}}{\hbar}E_{\mathrm{el}}\left[\boldsymbol{\Omega}_-(\mathbf{k}^{\mathrm{a}}(t))+\boldsymbol{\Omega}_-(\mathbf{k}^{\mathrm{b}}(t))\right]_z, \text{ for } \mathbf{E}_{\mathrm{el}}=E_{\mathrm{el}}\mathbf{e}_y.\end{aligned} \tag{5.8}$$

If $[\boldsymbol{\Omega}_-(\mathbf{k}^{\mathrm{a}}(t))]_z = [\boldsymbol{\Omega}_-(\mathbf{k}^{\mathrm{b}}(t))]_z$, one can directly extract the Berry curvature $[\boldsymbol{\Omega}_-(\mathbf{k}^{j}(t))]_z$ from this. By repeating the procedure for other pairs of electrons labeled by $j'=\mathrm{a}',\mathrm{b}'$ with initial momenta $\mathbf{k}_i^{j'}$ still chosen symmetrically but such that a different Berry curvature cut $[\boldsymbol{\Omega}_-(\mathbf{k}^{j'}(t))]_z$ is explored, one can eventually map out the entire momentum space. However, this is not our goal and we restrict ourselves to one pair of electrons for a proof of principle using the model systems introduced in Sec. 5.2 in the following.

We numerically compute the electron velocities by propagating the electrons with TQT and evaluating the COM observable, see Chap. 3. Thus, we obtain the full quantum mechanical velocities. By tuning the parameters such that we are in the adiabatic regime, these velocities should be equal to Eq. (5.7). The electrons are modeled as narrow Gaussian wave packets of width $\Delta k = 0.002\,\text{Å}^{-1}$ and initially given by

$$\Psi_j(\mathbf{k}, t=0) = \frac{1}{\Delta k\sqrt{\pi}}\exp\left(-\frac{1}{2\Delta k^2}\left(\mathbf{k}-\mathbf{k}_i^j\right)^2\right)\varphi_-(\mathbf{k}), \tag{5.9}$$

where $\varphi_-(\mathbf{k})$ is the eigenstate of the valence band of the respective model system, generally defined by Eq. (2.24). In order to achieve $[\boldsymbol{\Omega}_-(\mathbf{k}^{\mathrm{a}}(t))]_z = [\boldsymbol{\Omega}_-(\mathbf{k}^{\mathrm{b}}(t))]_z \equiv [\boldsymbol{\Omega}_-(\mathbf{k}^{\mathrm{a/b}}(t))]_z$ for the Bi_2Te_3 surface models, the electric field $\mathbf{E}_{\mathrm{el}}$ has to be applied along the x direction[3], i.e. $\mathbf{E}_{\mathrm{el}} = E_{\mathrm{el}}\mathbf{e}_x$. This coincides with the $\overline{\Gamma\mathrm{K}}$ direction of the Bi_2Te_3 surface. Accordingly, the Berry curvature is encoded in the y component of the velocity. For all model systems, a cancellation of the intraband velocities of that component is obtained by setting the initial momenta to $\mathbf{k}_i^{\mathrm{a}} = (-0.25, 0.1)\text{Å}^{-1}$ and $\mathbf{k}_i^{\mathrm{b}} = (-0.25, -0.1)\text{Å}^{-1}$. The electric field is implemented by adding the scalar potential $\phi_{\mathrm{el}}(\mathbf{r})$, with

[3]For the cone and gapped cone the field direction can in principle be chosen arbitrarily due to their rotational symmetry.

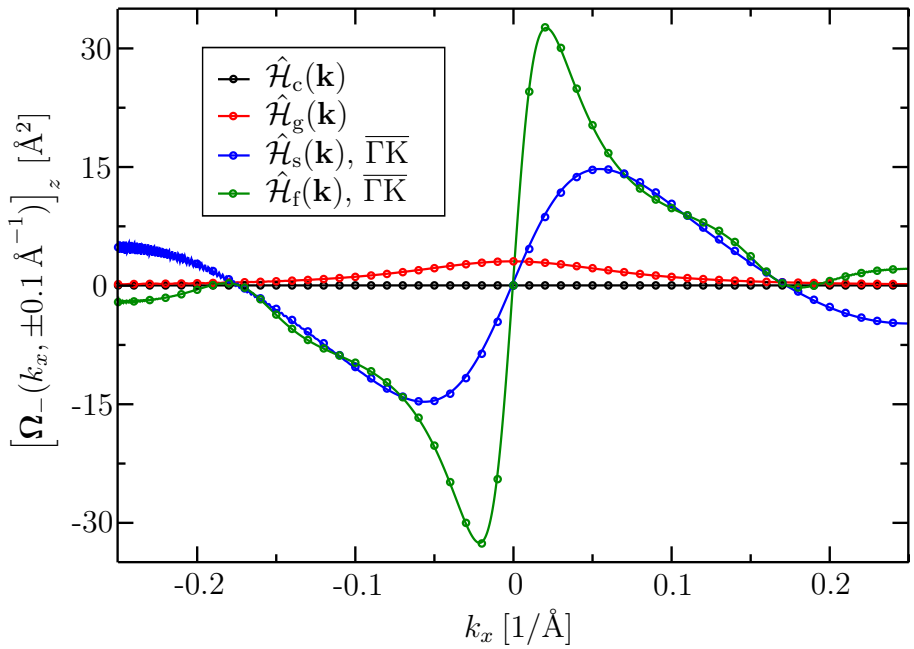

Fig. 5.4: Berry curvature of the model Hamiltonians extracted from the anomalous velocity (solid lines) and computed with Eq. (2.44) (circles). The data shows a cut along k_x for $k_y = \pm 0.1\,\text{Å}^{-1}$. The noise at the beginning of the curves is caused by the switch-on of the electric field in the simulations with TQT.

$\mathbf{E}_\text{el} = -\nabla_\mathbf{r}\phi_\text{el}(\mathbf{r})$, to the Hamiltonian, see Eq. (2.55). The electrons move adiabatically through the band when applying an electric field of strength $E_\text{el} = -0.05\,\text{MV cm}^{-1}$ for $\hat{\mathcal{H}}_{c/g/s}(\mathbf{k})$. Due to the lower energy scale of $\hat{\mathcal{H}}_f(\mathbf{k})$, in that model the field strength has to be reduced to $E_\text{el} = -0.01\,\text{MV cm}^{-1}$ in order to realize the adiabatic limit. For the simulations of $\hat{\mathcal{H}}_{c/g/f}(\mathbf{k})$ we use 1024×512 data points and a time step of $\delta t = 2\,\text{fs}$ in TQT. Due to the larger curvature of the bands of $\hat{\mathcal{H}}_s(\mathbf{k})$, for this Hamiltonian we need 2048×1024 data points and a time step of 0.5 fs. For all simulations the grid spacing is set to $\delta x = 6\,\text{Å}$ and $\delta y = 20\,\text{Å}$.

For our choice of initial momenta $\mathbf{k}_i^j$ and electric field direction, we can map the Berry curvature $[\mathbf{\Omega}_-(\mathbf{k})]_z$ for a cut at $k_y = \pm 0.1\,\text{Å}^{-1}$ and $k_x \geq -0.25\,\text{Å}^{-1}$. To this end, we take the computed velocities $[\mathbf{v}_{\mathbf{k}_i^j}(t)]_y$ and solve Eq. (5.8) for $[\mathbf{\Omega}_-(\mathbf{k}^{a/b}(t))]_z$. In Fig. 5.4 we plot the results against the x component of the time-evolved momenta $k_x^j(t)$ (solid lines)[4] and compare them to data points of the respective Berry curvatures calculated from Eq. (2.44) (circles). The good agreement verifies that we can actually extract the Berry curvature from our simulations.

[4]Note that the results for $\hat{\mathcal{H}}_{s/f}$ are slightly noisy at the beginning. This is caused by the switch-on of the electric field in the TQT simulations. Due to the field, the wave packets (5.9) are not perfect eigenstates of the Hamiltonian anymore and a small Zitterbewegung arises. For the (gapped) Dirac cone this effect is not resolved in the plot.

We emphasized that by applying the electric field in x direction, we study the $\overline{\Gamma\mathrm{K}}$ direction of the Bi_2Te_3 surface. By aligning the electric field with the y direction instead, i.e. $\mathbf{E}_{\mathrm{el}} = E_{\mathrm{el}}\mathbf{e}_y$, the electrons are driven along the $\overline{\Gamma\mathrm{M}}$ direction. For the (gapped) Dirac cone, we obtain the same results as for the $\overline{\Gamma\mathrm{K}}$ direction when accordingly choosing the initial momenta $\mathbf{k}_i^{\mathrm{a}} = (0.1, -0.25)\text{Å}^{-1}$ and $\mathbf{k}_i^{\mathrm{b}} = (-0.1, -0.25)\text{Å}^{-1}$ and evaluating $[\mathbf{v}_{\mathbf{k}_i^j}(t)]_x$, due to the system's rotational symmetry[5]. For the Bi_2Te_3 surface Hamiltonians $\hat{\mathcal{H}}_{\mathrm{s/f}}(\mathbf{k})$ with warping however, the Berry curvature is antisymmetric with respect to the k_y axis, hence $[\boldsymbol{\Omega}_-(\mathbf{k}^{\mathrm{a}}(t))]_z = -[\boldsymbol{\Omega}_-(\mathbf{k}^{\mathrm{b}}(t))]_z$, see Fig. 5.3(c) and (d). The anomalous velocities of the two modes cancel and no Berry curvature can be extracted, compare Eq. (5.8).

These results not only show how to map the Berry curvature but also which velocity components to expect for two test charges that evolve adiabatically. The symmetry of the band structure and the Berry curvature determine how the velocities of the two electrons add up. As presented here, for electrons distributed symmetrically in momentum space with respect to the driving, a velocity component perpendicular to the applied electric field can only survive as long as the Berry curvature is non-zero and not antisymmetric for the two electrons. The velocity parallel to the electric field solely consists of the intraband term in the adiabatic case. In the models considered here, these velocities are equal for both test charges and the total parallel velocity is simply twice the single-electron velocity.

5.4. Laser-driven dynamics – different regimes in momentum space

In Sec. 5.3 we considered a constant electric field and tuned the field strength and electron momentum such that the motion is in the adiabatic regime. As a next step, we introduce an electric field pulse $\mathbf{E}_{\mathrm{el}}(t)$ modeling the laser pulse from the experiment [81] and study which kind of transitions it can drive and how they affect the electron velocities. We write the pulse as

$$\mathbf{E}_{\mathrm{el}}(t) = E_{\mathrm{el}} \exp\left(-\frac{(t-t_0)^2}{2\Delta t^2}\right) \sin\left(2\pi\nu_{\mathrm{el}}\,(t-t_0)\right)\mathbf{e}_x, \tag{5.10}$$

[5]Note that for these simulations the TQT grid has to be rotated, i.e. we need 512×1024 data points and δx and δy are interchanged.

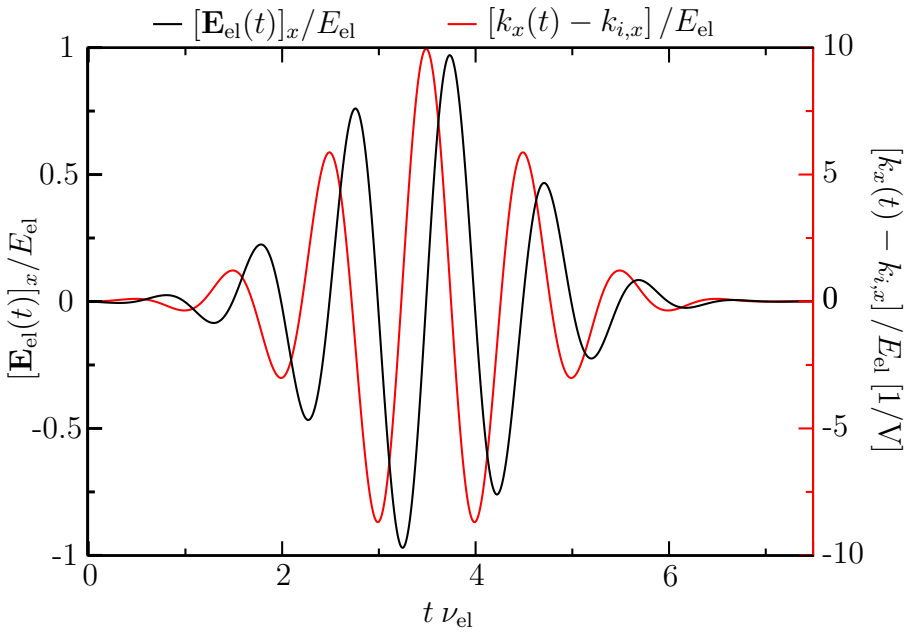

Fig. 5.5: Scaled electric field (black) and corresponding time-dependent momentum (red). As described by the acceleration theorem (2.56), the change in momentum $\dot{\mathbf{k}}(t)$ is proportional to the electric field.

assuming a perfectly Gaussian pulse shape with standard deviation $\Delta t = 40\,\mathrm{fs}$ and a constant carrier-wave frequency $\nu_{\mathrm{el}} = 25\,\mathrm{THz}$. We focus on polarization along the $\overline{\Gamma\mathrm{K}}$ direction of Bi_2Te_3 where the Berry curvature of the surface models with warping can be observed by propagating two symmetric test charges. The time shift $t_0 = 140\,\mathrm{fs}$ is introduced because calculations in TQT start at $t = 0$ and the pulse needs to have a negligible amplitude at that time. Just as the constant field, the pulse induces a shift in the momentum according to the acceleration theorem (2.56). This shift (red curve and axis) is plotted in Fig. 5.5 alongside with the pulse (black curve and axis). Whenever the electric field changes sign, the momentum shift changes direction. Accordingly, a state oscillates around its initial momentum $k_{i,x}$. Its momentum $k_y = k_{i,y}$ remains constant.

We explore the different transition regimes for the model Hamiltonians presented in Sec. 5.2. To this end, we simulate the time evolution of two symmetrically arranged wave packets $\Psi_j(\mathbf{k}, t)$, $j = \mathrm{a}, \mathrm{b}$, using TQT and compute their velocities with the COM observable introduced in Sec. 3.5. For the evaluation we consider the sum of the wave packet's velocities rescaled by the maximal parallel intraband velocity $v_x^{\max} = \left|\frac{2}{\hbar}\left[\nabla_{\mathbf{k}} E_-(\mathbf{k}^{\mathrm{a}}_{\max})\right]_x\right|$, where $\mathbf{k}^{\mathrm{a}}_{\max} = \mathbf{k}^{\mathrm{a}}(3.5/\nu_{\mathrm{el}})$. By projecting the wave packets $\Psi_j(\mathbf{k}, t)$ onto the eigenstates $\varphi_\pm(\mathbf{k})$ of the corresponding model at each time step during the propagation, their distribution over valence and conduction band can be traced, i.e.

$$|c_\pm(t)|^2 = \frac{1}{N}\int \mathrm{d}\mathbf{k}\ \left|\varphi_\pm^*(\mathbf{k})\ \Psi_j(\mathbf{k}, t)\right|^2, \tag{5.11}$$

where N is a constant that ensures that $|c_+(t)|^2 + |c_-(t)|^2 = 1$. As in Sec. 5.3, the initial wave packets are given by Eq. (5.9) with width $\Delta k = 0.002\,\text{Å}^{-1}$ and start in the valence band. The electric field pulse is included via the (now time-dependent) scalar potential $\phi_{\text{el}}(\mathbf{r}, t)$ and the grid is set to 1024×512 data points with $\delta x = 6\,\text{Å}$ and $\delta y = 20\,\text{Å}$ for all calculations. For simplicity we restrict our studies to wave packets with initial momentum[6] $\mathbf{k}_i = (0, \pm k_{i,y})\text{Å}^{-1}$. Then, the wave packets are initially located at the minimal energy gap $\Delta E(\mathbf{k}_i)$ encountered on the cut of the band structure[7] along $\pm k_{i,y}$ and oscillate around it during the pulse.

To categorize the transitions, we adapt the classification of regimes by Heide et al. [173], see Sec. 2.4 for a summary. For $\hat{\mathcal{H}}_{\text{c/g}}(\mathbf{k})$ we obtain exact results taking the Keldysh parameter $\gamma = \Delta E/(\sqrt{2}\hbar\Omega_{\text{R}})$ with Rabi frequency $\Omega_{\text{R}} = v_{\text{F}} e E_{\text{el}}/(h\nu_{\text{el}})$, the transition time $\tau_{\text{t}} = \pi/\Omega_{\text{R}}$, and the Landau-Zener transition probability $P_{\text{LZ}} = \exp(-2\pi\delta_{\text{LZ}})$ with $\delta_{\text{LZ}} = (\Delta E/2)^2/(2\hbar v_{\text{F}} e E_{\text{el}})$ as derived in [173] by setting $\hbar v_{\text{F}} = A$ and $\Delta E = \Delta E_{\text{c/g}}(\mathbf{k}_i)$. In principle, for $\hat{\mathcal{H}}_{\text{s/f}}(\mathbf{k})$ this approach is still a good approximation as long as $\mathbf{k}_i$ is in a range where the linear term dominates. Note however, that for $\hat{\mathcal{H}}_{\text{f}}(\mathbf{k})$ this range is rather limited and thus the approximation is not valid for most of the setups considered in the following. Since the gap $\Delta E(\mathbf{k}_i)$ is momentum dependent in 2D systems, we can employ the same pulse strength E_{el} to realize different regimes by simply varying the initial momentum $\mathbf{k}_i$ of our wave packets. For $E_{\text{el}} = 0.1\,\text{MV cm}^{-1}$ we access the adiabatic regime, resonant transitions and the nonimpulsive Landau-Zener regime. Only for the impulsive and adiabatic-impulsive Landau-Zener transitions we increase the field to $E_{\text{el}} = 1\,\text{MV cm}^{-1}$ for all model systems, as we have to decrease the transition time τ_{t} in order to realize them. For $E_{\text{el}} = 0.1\,\text{MV cm}^{-1}$ we use a time step $\delta t = 0.5\,\text{fs}$ in our simulations. For the larger field strengths we have to reduce it to $\delta t = 0.1\,\text{fs}$ in order to achieve convergence.

5.4.1. Adiabatic regime

In the adiabatic regime, no transitions occur and the test wave packets stay within the valence band throughout the full propagation. As for the constant field in Sec. 5.3, their velocities are given by the intraband velocity and for nonzero Berry curvature (i.e. for $\hat{\mathcal{H}}_{\text{g/s/f}}(\mathbf{k})$) an additional anomalous velocity

[6] Note that we suppress the superscript j labeling the wave packets from now on for better readability whenever it is not necessary for clarification.

[7] Compare Figs. 2.4, 5.1, and 5.2 for the local energy differences $\Delta E(\mathbf{k})$ of the models.

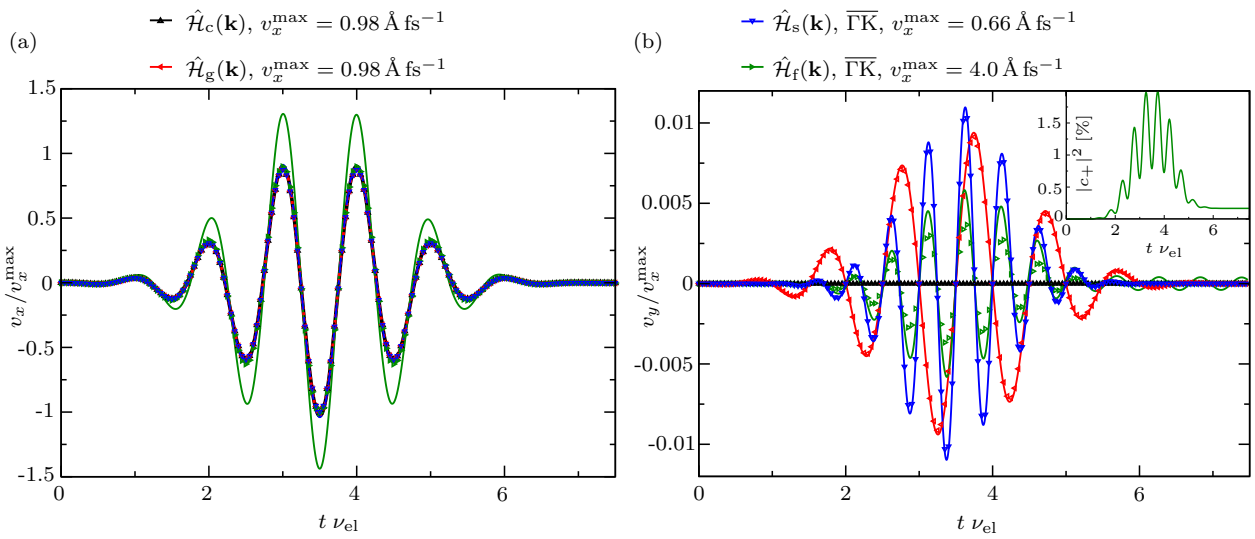

Fig. 5.6: Velocity expectation value for two symmetric test charges in the adiabatic regime, (a) parallel and (b) perpendicular to the driving field. The frequency of the perpendicular velocity component for $\hat{\mathcal{H}}_s(\mathbf{k})$ and $\hat{\mathcal{H}}_f(\mathbf{k})$ is twice the frequency as for $\hat{\mathcal{H}}_g(\mathbf{k})$. This frequency doubling is a direct consequence of the corresponding model system's Berry curvature. Comparing the results from the quantum mechanical simulation (lines) with the perturbative expectation from Eq. (5.7) (triangles) gives good agreement for $\hat{\mathcal{H}}_{c/g/s}(\mathbf{k})$. For $\hat{\mathcal{H}}_f(\mathbf{k})$ however, a slight mismatch in the amplitudes is observed. Additionally, in v_y a small Zitterbewegung remains after the pulse. The inset shows the corresponding occupation of the conduction band $|c_+|^2$ and confirms that the motion is not perfectly adiabatic for $\hat{\mathcal{H}}_f(\mathbf{k})$.

appears. To observe the adiabatic regime, we choose the initial momenta $\mathbf{k}_i$ such that no resonance condition is met, i.e. $\Delta E(\mathbf{k}_i) \neq h\nu_{el}$, and the transition probability P_{LZ} is approximately 0. In Fig. 5.6 we exemplarily show the summed velocities for $\mathbf{k}_i = (0, \pm 0.1)\text{Å}^{-1}$ computed for the model systems $\hat{\mathcal{H}}_{c/g/s}(\mathbf{k})$ and $\mathbf{k}_i = (0, \pm 0.15)\text{Å}^{-1}$ for $\hat{\mathcal{H}}_f(\mathbf{k})$ using TQT, and compare them to the velocities resulting from Eq. (5.7). Note that for the latter only the central mode $\mathbf{k}_i$ was taken into account.

The parallel component v_x only contains the intraband velocity in the adiabatic regime, for our symmetric test charges a, b with $E_-(\mathbf{k}^a(t)) = E_-(\mathbf{k}^b(t))$ it is given by[8]

$$\left[\mathbf{v}_{\mathbf{k}_i^a}(t) + \mathbf{v}_{\mathbf{k}_i^b}(t)\right]_x = \frac{2}{\hbar}\left[\nabla_{\mathbf{k}} E_-(\mathbf{k}^a(t))\right]_x . \tag{5.12}$$

As we set $k_{i,x} = 0$ in our calculations and the band structures are approximately parabolic along k_x for the chosen $k_{i,y}$, the temporal shape is dominated by $k_x(t)$, compare Fig. 5.6(a) and Fig. 5.5. Only the sign is inverted. By rescaling the velocities with their respective maximal intraband velocity v_x^{max}, all curves should fall on top of each other. For $\hat{\mathcal{H}}_{c/g/s}(\mathbf{k})$ this is actually the case and

[8] Note that the slope of the dispersion $E_-(\mathbf{k})$ is also important here. We choose the charges a, b such that the gradients of their dispersion are equal in x direction and of opposite sign in y direction, compare Sec. 5.3.

therefore we dashed some of the lines for better visibility. For $\hat{\mathcal{H}}_{\mathrm{c}}(\mathbf{k})$ and $\hat{\mathcal{H}}_{\mathrm{g}}(\mathbf{k})$ even the velocity $v_x^{\max}$ is equal. This shows that at $k_y = \pm 0.1\,\text{Å}^{-1}$ the small gap's influence on the bandstructure is negligible. For $\hat{\mathcal{H}}_{\mathrm{f}}(\mathbf{k})$ however we observe a mismatch in the amplitudes from Eq. (5.12) and the results from the TQT simulation. Additionally, after the pulse Zitterbewegung is discernible[9] in v_y. The inset of Fig. 5.7(b) shows the occupation $|c_+(t)|^2$ of the conduction band[10] for $\hat{\mathcal{H}}_{\mathrm{f}}(\mathbf{k})$. It confirms that up to two percent of the test charges temporarily switch band and an occupation of about 0.17% remains after the pulse. Therefore, for $\hat{\mathcal{H}}_{\mathrm{f}}(\mathbf{k})$ the dynamics deviate significantly from the purely adiabatic evolution. This also demonstrates that for $\hat{\mathcal{H}}_{\mathrm{f}}(\mathbf{k})$ already at $\mathbf{k}_i = (0, \pm 0.15)\text{Å}^{-1}$ the approximation of P_{LZ} from Ref. [173] is not valid anymore.

The perpendicular component v_y, see Fig. 5.6(b), is described by the anomalous velocities of both charges. It obtains its temporal shape from the product of electric field $|\mathbf{E}_{\mathrm{el}}(t)|$ and Berry curvature $\boldsymbol{\Omega}_-(\mathbf{k}^{\mathrm{a/b}}(t))$, see Eq. (5.8). Accordingly, even though it is two orders of magnitude smaller than v_x, it contains interesting information about the system's geometrical properties. For $\hat{\mathcal{H}}_{\mathrm{c}}(\mathbf{k})$ v_y is zero since its Berry curvature is zero. For $\hat{\mathcal{H}}_{\mathrm{g}}(\mathbf{k})$ the small mass gap gives rise to a non-zero Berry curvature with $\mathbf{k}$-dependent amplitude but constant sign. Hence, the temporal shape of v_y is defined by the electric field and the Berry curvature only modulates the amplitude. For $\hat{\mathcal{H}}_{\mathrm{s/f}}(\mathbf{k})$ however, the hexagonal warping induces a $\mathbf{k}$-dependent sign in the Berry curvature, which for $k_{i,x}^{\mathrm{a/b}} = 0$ means $\left[\boldsymbol{\Omega}_-(\mathbf{k}^{\mathrm{a/b}}(t))\right]_z \propto k_x^{\mathrm{a/b}}(t)$. Furthermore, $k_x^{\mathrm{a/b}}(t)$ is related to the electric field via the acceleration theorem (2.56). Neglecting the Gaussian envelope of the electric field (5.10), this gives

$$\begin{aligned}
\left[\mathbf{v}_{\mathbf{k}_i^{\mathrm{a}}}(t) + \mathbf{v}_{\mathbf{k}_i^{\mathrm{b}}}(t)\right]_y &= +\frac{\mathrm{e}}{\hbar}\left[\mathbf{E}_{\mathrm{el}}(t)\right]_x \left[\boldsymbol{\Omega}_-(\mathbf{k}^{\mathrm{a}}(t)) + \boldsymbol{\Omega}_-(\mathbf{k}^{\mathrm{b}}(t))\right]_z \\
&\propto \quad \left[\mathbf{E}_{\mathrm{el}}(t)\right]_x \left[k_x^{\mathrm{a}}(t) + k_x^{\mathrm{b}}(t)\right] \\
&\propto \quad \sin\left(2\pi\nu_{\mathrm{el}}(t-t_0)\right)\cos\left(2\pi\nu_{\mathrm{el}}(t-t_0)\right) \\
&\propto \quad \sin\left(4\pi\nu_{\mathrm{el}}(t-t_0)\right).
\end{aligned} \tag{5.13}$$

Hence, the symmetry of the Berry curvature of the models with hexagonal warping induces a frequency doubling for light fields applied along the $\overline{\Gamma\mathrm{K}}$

[9] Even though we are at $k_x = 0$, this does not contradict our conclusion from Eq. (5.6). Since the overall scale in Fig. 5.6(b) is so small, even the Zitterbewegung contributed by the width of the wave packet can be resolved.

[10] The occupation is the same for both test charges, thus we only plot the results for one of them.

direction of the crystal. This is also clearly visible when comparing v_y for $\hat{\mathcal{H}}_{\mathrm{s/f}}(\mathbf{k})$ with v_y for $\hat{\mathcal{H}}_{\mathrm{g}}(\mathbf{k})$ in Fig. 5.6(b). Concerning HHG, this argument from the adiabatic limit already suggests the importance of the Berry curvature for the frequencies and polarizations that are observed in the spectrum. We study this in more detail in Sec. 5.5 and Chaps. 6 and 7.

5.4.2. Resonant transitions: Rabi-like oscillations

Resonant transitions occur whenever the local energy difference $\Delta E(\mathbf{k})$ is an integer multiple of the photon energy $h\nu_{\mathrm{el}}$ of the laser pulse. In order to separate resonant transitions from Landau-Zener transitions, one has to consider the perturbative limit of light-matter interaction, i.e. the regime where the Keldysh parameter $\gamma > 1$. In that case the field strength E_{el} is low and accordingly only the first resonance with $h\nu_{\mathrm{el}} = \Delta E(\mathbf{k})$ is relevant [173]. In our case, $E_{\mathrm{el}} = 0.1\,\mathrm{MV\,cm^{-1}}$ and $h\nu_{\mathrm{el}} \approx 0.103\,\mathrm{eV}$. To study the resonance condition $h\nu_{\mathrm{el}} \approx \Delta E(\mathbf{k}_i)$ with test charges, we need to set $\mathbf{k}_i = (0, \pm 0.016)\text{Å}^{-1}$ for $\hat{\mathcal{H}}_{\mathrm{c/s}}(\mathbf{k})$, $\mathbf{k}_i = (0, \pm 0.015)\text{Å}^{-1}$ for $\hat{\mathcal{H}}_{\mathrm{g}}(\mathbf{k})$, and $\mathbf{k}_i = (0, \pm 0.085)\text{Å}^{-1}$ for $\hat{\mathcal{H}}_{\mathrm{f}}(\mathbf{k})$. The resulting total velocities and the corresponding occupation of the conduction band throughout the propagation are shown in Fig. 5.7. For better visibility, we introduced dashed and dotted lines for overlapping curves and multiplied the perpendicular velocity v_y of $\hat{\mathcal{H}}_{\mathrm{s}}(\mathbf{k})$ with a factor of ten. Again, we rescale the velocities with the intraband velocity $v_x^{\max}$ and only show the occupation of one test charge since both results are the same.

Typical features of resonant transitions are the build up of an occupation in the initially empty band – here the conduction band – and the emergence of Rabi-like oscillations for suitable pulse parameters. The former is nicely demonstrated in the occupation $|c_+(t)|^2$ recorded for $\hat{\mathcal{H}}_{\mathrm{f}}(\mathbf{k})$, see inset of Fig. 5.7(a). During the whole pulse duration, the occupation increases and reaches about 80% at the end of the pulse. Since our simulations do not contain any dissipation effects, the occupation remains there after the pulse. The latter appears for $\hat{\mathcal{H}}_{\mathrm{c/g/s}}(\mathbf{k})$. As the dispersion is almost identical for all three models for the chosen $\mathbf{k}_i$, the corresponding occupations are also almost equal. They too reach about 80% but already at $t \approx 3.8/\nu_{\mathrm{el}}$. Then, the population decreases again and levels at about 27% after the pulse. This behavior is associated with Rabi oscillations. They describe a cyclic population for periodically driven two-level systems around the resonance condition. The period T_{R} of such an occupation oscillation is given by the Rabi frequency $2\pi/T_{\mathrm{R}} = \Omega_{\mathrm{R}} = v_{\mathrm{F}} e E_{\mathrm{el}}/(h\nu_{\mathrm{el}})$ [173]. For $\hat{\mathcal{H}}_{\mathrm{c/g/s}}(\mathbf{k})$ we get $T_{\mathrm{R}} \approx 3.25/\nu_{\mathrm{el}}$ and

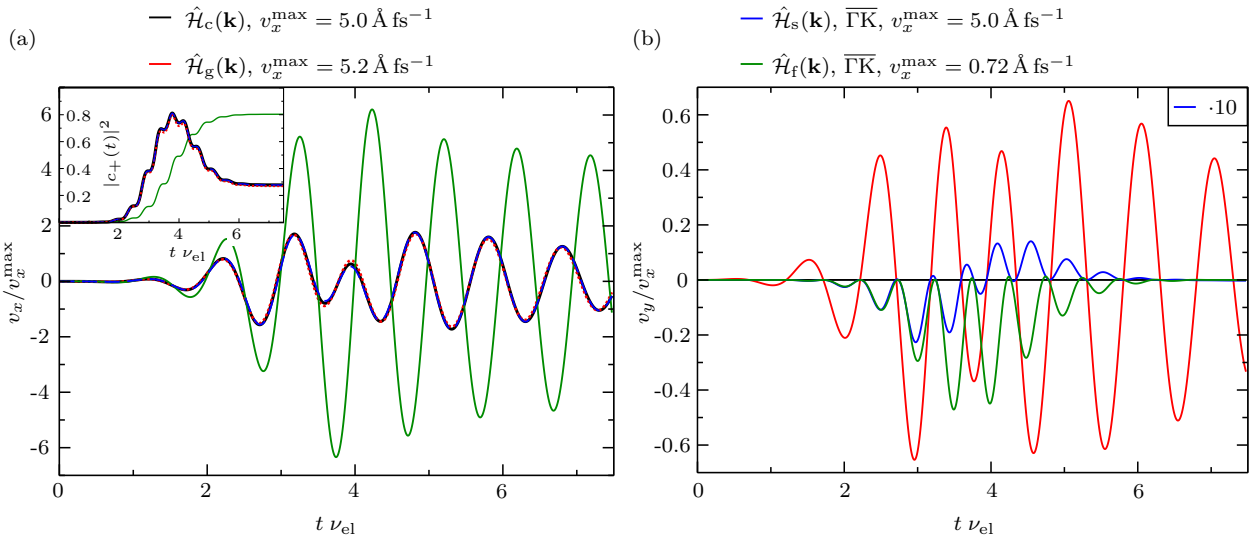

Fig. 5.7: Velocity expectation value for two symmetric test charges in the resonant regime, (a) parallel and (b) perpendicular to the driving field. The inset in panel (a) shows the corresponding conduction band occupations $|c_+(t)|^2$. In the resonant regime, they show Rabi-like oscillations. For all model systems, v_x consists of a mixture of intra- and interband velocity and Zitterbewegung occurs after the pulse. The perpendicular velocity v_y only contains interband contributions and is determined by the geometrical properties of the respective model. For better visibility, we multiplied v_y for $\hat{\mathcal{H}}_s(\mathbf{k})$ by a factor of ten.

for $\hat{\mathcal{H}}_f(\mathbf{k})$ $T_R \approx 17.5/\nu_{el}$. Since here we additionally have an energy dispersion and a pulse envelope, the situation is more complex. Still, the Rabi period T_R provides a rough estimate of how many oscillation cycles occur during our pulse. Accordingly, for $\hat{\mathcal{H}}_f(\mathbf{k})$ we see about half an oscillation, whereas for $\hat{\mathcal{H}}_{c/g/s}(\mathbf{k})$ about 2/3 of a cycle is performed[11]. By increasing the pulse duration or the electric field strength E_{el}, one can tune the population of the conduction band after the pulse. Remember however, that the field strength is limited by the requirement of $\gamma > 1$. An exploration of different Rabi frequencies in a gapped Dirac system is given in the master's thesis of Mario Ebner [163], which we supervised.

As a consequence of the important role of transitions in the resonant regime, the velocities of the test charges cannot be described by the perturbative approach (5.7) anymore. Instead, they are made up of intra- and interband contributions, see Eq. (2.58). Since we can only access the amplitude $|c_\pm(t)|$ of the state in the respective band but not its phase $\arg(c_\pm(t))$ using TQT[12], a quantitative

[11] Note that due to the pulse envelope, the beginnig of the simulation is not equal to the beginning of a Rabi cycle. The onset of the Rabi cycle takes place when the occupation $|c_+|^2$ starts to build up, which is at $t\nu_{el} \approx 2$ for the results presented here.

[12] Note that the reason for this is a random phase that is generated at each time step during propagation. In future works a fixed phase could be introduced in TQT to overcome this issue.

comparison of our results with Eq. (2.58) is not possible[13]. Nevertheless, we can draw some qualitative conclusions from the total velocities of both test charges depicted in Fig. 5.7. The intraband contribution is given by the band dispersion and the occupation of the respective band, thus oscillating with $k_x(t)$. The x component of the intraband velocity of both test charges is the same and adds up, whereas the y component has opposite sign and thus cancels, just as discussed for the adiabatic regime in Sec. 5.4.1. The interband contribution is defined by the velocity matrix elements $\mathbf{v}_{\mathbf{k}}^{+-} = (\mathbf{v}_{\mathbf{k}}^{-+})^*$ and the local energy difference $\Delta E(\mathbf{k})$. It can be considered as a time-dependent Zitterbewegung with frequency $\omega_{\mathrm{ZB}}(t) = \Delta E(\mathbf{k}(t))/\hbar$, compare Sec. 2.3. In v_x, intra- and interband contribution interfere. For the resonant regime, $\omega_{\mathrm{ZB}}(t) \approx 2\pi\nu_{\mathrm{el}}$ by definition. The momentum shift $k_x(t)$ induced by the pulse gives rise to a spread such that $\nu_{\mathrm{el}} \leq \omega_{\mathrm{ZB}}(t)/2\pi \leq 1.2\nu_{\mathrm{el}}$ for $\hat{\mathcal{H}}_{\mathrm{c/g/s}}(\mathbf{k})$ and $\nu_{\mathrm{el}} \leq \omega_{\mathrm{ZB}}(t)/2\pi \leq 1.06\nu_{\mathrm{el}}$ for $\hat{\mathcal{H}}_{\mathrm{f}}(\mathbf{k})$ here. Since the resulting detuning is rather small, the interference of both components is not apparent in the time-dependence of v_x. However, rescaling the velocities with $v_x^{\max} = \left|\frac{2}{\hbar}\left[\nabla_{\mathbf{k}} E_-(\mathbf{k}^{\mathrm{a}}_{\max})\right]_x\right|$, and thus comparing the amplitudes to the expectations from the adiabatic limit, reveals that the interference leads to a doubling of the amplitudes for $\hat{\mathcal{H}}_{\mathrm{c/g/s}}(\mathbf{k})$. For $\hat{\mathcal{H}}_{\mathrm{f}}(\mathbf{k})$ we even observe a maximal multiplication factor of about six. At the end of the pulse and afterwards, the intraband velocity goes to zero[14] and Zitterbewegung dominates the velocity v_x due to the state spreading over both valence and conduction band.

The perpendicular velocity v_y only consists of the combined interband velocity of both charges. Its main characteristics can be explained based on the Berry curvature. Even though the anomalous velocity is a bad approximation in the resonant regime, it is sufficient to predict the oscillation frequencies of v_y. Just as in the adiabatic limit, for $\hat{\mathcal{H}}_{\mathrm{c}}(\mathbf{k})$ the perpendicular velocity v_y is zero, whereas it oscillates with the pulse frequency ν_{el} for $\hat{\mathcal{H}}_{\mathrm{g}}(\mathbf{k})$ and with twice the pulse frequency for $\hat{\mathcal{H}}_{\mathrm{s/f}}(\mathbf{k})$. However, for $\hat{\mathcal{H}}_{\mathrm{s/f}}(\mathbf{k})$ v_y does not oscillate around zero as in the adiabatic limit. To fully understand this, one would have to analyze the interband velocity in detail, including the phases of $c_\pm(t)$. This connection is pointed out by the change of sign in v_y of $\hat{\mathcal{H}}_{\mathrm{s}}(\mathbf{k})$. It occurs exactly when the corresponding population of the conduction band starts to decrease again. After the pulse, Zitterbewegung is only resolved for the gapped Dirac cone $\hat{\mathcal{H}}_{\mathrm{g}}(\mathbf{k})$ in Fig. 5.7(b). This can be understood by looking at the commutators of the respective velocity operators with their

[13] However, we refer to the master's theses of Ebner [163] and Riedel [240] for a more detailed analysis of the phase's influence on the total velocity of several test charges.

[14] Note that it only goes to zero since the test charges are at $k_x = 0$. Otherwise, it would go to a constant value.

Hamiltonians. As discussed in Sec. 5.2, for $k_x = 0$ only for the gapped cone $\hat{\mathcal{H}}_{\mathrm{g}}(\mathbf{k})$ Zitterbegwegung can arise in v_y. Note that during the pulse the electric field alters the commutator and shifts k_x, therefore then $v_y \neq 0$ for $\hat{\mathcal{H}}_{\mathrm{s/f}}(\mathbf{k})$ as well, but with a smaller amplitude than for $\hat{\mathcal{H}}_{\mathrm{g}}(\mathbf{k})$.

5.4.3. Landau-Zener tunneling

Transitions in the strong-field regime, i.e. where $\gamma < 1$, are best described by Landau-Zener tunneling. As discussed by Heide et al. [173], one can subdivide the Landau-Zener regime in three different types which we will discuss in the following.

Nonimpulsive Landau-Zener regime

According to Heide et al. [173], the nonimpulsive Landau-Zener regime is characterized by smooth transitions and a return of the propagated state to its initial band after the pulse. To study this regime, we use the same field strength, $E_{\mathrm{el}} = 0.1\,\mathrm{MV\,cm^{-1}}$, as for the adiabatic and resonant regime, see Secs. 5.4.1 and 5.4.2. By setting $\mathbf{k}_i = (0, \pm 0.007)\mathrm{\AA}^{-1}$ for all model systems, we obtain $\gamma \approx 1.39$ for $\hat{\mathcal{H}}_{\mathrm{g}}(\mathbf{k})$ and $\gamma \approx 1.02$ for $\hat{\mathcal{H}}_{\mathrm{c/s/f}}(\mathbf{k})$. These values do not fulfill $\gamma < 1$ but are still sufficient to observe the nonimpulsive Landau-Zener regime. The corresponding estimates for the Landau-Zener transition probability are $P_{\mathrm{LZ}} \approx 0.41$ for $\hat{\mathcal{H}}_{\mathrm{g}}(\mathbf{k})$, $P_{\mathrm{LZ}} \approx 0.60$ for $\hat{\mathcal{H}}_{\mathrm{c/s}}(\mathbf{k})$, and $P_{\mathrm{LZ}} \approx 0.91$ for $\hat{\mathcal{H}}_{\mathrm{f}}(\mathbf{k})$. In Fig. 5.8 we show the results of the velocities and occupations obtained by propagating the two test charges in TQT for each model. Again, the two test charges have the same occupation and we only plot the resulting $|c_+(t)|^2$ for one of them. Additionally we multiplied v_y of $\hat{\mathcal{H}}_{\mathrm{s}}(\mathbf{k})$ by a factor of ten for better visibility.

The occupations $|c_+(t)|^2$ of the conduction band depicted in the inset of Fig. 5.8(a) agree with the described features of the nonimpulsive regime. However, even though the transition probability P_{LZ} is highest for $\hat{\mathcal{H}}_{\mathrm{f}}(\mathbf{k})$ and smallest for $\hat{\mathcal{H}}_{\mathrm{g}}(\mathbf{k})$, the latter reaches the largest occupation whereas the former has the least transitions during the pulse. To understand this, one has to take the transition time $\tau_{\mathrm{t}} = \pi/\Omega_{\mathrm{R}}$ into account, see Sec. 2.4 for an introduction. If $\tau_{\mathrm{t}} > 1/\nu_{\mathrm{el}}$, a full Landau-Zener transition takes longer than one optical half cycle. Hence, it does not reach its maximum and the transition appears

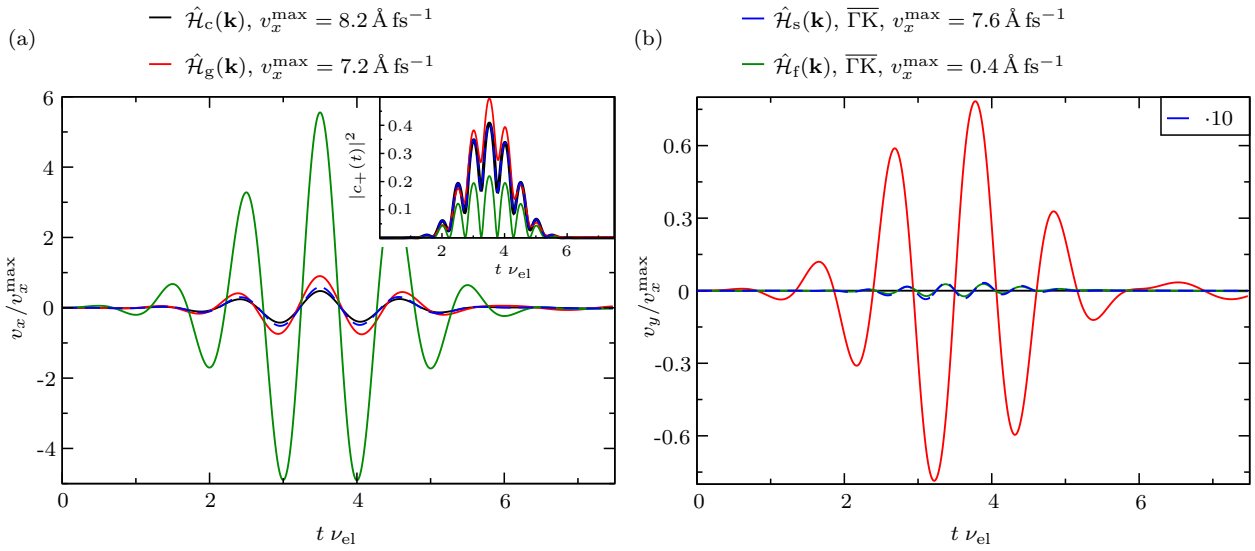

Fig. 5.8: Velocity expectation value for two symmetric test charges in the nonimpulsive Landau-Zener regime, (a) parallel and (b) perpendicular to the driving field. The inset in panel (a) shows the corresponding conduction band occupations $|c_+(t)|^2$. In the nonimpulsive Landau-Zener regime, they change smoothly and return to (approximately) zero after the pulse. Only for $\hat{\mathcal{H}}_g(\mathbf{k})$ a small occupation of 0.3 % remains and Zitterbewegung appears in both v_x and v_y. For better visibility, we multiplied v_y for $\hat{\mathcal{H}}_s(\mathbf{k})$ by a factor of ten.

smooth in a time-resolved plot. Since τ_t only depends on the field strength E_{el} and amplitude ν_{el}, here it is simply half of the Rabi period T_R we computed in Sec. 5.4.2, i.e. $\tau_t \approx 1.625/\nu_{el}$ for $\hat{\mathcal{H}}_{c/g/s}(\mathbf{k})$ and $\tau_t \approx 8.75/\nu_{el}$ for $\hat{\mathcal{H}}_f(\mathbf{k})$. Despite these times being only a rough estimate, they show that for $\hat{\mathcal{H}}_f(\mathbf{k})$ the states complete much less of their transitions than for $\hat{\mathcal{H}}_{c/g/s}(\mathbf{k})$. This results in the occupation $|c_+(t)|^2$ being smaller for $\hat{\mathcal{H}}_f(\mathbf{k})$ than for the other models. Unfortunately, this does not explain why $|c_+(t)|^2$ is larger for $\hat{\mathcal{H}}_g(\mathbf{k})$ than for $\hat{\mathcal{H}}_{c/s}(\mathbf{k})$. Finding the reason for that requires further investigation.

As discussed in Sec. 5.4.2, v_x contains both intra- and interband velocity. On first glance, the qualitative features of the corresponding velocities are similar to those observed in the adiabatic regime, compare Fig. 5.8 to Fig. 5.6. However, the sign of the oscillations appears to be inverted with respect to the adiabatic regime and for $\hat{\mathcal{H}}_f(\mathbf{k})$ the amplitude is increased by approximately a factor of four. These observations are fingerprints of the presence of transitions and indicate that the interband velocity dominates. The sign change is probably due to the phase introduced by the amplitudes $c_\pm(t)$. As before, v_y only contains the interband velocities. Its frequency again depends on the model system and results from the respective Berry curvature. As for v_x, the transitions lead to a change of the velocity's phase compared to the adiabatic case. Additionally, for $\hat{\mathcal{H}}_g(\mathbf{k})$ about 0.3 % of the test charges remain in the conduction band, resulting in a distinguishable Zitterbewegung after the pulse

in both v_x and v_y.

Impulsive and adiabatic-impulsive Landau-Zener regime

In order to access the impulsive and adiabatic-impulsive Landau-Zener regime, one has to reduce the transition time τ_t such that $\tau_\mathrm{t} < 1/\nu_\mathrm{el}$. Then, a full Landau-Zener transition is faster than an optical half cycle and the occupation jumps whenever a transition occurs instead of changing smoothly. For our pulse, $1/\nu_\mathrm{el} = 40\,\mathrm{fs}$ and we realize $\tau_\mathrm{t} < 1/\nu_\mathrm{el}$ by increasing the pulse strength E_el by a factor of ten to $E_\mathrm{el} = 1\,\mathrm{MV\,cm^{-1}}$. Accordingly, the estimated transition times for this field strength are $\tau_\mathrm{t} \approx 0.1625/\nu_\mathrm{el}$ for $\hat{\mathcal{H}}_\mathrm{c/g/s}(\mathbf{k})$ and $\tau_\mathrm{t} \approx 0.875/\nu_\mathrm{el}$ for $\hat{\mathcal{H}}_\mathrm{f}(\mathbf{k})$.

Heide et al. [173] characterize the impulsive Landau-Zener regime by a conduction band occupation that jumps from zero to one and back to zero almost perfectly within an optical cycle. This requires $P_\mathrm{LZ} \approx 1$, which is not achievable in our setup[15]. Nevertheless, by setting $\mathbf{k}_i = (0, \pm 0.018)\text{Å}^{-1}$ for $\hat{\mathcal{H}}_\mathrm{c/g/s}(\mathbf{k})$ and $\mathbf{k}_i = (0, \pm 0.1)\text{Å}^{-1}$ for $\hat{\mathcal{H}}_\mathrm{f}(\mathbf{k})$, we obtain a qualitatively similar behavior, only with jumps to values $|c_+(t)|^2 < 1$. To be precise, we estimate the transition probability $P_\mathrm{LZ} \approx 0.72$ for $\hat{\mathcal{H}}_\mathrm{c/s}(\mathbf{k})$, $P_\mathrm{LZ} \approx 0.69$ for $\hat{\mathcal{H}}_\mathrm{g}(\mathbf{k})$, and $P_\mathrm{LZ} \approx 0.15$ for $\hat{\mathcal{H}}_\mathrm{f}(\mathbf{k})$. But remember that the latter is a bad approximation[16], as is confirmed by the numerical results for the occupation depicted in Fig. 5.9(a). For $\hat{\mathcal{H}}_\mathrm{c/g/s}(\mathbf{k})$ the jumps are at least comparable to the estimated transition probabilities. For $\hat{\mathcal{H}}_\mathrm{f}(\mathbf{k})$ however they are about $|c_+(t)|^2 \approx 0.5$ instead of $|c_+(t)|^2 \approx 0.15$ as suggested by the estimated P_LZ. For the models with warping, i.e. $\hat{\mathcal{H}}_\mathrm{s}(\mathbf{k})$ and $\hat{\mathcal{H}}_\mathrm{f}(\mathbf{k})$, we find that the transitions are not the same for both modes. These discrepancies could be caused by the Stückelberg phase but further investigation is necessary for a better understanding. The corresponding velocities are shown in Fig. 5.9(b) and (c). The larger field strength and the abrupt transitions, as compared to the nonimpulsive Landau-Zener regime in Fig. 5.8, lead to a complicated temporal profile of both parallel and perpendicular velocity. In v_x Zitterbewegung remains after the pulse for

[15] $P_\mathrm{LZ} \approx 1$ would require starting the wave packets at the Dirac point. Since the eigenstates $\varphi_\pm(\mathbf{k} = 0)$ are not well-defined at that point, this leads to large numerical errors in the propagation of wave packets that are narrow in momentum space. For the large wave packets employed in Chaps. 6 and 7 however, the errors are negligible and including the Dirac point is possible.

[16] Note that this also applies to the transition time τ_t. For $\hat{\mathcal{H}}_\mathrm{f}(\mathbf{k})$ we only found impulsive Landau-Zener transitions for $\mathbf{k}_i \gtrsim (0, \pm 0.05)\text{Å}^{-1}$. We suspect, that then the effective v_F including the warping is large enough such that the actual transition time τ_t is sufficiently small to be in the impulsive Landau-Zener regime.

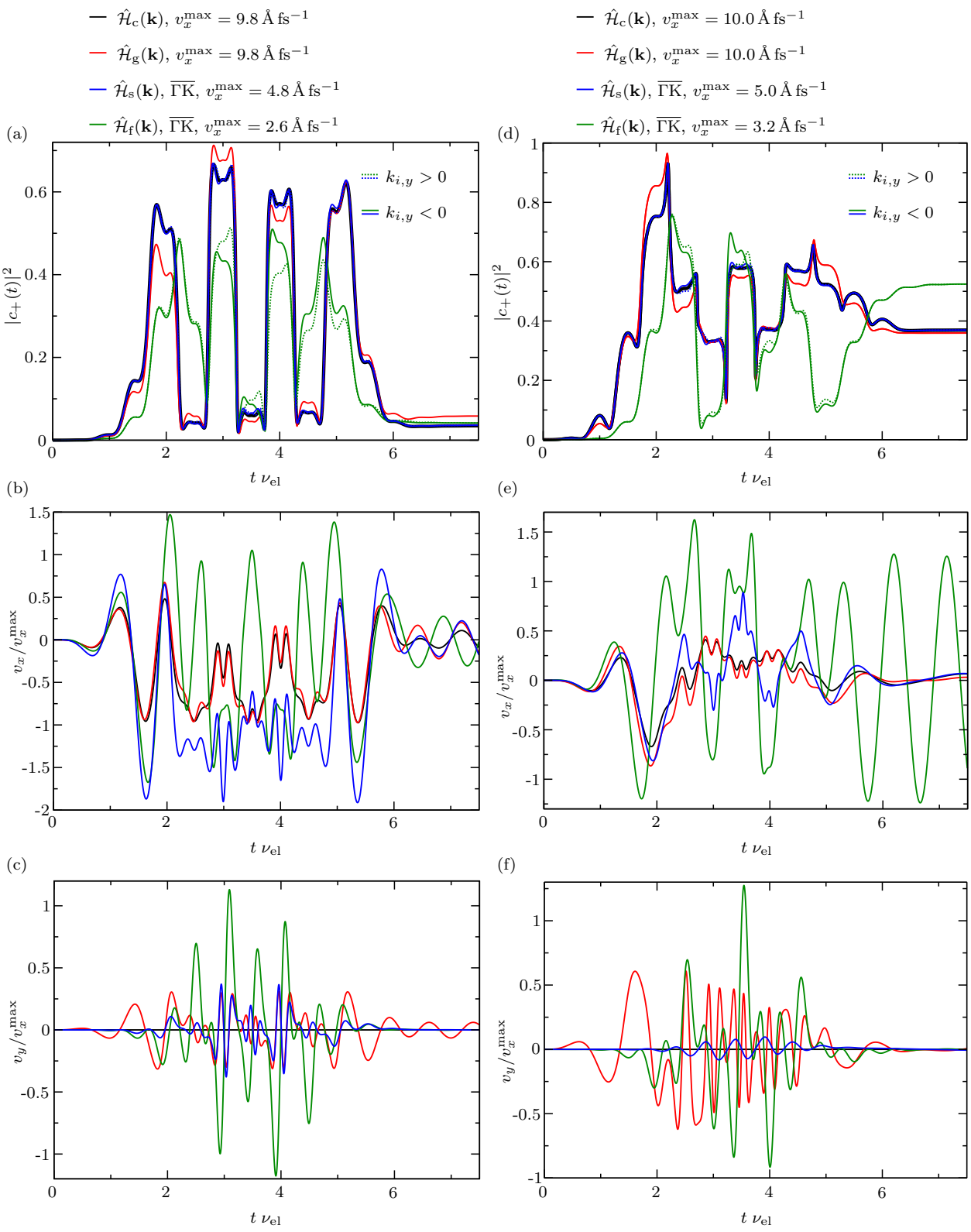

Fig. 5.9: Conduction band occupations $|c_+(t)|^2$ and velocity expectation values for two symmetric test charges in the impulsive (left side) and adiabatic-impulsive (right side) Landau-Zener regime. Panel (b) and (e) show the velocity parallel to the driving field and (c) and (f) the velocity perpendicular to it. Both regimes are characterized by abrupt jumps in the occupation and the velocities have a complicated temporal profile. In the adiabatic-impulsive regime, an occupation builds up in the conduction band. For the Hamiltonians with warping, $\hat{\mathcal{H}}_{s/f}(\mathbf{k})$, the transitions for $\pm k_{i,y}$ differ and we show both here.

all systems and the cone $\hat{\mathcal{H}}_{\mathrm{c}}(\mathbf{k})$ and gapped cone $\hat{\mathcal{H}}_{\mathrm{g}}(\mathbf{k})$ show similar results. Noticeably, for all systems except the fitted Hamiltonian $\hat{\mathcal{H}}_{\mathrm{f}}(\mathbf{k})$, v_x does not oscillate around zero but is negative during the central three oscillation cycles of the pulse. This is caused by the jumps of the occupation between valence and conduction band in combination with the intraband motion from positive to negative momentum. When these two processes are timed as for the test charges considered here, they result in a constant sign of the parallel velocity. For $\hat{\mathcal{H}}_{\mathrm{f}}(\mathbf{k})$ however the interband velocity is dominant, as already discussed for the resonant and nonimpulsive Landau-Zener regime. Therefore, its parallel velocity still oscillates around zero. For the other systems, the interband velocity mainly appears as high-frequency oscillations on top of the intraband velocity. As for the other regimes, v_y only contains the interband velocities and reflects the geometrical properties of the model systems. However, especially for $\hat{\mathcal{H}}_{\mathrm{g}}(\mathbf{k})$ and $\hat{\mathcal{H}}_{\mathrm{s}}(\mathbf{k})$ the encoded frequencies are not easily visible anymore and both velocities appear rather similar. In Sec. 5.5.2 we study the corresponding HH spectra of both velocity components for deeper insights.

The adiabatic-impulsive Landau-Zener regime is also characterized by jumps of the occupation instead of smooth transitions. However, according to Heide et al. [173] a Stückelberg phase modifies the repeated transitions such that each jump has a different final value and an occupation builds up in the conduction band. They claim that this regime is best realized for $P_{\mathrm{LZ}} \approx 0.5$ since then the state is distributed equally over both bands after the first transition and interference is strongest. However, there are no strict boundaries separating the regimes. In Fig. 5.9(d) we show occupations with the characteristic behavior obtained for test charges with $\mathbf{k}_i = (0, \pm 0.007)\text{Å}^{-1}$ for $\hat{\mathcal{H}}_{\mathrm{c/g/s}}(\mathbf{k})$ and $\mathbf{k}_i = (0, \pm 0.09)\text{Å}^{-1}$ for $\hat{\mathcal{H}}_{\mathrm{f}}(\mathbf{k})$. These parameters correspond to the transition probabilities $P_{\mathrm{LZ}} \approx 0.95$ for $\hat{\mathcal{H}}_{\mathrm{c/s}}(\mathbf{k})$, $P_{\mathrm{LZ}} \approx 0.92$ for $\hat{\mathcal{H}}_{\mathrm{g}}(\mathbf{k})$ and $P_{\mathrm{LZ}} \approx 0.21$ for $\hat{\mathcal{H}}_{\mathrm{f}}(\mathbf{k})$. Again, the latter is a bad approximation since the first Landau-Zener transition reaches $|c_+(t)|^2 \approx 0.75$. As in the impulsive Landau-Zener regime, for the models with warping, especially $\hat{\mathcal{H}}_{\mathrm{f}}(\mathbf{k})$, the occupations $|c_+(t)|^2$ are not equal for the two test charges. Note also that for all systems $\mathbf{k}_i$ is close to the resonance conditions, see Sec. 5.4.2 for comparison, and the test charges cross points with $\Delta E(\mathbf{k}) \approx h\nu_{\mathrm{el}}$ when moving through momentum space. This implies that one can also interpret the adiabatic-impulsive Landau-Zener regime as an interplay of Landau-Zener transitions and resonant transitions. In Fig. 5.9(e) and (f) we show the corresponding velocities. Due to the occupation build-up in the conduction band, one would expect Zitterbewegung for all systems in v_x and for $\hat{\mathcal{H}}_{\mathrm{g}}(\mathbf{k})$ in v_y. However, it is only clearly visible for $\hat{\mathcal{H}}_{\mathrm{f}}(\mathbf{k})$. We suspect that a spatial separation of the

wave-packet parts in the other systems causes the absence of Zitterbewegung after the pulse there but this remains to be verified. Besides that, v_x exhibits a similar complexity as in the impulsive Landau-Zener regime for all model systems. For the warped Hamiltonian $\hat{\mathcal{H}}_{\mathrm{s}}(\mathbf{k})$, the perpendicular velocity v_y is again dominated by the frequency induced by the Berry curvature, compare Sec. 5.4.1. We do not know why this is the case. For the fitted Hamiltonian $\hat{\mathcal{H}}_{\mathrm{f}}(\mathbf{k})$, v_y has a similar temporal shape as in the impulsive Landau-Zener regime, whereas for the gapped Hamiltonian $\hat{\mathcal{H}}_{\mathrm{g}}(\mathbf{k})$, v_y appears to be dominated by Zitterbewegung after $t \approx 2.5\nu_{\mathrm{el}}$, as indicated by the decaying amplitude. The decay to approximately zero also supports our suspicion that the missing Zitterbewegung after the pulse is due to a spatial separation of the wave-packet parts.

5.4.4. Summary

In summary, the results presented within this section confirm that all transition regimes determined by Heide et al. [173] can be realized in the effective Dirac models introduced in Sec. 5.2. One only has to tune the initial momenta $\mathbf{k}_i$ of the propagated wave packets and the field strength E_{el} of the applied electric pulse (5.10) accordingly.

In the adiabatic regime, no transitions occur and the velocities can be described semiclassically using Eq. (5.7). In all other regimes, transitions become important and the semiclassical approximation is not valid anymore. The resonant regime is characterized by remnant occupations after the pulse and Rabi-like oscillations of the band occupation, whereas in the nonimpulsive Landau-Zener regime the population of the conduction band changes smoothly, has a symmetric time profile around the pulse center, and returns to zero after the pulse. In all of these regimes the Berry curvature of the underlying model system leaves clear fingerprints on the perpendicular velocity v_y. This results in $v_y = 0$ at all times t for the simple Dirac cone $\hat{\mathcal{H}}_{\mathrm{c}}(\mathbf{k})$, v_y oscillating with the pulse frequency ν_{el} for the gapped Dirac cone $\hat{\mathcal{H}}_{\mathrm{g}}(\mathbf{k})$, and a frequency doubling in v_y for the Hamiltonians $\hat{\mathcal{H}}_{\mathrm{s,f}}(\mathbf{k})$ with hexagonal warping. The parallel velocity v_x on the other hand is dominated by the driving frequency ν_{el} in these regimes for all model systems.

In the impulsive and adiabatic-impulsive Landau-Zener regime, the transition time τ_{t} is much shorter than an optical cycle, i.e. $\tau_{\mathrm{t}} < 1/\nu_{\mathrm{el}}$. This results in jumps in the population instead of smooth transitions. In the impulsive regime,

all jumps have similar height and the occupation of the conduction band almost returns to zero after the pulse. In the adiabatic-impulsive regime, however, the Stückelberg phase leads to all jumps being different and a remnant occupation of the conduction band after the pulse. The dynamics are strongly nonlinear in both regimes, therefore the characteristics in the velocities are less clear then before and require further analysis in frequency space, see Sec. 5.5.

For all regimes, as long as the different wave-packet parts still overlap in real space, Zitterbewegung can be observed whenever an occupation remains in the conduction band after the pulse. This Zitterbewegung appears in v_x for all model systems and in v_y for the gapped cone $\hat{\mathcal{H}}_{\mathrm{g}}(\mathbf{k})$ only, as explained in Sec. 5.2.

5.5. High-harmonic generation

We discuss different transition regimes and the corresponding velocity expectation values for two symmetric test charges in Sec. 5.4. For the results with low driving field strength $E_{\mathrm{el}} = 0.1\,\mathrm{MV\,cm^{-1}}$ the main frequency of both the velocity v_x parallel to the driving field and v_y perpendicular to it are visible to the naked eye. For the higher field strength $E_{\mathrm{el}} = 1\,\mathrm{MV\,cm^{-1}}$ this is not as easy anymore. In order to verify our observations for the low field strength and to gain more insights into the high-field-strength dynamics we study the corresponding HHs spectra in the following. In Sec. 2.3.3 we discuss how the HHs spectra are related to the velocity based on Lamor's formula and in App. A.9 we show the technical details of our evaluation.

5.5.1. Influence of the Berry curvature

For the transition regimes realized with $E_{\mathrm{el}} = 0.1\,\mathrm{MV\,cm^{-1}}$ we found that the parallel velocity is dominated by the driving frequency ν_{el} whereas the perpendicular velocity's main frequency depends on the underlying model system. When its Berry curvature is zero as for the Dirac cone $\hat{\mathcal{H}}_{\mathrm{c}}(\mathbf{k})$, the total velocity v_y of the two test charges is also zero as there is no anomalous velocity. For the gapped cone $\hat{\mathcal{H}}_{\mathrm{g}}(\mathbf{k})$ the Berry curvature has a constant sign and the velocity v_y is non-zero and oscillates with the driving frequency ν_{el}. Introducing the hexagonal warping as in the surface Hamiltonian $\hat{\mathcal{H}}_{\mathrm{s}}(\mathbf{k})$ and

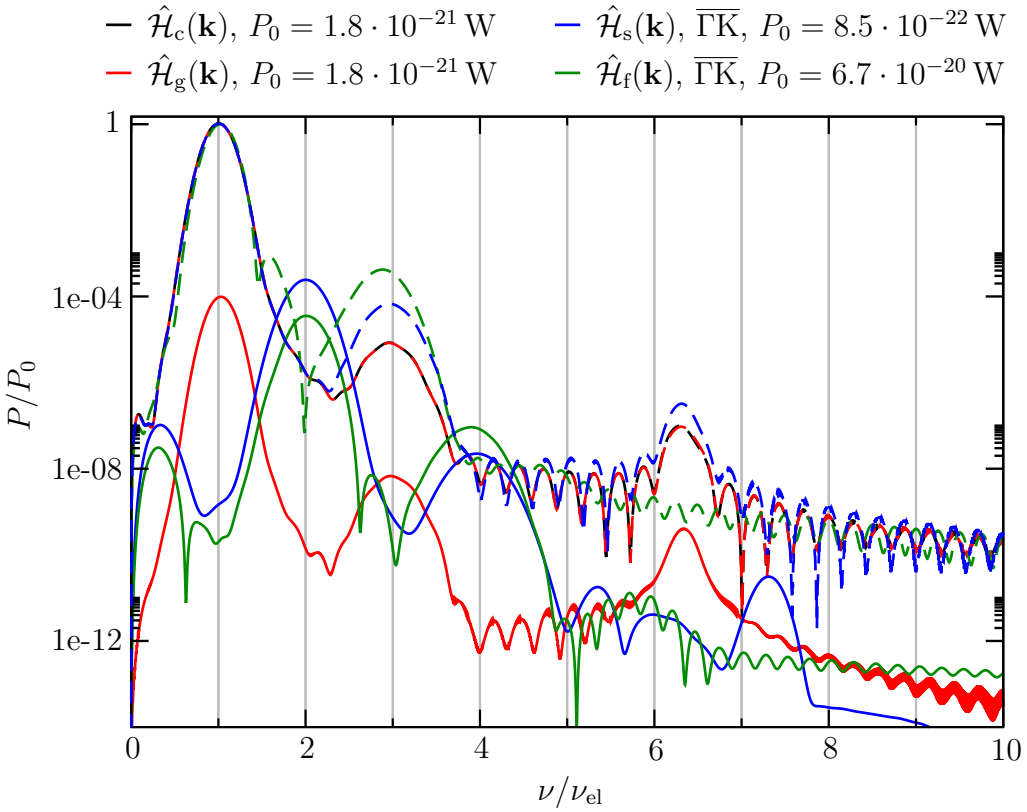

Fig. 5.10: HHs spectrum of the test charges in the adiabatic regime. The respective velocities are plotted in Fig. 5.6. To distinguish parallel and orthogonal emission, we dashed the spectra belonging to v_x. As predicted, the orthogonal emission P_y is zero for the Dirac cone $\hat{\mathcal{H}}_c(\mathbf{k})$, at odd orders for the gapped cone $\hat{\mathcal{H}}_g(\mathbf{k})$, and shifts to even orders for the Hamiltonians with hexagonal warping $\hat{\mathcal{H}}_{s/f}(\mathbf{k})$. Note that the orthogonal spectrum of $\hat{\mathcal{H}}_c(\mathbf{k})$ is not shown since it is below the scale of the plot. We normalized the power P with $P_0 = P_x(\nu_{el})$ for each system.

the fitted Hamiltonian $\hat{\mathcal{H}}_f(\mathbf{k})$ for the Bi_2Te_3 surface states comes along with a Berry curvature with threefold symmetry and alternating sign along the $\overline{\Gamma K}$ direction of the crystal. As discussed in Sec. 5.4.1, this sign change leads to a frequency doubling of v_y.

In Fig. 5.10 we exemplarily show the HHs spectra of the test charges in the adiabatic regime, see Fig. 5.6 for the corresponding velocities. The dashed lines are the curves for parallel emission $P_x(\nu)$, the solid lines represent the perpendicular component $P_y(\omega)$. For better comparability we renormalize all spectra with the first peak of the parallel component, $P_0 = P_x(\nu_{el})$. Then, the first peaks of all systems fall on top of each other. The efficiency of the emission of the third harmonic with parallel polarization is already system dependent[17] and highest for the fitted Hamiltonian $\hat{\mathcal{H}}_f(\mathbf{k})$, hinting a stronger nonlinearity of the bands in this system. After the third peak, the spectra reach their noise level. In the parallel spectra of $\hat{\mathcal{H}}_{c/g/s}(\mathbf{k})$ we find another peak around $\nu \approx 6.3\nu_{el}$. It is the resonance peak of the test charges at their

[17] Note that for $\hat{\mathcal{H}}_c(\mathbf{k})$ and $\hat{\mathcal{H}}_g(\mathbf{k})$ the parallel spectra are completely equal, just as the corresponding velocities.

initial momentum $\mathbf{k}_i = (0, \pm 0.1)\text{Å}^{-1}$, since $\Delta E(\mathbf{k}_i) \approx 6.3 h\nu_{\text{el}}$. Excluding this peak, we can conclude that in the adiabatic regime we observe only odd HH orders in the parallel component. The perpendicular spectra $P_y(\omega)$ on the other hand depend on the geometric properties of the model Hamiltonians, as already predicted from the corresponding velocities in Sec. 5.4.1. For the Dirac cone $\hat{\mathcal{H}}_{\text{c}}(\mathbf{k})$ no perpendicular emission is observed, its power $P/P_0 \approx 9 \cdot 10^{-22}$ is below the scale of our plot. For $\hat{\mathcal{H}}_{\text{g}}(\mathbf{k})$ the peaks are the same as for the parallel component but with lower amplitude. Only for the systems with hexagonal warping, i.e. $\hat{\mathcal{H}}_{\text{s}}(\mathbf{k})$ and $\hat{\mathcal{H}}_{\text{f}}(\mathbf{k})$, the peaks are shifted to even orders and of higher amplitude than the parallel spectrum at these frequencies. For $\hat{\mathcal{H}}_{\text{f}}(\mathbf{k})$ the noise level is reached after the fourth order even though a sixth order peak is indicated slightly. The spectrum of $\hat{\mathcal{H}}_{\text{s}}(\mathbf{k})$ appears to have a peak structure up to $\nu/\nu_{\text{el}} \approx 8$, however the origin of the peaks after the fourth harmonic are unclear to us.

In summary already in the adiabatic regime we find confirmation of the relation between Berry curvature and the polarization of the emitted harmonics. The spectra of the velocities for our test cases in the resonant and the nonimpulsive Landau-Zener regime contain the same qualitative features, only the relative amplitudes of the peaks shift depending on the regime and thus the initial momentum. We discuss them in App. A.6 for the sake of completeness.

5.5.2. Increasing the field strength

By increasing the field strength to $E_{\text{el}} = 1\,\text{MV}\,\text{cm}^{-1}$ we study the impulsive and adiabatic-impulsive Landau-Zener regime in Sec. 5.4.3. In Fig. 5.11 we show the corresponding HH emission. To distinguish emission parallel and perpendicular to the driving field, we dash the spectra of the parallel velocity v_x. In contrast to the low-field limit, we do not find clearly distinguished, single peaks for the first harmonics anymore. Therefore we normalize the spectra to the highest peak around $\nu/\nu_{\text{el}} \approx 1$ of the parallel spectrum, as indicated by the dots. For better visibility, we plot the spectra of the fitted Hamiltonian $\hat{\mathcal{H}}_{\text{f}}(\mathbf{k})$ separately, see Fig. 5.11(b) and (d).

Due to the higher field strength, in all settings the spectrum reaches its noise level at frequencies $\nu > 10\nu_{\text{el}}$. However, as indicated by the rich patterns of the velocity curves in Fig. 5.9, the spectra contain various frequencies and not all peaks can be related to multiples of the driving frequency ν_{el}. Additionally, we find that the emission depends not only on the Berry curvature but also on

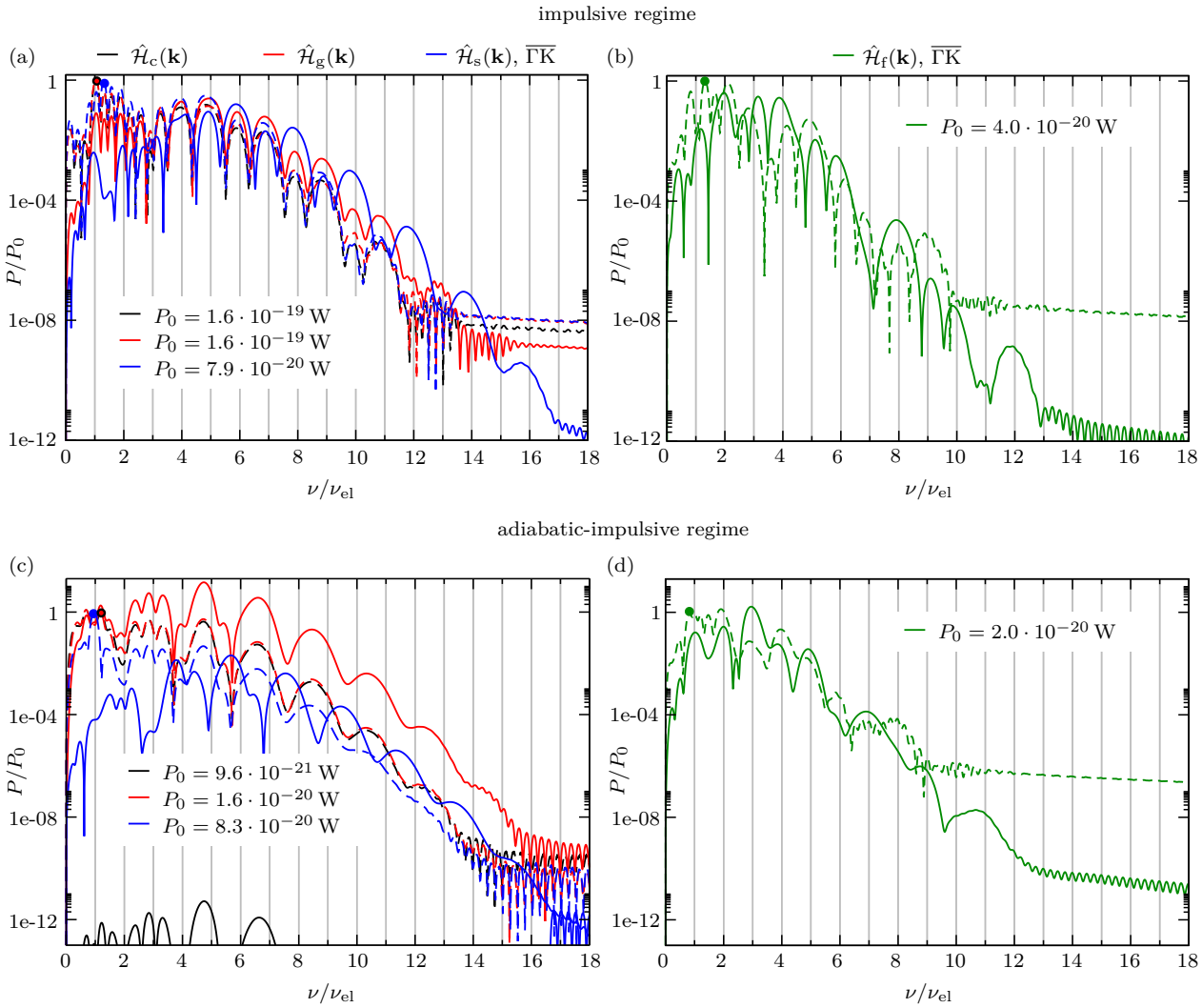

Fig. 5.11: HHs spectrum of two test charges in the (a), (b) impulsive and (c), (d) adiabatic-impulsive Landau-Zener regime. The respective velocities are plotted in Fig. 5.9. To distinguish parallel and orthogonal emission, we dashed the spectra belonging to v_x. The dots mark the peak from which we extracted the power P_0 for each system since at low frequencies the peaks are split. In the adiabatic-impulsive regime, panel (c), the parallel and orthogonal peaks of $\hat{\mathcal{H}}_{c/g/s}(\mathbf{k})$ are not located at integer values of ν/ν_{el}. The symmetry properties of the Berry curvature are not as clearly visible as in the low-field regimes, compare Fig. 5.10. Still, the orthogonal emission P_y is (approximately) zero for the Dirac cone $\hat{\mathcal{H}}_c(\mathbf{k})$ in both regimes and for the gapped cone $\hat{\mathcal{H}}_g(\mathbf{k})$ parallel and orthogonal component have almost the same peak structure only with shifted amplitudes. For the warped Hamiltonians $\hat{\mathcal{H}}_s(\mathbf{k})$ and $\hat{\mathcal{H}}_f(\mathbf{k})$ both components contain odd and even orders, but their intensity still alternates from parallel to orthogonal emission.

the energy scales of the model system. The parallel emission P_x of the cone $\hat{\mathcal{H}}_{\mathrm{c}}(\mathbf{k})$, the gapped cone $\hat{\mathcal{H}}_{\mathrm{g}}(\mathbf{k})$ and surface Hamiltonian $\hat{\mathcal{H}}_{\mathrm{s}}(\mathbf{k})$ is qualitatively the same, whereas the fitted Hamiltonian $\hat{\mathcal{H}}_{\mathrm{f}}(\mathbf{k})$ differs and reaches its noise level already for lower frequencies.

In the impulsive Landau-Zener regime, see panels (a) and (b), clear harmonic peaks emerge for frequencies $\nu \geq 4\nu_{\mathrm{el}}$ and we restrict the following discussion to the clean region. For all systems except the pure Dirac cone $\hat{\mathcal{H}}_{\mathrm{c}}(\mathbf{k})$, both parallel and orthogonal emission contain odd and even orders. The influence of the Berry curvature is not as dominant as in the low-field regime discussed in Sec. 5.5.1. Nevertheless, for the warped Hamiltonians $\hat{\mathcal{H}}_{\mathrm{s}}(\mathbf{k})$ and $\hat{\mathcal{H}}_{\mathrm{f}}(\mathbf{k})$ the peak of highest intensity switches from parallel to perpendicular component with odd and even orders, whereas for the gapped cone $\hat{\mathcal{H}}_{\mathrm{g}}(\mathbf{k})$ the perpendicular emission is always stronger than the parallel one. When comparing the orthogonal emission P_y of the gapped cone $\hat{\mathcal{H}}_{\mathrm{g}}(\mathbf{k})$ and the surface Hamiltonian $\hat{\mathcal{H}}_{\mathrm{s}}(\mathbf{k})$ one finds an alternating pattern just as in the low-field regime. By solely examining their time-dependent velocities $v_y(t)$ in Fig. 5.9(c), one might have expected that both contain the same frequencies. The alternating intensities of those frequencies only appear when analyzing the corresponding spectra.

In the adiabatic-impulsive Landau-Zener regime, see panels (c) and (d), the qualitative difference of the fitted Hamiltonian $\hat{\mathcal{H}}_{\mathrm{f}}(\mathbf{k})$ to the other three models is even more apparent. Here, the harmonic peaks lie at integer multiples of the driving frequency ν_{el} for the fitted Hamiltonian $\hat{\mathcal{H}}_{\mathrm{f}}(\mathbf{k})$ but are shifted to noninteger values for the models $\hat{\mathcal{H}}_{\mathrm{c/g/s}}(\mathbf{k})$. However, in contrast to the impulsive regime, the peaks of $\hat{\mathcal{H}}_{\mathrm{c/g/s}}(\mathbf{k})$ are separated by $2\nu_{\mathrm{el}}$ like in the low-field case. Only for the fitted Hamiltonian $\hat{\mathcal{H}}_{\mathrm{f}}(\mathbf{k})$ both components contain odd and even orders. For all models we can retrieve the characteristic pattern determined by the respective Berry curvature, namely no perpendicular emission for the Dirac cone $\hat{\mathcal{H}}_{\mathrm{c}}(\mathbf{k})$, perpendicular and parallel emission at the same frequencies for the gapped cone $\hat{\mathcal{H}}_{\mathrm{g}}(\mathbf{k})$ and alternating frequencies of perpendicular and parallel emission for the warped Hamiltonians $\hat{\mathcal{H}}_{\mathrm{s}}(\mathbf{k})$ and $\hat{\mathcal{H}}_{\mathrm{f}}(\mathbf{k})$. Especially for $\hat{\mathcal{H}}_{\mathrm{c/g/s}}(\mathbf{k})$ this pattern is more dominant in the adiabatic-impulsive Landau-Zener regime than for the impulsive Landau-Zener regime. Besides the shift of the peaks to noninteger multiples of ν_{el} and the noisy structure for $\nu \lesssim 4\nu_{\mathrm{el}}$, the Berry curvature features are as clear as in the low-field regime, see Fig. 5.10 for comparison.

5.5.3. Conclusion

In this section we have explored how the HHs spectra of two test charges change depending on the underlying model system and the dominating transition regime. The latter is determined by the applied pulse and the dispersion seen by the test charges, which again depends on the initial momentum $\mathbf{k}_i$ of the states. Even though the results vary for the different test cases, we found imprints of the Berry curvature on the emitted harmonics with polarization perpendicular to the driving field in all of them. In order to achieve an alternating polarization between odd and even orders, as observed experimentally for the Bi_2Te_3 surface [81], including the hexagonal warping term is crucial. The fitted Hamiltonian $\hat{\mathcal{H}}_\mathrm{f}(\mathbf{k})$ used for the description of the experiment in [81] gives different results than the simpler surface Hamiltonian $\hat{\mathcal{H}}_\mathrm{s}(\mathbf{k})$ proposed in other literature [87, 88] regarding the onset of the noise level and thus the last resolved HH peak as well as the relative amplitude of odd and even order harmonics. These differences can be attributed to the stronger warping in the fitted Hamiltonian $\hat{\mathcal{H}}_\mathrm{f}(\mathbf{k})$ as well as the smaller energy difference $\Delta E(\mathbf{k})$ between its bands, compare Figs. 5.2 and 2.4. Nevertheless, the simpler surface model $\hat{\mathcal{H}}_\mathrm{s}(\mathbf{k})$ is sufficient to capture the relevant qualitative features.

In the low-field regime discussed in Sec. 5.5.1, only a few harmonic orders emerge but the spectra are clean. In the high-field regime in Sec. 5.5.2 on the other hand, a larger frequency range is covered but the initial momentum $\mathbf{k}_i$ plays a distinctive role in the quality of the spectrum. In a real system like the Bi_2Te_3 surface, however, the emission is not determined by single test charges but a Fermi sea that covers a large area of momentum space. Hence, also various transition regimes enter the actual spectrum. In order to capture the dynamics of a Fermi sea, we developed a new method based on wave packets that are large in momentum space compared to the narrow ones used as test charges in this chapter. We introduce this method in Chap. 6.

6. Wave-packet approach for high-harmonic generation from a Fermi sea

6.1. Motivation

For the theoretical investigation of HHG in atoms, molecules, and solids, various models have been developed in the last decades. In the following, we focus on the research concerning solids. An overview of this field is given in the review articles [93, 94]. The most commonly used numerical methods are the semiconductor Bloch equations [95], time-dependent DFT [96, 97] and methods based on solving the time-dependent Schrödinger equation [98].

In this work, we aim at a deeper physical understanding of the quantum processes involved in HHG in TI surface states. Therefore, we want to employ a method that captures the relevant physics while being based on a minimal model and as illustrative as possible. In Chap. 5 we have already shown that we can compute the velocity and emitted spectrum of single test charges in laser-driven systems by simulating their time evolution with TQT. Ultimately, this is a numerical method for solving the time-dependent Schrödinger equation that is applicable to continuum Hamiltonians in mixed position- and momentum-space representation. In the literature, typically lattice-periodic Hamiltonians are employed as models and the initial states can be expressed in the Bloch basis[1]. Then, the Schrödinger equation is solved in position space only. Physical observables are either obtained by integrating over the full BZ [98, 103–105] or within the single-active-electron approximation [99–101]. The limitations of this approximation are investigated in Ref. [102]. The authors compare HHs spectra obtained from solving the semiconductor Bloch equations for a 1D model system with those from the

[1] An overview of different bases and the corresponding equations of motion can be found in the tutorial [172].

time-dependent Schrödinger equation in single-active-electron approximation. They find that for a single electron the spectra contain both odd and even orders, as well as noninteger harmonics, whereas only the odd orders survive interference effects when including all occupied states in the calculation. Our approach in Chap. 5 is comparable to the single-active-electron approximation. The differences are that we add the observables of two symmetric test charges and explore different cuts through momentum space instead of only the point of minimal band gap. Nevertheless, the resulting spectra show similar features as described in Ref. [102]. Since in experiments the laser pulse inevitably drives all electrons located within the range of its spot size and penetration depth of the illuminated crystal, the measured signal is the total of all generated radiation. Thus, including all initially occupied states when calculating observables is more realistic than the single-active-electron approximation.

In order to improve our results, we have to modify our method from Chap. 5 such that it represents a completely filled band. Still, we keep using the effective Hamiltonian (2.21) to describe the TI surface states. As shown in the experiment in Ref. [81], the bulk bands do not contribute to the HH emission for frequencies below the bulk band gap. In Chap. 5 we have thoroughly compared the surface Hamiltonian $\hat{\mathcal{H}}_\mathrm{s}(\mathbf{k})$ from Eq. (2.21) to the fitted Hamiltonian $\hat{\mathcal{H}}_\mathrm{f}(\mathbf{k})$, see Eq. (5.1), originally introduced in Ref. [81], and found quantitative differences. Nevertheless, we confirmed that due to having the same symmetries, both Hamiltonians show the same qualitative features in their HHs spectra. Since the fitted Hamiltonian only works on a limited momentum window in TQT and is numerically more expensive, see App. A.4, we restrict our studies of the Bi_2Te_3 surface to the literature model $\hat{\mathcal{H}}_\mathrm{s}(\mathbf{k})$ from now on. We include the laser pulse in the length gauge (2.55) and compute the time evolution of states by solving the time-dependent Schrödinger equation in TQT. Its advantages compared to time-dependent DFT are that it is computationally less expensive and the results are easier to interpret intuitively. The semiconductor Bloch equations, on the other hand, have already been applied to TI surface states and general Dirac materials [81, 107, 108]. The method we introduce in the following allows for a different perspective on the processes leading to HHG. Additionally, in contrast to the semiconductor Bloch equations from the cited studies, in TQT we can include potentials in position space[2] even though the system's Hamiltonian is defined in momentum space. This offers the possibility of going beyond the dipole approximation of the light field and including orbital magnetic field effects, as we discuss in more detail in Chap. 7. In future research one could also think

[2]Note that in the last years an approach has been developed that treats the semiconductor Bloch equations in the Wannier basis [241]. Using this basis, including real-space potentials is not an issue anymore.

about applying structured light [242] instead of a Gaussian laser beam.

6.2. Introduction of methodology

In order to improve our model from Chap. 5, we construct our initial wave packets such that their propagation serves for computing observables that are equivalent to those of a Fermi sea. As exploited in TKWANT for transport calculations [187] and more formally demonstrated in App. A.7, in non-interacting systems with unitary time evolution including Pauli blocking into the calculation of observables does not require propagating the anti-symmetric many-particle wave function. It is sufficient to compute the time evolution of all initially occupied states like for single particles[3]. In a non-interacting framework, all single-particle states lying within the same band can be combined into one wave packet and thus are propagated simultaneously. When calculating observables described by operators that are not diagonal in the eigenbasis of the Hamiltonian, such as the velocity operator, see Sec. 2.3, this separate treatment of wave packets initialized in the conduction and valence band is important. Otherwise, the off-diagonal entries of the operator would lead to unphysical interference between two distinct single-particle wave functions. For the velocity operator, including states from several bands in the initial wave packet would lead to spurious interband velocities, compare Eq. (2.58).

We focus on a two-band system here but adapting the presented formalism to more-band systems is trivial. To describe the full Fermi sea dynamics we need a maximum of two wave packets $\Psi_\pm(\mathbf{k}, t)$, where $\pm$ labels the band index of the states at initial time $t = 0$, "+" meaning the conduction and "−" the valence band, see the sketch in Fig. 6.1(a). The initial wave packets $\Psi_\pm(\mathbf{k}, 0)$ are defined in momentum space and can be written as

$$\Psi_\pm(\mathbf{k}, 0) = \frac{1}{\sqrt{N}}\, g_\pm(\mathbf{k})\varphi_\pm(\mathbf{k}), \tag{6.1}$$

where $\varphi_\pm(\mathbf{k})$ is the spinor defining the eigenstates of the Hamiltonian $\hat{\mathcal{H}}(\mathbf{k}, t = 0)$ and $g_\pm(\mathbf{k})$ is a band- and $\mathbf{k}$-dependent envelope function specified in more detail later. The factor $\frac{1}{\sqrt{N}}$ ensures normalization of the total wave packet

[3]Note that for undriven systems one finds that only the states close to the Fermi surface contribute to observables. Since we consider systems under strong driving here, also states below the Fermi surface are important.

$\Psi_\pm(\mathbf{k},0)$ such that

$$1 = \int \mathrm{d}\mathbf{k}\ \Psi_\pm^*(\mathbf{k},0)\ \Psi_\pm(\mathbf{k},0). \tag{6.2}$$

This normalization implies that the contribution of single $\mathbf{k}$ modes to an observable scales with the size of the wave packet in momentum space. One should be aware of this scaling when comparing data of differently sized wave packets and compensate for it if necessary, as demonstrated in Sec. 6.7 for the computation of HHG for different Fermi energies.

The Fermi energy E_F and the temperature T of the initially equilibrated system set a natural upper bound for the wave packets in energy and therefore also in momentum. At zero temperature, the highest occupied states lie at the Fermi energy E_F. If the Fermi energy E_F is in the valence band or between the bands, $g_+(\mathbf{k}) = 0$ for all $\mathbf{k}$ and $g_-(\mathbf{k}) = 0$ for $E_-(\mathbf{k}) > E_\mathrm{F}$. If E_F lies in the conduction band, $g_+(\mathbf{k}) = 0$ for $E_+(\mathbf{k}) > E_\mathrm{F}$ and $g_-(\mathbf{k}) = 1$ for all $\mathbf{k}$ in principle. For finite temperature, a drop off modulated by the Fermi-Dirac distribution

$$g_\pm(\mathbf{k}) = \frac{1}{1 + \mathrm{e}^{-[E_\mathrm{F} - E_\pm(\mathbf{k})]/(k_\mathrm{B}T)}}, \tag{6.3}$$

with the Boltzmann constant k_B, is introduced. Here, $\pm$ is the band the Fermi energy lies in. A more detailed description as well as an analysis of the influence of the Fermi energy on the emitted HHs is given in Sec. 6.7.

Since we consider effective model Hamiltonians, no band bottom or BZ boundary exists. In our models, the bands extend to infinity in momentum and thus the wave packet in the conduction band would be infinitely large. In the numerical simulations however, the momentum grid is limited to a finite number of points. Additionally, the effective model is only a valid approximation of a physical system within a certain energy window. Therefore, we have to find a lower bound for the initial wave packet $\Psi_-(\mathbf{k},0)$ in the conduction band. To establish this lower bound, we have to determine which states actually contribute to the desired observable. If this range is not within the range of validity of the effective model, another description of the system has to be considered.

For HH generation, applying a strong electric field pulse $\mathbf{E}_\mathrm{el}(t)$ is necessary. It moves the states through momentum space and causes transitions between the bands. In this way, states initially below the Fermi surface can also contribute to observables, such as the total velocity, during propagation. In Sec. 2.4 we summarized different types of transition mechanisms focusing on those occurring at avoided crossings of the bandstructure. For a filled band however, the situation is more complicated since not all states pass an avoided crossing

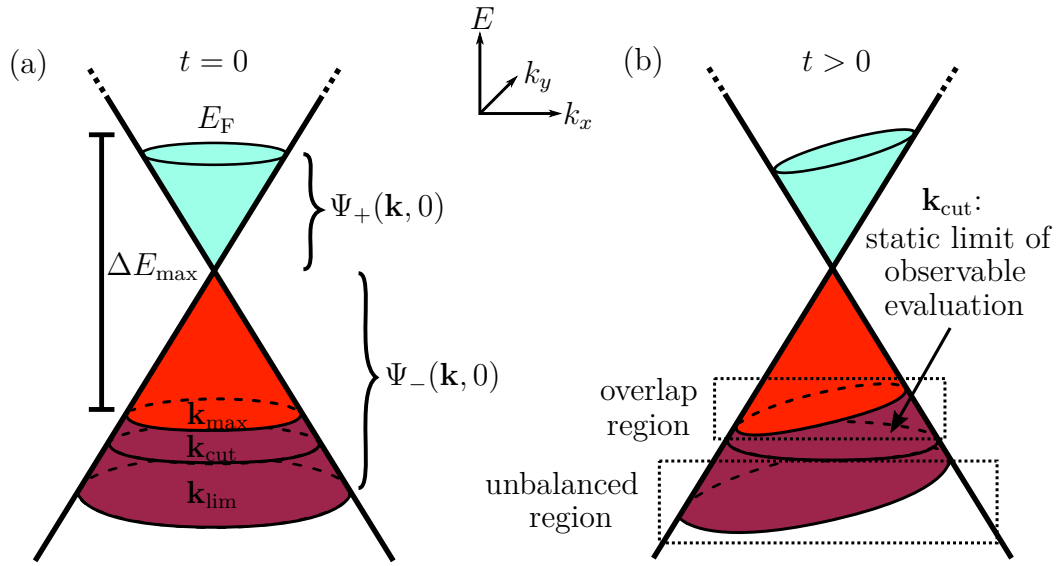

Fig. 6.1: Sketch of the wave packets constituting a Fermi sea at $T = 0\,\mathrm{K}$ and E_F in the conduction band. (a) Wave packets at $t = 0$. The conduction band is filled up to the Fermi energy E_F and described by the initial wave packet $\Psi_+(\mathbf{k}, 0)$. The wave packet $\Psi_-(\mathbf{k}, 0)$ initialized in the valence band is limited by the momenta $\mathbf{k}_\mathrm{lim}$. The light red area limited by the momenta $\mathbf{k}_\mathrm{max}$ and the energy difference ΔE_max marks the region where transitions can be driven by the laser pulse. Observables have to be evaluated up to the static boundary set by the momenta $\mathbf{k}_\mathrm{cut}$. (b) Wave packets during the propagation, neglecting transitions. The applied electric field shifts the states in momentum space, changing the bounds of the wave packets and creating an overlap region between states initially above and below $\mathbf{k}_\mathrm{max}$. To account for this overlap while simulating a filled valence band, observables have to be evaluated up to $\mathbf{k}_\mathrm{cut}$. It is chosen such that all states above $\mathbf{k}_\mathrm{cut}$ are always covered by the wave packet. States lying below $\mathbf{k}_\mathrm{cut}$ must not contribute to the total observables since a balanced occupation is not guaranteed.

during their propagation. As studied by Mario Ebner in his master's thesis under our supervision [163], the transition probability in a two-band system under the influence of an electric field is proportional to the scalar product of the electric field $\mathbf{E}_\mathrm{el}(t)$ and the transition matrix element $\boldsymbol{\mathcal{A}}_{+-}(\mathbf{k}(t))$, but also influenced by the phases acquired by the state before undergoing the transition. Accordingly, the details of the transition processes are system dependent. In Sec. 6.3 we analyze how to determine the lower bound of the wave packet based on the momentum-dependent transitions when computing HHG in the Bi_2Te_3 surface states (2.21). For now, let us just state that there exists a momentum area limited by $\mathbf{k}_\mathrm{max}$, that is defined by an energy difference $\Delta E_\mathrm{max} = E_+(\mathbf{k}_\mathrm{max}) - E_-(\mathbf{k}_\mathrm{max})$ between valence and conduction band, in which the relevant transitions take place.

To establish the lower bound of $\Psi_-(\mathbf{k}, 0)$ we also have to take the field-induced motion through momentum space into account, see Eq. (2.56). In Fig. 6.1(b) the wave packet movement neglecting transitions is depicted schematically to illustrate the significance of the different $\mathbf{k}$ boundaries introduced in the

following. The electric field shifts the states through momentum space such that at times $t > 0$ states initially defined by $\mathbf{k}_{\max}$ move to lower energies and states initially below $\mathbf{k}_{\max}$ enter the region with relevant transition probabilities. To account for this overlap region, the wave packet has to be extended in momentum. The corresponding cut-off momenta $\mathbf{k}_{\text{cut}}$ should be chosen such that they fulfill

$$|\mathbf{k}_{\text{cut}}| \geq \left|\mathbf{k}_{\max} - \frac{e}{\hbar}\int_0^t \mathbf{E}_{\text{el}}(t')\mathrm{d}t'\right| \tag{6.4}$$

at all times t, where we require that $\mathbf{k}_{\max}$ and $\mathbf{k}_{\text{cut}}$ point in the same direction[4], i.e. $\mathbf{k}_{\max} \parallel \mathbf{k}_{\text{cut}}$. In Sec. 6.3 we investigate how to appropriately set the limits $\mathbf{k}_{\text{cut}}$ taking into account that they also determine the region in which observables have to be evaluated, as will be discussed in more detail later.

To set the actual lower bound of the wave packet, we additionally have to account for the unbalanced region, also illustrated in Fig. 6.1(b). If one would take a wave packet that just ends at the momenta $\mathbf{k}_{\text{cut}}$ at inital time $t = 0$, later during propagation $|\Psi_-(\mathbf{k}_{\text{cut}}, t)|^2 = 0$ due to the momentum shift. Hence, the wave packet $\Psi_-(\mathbf{k}, 0)$ has to be extended to momenta $\mathbf{k}_{\text{lim}}$ such that $|\Psi_-(\mathbf{k}_{\text{cut}}, t)|^2 = |\Psi_-(\mathbf{k}_{\text{cut}}, 0)|^2 > 0$ for all t included in the propagation[5]. Accordingly, $\mathbf{k}_{\text{lim}}$ is defined similar to $\mathbf{k}_{\text{cut}}$ in Eq. (6.4), requiring

$$|\mathbf{k}_{\text{cut}}| < \left|\mathbf{k}_{\text{lim}} - \frac{e}{\hbar}\int_0^t \mathbf{E}_{\text{el}}(t')\mathrm{d}t'\right| \tag{6.5}$$

at all times t, for the momenta $\mathbf{k}_{\text{lim}}$ and $\mathbf{k}_{\text{cut}}$ pointing in the same direction. For simplicity, in practice we choose the $\mathbf{k}_{\text{lim}}$ such that they are all of the same length $|\mathbf{k}_{\text{lim}}|$. Then, the lower bound of the wave packet can be defined by a Gaussian decay,

$$g_-(\mathbf{k}) = \exp\left[-\frac{\left(|\mathbf{k}| - |\mathbf{k}_{\text{lim}}|\right)^2}{2\Delta k^2}\right], \text{ for } |\mathbf{k}| \geq |\mathbf{k}_{\text{lim}}|, \tag{6.6}$$

where the width Δk is chosen such that the decay is fast but numerically smooth.

As already discussed, for states outside of the bound defined by the momenta $\mathbf{k}_{\text{cut}}$ a balanced occupation is not guaranteed throughout propagation. This can lead to spurious contributions when calculating observables over the full

[4]Note that in systems without rotational symmetric bands, such as e.g. the Bi_2Te_3 surface states with warping (2.21), $|\mathbf{k}_{\text{cut}}|$ becomes angle-dependent.

[5]Remember that the "$-$" in the index marks the initial band of $\Psi_-(\mathbf{k}_{\text{cut}}, t)$. Due to transitions, at $t > 0$ the state can have non-zero amplitudes in both bands but its total amplitude squared over both bands has to be conserved in a filled band.

wave packet. To avoid artificial effects due to the limitation of the wave packet at low energies, observables are only evaluated for the wave-packet parts within the momentum area limited by the momenta $\mathbf{k}_{\mathrm{cut}}$. In this work, the relevant observable is the velocity. For the wave packets $\Psi_{\pm}(\mathbf{k},t)$ it is obtained by

$$\mathbf{v}_{\pm}(t) = \int \Psi_{\pm}^{*}(\mathbf{k},t)\ \hat{\mathbf{v}}_{\mathbf{k}}(t)\ \Psi_{\pm}(\mathbf{k},t)\ \mathrm{d}\mathbf{k}, \tag{6.7}$$

the velocity operator taking the form $\hat{\mathbf{v}}_{\mathbf{k}}(t) = \frac{1}{\hbar}\nabla_{\mathbf{k}}\hat{\mathcal{H}}(\mathbf{k},t)$ in $\mathbf{k}$ space, compare Eq. (2.46). During the propagation, transitions may occur and $\Psi_{\pm}(\mathbf{k},t)$ is not consisting of pure conduction or valence band eigenstates anymore. Thus, computing the velocity via Eq. (6.7) includes both diagonal and off-diagonal velocity contributions. The wave packets $\Psi_{\pm}(\mathbf{k},t)$ are not coupled since they describe a collection of non-interacting single-particle states. Hence, their velocities have to be computed separately to avoid unphysical interference terms between different particles. As discussed before, we have to introduce a cut off at $\mathbf{k}_{\mathrm{cut}}$ in $\mathbf{v}_{-}(t)$ to obtain the velocity for a filled band, i.e.

$$\mathbf{v}_{-}^{\mathrm{cut}}(t) = \int f(\mathbf{k})\ \Psi_{-}^{*}(\mathbf{k},t)\ \hat{\mathbf{v}}_{\mathbf{k}}(t)\ \Psi_{-}(\mathbf{k},t)\ \mathrm{d}\mathbf{k}, \tag{6.8}$$

where $f(\mathbf{k})$ is a function defining the described cut off. We call this function *k-mask* from now on. The total velocity of the Fermi sea is then given by $\mathbf{v}(t) = \mathbf{v}_{+}(t) + \mathbf{v}_{-}^{\mathrm{cut}}(t)$. Note that we implemented both $\mathbf{v}_{\pm}(t)$ and $\mathbf{v}_{-}^{\mathrm{cut}}(t)$ as an observable in TQT, see Sec. 3.5.

There exist various options for defining the k-mask $f(\mathbf{k})$ in line with the condition (6.4) for the cut-off momenta $\mathbf{k}_{\mathrm{cut}}$. As we show in Sec. 6.3, choosing the momenta $\mathbf{k}_{\mathrm{cut}}$ is not equivalent to fully converging the velocity expectation value $\mathbf{v}_{-}^{\mathrm{cut}}(t)$. Instead, it means to determine reasonable, physical criteria that decide which states contribute to the HHG process and which states can be neglected. For approaches based on the semiconductor Bloch equations, a similar effect is achieved by including finite intra- and interband dephasing times. Accordingly, the optimal choice of $\mathbf{k}_{\mathrm{cut}}$ and $f(\mathbf{k})$ depends on the underlying model system. We exemplarily discuss our standard k-mask as well as the influence of differently shaped k-masks in Sec. 6.3 for the Bi_2Te_3 surface Hamiltonian (2.21).

6.3. Demonstration for the Bi_2Te_3 surface states

6.3.1. Definition of the initial setup

In Sec. 6.2 we introduced the concept of our wave-packet approach for simulating the dynamics of a Fermi sea. Now, we apply this method to the Bi_2Te_3 surface model (2.21) in order to investigate HHG. We use this first application to provide a detailed guide on how to use the newly developed approach, including all relevant sanity checks as well as evaluation methods. The laser pulse driving the electron dynamics is given by Eq. (5.10),

$$\mathbf{E}_{\mathrm{el}}(t) = E_{\mathrm{el}} \exp\left(-\frac{(t-t_0)^2}{2\Delta t^2}\right) \sin\left(2\pi\nu_{\mathrm{el}}\,(t-t_0)\right) \mathbf{e}_x. \tag{6.9}$$

We take the same parameters as for the test charges in Sec. 5.4, i.e. $\Delta t = 40\,\mathrm{fs}$, $\nu_{\mathrm{el}} = 25\,\mathrm{THz}$, $t_0 = 140\,\mathrm{fs}$, and polarization along the $\overline{\Gamma\mathrm{K}}$ direction of the crystal. For the field strength E_{el} we choose the value $E_{\mathrm{el}} = 0.5\,\mathrm{MV\,cm^{-1}}$. Note that, except for the comparison with driving along ΓM in Sec. 6.4, we always choose the laser pulse such that $\mathbf{E}_{\mathrm{el}} \parallel \mathbf{e}_x$. For the sake of readability, apart from Sec. 6.4, we refrain from explicitly stating that we are referring to the dynamics for driving along the $\overline{\Gamma\mathrm{K}}$ direction.

For simplicity, we set the Fermi energy $E_{\mathrm{F}} = 0$ such that it lies at the Dirac point, resulting in a filled valence band and an empty conduction band. Then, we only have to propagate the wave packet $\Psi_-(\mathbf{k}, t)$ in TQT. To define it based on Eq. (6.1) with

$$g_-(\mathbf{k}) = \begin{cases} 1 & , \text{ for } |\mathbf{k}| < |\mathbf{k}_{\mathrm{lim}}| \\ \exp\left[-\frac{(|\mathbf{k}|-|\mathbf{k}_{\mathrm{lim}}|)^2}{2\Delta k^2}\right] & , \text{ for } |\mathbf{k}| \geq |\mathbf{k}_{\mathrm{lim}}| \end{cases} \tag{6.10}$$

and Gaussian decay of width $\Delta k = 0.01\,\mathrm{Å}^{-1}$, we need to set a value for $|\mathbf{k}_{\mathrm{lim}}|$. In principle, this requires an estimate of the limiting momenta $\mathbf{k}_{\mathrm{cut}}$. We are not yet aware of a reasonable method to do this without monitoring the transitions of a large wave packet first. Nevertheless, as soon as the limits $\mathbf{k}_{\mathrm{cut}}$ are determined for one field strength, we can extrapolate the limits for other field strengths, as we demonstrate in Sec. 6.6.2. For the calculations presented in the following, we set $|\mathbf{k}_{\mathrm{lim}}| = 0.22\,\mathrm{Å}^{-1}$. Then we need 2048×1024 grid points and a spacing of $\delta x = 6\,\mathrm{Å}$ and $\delta y = 10\,\mathrm{Å}$ in real space for the propagation of $\Psi_-(\mathbf{k}, t)$ in TQT. The time step is set to $\delta t = 0.1\,\mathrm{fs}$.

6.3.2. Monitoring transitions in momentum space

While propagating the wave packet $\Psi_-(\mathbf{k},t)$ in TQT, we record the time and momentum resolved occupation

$$|c_{\mathbf{k},\pm}(t)|^2 = N|\varphi^*_\pm(\mathbf{k})\Psi_-(\mathbf{k},t)|^2. \tag{6.11}$$

In Fig. 6.2 we show snapshots of $|c_{\mathbf{k},-}(t)|^2$ at different times t. The insets depict the momentum displacement $k_x(t) - k_x(0)$, the respective time t of the snapshot is marked by a red cross. The wave packet $\Psi_-(\mathbf{k},t)$ is initialized in the valence band and centered around the Dirac point $\mathbf{k} = (0,0)$. As defined in Eq. (6.10), all momenta are equally occupied up to the radius $|\mathbf{k}_{\text{lim}}|$, then the wave packet smoothly decays to zero, see panel (a). During the pulse $\mathbf{E}_{\text{el}}(t)$, panel (b) - (e), the wave packet moves in momentum space and around the Dirac point transitions occur. When states directly cross the Dirac point, they are completely transferred from one band to the other, which is in accordance to the impulsive Landau-Zener transitions studied in Sec. 5.4. The transitions around the Dirac point are more diverse and their full classification remains an open task for future research. We also observe a complicated interference pattern that results in a remnant occupation in the conduction band after the pulse, see panel (f). This occupation is not balanced and manifests itself in a residual current [243].

Based on these insights in the distribution of the transitions in momentum space, we estimate momenta $\mathbf{k}_{\text{cut}}$, up to which observables have to be evaluated in order to include all relevant[6] dynamics, and thus define the k-mask $f(\mathbf{k})$. As our standard k-mask we pick a simple sigmoid function

$$f(\mathbf{k}) = \frac{1}{1 + \mathrm{e}^{a[\Delta E(\mathbf{k}) - \Delta E_{\text{cut}}]}}, \tag{6.12}$$

where $\Delta E = E_+(\mathbf{k}) - E_-(\mathbf{k})$ with the energies $E_\pm(\mathbf{k})$ from Eq. (2.22). The parameter $a = 900\,\mathrm{eV}^{-1}$ is chosen such that a numerically smooth but fast cut off is achieved. The boundary of the k-mask is given by the local energy gap ΔE_{cut} which we set by fixing $\mathbf{k}_{\text{cut}} = (k_{x,\text{cut}}, 0)$ on the k_x axis. The black lines in Fig. 6.2 indicate these boundaries for $k_{x,\text{cut}} \in [0.11, 0.16]\text{Å}^{-1}$ in steps of $0.01\,\text{Å}^{-1}$. Within the resolution of Fig. 6.2 all of these k-masks include the dominating transitions and are covered by the wave packet $\Psi_-(\mathbf{k},t)$ at all times. In Sec. 6.3.3 we study in more detail whether this first impression on the included transitions is correct. To ensure the coverage of the k-mask, we

[6] We discuss what we mean by *relevant* in Sec. 6.3.3.

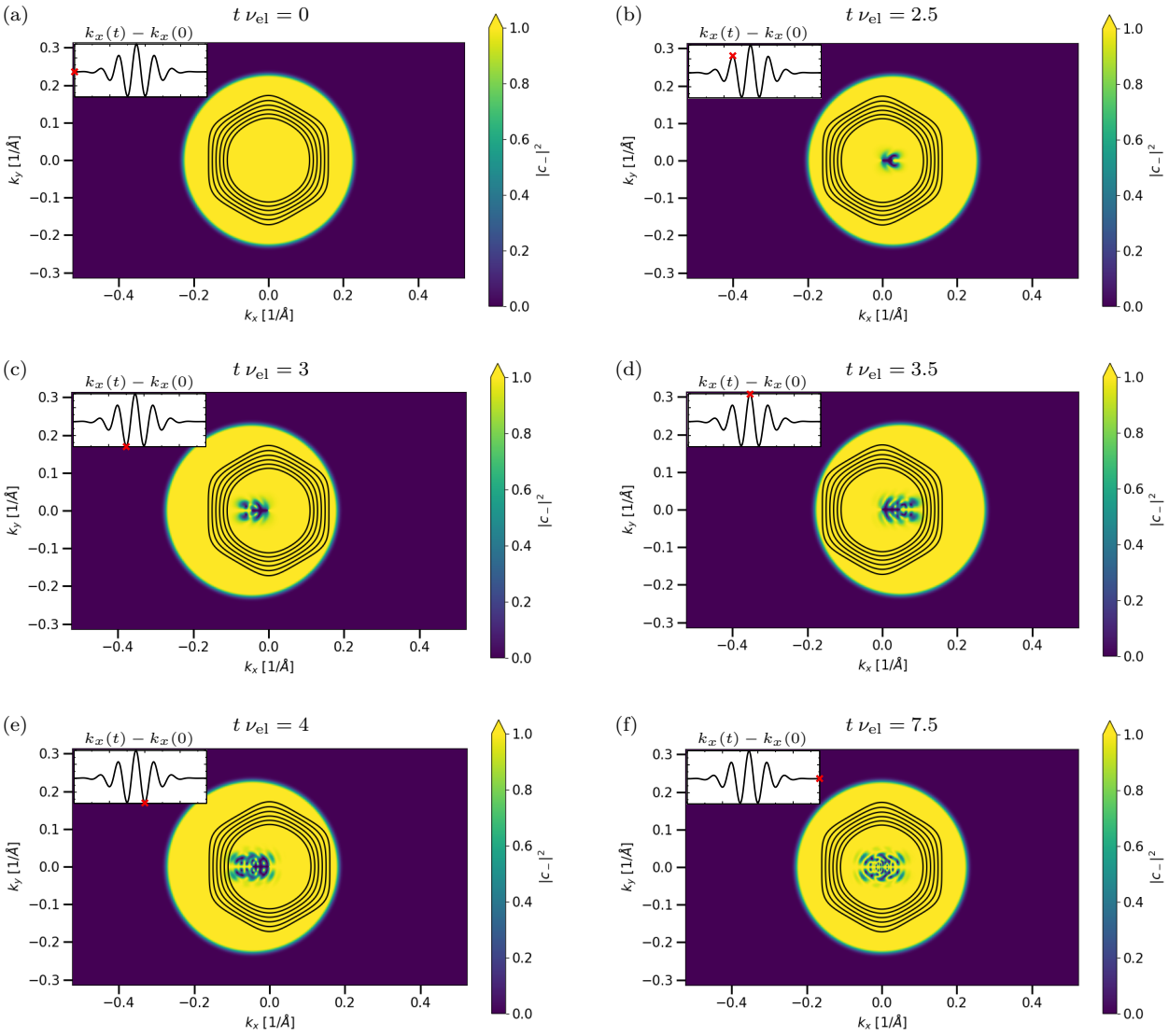

Fig. 6.2: Snapshots of $\Psi_-(\mathbf{k}, t)$ at different times t projected on the valence band. The insets show the course of $k_x(t) - k_x(0)$, the time t at which the respective snapshot is taken is marked by the red cross. The occupation $|c_{\mathbf{k},-}|^2$ is renormalized such that $1 = |c_{\mathbf{k},-}|^2 + |c_{\mathbf{k},+}|^2$ at each momentum $\mathbf{k}$ with $|\mathbf{k}| \leq |\mathbf{k}_{\mathrm{lim}}|$. The black lines represent k-masks with different boundaries ΔE_{cut}. Initially, the Gaussian wave packet is centered around the Dirac point $\mathbf{k} = (0, 0)$ and fully in the valence band, see panel (a). Then, the electric field pulse drives transitions in the region around the Dirac point. As shown in panel (b) - (e), states crossing the Dirac point completely switch from one band to the other, whereas around the Dirac point a complicated interference pattern appears. These interferences result in a remnant occupation after the pulse, see panel (f).

compute the momentum expectation value $\langle k_x(t)\rangle_{\text{cut}}$ of the wave packet inside the k-mask using the COM observable in momentum space[7], see Sec. 3.5 for an introduction. As long as $\langle k_x(t)\rangle_{\text{cut}} \approx 0$ for all times t, the k-mask $f(\mathbf{k})$ lies within the boundaries of the wave packet and Eq. (6.5) is fulfilled. The corresponding data for $k_{x,\text{cut}} = 0.16\,\text{Å}^{-1}$ is shown in App. A.8 and confirms that all k-masks in Fig. 6.2 comply with Eq. (6.5). Additionally, we evaluate $\langle k_x(t)\rangle_{\text{cut}}$ for $k_{x,\text{cut}} = 0.17\,\text{Å}^{-1}$ and find that there Eq. (6.5) is not satisfied anymore.

6.3.3. Determining the k-mask boundary

So far, we only stated that the k-mask has to cover all relevant transitions, but without specifying what *relevant* actually means. In this section, we study the velocity and HH emission of $\Psi_-(\mathbf{k}, t)$ resulting from applying the k-mask (6.12) with the boundaries $k_{x,\text{cut}} \in [0.11, 0.16]\text{Å}^{-1}$ in steps of $0.01\,\text{Å}^{-1}$, as depicted in Fig. 6.2. Based on our findings, we define criteria for *relevant transitions* and discuss the validity of our approach.

Since, within the k-mask, $\Psi_-(\mathbf{k}, t)$ represents the time evolution of an initially filled valence band, its velocity $\mathbf{v}_-^{\text{cut}}(t)$, Eq. (6.8), is zero as long as no transitions occur. As studied in Sec. 6.3.2, the applied pulse $\mathbf{E}_{\text{el}}(t)$ drives transitions around the Dirac point and after the pulse a residual occupation remains in the conduction band. In principle, by including a sufficiently large momentum range in the k-mask, the velocity $\mathbf{v}_-^{\text{cut}}(t)$ should converge. However, we find that even though the discrepancies between the curves decrease with increasing k-mask, we do not reach full convergence within the range of the k-masks depicted in Fig. 6.2. In Fig. 6.3 we show both the v_x and v_y component of $\mathbf{v}_-^{\text{cut}}(t)$ rescaled with the absolute value of the maximal intraband velocity[8] $v_x^{\max} = |-0.182\,56\,\text{Å}\,\text{fs}^{-1}|$. The insets show the difference of the velocities with respect to the results for the largest k-mask, i.e. $k_{x,\text{cut}} = 0.16\,\text{Å}^{-1}$. For v_x (v_y), the curves have deviations of up to two (one) percent of $v_x^{\max}$. Nevertheless, with respect to HHG, the order of magnitude of the deviations is inconclusive.

In Fig. 6.4 we plot the HHs spectra of $\mathbf{v}_-^{\text{cut}}(t)$, see Sec. 2.3.3 and App. A.9 for the technical details. The powers are normalized to the power $P_0 = 3.2 \cdot 10^{-23}\,\text{W}$

[7] Note that usually we only apply this test since it is easier, faster, and takes less storage than computing and evaluating $|c_{\mathbf{k},\pm}(t)|^2$.

[8] The computation and evaluation of the intraband velocity is discussed in more details later.

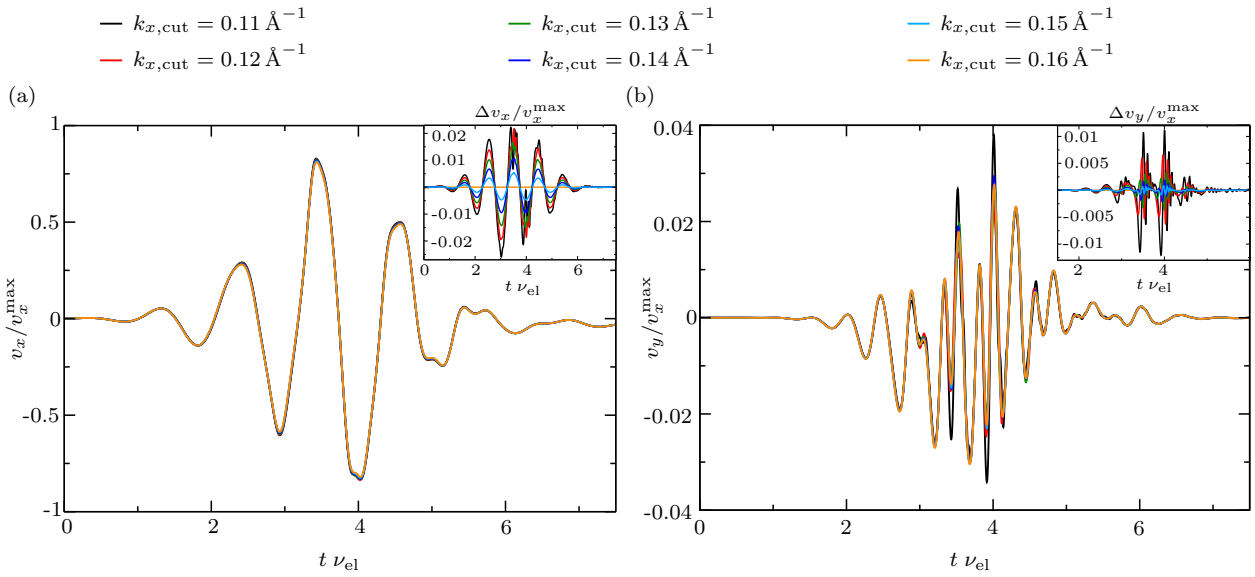

Fig. 6.3: Velocity $\mathbf{v}_-^{\mathrm{cut}}(t)$ of $\Psi_-(\mathbf{k},t)$ evaluated for the k-mask (6.12) with different $k_{x,\mathrm{cut}}$, (a) parallel and (b) perpendicular to the driving field. The velocities are normalized to the absolute value of the maximal intraband velocity $v_x^{\max} = |-0.182\,56\,\text{Å}\,\text{fs}^{-1}|$ corresponding to $k_{x,\mathrm{cut}} = 0.16\,\text{Å}^{-1}$. The insets show the deviations $\Delta v_{x/y}$ of the velocities obtained for different k-masks with respect to the results for $k_{x,\mathrm{cut}} = 0.16\,\text{Å}^{-1}$. We do not reach full convergence but the deviations decrease with increasing k-mask size.

of the first harmonic for $k_{x,\mathrm{cut}} = 0.16\,\text{Å}^{-1}$. Both parallel emission P_x and perpendicular emission P_y are approximately equal for all k-masks for the first five harmonics. Then, the spectra reach a plateau and the amplitude of the peaks decreases with increasing $k_{x,\mathrm{cut}}$. For the parallel emission P_x, this decrease leads to the peaks almost reaching noise level for $k_{x,\mathrm{cut}} = 0.16\,\text{Å}^{-1}$. The perpendicular emission P_y on the other hand is more robust and generally has a noise level about four orders of magnitude lower than P_x. Despite of this amplitude scaling, we observe that the frequency of the peaks is equal for all $k_{x,\mathrm{cut}}$ up to a certain harmonic indicated by an arrow in Fig. 6.4. At the marked frequency, the spectrum for $k_{x,\mathrm{cut}} = 0.11\,\text{Å}^{-1}$ has a double peak. The same feature is observable for all k-masks but shifts from one peak to the next highest for each step of $k_{x,\mathrm{cut}}$.

From these findings we conclude that full convergence of the velocity is not necessary as long as only qualitative statements about the emitted HHs are required. Then, including all relevant transitions can be understood as including a sufficiently large momentum area such that the position of the harmonics is fixed in the frequency range of interest. However, when aiming for quantitative information such as the ratio between parallel and perpendicular polarization of the harmonics or the cut-off frequency, the results depend on the choice of the k-mask boundary. Physically, setting the k-mask is similar

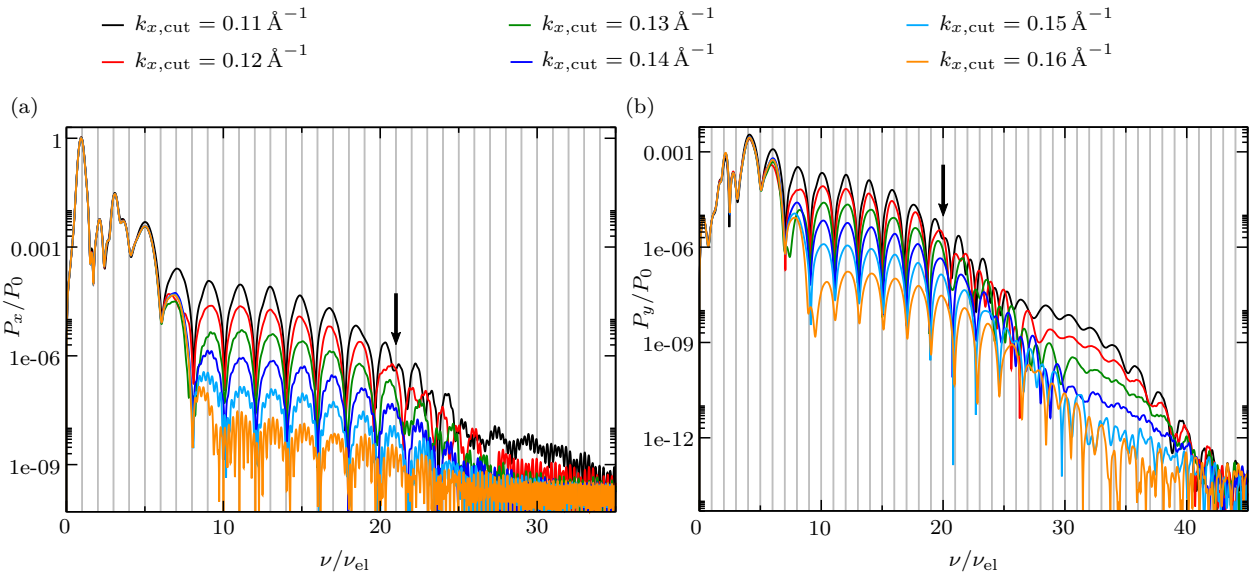

Fig. 6.4: HH spectra corresponding to $\mathbf{v}_-^{\mathrm{cut}}(t)$ of $\Psi_-(\mathbf{k}, t)$ evaluated for the k-mask (6.12) with different $k_{x,\mathrm{cut}}$, (a) parallel and (b) perpendicular to the driving field. We normalize P_x and P_y to the power $P_0 = 3.2 \cdot 10^{-23}\,\mathrm{W}$ of the first harmonic for $k_{x,\mathrm{cut}} = 0.16\,\text{Å}^{-1}$. For the lowest harmonics, the spectra are approximately converged. Then, they reach a plateau where the frequency position of the peaks is still equal for all k-masks but their amplitude decreases with increasing $k_{x,\mathrm{cut}}$. Starting from the harmonic indicated by the arrow, double-peak structures appear. The onset of this regime shifts from one peak to the next highest for each step of $k_{x,\mathrm{cut}}$. We conclude that the spectra can be considered for qualitative statements until they enter this last regime.

to introducing a momentum-dependent dephasing time. We say *similar* since even though we discard the dynamics outside of the k-mask, we do not include any dephasing mechanisms in our simulations. Thus, states that temporarily leave the region of the mask still evolve coherently and do not loose their phase information.

Altogether, whether and with which boundary the k-mask approach is suitable for quantitative comparison to experiments depends on the studied material. Within this work, we focus on extracting qualitative properties of HHG from the Bi_2Te_3 surface states (2.21) but also explore how the k-mask boundary and HH power scale with the field strength, see Sec. 6.6.2. As stated in Ref. [81], the intraband dephasing time of Bi_2Te_3 is at least 1 ps, whereas the interband dephasing time was set to 10 fs in the simulations based on the semiconductor Bloch equations. This suggests that we obtain the most realistic results within our wave-packet approach by converging the intraband contribution to the velocity $\mathbf{v}_-^{\mathrm{cut}}(t)$. As confirmed in the following, this convergence is achieved within the explored range, meaning that we only discard interband contributions when setting the k-mask accordingly. The thus introduced momentum-dependent interband dephasing offers a complementary approach to the semiconductor Bloch equations applied in Ref. [81].

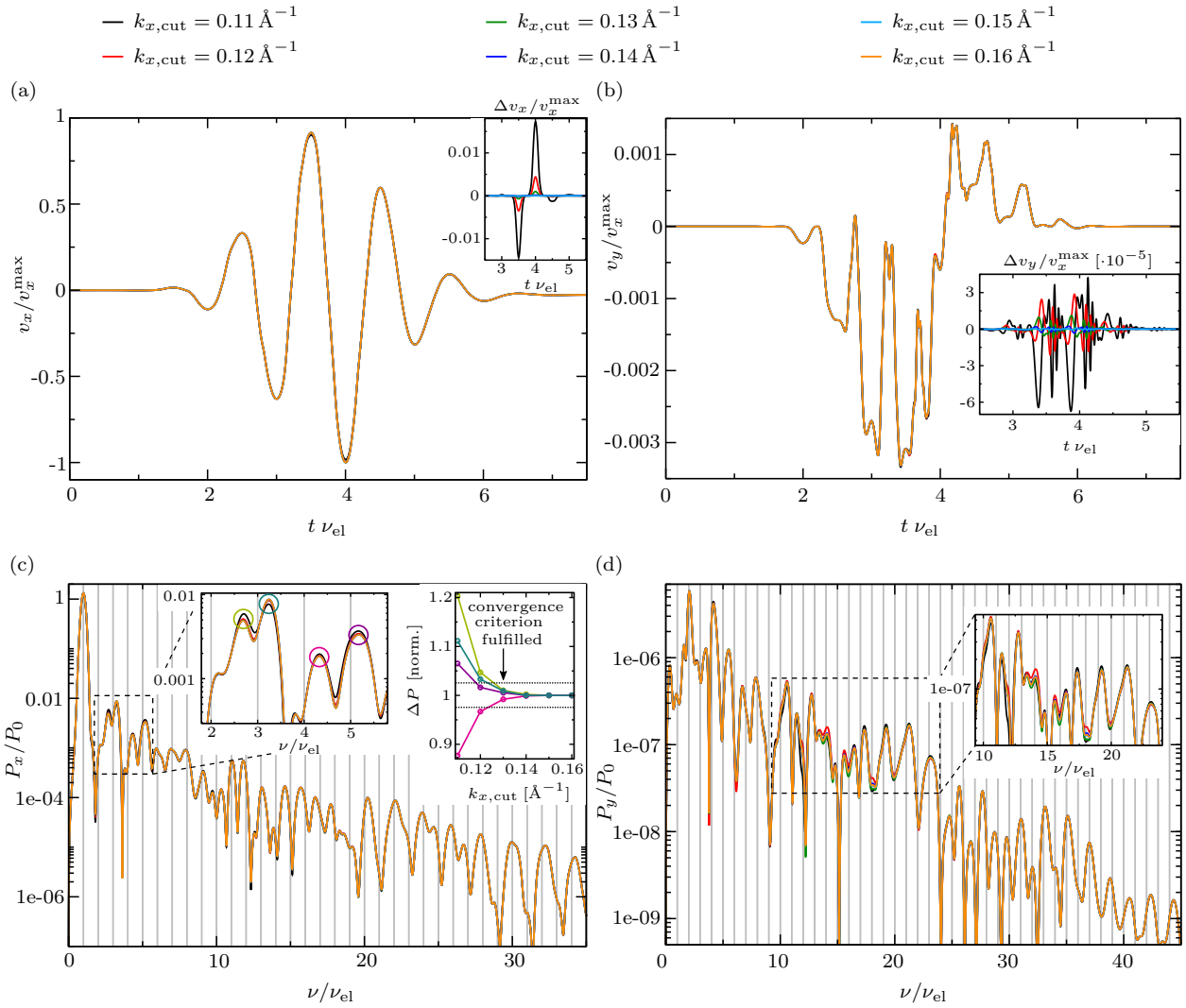

Fig. 6.5: Intraband velocities and corresponding HH spectra for $\Psi_-(\mathbf{k}, t)$ evaluated for the k-mask (6.12) with different $k_{x,\mathrm{cut}}$, (a), (c) parallel and (b), (d) perpendicular to the driving field. We normalize the velocities to the absolute value of the maximal intraband velocity $v_x^{\max} = |-0.182\,56\,\text{Å fs}^{-1}|$ corresponding to $k_{x,\mathrm{cut}} = 0.16\,\text{Å}^{-1}$ and the power spectra P_x and P_y to the power $P_0 = 3.2 \cdot 10^{-23}\,\text{W}$ of the first harmonic in the total spectrum for $k_{x,\mathrm{cut}} = 0.16\,\text{Å}^{-1}$. For the time-resolved velocites, the deviations $\Delta v_{x/y}$ decrease with increasing mask size, see insets of panel (a) and (b). The perpendicular spectra are not fully converged for any of the k-masks. Since the overall amplitude of P_y is three to four orders of magnitude below the parallel emission P_x and the total spectrum in Fig. 6.4 shows that the perpendicular spectrum is less affected by noise when increasing the k-mask, we focus on the parallel emission when determining the optimal mask boundary. To define a quantitative convergence criterion, we focus on the region with the largest deviations in P_x, see zoom in panel (c). As analyzed in the inset next to this zoom, the deviations ΔP of the highlighted peaks, normalized with respect to the results for $k_{x,\mathrm{cut}} = 0.16\,\text{Å}^{-1}$, converge exponentially fast with growing mask size. Throughout this work, we settle for the smallest k-mask with variations below $\pm 2.5\,\%$ with respect to the reference k-mask. Accordingly, for $E_{\mathrm{el}} = 0.5\,\text{MV cm}^{-1}$ we choose $k_{x,\mathrm{cut}} = 0.13\,\text{Å}^{-1}$.

The definitions of intra- and interband velocity are reviewed in Sec. 2.3, and the corresponding observables in TQT are introduced in Sec. 3.5. The intraband velocities of $\Psi_-(\mathbf{k}, t)$ are plotted in Fig. 6.5(a) and (b) for the different k-masks. Like the total velocity in Fig. 6.3, the curves are rescaled with the absolute value of the maximum intraband velocity, $v_x^{\max} = |-0.182\,56\,\text{Å}\,\text{fs}^{-1}|$. As shown in the insets, the deviations $\Delta v_{x/y}$ from the respective velocity component for $k_{x,\text{cut}} = 0.16\,\text{Å}^{-1}$ decrease with increasing $k_{x,\text{cut}}$. For $k_{x,\text{cut}} \geq 0.13\,\text{Å}^{-1}$, the difference in v_x is less than or equal to 0.1 % of $v_x^{\max}$. Since the intraband velocity v_y itself is already three orders of magnitude smaller than $v_x^{\max}$ for all k-masks[9], we refrain from further interpretation of its deviations Δv_y.

Moreover, for the evaluation of the total velocity, compare Figs. 6.3 and 6.4, we observed that quantifying the discrepancies in the time domain is inconclusive with respect to the corresponding HHs spectra. Therefore, we perform a deeper analysis of the spectra generated by the intraband velocities, as shown in Fig. 6.5(c) and (d). Again, we normalize the spectra to the power $P_0 = 3.2 \cdot 10^{-23}\,\text{W}$ of the first harmonic in the total spectrum. Unlike the full spectra in Fig. 6.4, the intraband spectra appear almost equal for all k-masks. For a more quantitative comparison, we focus on the peaks with the largest deviations in the parallel emission, as highlighted in the zoom in Fig. 6.5(c). In the inset, we plot the scaling ΔP of the peaks, marked by different colors, with respect to the k-mask boundary. We normalize the curves to the emitted power for the corresponding largest k-mask with $k_{x,\text{cut}} = 0.16\,\text{Å}^{-1}$. This analysis reveals an exponentially fast convergence with increasing mask size. However, the studies on the full spectra in Fig. 6.4 showed that the resolution of the parallel emission decreases for larger k-masks. Therefore, we define the convergence criterion such that we settle for a mask size in the center of the explored range. To be precise, we choose the smallest k-mask with deviations ΔP inside the window of ±2.5 % around the reference k-mask. Accordingly, for $E_{\text{el}} = 0.5\,\text{MV}\,\text{cm}^{-1}$, we set $k_{x,\text{cut}} = 0.13\,\text{Å}^{-1}$.

Concerning the perpendicular emission, see Fig. 6.5(d), small deviations are resolved for all values of $k_{x,\text{cut}}$. Nevertheless, since the parallel intraband spectrum is three to four orders of magnitude larger than the perpendicular

[9] This overall small amplitude is understood by considering that the intraband velocity originates from an unbalanced occupation. As demonstrated by the momentum resolved transitions in Fig. 6.2, along k_x an unbalanced occupation is clearly visible due to the symmetry breaking caused by the electric field (6.9). This unbalancing gives rise to the x component of the intraband velocity. Along k_y however, the occupation appears balanced for all snapshots in Fig. 6.2. Nevertheless, as observed for the single test charges in Sec. 5.4.3, small deviations between states at $\pm k_y$ are possible, leading to a relatively small but non-zero intraband velocity in y direction.

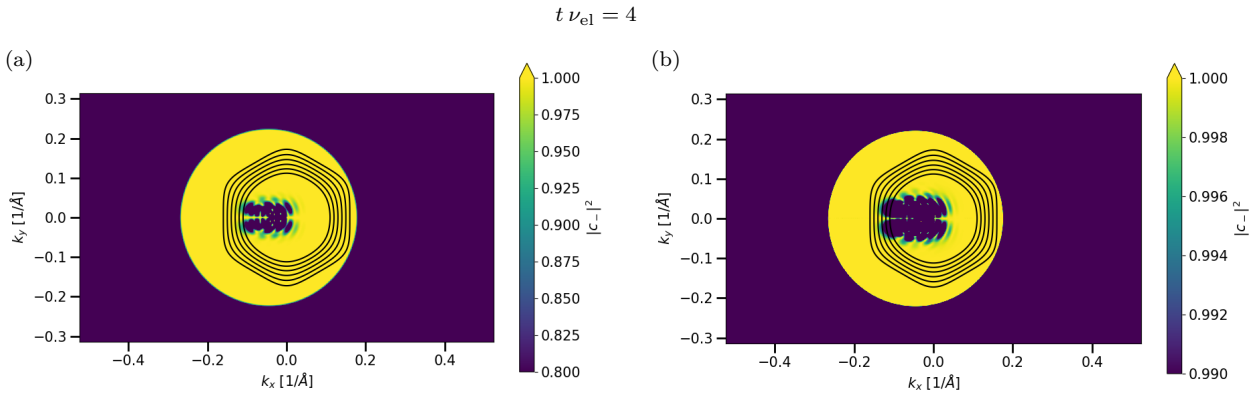

Fig. 6.6: Snapshots of $\Psi_-(\mathbf{k}, t)$ at $t\ \nu_{\mathrm{el}} = 4$ projected on the valence band with differently resolved color bars. Like in Fig. 6.2, the occupation $|c_{\mathbf{k},-}|^2$ is renormalized, such that $1 = |c_{\mathbf{k},-}|^2 + |c_{\mathbf{k},+}|^2$ at each momentum $\mathbf{k}$ with $|\mathbf{k}| \leq |\mathbf{k}_{\mathrm{lim}}|$, and the black lines represent the k-masks considered within this section. When starting the color bar at $|c_-|^2 = 0.8$, see panel (a), we resolve that the k-mask with $k_{x,\mathrm{cut}} = 0.11\,\text{Å}^{-1}$ neglects some transitions where less than $\sim 20\,\%$ of the state switch to the valence band. By increasing the lower end of the bar to $|c_-|^2 = 0.99$, see panel (b), we find that by choosing $k_{x,\mathrm{cut}} = 0.13\,\text{Å}^{-1}$ for the k-mask, we include all transitions where up to $\sim 99\,\%$ of the state remain in the valence band. This finding supports considering $k_{x,\mathrm{cut}} = 0.13\,\text{Å}^{-1}$ as the optimal k-mask boundary.

one[10] and additionally the total perpendicular spectrum appears less affected by noise when increasing the k-mask, compare Fig. 6.4, we determine the k-mask boundary based on the parallel emission only. Besides the convergence, we note that the intraband spectra do not show clean HH peaks as compared to the total spectra. This property highlights the importance of the interband velocity for the process of HHG in Bi_2Te_3 surface states. We do not perform a deeper analysis on the interplay between intra- and interband velocity concerning HHG in this work, but leave this as a task for future research.

In Sec. 6.3.2 we state that within the resolution of the occupation plots in Fig. 6.2 the dominating transitions are included in all k-masks. When changing the scale of the color map such that it only resolves band occupations of $|c_-|^2 \geq 80\,\%$ and $|c_-|^2 \geq 99\,\%$, respectively, see Fig. 6.6, we find that actually the k-mask with $k_{x,\mathrm{cut}} = 0.11\,\text{Å}^{-1}$ only covers the regions where up to $\sim 20\,\%$ of the state switch to the conduction band. When setting $k_{x,\mathrm{cut}} = 0.13\,\text{Å}^{-1}$ on the other hand, also transitions where up to $\sim 99\,\%$ of the state remain in the valence band are considered. This observation offers an alternative criterion for defining the k-mask boundary which confirms that $k_{x,\mathrm{cut}} = 0.13\,\text{Å}^{-1}$ is a suitable choice for the parameters studied here. Nevertheless, since saving the momentum-resolved occupations is storage intensive, we mainly employ the

[10] Note that this difference in magnitude is also reflected by the corresponding velocities, as discussed previously.

convergence of the intraband velocities and spectra for the remainder of this work.

6.3.4. Influence of the k-mask shape

With our standard k-mask, defined in Sec. 6.3.2 based on the local energy difference $\Delta E(\mathbf{k})$, we focus on convergence of the spectrum along the k_x direction. However, the snapshots of the momentum-resolved occupations in Figs. 6.2 and 6.6 show that the extent of the region with transitions in k_y direction is smaller than in k_x direction due to the polarization of the electric field. Therefore, one might consider a k-mask that is rather elliptical than circular more suitable. In this section we define a k-mask that is adapted to the shape of the transition region in momentum space and explore the influence of its boundary in k_y direction on the resulting HHs spectrum. We call it *minimal k-mask* $f_{\min}(\mathbf{k})$ from now on. For simplicity, we thereby keep the boundary in k_x fixed at $k_{x,\mathrm{cut}} = 0.13\,\text{Å}^{-1}$, as determined in Sec. 6.3.3.

We base the description of this minimal k-mask on sigmoid functions similar to Eq. (6.12). Since we now change the boundary in k_y direction while keeping it fixed in k_x, we set the limiting energy gap ΔE_{cut} by specifying $\mathbf{k}_{\mathrm{cut}} = (0, k_{y,\mathrm{cut}})$ on the k_y axis. In order to achieve a more elliptical shape, we then define a momentum shift $\mathbf{k}_{\mathrm{shift}}$ that shifts the energy difference $\Delta E(\mathbf{k})$ such that on the k_x axis $\Delta E_{\mathrm{cut}} = \Delta E(\mathbf{k} \pm \mathbf{k}_{\mathrm{shift}})$ for $\mathbf{k} = \mp(0.13, 0)\text{Å}^{-1}$. Assuming a perfectly circular energy contour for simplification, we define $\mathbf{k}_{\mathrm{shift}}$ as $\mathbf{k}_{\mathrm{shift}} = (0.13, 0)\text{Å}^{-1} - (k_{y,\mathrm{cut}}, 0)$, where $k_{y,\mathrm{cut}} < 0.13\,\text{Å}^{-1}$. Finally, the minimal k-mask $f_{\min}(\mathbf{k})$ is described as

$$f_{\min}(\mathbf{k}) = \begin{cases} \left[1 + \exp\left[a\left(\Delta E(\mathbf{k} + \mathbf{k}_{\mathrm{shift}}) - \Delta E_{\mathrm{cut}}\right)\right]\right]^{-1} & , \text{ for } k_x + |\mathbf{k}_{\mathrm{shift}}| < 0 \\ \left[1 + \exp\left[a\left(\Delta E(\mathbf{k} - \mathbf{k}_{\mathrm{shift}}) - \Delta E_{\mathrm{cut}}\right)\right]\right]^{-1} & , \text{ for } k_x - |\mathbf{k}_{\mathrm{shift}}| > 0\,, \\ \left[1 + \exp\left[a\left(\Delta E(0, k_y) - \Delta E_{\mathrm{cut}}\right)\right]\right]^{-1} & , \quad \text{otherwise} \end{cases} \tag{6.13}$$

with $a = 900\,\text{eV}$ as for the standard mask (6.12). We change $k_{y,\mathrm{cut}}$ in steps of $0.01\,\text{Å}^{-1}$ within the range $k_{y,\mathrm{cut}} \in [0.05, 0.12]\,\text{Å}^{-1}$ here.

In panel (a) of Fig. 6.7 we depict the contours of the different k-masks $f_{\min}(\mathbf{k})$ on top of the momentum resolved transitions $|c_-|^2$ at $t\nu_{\mathrm{el}} = 3.5, 4, 4.5$ with the color scale ranging from 0.99 to 1. For the smallest presented $k_{y,\mathrm{cut}}$, the masks show the required elliptical shape, whereas for increasing $k_{y,\mathrm{cut}}$ they approach the shape of the standard k-mask $f(\mathbf{k})$. In analogy to the plot for

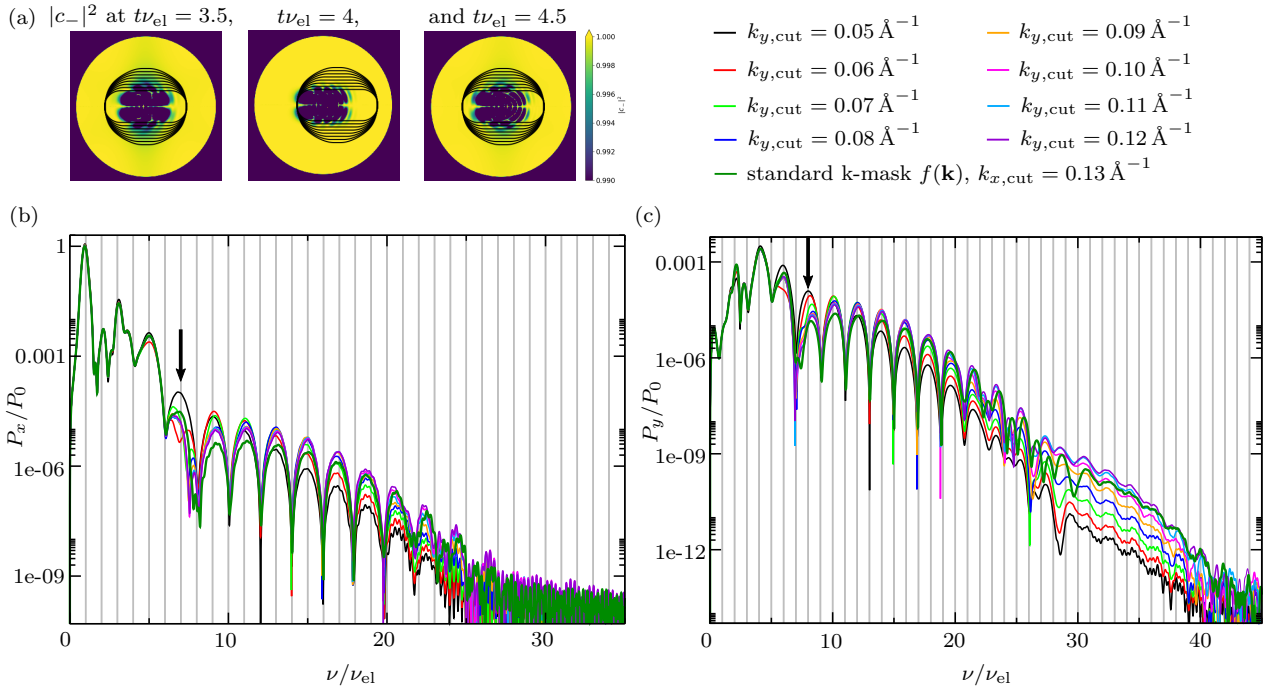

Fig. 6.7: Analysis of the influence of the minimal k-mask (6.13) for different $k_{y,\mathrm{cut}}$. (a) Occupation $|c_-|^2$ of the valence band, color coded in the range 0.99–1 , alongside the different k-masks at different times t. The minimal k-mask is better adopted to the transition region than the standard k-mask (6.12). For $k_{y,\mathrm{cut}} = 0.07\,\text{Å}^{-1}$ the mask includes all transitions with at least $\sim 1\,\%$ of the state switching band. HH spectra (b) parallel and (c) perpendicular to the driving field corresponding to $\mathbf{v}_-^{\mathrm{cut}}(t)$ of $\Psi_-(\mathbf{k}, t)$ evaluated for the k-masks displayed in (a) compared to those evaluated for the standard k-mask (6.12) with $k_{x,\mathrm{cut}} = 0.13\,\text{Å}^{-1}$ (dark green). We normalize P_x and P_y to the power $P_0 = 3.4 \cdot 10^{-23}\,\mathrm{W}$ of the first harmonic of the parallel spectrum P_x for the standard mask. The spectra are approximately converged for the first harmonics for $k_{y,\mathrm{cut}} \geq 0.07\,\text{Å}^{-1}$. Starting from the peak indicated by the arrow, the impact of $k_{y,\mathrm{cut}}$ on the peak height varies for each peak. In contrast to the convergence along k_x, see Fig. 6.4, the parallel spectrum P_x is above noise level for all $k_{y,\mathrm{cut}}$.

$f(\mathbf{k})$ at $t\nu_{\mathrm{el}} = 4$, see Fig. 6.6(b), we find that the mask with $k_{y,\mathrm{cut}} = 0.07\,\text{Å}^{-1}$ already includes all transitions where up to $\sim 99\,\%$ of the state remain in the valence band. Note however that along the k_y direction we observe the outermost relevant momenta when the electric field is maximal and the wave packet centered around the Dirac point due to the avoided crossing along the k_y axis. Along the k_x direction instead the maximal momentum shift is crucial when determining the momentum boundary.

The graphs in panel (b) and (c) of Fig. 6.7 depict the HHs spectra corresponding to the different k-masks. We compare them against the results from the standard k-mask with $k_{x,\mathrm{cut}} = 0.13\,\text{Å}^{-1}$, which are highlighted in dark green. All spectra are renormalized to the first-order peak of the parallel spectrum for the standard k-mask, namely $P_0 = 3.4 \cdot 10^{-23}\,\mathrm{W}$. Like for the boundary variations of the standard k-mask, see Fig. 6.4, the spectra are approximately

converged for the lowest harmonics as soon as all transitions with at least $\sim 1\,\%$ of the state switching band are included within the k-mask. As discussed before, this is achieved for $k_{y,\mathrm{cut}} = 0.07\,\text{Å}^{-1}$ here. But for harmonics within the plateau the influence of $k_{y,\mathrm{cut}}$ is different on every peak. The onset of the plateau is indicated by the arrow for both polarizations. The value of the marked peak is highest for the smallest k-mask and its position in frequency drifts with $k_{y,\mathrm{cut}}$. By comparing to the results of the standard k-mask, Fig. 6.4, we observe that the marked harmonic is only part of the plateau for the lowest $k_{x,\mathrm{cut}}$, indicating that at this order the transition between two regimes occurs. Unlike the k_x boundary, different choices of k_y do not have a relevant influence on the ratio between peak height and the noise level, meaning that for all $k_{y,\mathrm{cut}}$ good spectral resolution is achieved.

We conclude that the choice of the k-mask and its shape has a quantitative influence on the obtained HHs spectrum. Accordingly, comparison to experimental data could reveal whether there exists a momentum dependent dephasing in the investigated material. Additionally, a more detailed study on the scaling of different harmonics with the k-mask boundaries could provide a deeper understanding of how different states contribute to the HHG process. On the other hand, the position of the peaks is mainly independent on the mask choice, making qualitative statements about HHG from different model Hamiltonians possible even without precise knowledge about the dephasing properties. Since the definition of the k-mask (6.12) is simpler than that of the minimal k-mask (6.13), we continue taking (6.12) as standard k-mask for the qualitative studies presented in the rest of this thesis.

6.3.5. Comparison to the full wave packet without k-mask

So far we have investigated how the HHs spectra depend on the boundaries of the k-mask in momentum space. As a last step, we compare the results for the standard k-mask $f(\mathbf{k})$ with $k_{x,\mathrm{cut}} = 0.13\,\text{Å}^{-1}$ to results obtained for full wave packets without applying a k-mask. Then, the velocities arising within the unbalanced region, compare Fig. 6.1, are not excluded.

For the full wave packets on the one hand we choose $\Psi_-(\mathbf{k}, t)$ defined by Eqs. (6.1) and (6.10) with $|\mathbf{k}_{\mathrm{lim}}| = 0.22\,\text{Å}^{-1}$, i.e. the wave packet from which we also obtain the results with the k-mask. And on the other hand, we propagate a wave packet that initially covers the momentum area of the k-mask and thus is also defined based on Eq. (6.1) but by a sigmoid function

like the standard k-mask (6.12),

$$g_{-}(\mathbf{k}) = \left[1 + \exp\left[a\left(\Delta E(\mathbf{k}) - \Delta E_{\mathrm{lim}}\right)\right]\right]^{-1}, \tag{6.14}$$

where $\Delta E_{\mathrm{lim}} = E_{+}(\mathbf{k}_{\mathrm{lim}}) - E_{-}(\mathbf{k}_{\mathrm{lim}})$ with $\mathbf{k}_{\mathrm{lim}} = (k_{x,\mathrm{cut}}, 0) = (0.13, 0)\text{Å}^{-1}$ and $a = 100\,\mathrm{eV}^{-1}$. The velocities and HHs spectra of the three cases are compared in Fig. 6.8. We dashed the curves belonging to the components parallel to the driving field in order to distinguish them from the perpendicular ones. The velocities in panel (a) are rescaled to the respective maximal intraband velocity v_x^{max} and for better visibility we multiplied the perpendicular velocities by a factor of five. The spectra in panel (b) are normalized to the power P_0 of the first harmonic of the respective parallel emission.

The comparison of the velocities in Fig. 6.8(a) shows the dominance of the contributions from the unbalanced region when included in the evaluation. For both wave packets without k-mask the sign of the parallel velocity component is inverted with respect to the velocity evaluated inside the k-mask. As discussed in Sec. 6.3.3, within the k-mask the velocity depends on the transitions whereas in the unbalanced region the velocity is determined by the momentum shift due to the electric field $\mathbf{E}_{\mathrm{el}}(t)$. When analyzing the signs of the respective velocity contributions, one finds that they are always opposite. In the inset of Fig. 6.8(a) we sketch this analysis for an exemplary point in time and a 1D Dirac system. We only consider a limited number of states that are covered by the wave packet. We represent them as filled (empty) circles when they are occupied (unoccupied). In the depicted case, within the k-mask region the velocity has negative sign, whereas in the unbalanced region a positive velocity prevails. Since the unbalanced region contains more unbalanced states, the total velocity is positive. Accordingly, the sign of the parallel velocity reflects whether the velocity contribution from within or outside of the k-mask is larger and thus dominating. For the perpendicular velocity however, only the balancing of the wave packet along k_y plays a role. Since the applied electric field drives along the k_x direction and our wave packets are initially centered around the Dirac point at $\mathbf{k} = (0, 0)$, balancing along k_y is only broken by non-symmetric transitions and not by the driving itself. Hence, the perpendicular velocities mainly differ in amplitude for the three distinct cases. For the wave packet with $|\mathbf{k}_{\mathrm{lim}}| = 0.22\,\text{Å}^{-1}$, evaluated with and without k-mask, this amplitude difference is caused by the interband contributions from states outside of the k-mask. Concerning the wave packet with envelope (6.14), one also has to take into account that due to its smaller total size in momentum space our normalization, see Eq. (6.2), leads to a higher weighting of the occupied states, affecting the amplitude of the observed velocity.

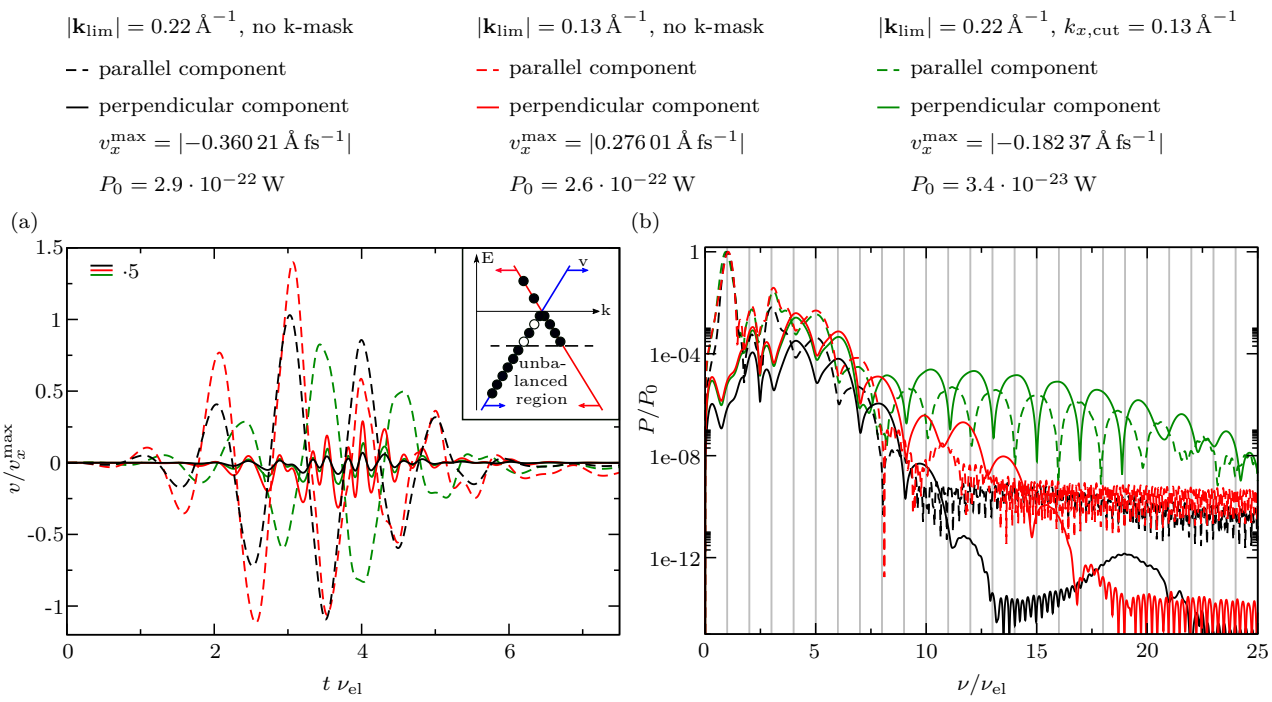

Fig. 6.8: Comparison of (a) velocity and (b) HHs obtained with and without k-mask for differently sized wave packets. The velocities are normalized to their respective maximal intraband velocity $v_x^{\max}$ and the spectra to the power P_0 of their first harmonic. The perpendicular velocity components are multiplied by a factor of five for better visibility. Including the unbalanced region into the evaluation leads to a sign change in the parallel velocity, whereas it only affects the amplitude of the perpendicular one. The inset in panel (a) sketches the reason for this sign change for a 1D Dirac system. The region covered by the wave packet is represented by circles which are filled (empty) for occupied (unoccupied) states. In the unbalanced region the velocity is positive, while in the area of the k-mask a negative velocity dominates. Since the unbalanced region contains more states, it determines the sign of the total velocity when included in the evaluation. Concerning the HHs spectra, applying the k-mask reveals the plateau which otherwise cannot be resolved due to the influence of the unbalanced region on the velocity. Additionally, the k-mask leads to a shift of the noise level to higher harmonic orders. Nevertheless, all spectra exhibit the alternating pattern between parallel and perpendicular polarization which is caused by the Berry curvature of the warped Bi_2Te_3 surface Hamiltonian (2.21).

The corresponding HHs spectra in Fig. 6.8(b) reveal that for both the parallel and perpendicular emission the k-mask, and thus an evaluation simulating a filled Fermi sea, as discussed in Sec. 6.2, leads to the appearance of the plateau in the spectra. For the full wave packet with $|\mathbf{k}_{\mathrm{lim}}| = 0.22\,\text{Å}^{-1}$, the HHs amplitude decreases exponentially with increasing harmonic order. The last distinguishable peak lies at the twelfth harmonic. For the smaller wave packet with envelope (6.14), the exponential decay is interrupted around the eleventh harmonic, but no full plateau is formed. The last distinct peak lies around the 18^{th} harmonic and is not centered around an integer multiple of the driving frequency. Only for the k-mask we observe the plateau and clean harmonics at integer multiples up to the 19^{th} order. Then, the peaks start to split and shift

to non-integer multiples, even though the noise level is not reached before the $\sim 25^{\text{th}}$ ($\sim 40^{\text{th}}$) harmonic for the parallel (perpendicular) component, compare Figs. 6.4 and 6.7. Besides, we find that up to the onset of the plateau at $\nu/\nu_{\text{el}} = 8$, the spectra of the three cases are almost equal, even though for the large wave packet with $|\mathbf{k}_{\text{lim}}| = 0.22\,\text{Å}^{-1}$, apart from the first harmonic, the peaks are shifted to a lower amplitude than for the other cases. Additionally, all data sets exhibit the same alternating pattern between odd and even orders, and parallel and perpendicular emission. We already saw this behavior for the single test charges in Sec. 5.5. Since the pattern is caused by the Berry curvature of the model system, it is a fundamental property of the underlying Hamiltonian and therefore it is not surprising that it persists independently of the evaluation method and analyzed momentum-space area.

6.3.6. Conclusion

Within this section, we have demonstrated how HH emission from Bi_2Te_3 surface states is computed using a method based on wave packets. The key idea of this newly developed approach is to restrict the momentum area over which observables are calculated using a k-mask. This mask should be chosen such that it includes all *relevant* dynamics occurring in the system. We estimate reasonable boundaries for the k-mask by monitoring how transitions between valence and conduction band are distributed in momentum space. The shape of this distribution is elliptical due to the symmetry breaking induced by the field direction of the applied laser pulse. Nevertheless, we define the limits of our standard k-mask by the local energy difference between valence and conduction band, which results in an almost circular mask shape for the Bi_2Te_3 surface model (2.21). A variation of the boundaries of this k-mask demonstrates that the power of the emitted HHs decreases with increasing mask size, while the frequency of the peaks is mostly independent of the k-mask. Comparing the results for this standard k-mask to those obtained for a minimal k-mask adapted to the elliptical shape of the transition region confirms that the frequency of the peaks is independent of the k-mask shape. Still, we find an irregular dependency of the peak height of the HH orders on the boundary of the minimal k-mask in k_y direction. Lastly, we examine how the resulting spectra change when we do not apply any k-mask. Without a mask, the computed velocities contain spurious contributions caused by the finite wave packet in momentum space. These contributions modify the spectra such that the plateau we find when using the minimal or standard k-mask is not resolved anymore. Moreover, the cutoff of the spectra is shifted

to lower frequencies. We conclude that limiting the evaluated momentum space with a k-mask to model a completely filled band is crucial for obtaining qualitatively meaningful spectra.

In order to make quantitative statements, one has to settle for a criterion on how to exactly define the k-mask. For Bi_2Te_3 surface states, experimental results indicate that only the interband dynamics are damped by dephasing [80, 81]. Therefore, we determine the optimal limit for the k-mask based on the convergence of the intraband contribution to the emitted HHs. Since the standard k-mask applied in Sec. 6.3.3 is simpler and also has a larger impact on the resulting spectra than the minimal k-mask, we choose this mask shape for the remainder of this work. To set the k-mask boundary, we focus on the intraband emission with polarization parallel to the driving laser field. From these spectra, we choose the smallest k-mask for which the deviations are below $\pm 2.5\,\%$ as compared to the values to which the parallel intraband spectrum converges. For the electric peak field $E_{\mathrm{el}} = 0.5\,\mathrm{MV\,cm^{-1}}$ studied throughout this section, the described convergence criterion results in the k-mask with limit $k_{x,\mathrm{cut}} = 0.13\,\mathrm{\AA}^{-1}$.

6.4. Driving along the $\overline{\Gamma M}$ direction

So far, we have always applied the electric field pulse along the $\overline{\Gamma K}$ direction of the Bi_2Te_3 surface, i.e. $\mathbf{E}_{\mathrm{el}} \parallel \mathbf{e}_x$. Now, we rotate the pulse by 90° such that $\mathbf{E}_{\mathrm{el}} \parallel \mathbf{e}_y$. Except for the interchange of $\mathbf{e}_x \to \mathbf{e}_y$, the pulse is still defined by Eq. (6.9). Since with this rotated pulse the electrons are driven along the $\overline{\Gamma M}$ direction, states with parallel trajectories and opposite momenta $\pm k_y$ experience a Berry curvature of opposite sign. Therefore, we expect no perpendicular velocity component, compare Sec. 5.3, and thus no generation of harmonics with polarization perpendicular to the incoming radiation. For our simulations we keep the initial wave packet as defined in Eq. (6.10), but adjust the grid in TQT to 1024×2048 grid points with spacing $\delta x = 10\,\mathrm{\AA}$ and $\delta y = 6\,\mathrm{\AA}$. For the evaluation we employ the standard k-mask (6.12). As for driving along the $\overline{\Gamma K}$ direction, our convergence criterion is fulfilled for $k_{x,\mathrm{cut}} = 0.13\,\mathrm{\AA}^{-1}$.

In panel (a) of Fig. 6.9 we compare the parallel (solid lines) and perpendicular (dashed lines) velocity components for driving along the two crystal axes, where parallel and perpendicular refers to the polarization of the respective

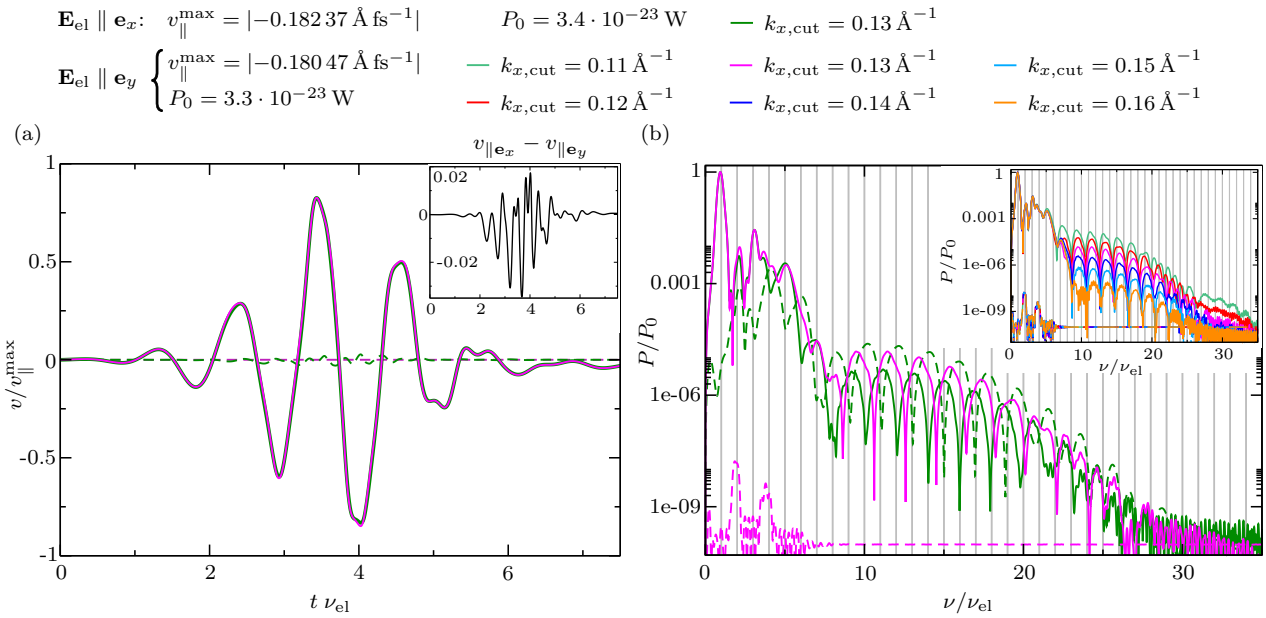

Fig. 6.9: Comparison of (a) velocity and (b) HHs obtained for an electric field polarized along the $\overline{\Gamma\mathrm{M}}$ and the $\overline{\Gamma\mathrm{K}}$ direction of the Bi_2Te_3 surface. The velocities are normalized to their respective maximal intraband velocity $v_\parallel^{\max}$ and the spectra to the power P_0 of their first harmonic. The components parallel to the respective driving are shown as solid lines, whereas the perpendicular components are dashed. For $\mathbf{E}_{\mathrm{el}} \parallel \mathbf{e}_y$ the velocity and emission perpendicular to the driving is zero. The inset in panel (a) shows the difference of the parallel velocities for the two field directions. This difference results in a frequency shift of the higher-order harmonic peaks in the spectra depicted in panel (b). The inset in panel (b) demonstrates the scaling of the spectra for driving along the $\overline{\Gamma\mathrm{M}}$ direction with respect to the k-mask size. It is similar to the results obtained for driving along the $\overline{\Gamma\mathrm{K}}$ direction in Fig. 6.4.

field pulse. As predicted, the perpendicular velocity is zero when the electric field is applied along the $\overline{\Gamma\mathrm{M}}$ direction. The deviations in the parallel velocities are only revealed when plotting the difference $v_{\parallel\mathbf{e}_x} - v_{\parallel\mathbf{e}_y}$, see the inset of panel (a). That these deviations are of higher frequency than the incoming pulse is confirmed by the corresponding HHs spectra in Fig. 6.9(b). When normalizing the spectra to their respective first harmonic $P_0 = P_\parallel(\nu_{\mathrm{el}})$, the first peaks of the parallel spectra fall on top of each other with only small quantitative variations for $1 < \nu/\nu_{\mathrm{el}} < 8$. For higher harmonic orders however, the parallel emission for driving along the $\overline{\Gamma\mathrm{M}}$ direction does not have integer multiples of the driving frequency but lies in between the peaks of the spectra for driving along the $\overline{\Gamma\mathrm{K}}$ direction. Comparison of the spectra for the two pulse directions implies that for driving along the $\overline{\Gamma\mathrm{M}}$ direction the Berry curvature imprints on the parallel emission, leading to a shift of the peak positions. Such a Berry curvature effect cannot be explained by the anomalous velocity (2.59). Confirmation of our hypothesis would require higher-order expansions of (2.59) and also a more extensive comparison of HHG for driving along the two different directions. This is beyond the scope of this thesis but will be considered in future research. The scaling of the HHs spectra for

$\mathbf{E}_{\mathrm{el}} \parallel \mathbf{e}_y$ with the k-mask boundary $k_{x,\mathrm{cut}}$ is depicted in the inset of panel (b). Like for driving along the $\overline{\Gamma\mathrm{K}}$ direction, compare Fig. 6.4, the first harmonics of the parallel emission are independent of the choice of $k_{x,\mathrm{cut}}$, whereas the amplitude of the peaks decreases with increasing k-mask in the range of the plateau. The perpendicular emission is approximately zero independently of the k-mask choice.

6.5. Comparison to a gapped Dirac cone system

In Chap. 5 we have extensively studied how the dynamics of single test charges are influenced by different Berry curvatures of the underlying model system. We found that for a gapped Dirac cone parallel and perpendicular harmonics have the same spectral features whereas for the Bi_2Te_3 surface Hamiltonian with hexagonal warping an alternating pattern arises for driving along the $\overline{\Gamma\mathrm{K}}$ direction. This alternating pattern is reproduced with the Fermi sea approach, as demonstrated in Sec. 6.3. In the following, we compare the Fermi sea dynamics of the Bi_2Te_3 surface states with driving along $\overline{\Gamma\mathrm{K}}$ direction ($\hat{\mathcal{H}}_{\mathrm{s}}(\mathbf{k})$ in (5.1)) to those of a gapped Dirac cone ($\hat{\mathcal{H}}_{\mathrm{g}}(\mathbf{k})$ in (5.1)). We apply the pulse (6.9) with strength $E_{\mathrm{el}} = 0.5\,\mathrm{MV\,cm^{-1}}$ to both systems. The initial wave packets are defined by Eq. (6.10) and the k-masks by Eq. (6.12). Also for the gapped cone our convergence criterion is fulfilled for $k_{x,\mathrm{cut}} = 0.13\,\mathrm{\AA}^{-1}$ and the parameters of the simulation can be set as described for Bi_2Te_3 in Sec. 6.3.1.

The results of our comparison are shown in Fig. 6.10. Panel (a) contains the time-dependent velocities and panel (b) the corresponding HHs spectra. To distinguish components parallel and perpendicular to the driving field, we dashed all lines referring to the latter. We find that the parallel velocities are almost identical, whereas the perpendicular ones differ both qualitatively and quantitatively. As for the single test charges in Sec. 5.4, the perpendicular velocity for the gapped Dirac cone is larger than for the Bi_2Te_3 surface Hamiltonian with warping. These findings are also reflected in the emitted HHs. The parallel emission is approximately the same for both systems up to the seventh harmonic. Then, at the plateau, the emission from the gapped cone is larger but in the end decreases faster into noise than the parallel emission from the Bi_2Te_3 surface. For the perpendicular components on the other hand, up to the seventh harmonic the emission from the gapped cone is larger. More importantly, the perpendicular peaks for the gapped cone are

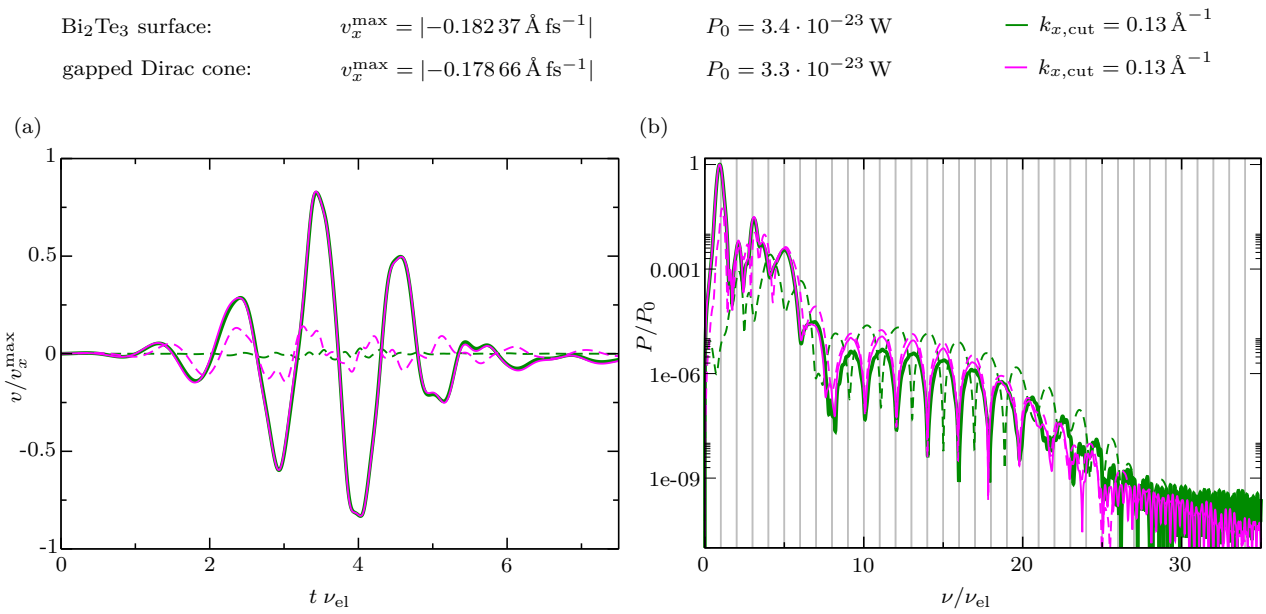

Fig. 6.10: Comparison of (a) velocity and (b) HHs obtained for a gapped Dirac cone system and the Bi_2Te_3 surface Hamiltonian (2.21). The velocities are normalized to their respective maximal intraband velocity $v_x^{\max}$ and the spectra to the power P_0 of their first harmonic. The components parallel to the driving field are shown as solid lines, whereas the perpendicular components are dashed. The parallel velocities and spectra are almost identical except for some quantitative deviations at the high-order harmonics. The perpendicular velocity on the other hand is larger for the gapped cone than for the warped surface states. At low frequencies, this also applies to the emitted harmonics. The qualitative differences in the perpendicular velocities result in perpendicular emission at even orders from the gapped cone and at odd orders for the Bi_2Te_3 surface states. This discrete shift confirms the observation about the relation between Berry curvature and the frequencies of the emitted harmonics made for the single test charges in Sec. 5.5.

located at odd orders just like the corresponding parallel component instead of being shifted to even orders as for the warped Bi_2Te_3 surface states. This confirms that our observation about the relation between Berry curvature and the frequencies of the emitted harmonics also holds when propagating a full Fermi sea instead of single test charges.

The discrete shift between the perpendicular emission from a gapped Dirac cone and a warped Bi_2Te_3 surface raises the question whether the two spectra can be continuously transformed into one another or are separated by a sudden switching. In Sec. 7.3.1 we explore this transition by introducing a gap in the Bi_2Te_3 surface Hamiltonian (2.21) with a magnetic field and then tuning either the width of the gap or the strength of the warping parameter R.

6.6. Variation of the field strength

6.6.1. Comparison with single test charges

As discussed in the motivation 6.1, the spectra we compute in Sec. 5.5 based on the propagation of two test charges resemble the single-active electron approximation [102]. The results we present in Sec. 6.3 already indicate that with our approach for simulating the full Fermi sea dynamics we obtain cleaner spectra and resolve higher harmonic orders than with the propagation of solely two test charges. However, so far we only investigated the moderate electric field strength $E_{\mathrm{el}} = 0.5\,\mathrm{MV\,cm^{-1}}$. Here, we extend these studies to the low- and high-field regime discussed in Sec. 5.5 and compare the HHs spectra of both approaches for the Bi_2Te_3 surface Hamiltonian (2.21), i.e. $\hat{\mathcal{H}}_{\mathrm{s}}(\mathbf{k})$ in Sec. 5.5.

For the test charges we consider the results for the wave packets with initial momentum $\mathbf{k}_i = (0, \pm 0.007)\mathrm{Å}^{-1}$, i.e. as close to the Dirac point as possible[11], since for the single-active electron approximation typically the state at the minimal band gap is examined. For the pulse we keep the description (6.9) but with field strengths $E_{\mathrm{el}} = 0.1\,\mathrm{MV\,cm^{-1}}$ and $E_{\mathrm{el}} = 1\,\mathrm{MV\,cm^{-1}}$ as in Sec. 5.5. To simulate the full Fermi sea, we propagate wave packets with envelope (6.10) and $|\mathbf{k}_{\mathrm{lim}}| = 0.15\,\mathrm{Å}^{-1}$ ($|\mathbf{k}_{\mathrm{lim}}| = 0.35\,\mathrm{Å}^{-1}$) for $E_{\mathrm{el}} = 0.1\,\mathrm{MV\,cm^{-1}}$ ($E_{\mathrm{el}} = 1\,\mathrm{MV\,cm^{-1}}$). The time step is set to $\delta t = 0.5\,\mathrm{fs}$ ($\delta t = 0.03\,\mathrm{fs}$) and the numerical grid has 2048×1024 (4096×4096) points with spacing $\delta x = 6\,\mathrm{Å}$ ($\delta x = 6\,\mathrm{Å}$) and $\delta y = 10\,\mathrm{Å}$ ($\delta y = 6\,\mathrm{Å}$)[12]. Our convergence criterion is fulfilled for $k_{x,\mathrm{cut}} = 0.05\,\mathrm{Å}^{-1}$ ($k_{x,\mathrm{cut}} = 0.21\,\mathrm{Å}^{-1}$). In Sec. 6.6.2 a more detailed analysis of the relation between $k_{x,\mathrm{cut}}$ and the field strength E_{el} is performed.

In Fig. 6.11 we plot the normalized spectra obtained for the full Fermi sea and the single test charges for comparison. Panel (a) contains the low-field regime and panel (b) the high-field regime with an inset zooming into the low-order harmonics. Note that the power P_0 of the first harmonic is larger for the single test charges due to the normalization of our wave packets[13],

[11] Remember that for the narrow wave packets numerical issues at the Dirac point limit the momenta $\mathbf{k}_i$ we can study. For the large wave packets employed for our Fermi sea approach on the other hand these problems are negligible.

[12] Note that for the high field strength a smaller lattice spacing in y direction is necessary to fit the large wave packet with $|\mathbf{k}_{\mathrm{lim}}| = 0.35\,\mathrm{Å}^{-1}$ into the momentum space grid with boundary $|k_y^{\mathrm{max}}| = \pi/\delta y$.

[13] If we would want to compare these quantities and not only the renormalized spectra, we would have to compensate for the different wave-packet sizes in momentum space.

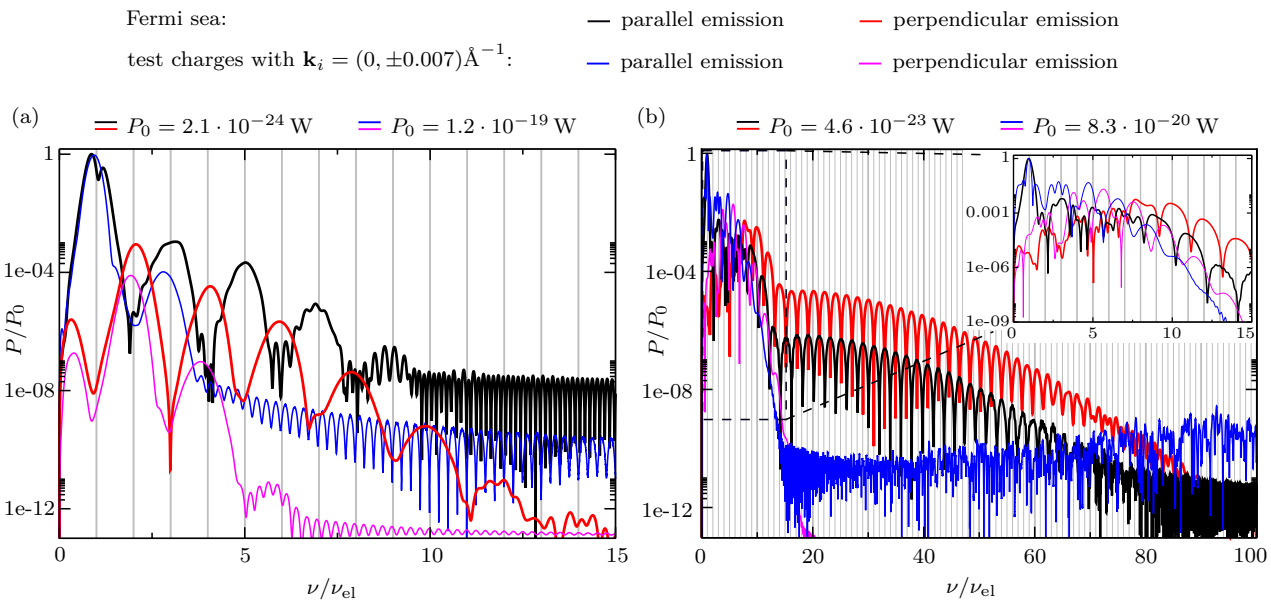

Fig. 6.11: Comparison of HHG obtained for single test charges and our Fermi sea approach for (a) $E_{el} = 0.1\,\text{MV}\,\text{cm}^{-1}$ and (b) $E_{el} = 1\,\text{MV}\,\text{cm}^{-1}$. The spectra are normalized to the power P_0 of their first harmonic. In the low-field regime, already the single test charges generate clean harmonics, but only reproduce the lowest orders. For the high-field regime however, solely including the full Fermi sea reveals integer harmonics up to high orders ≥ 60. Nevertheless, as shown in the inset in panel (b), at low frequencies for both approaches the peaks are not clearly distinguishable and have a fine structure. This might be due to resonance effects and/or Zitterbewegung.

as discussed in Eq. (6.2). For $E_{el} = 0.1\,\text{MV}\,\text{cm}^{-1}$ already the single-active electron approximation delivers clean spectra but contains only the first two peaks of parallel and perpendicular emission, respectively. By employing the Fermi sea approach, the parallel (perpendicular) spectrum is extended up to ninth (twelfth) order. In the high-field regime, the Fermi sea approach reveals clean HHs up to at least 60^{th} order with alternating polarization pattern of odd and even harmonics whereas for the test charges not even the 20^{th} order is resolved. Additionally, the zoom into the low-order harmonics shows that the peak positions shift when including all states into the propagation. The first harmonics (up to $\sim$ eighth order) are not sharply distinguished in both approaches. Instead, they are split into multiple peaks. As discussed in App. A.6, this could be caused by the competition between resonance peaks and HHs, but also Zitterbewegung might play a role here. A deeper analysis of the contributions to this spectral range remains to be done in future research. Overall, our findings confirm that – especially for high field strengths – including the full Fermi sea is necessary in order to obtain clean HHs and realistic cut-off frequencies.

6.6.2. Scaling of the emitted power and the k-mask size

In this section we explore the peak-field dependent scaling of the power P of different harmonic orders as well as of the boundary $k_{x,\mathrm{cut}}$ of the k-mask fulfilling our convergence criterion, as discussed in Sec. 6.3.3. To this end, we vary the field strength from 0.1–1 MV cm^{-1} in steps of 0.1 MV cm^{-1} and compute HHs spectra for the Bi_2Te_3 surface Hamiltonian (2.21) as in Sec. 6.6.1. The simulation parameters are given in App. A.10 alongside the values of $k_{x,\mathrm{cut}}$, the extracted powers P/P_0, and the powers P_0 of the first harmonic to which we normalized the spectra shown in Fig. 6.12.

Panel (a) depicts the emission with polarization parallel to the driving field, whereas panel (b) contains the spectra with polarization perpendicular to the incoming laser radiation. For both components we include a close up on the first 20 harmonics in the lower row. We find that the number of clearly distinguishable harmonics increases with the peak strength E_{el}, even though a more sophisticated quantification is difficult due to noise and non-integer harmonic peaks arising at the respective highest orders of the spectra. Interestingly, the noise level is approximately the same for all perpendicular spectra, whereas it decreases with increasing field strength for the parallel component. The reason for this difference between the two components is unclear to us and could be part of future research.

In the inset of panel (a) in Fig. 6.12 we plot the scaling of the power P of four harmonic orders with the field strength[14] E_{el}. We choose one peak within the initial intensity fall off and one peak at the onset of the plateau for each polarization direction. The corresponding peak positions are indicated by the accordingly colored arrows. We find that for all orders the power initially rises exponentially with the field strength but then reaches a plateau and/or even slightly decreases ($\leq$ one order of magnitude) before it rises again but with a smaller rate[15]. In the experiment in Ref. [81] also two different scaling regimes were observed, but without a plateau or decrease in between. However, here we employ different parameters for the model Hamiltonian than proposed in Ref. [81] and also apply a smaller driving frequency ($\nu_{\mathrm{el}} = 25$ THz instead of $\nu_{\mathrm{el}} = 28$ THz as in Ref. [81]). Additionally, in Sec. 6.3.4 we found a dependence of the higher-order peaks on the k-mask shape and we cannot fully exclude

[14] Note that we propagated wave packets of different widths here and scaled the spectra to their respective first harmonic with power P_0. Therefore, the comparison is always relative to the first harmonic and further evaluation would be necessary to obtain an absolute result.

[15] We refrain from extracting the scaling law $P/P_0 \propto E_{\mathrm{el}}^n$ since a larger evaluation range would be necessary for a reliable fit of the curves.

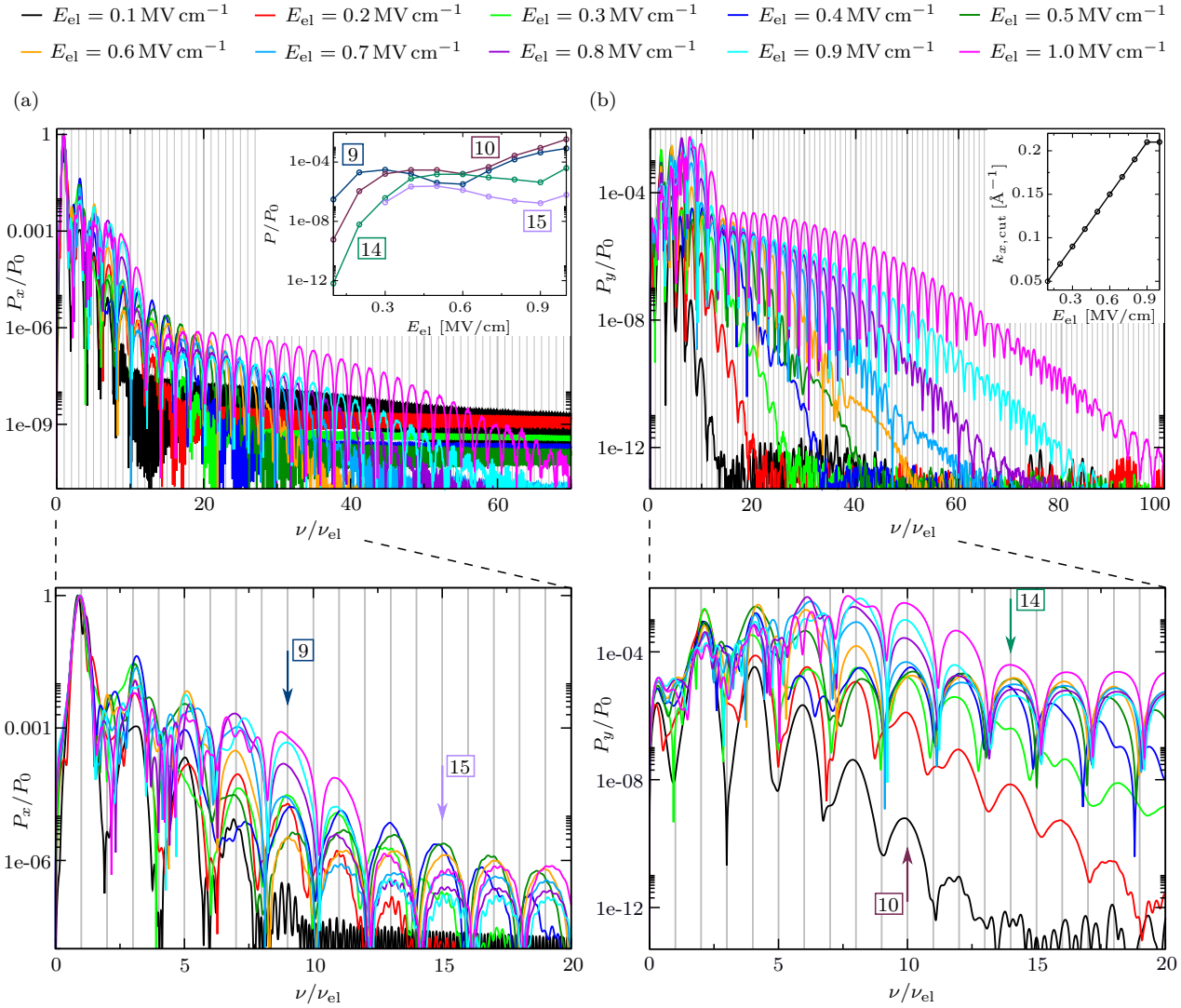

Fig. 6.12: HHs spectra for different peak fields E_{el} with polarization (a) parallel and (b) perpendicular to the driving field. The spectra are normalized to the power P_0 of their first harmonic, the corresponding values are given in App. A.10. The lower row displays a close up on the first 20 harmonics of both polarization directions. The highest resolved harmonic orders increase with the field strength. The inset in panel (a) shows the scaling of the power P of the harmonic orders indicated by the accordingly colored arrows. Thereby, we focus on one peak from the initial intensity fall off and one peak at the onset of the plateau for each polarization. All four orders first grow exponentially with E_{el} until reaching a plateau or even a small decrease. Then, they again increase exponentially but with a slower rate. The inset in panel (b) depicts the scaling of the k-mask boundary $k_{x,cut}$ with the field strength. Within the accuracy of our method, we find a perfectly linear dependence apart from the highest field strength. There, a revision of our convergence procedure is necessary.

that evaluating the powers relative to their first harmonic P_0 plays a role due to the wave-packet sizes depending on the field strength. Therefore, the analysis presented here could be revised in future research and also extended to the fitted Hamiltonian from Ref. [81]. On top of that, a variation of the pulse frequency ν_{el} should be included in order to study its influence on the generated HHs. A comparison of the field dependence of the HH powers for different k-masks and the experimental results could serve for determining the most realistic k-mask and allow for a deeper understanding of the momentum dependency of the actual Bi_2Te_3 surface states.

The inset of Fig. 6.12(b) shows the scaling of the k-mask boundary $k_{x,\mathrm{cut}}$ with the field strength E_{el}. Since the presented analysis is mainly intended as a guide for narrowing down the momentum area of interest when simulating a new field strength, we do not include any error bars even though our method for determining $k_{x,\mathrm{cut}}$ is not exact. Additionally, as in Sec. 6.3.3, we only consider steps of $0.01\,\text{Å}^{-1}$, which results in a perfectly linear relation between $k_{x,\mathrm{cut}}$ and the field strength. Repeating the analysis with a finer resolution of different $k_{x,\mathrm{cut}}$ would be necessary to confirm this perfect behavior. Only the boundary $k_{x,\mathrm{cut}}$ for the highest field strength, $E_{\mathrm{el}} = 1.0\,\mathrm{m\,V\,cm^{-1}}$, falls out of line. This indicates that we have to redo our convergence test for this value. However, the k-mask with $k_{x,\mathrm{cut}} = 0.21\,\text{Å}^{-1}$ is the largest that lies within the boundaries of the wave packet propagated here. Therefore, repeating the convergence test also requires propagating a larger wave packet and adjusting the parameters of the simulation, which we leave as a task for future work. Especially since, with respect to the results for the other field strengths, the spectra for $E_{\mathrm{el}} = 1.0\,\mathrm{m\,V\,cm^{-1}}$ appear to be sufficiently converged in order to extract the statements we discussed in this section.

6.7. Influence of the Fermi energy

So far, we have evaluated HHG for systems with Fermi energy at the Dirac point, i.e. with $E_{\mathrm{F}} = 0$ for the Bi_2Te_3 surface Hamiltonian defined in Eq. (2.21). In this section, we explore how shifting the Fermi energy into the valence or conduction band affects the HHs spectrum emitted from the Bi_2Te_3 surface. Thereby we also provide a guide on how to adjust the propagated wave packets in order to take the Fermi energy into account correctly.

As discussed in the introduction of our Fermi sea method in Sec. 6.2, the

initial wave packets $\Psi_\pm(\mathbf{k},0)$ are generally defined by an envelope function $g_\pm(\mathbf{k})$ and the eigenstates $\varphi_\pm(\mathbf{k})$ of the respective model system, see Eq. (6.1). When the Fermi energy lies within the valence band, i.e. $E_\mathrm{F} \leq 0$, it is sufficient to propagate the wave packet $\Psi_-(\mathbf{k},t)$, whereas for a Fermi energy in the conduction band, i.e. $E_\mathrm{F} > 0$, also the propagation of the wave packet $\Psi_+(\mathbf{k},t)$ has to be computed. The insets of Fig. 6.13(a) and (c) sketch the two situations. The Fermi energy E_F defines the Fermi wave vector $\mathbf{k}_\mathrm{F}$ with $E_\pm(\mathbf{k}_\mathrm{F}) = E_\mathrm{F}$, where $\pm$ has to be chosen according to the Fermi energy. Since the energy contours for the warped surface Hamiltonian (2.21) are generally not rotationally symmetric with momentum $\mathbf{k}$, the Fermi wave vector is angle dependent. In our simulations we adjust the Fermi energy by fixing the Fermi wave vector along the k_x axis, i.e. $\mathbf{k}_\mathrm{F} = (k_\mathrm{F}, 0)$.

For $E_\mathrm{F} < 0$, the wave packet $\Psi_-(\mathbf{k},0)$ cannot be described by a disk in momentum space with a Gaussian decay at the border as in Eq. (6.10). Instead, a hole has to be cut out in the center with boundary defined by the Fermi energy E_F. This hole is realized using the Fermi-Dirac distribution (6.3) and the envelope $g_-(\mathbf{k})$ is then given as

$$g_-(\mathbf{k}) = \begin{cases} \left[1 + \exp\left[-\left(E_\mathrm{F} - E_-(\mathbf{k})\right)/k_\mathrm{B}T\right]\right]^{-1} & , \text{ for } |\mathbf{k}| < |\mathbf{k}_\mathrm{lim}| \\ \exp\left[-\frac{\left(|\mathbf{k}|-|\mathbf{k}_\mathrm{lim}|\right)^2}{2\Delta k^2}\right] & , \text{ for } |\mathbf{k}| \geq |\mathbf{k}_\mathrm{lim}| \end{cases}, \tag{6.15}$$

where we set $1/k_\mathrm{B}T = 900\,\mathrm{eV}^{-1}$, i.e. $T \approx 13\,\mathrm{K}$, in order to achieve a numerically smooth decay. We apply the pulse (6.9) with peak field $E_\mathrm{el} = 0.5\,\mathrm{MV\,cm}^{-1}$ for the subsequent studies and thus set $|\mathbf{k}_\mathrm{lim}| = 0.22\,\mathrm{Å}^{-1}$. For computing the velocity $\mathbf{v}_-^\mathrm{cut}(t)$, we use the standard k-mask (6.12) with boundary $k_{x,\mathrm{cut}} = 0.13\,\mathrm{Å}^{-1}$. Then, the Fermi energy has to be chosen such that, during the time evolution, the Fermi wave vectors $\mathbf{k}_\mathrm{F}(t)$ shifted in momentum by the electric field pulse do not cross the boundary $k_{x,\mathrm{cut}}$ of the k-mask. Otherwise, not all relevant velocities would be included in the evaluation or the k-mask would have to be increased in order to obtain physical results. For the simulations in TQT we choose the same system parameters as in Sec. 6.3.1.

In the case $E_\mathrm{F} > 0$, the wave packet $\Psi_-(\mathbf{k},0)$ is again defined by the envelope (6.10). Additionally, we need to propagate $\Psi_+(\mathbf{k},t)$ in an extra simulation in order to prevent interferences between $\Psi_-(\mathbf{k},t)$ and $\Psi_+(\mathbf{k},t)$, compare Sec. 6.2. The wave packet $\Psi_+(\mathbf{k},0)$ is simply described by the Fermi-Dirac distribution (6.3), i.e. its envelope $g_+(\mathbf{k})$ reads

$$g_+(\mathbf{k}) = \left[1 + \exp\left[-\left(E_\mathrm{F} - E_+(\mathbf{k})\right)/k_\mathrm{B}T\right]\right]^{-1}, \tag{6.16}$$

where we set $1/k_\mathrm{B}T = 900\,\mathrm{eV}^{-1}$ like for the case $E_\mathrm{F} < 0$. Note that when simulating the evolution of $\Psi_+(\mathbf{k},t)$ we do not need to include a k-mask in the

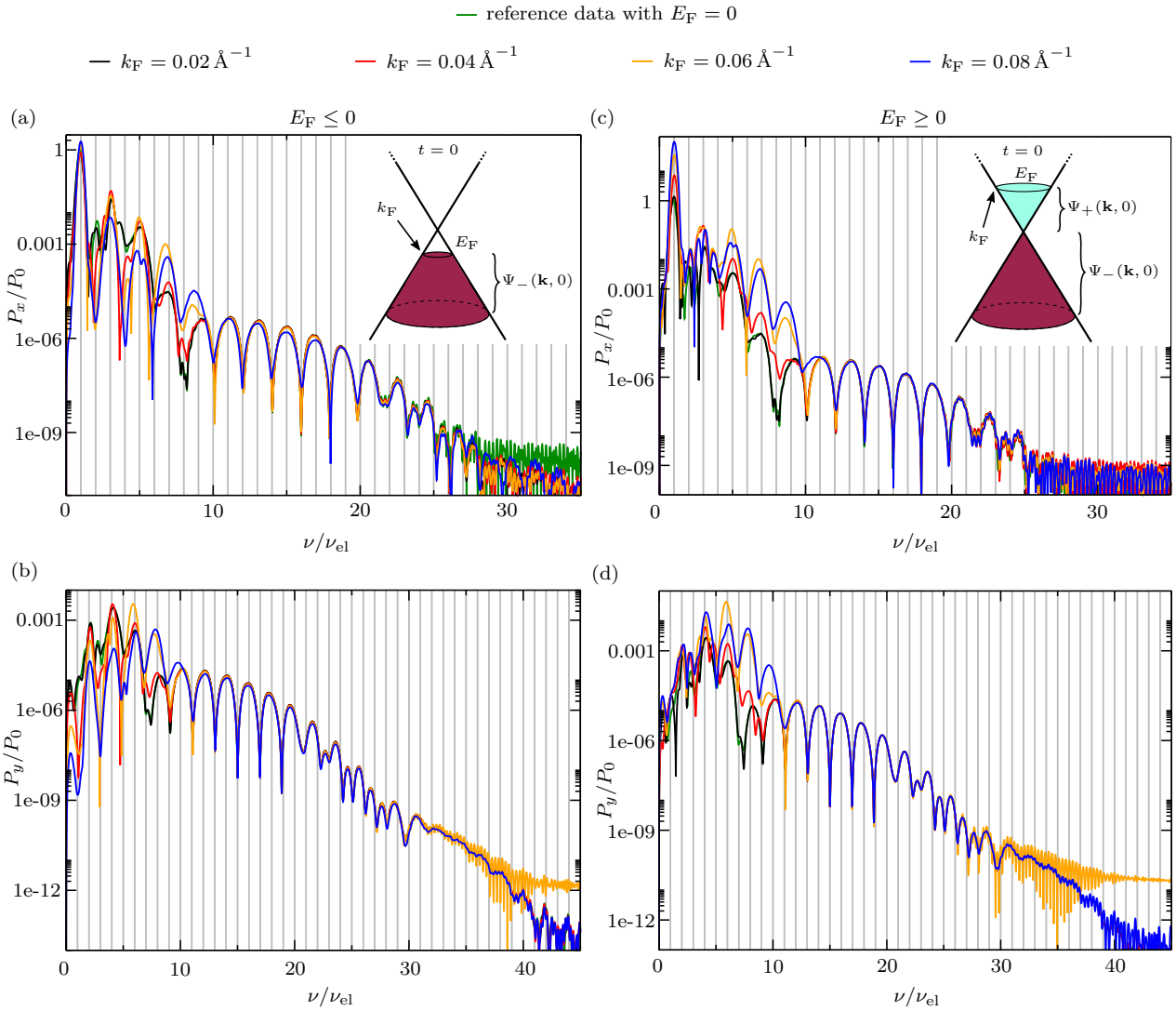

Fig. 6.13: HHG from the Bi_2Te_3 surface for different Fermi energies E_F. The spectra are normalized to the power $P_0 = 3.4 \cdot 10^{-23}\,W$ of the first harmonic of the reference data with $E_F = 0$. The left column depicts the results for $E_F \leq 0$ and the right column those for $E_F \geq 0$. In both cases, the Fermi energy is specified by the Fermi wave vector $\mathbf{k}_F = (k_F, 0)$. Panels (a) and (c) show the emission parallel to the applied pulse, whereas panels (b) and (d) display the perpendicular component. In all cases the high-order harmonics ($\nu/\nu_{el} \gtrsim 11$) are (almost) not dependent on the Fermi energy E_F. The low-order harmonics on the other hand vary with E_F. Their relative power P/P_0 changes with the Fermi energy and different peaks become particularly prominent. Especially lowering the Fermi energy in the valence band reduces the fine structure of the first harmonics and leads to a cleaner peak structure. These findings indicate that a closer analysis of the dynamics around the Dirac point could reveal the quantum processes that give rise to the fine structure, whereas focusing on states farther away from the Dirac point could show the origin of the higher-order harmonics.

computation of the velocity $\mathbf{v}_+(t)$, see Eq. (6.7), since unbalanced occupations in the conduction band are physical. For $\Psi_-(\mathbf{k},t)$ we employ our standard k-mask as defined in Eq. (6.12) with boundary $k_{x,\mathrm{cut}} = 0.13\,\text{Å}^{-1}$ to calculate $\mathbf{v}_-^{\mathrm{cut}}(t)$ based on Eq. (6.8), as for the simulations with $E_\mathrm{F} < 0$. Likewise, the parameters in TQT are set as described in Sec. 6.3.1 for all cases. When evaluating the total velocity $\mathbf{v}(t) = \mathbf{v}_+(t) + \mathbf{v}_-^{\mathrm{cut}}(t)$ of the Fermi sea, we have to take into account that the normalization of the wave packets is dependent on the wave-packet size in momentum space, compare Eq. (6.2). The details of the rescaling necessary to compute $\mathbf{v}(t)$ and to achieve quantitative comparability of the results for all Fermi energies are discussed in App. A.11.

In Fig. 6.13 we display the results for different Fermi energies E_F. Remember that we define the Fermi energy E_F by fixing the Fermi wave vector along the k_x axis, i.e. $\mathbf{k}_\mathrm{F} = (k_\mathrm{F}, 0)$ and thus $E_\mathrm{F} = E_\pm(\mathbf{k}_\mathrm{F})$. In the left column, we consider the case $E_\mathrm{F} \leq 0$, with the parallel emission in panel (a) and perpendicular emission in panel (b). Likewise, in the right column, we study the case $E_\mathrm{F} \geq 0$, with the parallel emission in panel (c) and perpendicular emission in panel (d). All spectra are normalized to the power $P_0 = 3.4 \cdot 10^{-23}\,\mathrm{W}$ of the first harmonic of the reference data with $E_\mathrm{F} = 0$. First of all, we find that the high-order harmonics ($\nu/\nu_\mathrm{el} \gtrsim 11$) are almost independent of the Fermi energy for all considered parameters. Since neither positive nor negative Fermi energy influence the states initially close to the boundary $k_{x,\mathrm{cut}}$ of the k-mask, this finding indicates that the higher harmonics are mainly contributed by these outermost states. In turn, the low-order harmonics vary with E_F. For positive Fermi energy, especially the power of the first harmonic increases by up to almost two orders of magnitude. For the other harmonics, the power varies with the Fermi energy in a more complicated manner, which has to be investigated further in future research. For negative Fermi energy, the most particular observation is that decreasing the Fermi energy reduces the fine structure of the low-order harmonics, giving rise to a cleaner peak structure. This suggests that this fine structure stems from the states initially located close around the Dirac point.

Overall, our observations indicate that a closer analysis of the dynamics around the Dirac point could reveal the quantum processes that give rise to the fine structure in future research. Likewise, focusing on states farther away from the Dirac point could show the origin of the higher-order harmonics.

6.8. Summary

In this chapter, we presented a novel method using wave packets for simulating HHG from a Fermi sea. The twist of this method is that by introducing a k-mask that limits the evaluated momentum space in the valence band, observables can be calculated for a Fermi sea even in effective model systems without band bottom. The time evolution of the wave packets is computed by solving the time-dependent Schrödinger equation without dephasing. By multiplying the resulting velocity with a Gaussian decay, which is a procedure also used in approaches with dephasing [172], and by discarding the dynamics outside of the k-mask a basic kind of dephasing is realized.

After a general description of the fundamental concepts, we demonstrated how to apply this method in order to compute HHG from Bi_2Te_3 surface states. To this end we focused on the model Hamiltonian (2.21) with hexagonal warping and an electric field pulse polarized along the $\overline{\Gamma K}$ direction of the crystal. But we also included a comparison to HHG for driving along the $\overline{\Gamma M}$ direction and from a gapped Dirac system without warping. First however, we thoroughly analyzed how the resulting HHs spectrum depends on the size and shape of the k-mask. These studies on the one hand showed that the position of the HH peaks is independent of the details of the k-mask, but on the other hand they revealed the importance of these details with respect to a quantitative evaluation of the spectra. Accordingly, our method solely allows for qualitative statements as long as no details about the momentum dependence of dephasing in the studied materials are known. For Bi_2Te_3 experiments found intraband dephasing times of at least 1 ps [80], whereas only 10 fs were assumed for the interband dephasing time in simulations based on the semiconductor Bloch equations [81]. Therefore, we expect that we obtain the most realistic results by only converging the parallel spectra from the intraband component of the velocity with respect to the k-mask. Then, only interband contributions are discarded from our observables. Also for the semiconductor Bloch equations, the choice of the interband dephasing time is oftentimes based on fitting the results to reference data [107]. Thus, our k-mask approach offers a valuable perspective on the HHG process and potentially new insights in the role of dephasing.

Having established a convergence criterion and k-mask shape, we contrasted results from our Fermi sea approach against those achieved without a k-mask and from two test charges only. This comparison highlights how much the spectral quality improves when taking the Fermi sea into account correctly. A

variation of the applied field strength gave first insights into the dependence of the emitted harmonics and the k-mask definition on the peak field of the laser pulse. Lastly, we investigated how the HHs spectra are affected by tuning the Fermi energy. We found that only the power and peak shape of the low-order harmonics vary with the Fermi energy, whereas the high-order harmonics remain (almost) the same for all studied cases. This indicates that the high-order harmonics are mainly emitted from states closer to the boundary of our k-mask and thus far away from the Dirac point, whereas the low-order harmonics are influenced by all parts of the evaluated momentum space but mainly generated by states passing close to the Dirac point. This impression is also supported by the results of the variation of the k-mask size, since there the low-order harmonics were unaffected by increasing the k-mask whereas the high-order harmonics changed.

In summary, our findings confirm that our wave-packet-based method for calculating HHG from a Fermi sea is a powerful, complementary approach for studying HHG using effective model Hamiltonians. Additionally, our observations suggest that considering the momentum dependence of the emitted harmonics and also of the dephasing times is an important step towards a better understanding of the quantum processes entering the HHG process as well as for achieving a better agreement between theory and experiment. Another advantage of our newly developed method is that it allows for integrating spatially dependent potentials. In principle, this enables considering not only the electric but also the magnetic component of the light wave. In Chap. 7 we present first studies on the influence of constant magnetic fields on HHG from TI surface states using the approach presented here, and give an outlook on how to include the pulse as an actual electro*magnetic* wave.

7. Magnetic-field effects on high-harmonic generation

7.1. Motivation

Already in 1865, Maxwell established the classical interpretation of light as an electromagnetic wave [4]. Nevertheless, in studies of light-matter interaction, typically the magnetic component of the light field is neglected, even though there exist phenomena where the magnetic wave plays a key role. Such optical processes are e.g. chiral light-matter interactions [244], the enhancement of Raman optical activity [245] or dipole-forbidden optical transitions in photochemistry [246]. Also, efforts have been made to disentangle the contributions of electric- and magnetic-dipole transitions in lanthanide ions in experiment [247]. Still, oftentimes neglecting the magnetic field $\mathbf{B}(\mathbf{r}, t)$ is justified due to its small amplitude compared to the electric wave $\mathbf{E}_{\mathrm{el}}(\mathbf{r}, t)$. The relation between the peak strength of both fields is given by the refractive index n_{r} of the medium and the speed of light c as $|\mathbf{B}| = \frac{n_{\mathrm{r}}}{c}|\mathbf{E}_{\mathrm{el}}|$, see Sec. 7.4 for details. For bulk Bi_2Te_3 the refractive index is $n_{\mathrm{r}} \approx 10$. Thus, for an electric peak field $|\mathbf{E}_{\mathrm{el}}| \approx 3\,\mathrm{MV\,cm^{-1}}$, as applied for the HHG experiments in Ref. [81], magnetic peak fields of up to $|\mathbf{B}| \approx 10\,\mathrm{T}$ occur in the crystal. With these field strengths in mind, the question whether and how magnetic fields influence HHG in Bi_2Te_3 surface states arises.

First studies in this direction have been conducted by Junck et al. [248]. They theoretically investigated the photocurrent response of TI surface states under circularly polarized light, taking the magnetic field component as well as the hexagonal warping into account. They found that the dominant photogalvanic current is helicity independent and results from the interplay of the orbital and the Zeeman coupling of the magnetic wave to the system. Even though excitations are mainly induced by the orbital coupling, a net photogalvanic charge current only arises when including the hexagonal warping term and applying an additional in-plane magnetic field. However, they did

not investigate time-dependent currents and short laser pulses. In this chapter, we extend our studies from Chap. 6 on HHG in Bi_2Te_3 surface states by including an additional magnetic field. We start by summarizing the effects of the Zeeman coupling of a constant magnetic field as found by Alexander Riedel during his master's project under our supervision [240]. Then, we conduct first studies on the influence of orbital effects on HHG from a simple Dirac cone without hexagonal warping. Lastly, we discuss how the magnetic component of the light field could be included in the model of the laser pulse and give an outlook on how the formalism we developed in Chap. 6 could be modified in order to treat the full electromagnetic field.

7.2. Bi_2Te_3 surface states in a constant, in-plane magnetic field

When a magnetic field is aligned in plane with a system, the external field induces a Zeeman effect but there exists no orbital coupling. In an effective model such as employed throughout this work, the strength of this Zeeman coupling is described by an effective g factor [249, 250]. The value of this g factor is material-dependent and can also vary with the direction of the applied field. For the Bi_2Te_3 surface Hamiltonian (2.21) the effective g factor for in-plane magnetic fields $\mathbf{B}$ has been calculated as $g_{\text{eff}}^{x/y} = 2.6$ for both $\mathbf{B} \parallel \mathbf{e}_x$ and $\mathbf{B} \parallel \mathbf{e}_y$ [87]. The total effective Hamiltonian then reads

$$\begin{aligned}\hat{\mathcal{H}}(\mathbf{k}) =& D(k_x^2 + k_y^2)\mathbb{1} + A(k_y\sigma_x - k_x\sigma_y) \\ &+ 2R(k_x^3 - 3k_xk_y^2)\sigma_z + \frac{1}{2}g_{\text{eff}}^{x/y}\mu_{\text{B}}\left(B_x\sigma_x + B_y\sigma_y\right),\end{aligned} \tag{7.1}$$

where μ_{B} is the Bohr magneton and B_x (B_y) the magnetic field component along the x (y) direction. Rauch et al. investigated the influence of such Zeeman coupling on the Bi_2Te_3 surface states [251]. They computed the topological invariants for a tight-binding model of the bulk crystal with different Zeeman terms and found that for $\mathbf{B} \parallel \mathbf{e}_x$ the system remains topological and no gap is opened in the Dirac cone at the surface. For $\mathbf{B} \parallel \mathbf{e}_y$ (and also for the out-of-plane configuration $\mathbf{B} \parallel \mathbf{e}_z$) however, the topological protection is lifted and the surface states become gapped. This anisotropy is due to the dual topological character of TIs from the Bi_2Te_3 family. Without external perturbations, these materials are in a $\mathcal{Z}_2$ topological phase and in a topological crystalline phase with mirror Chern number -1 simultaneously. TIs with $\mathcal{Z}_2$ invariant are characterized by spin polarized surface states that cross the

fundamental band gap. Their topological protection stems from TRS and can thus be destroyed by magnetic perturbations. In Chern insulators on the other hand, the topological protection stems from the crystal symmetry. This protection can only be lifted by breaking the mirror symmetry of the crystal, which is e.g. achieved by applying a magnetic field within the mirror plane. For Bi_2Te_3 this mirror plane is oriented along the y direction. Therefore, for $\mathbf{B} \parallel \mathbf{e}_y$ (and $\mathbf{B} \parallel \mathbf{e}_z$) both topological protections are eliminated and a band gap opens, whereas for $\mathbf{B} \parallel \mathbf{e}_x$ the crystalline topological phase is still intact and the Dirac point of the surface states only shifts in momentum.

In his master's thesis under our supervision, Alexander Riedel investigated the influence of in- and out-of-plane Zeeman fields on the dynamics of Bi_2Te_3 surface electrons driven by ultrashort laser pulses [240]. In the following, we summarize his findings for the in-plane configuration. His results for the out-of-plane magnetic field are discussed in Sec. 7.3.1. Note that for his simulations Riedel employed the Hamiltonian parameters from Ref. [88] instead of the prefactors from Ref. [87] we used for the Bi_2Te_3 surface Hamiltonian (2.21) throughout this work. Additionally, Riedel omitted the PHS-breaking term, i.e. $D = 0$ in his calculations. For better comparability with the out-of-plane magnetic field, Riedel increased the effective in-plane g factor to $g_{\text{eff}}^{x/y} = g_{\text{eff}}^{z} = 13$ such that it matches the out-of-plane g factor g_{eff}^{z}. His definition of the electric field pulse was similar to Eq. (5.10) but with a cosine instead of a sine function and a peak field $E_{\text{el}} = 0.3\,\text{MV}\,\text{cm}^{-1}$. For the Fermi sea calculations presented here, the k-mask was set based on Eq. (6.12) with $\Delta E_{\text{cut}} = 0.285\,\text{eV}$.

In Fig. 7.1 we show how the velocities change for the described system parameters when applying an in-plane magnetic field in addition to the electric field pulse $\mathbf{E}_{\text{el}}$. Panels (a) and (c) treat the configuration $\mathbf{B} \parallel \mathbf{e}_x$ and panels (b) and (d) the one with $\mathbf{B} \parallel \mathbf{e}_y$. Likewise, in panels (a) and (b) the electric field pulse is aligned along the $\overline{\Gamma\text{K}}$ axis of the Bi_2Te_3 surface, i.e. $\mathbf{E}_{\text{el}} \parallel \mathbf{e}_x$, and in panels (c) and (d) the pulse drives the electrons along the $\overline{\Gamma\text{M}}$ direction, i.e. $\mathbf{E}_{\text{el}} \parallel \mathbf{e}_y$. The insets of panels (a) and (c) depict the velocities for $|\mathbf{B}| = 0$, whereas the main graphs display the difference Δv of this velocity and the corresponding results for $|\mathbf{B}| > 0$. We rescaled all data with the maximal parallel velocities $v_x^{\max} = |-0.089\,57\,\text{Å}\,\text{fs}^{-1}|$ and $v_y^{\max} = |-0.098\,05\,\text{Å}\,\text{fs}^{-1}|$, respectively. In order to discriminate between parallel and perpendicular velocity, we dashed the curves representing the component parallel to the driving field.

On the whole, the variations caused by the magnetic field are at least two

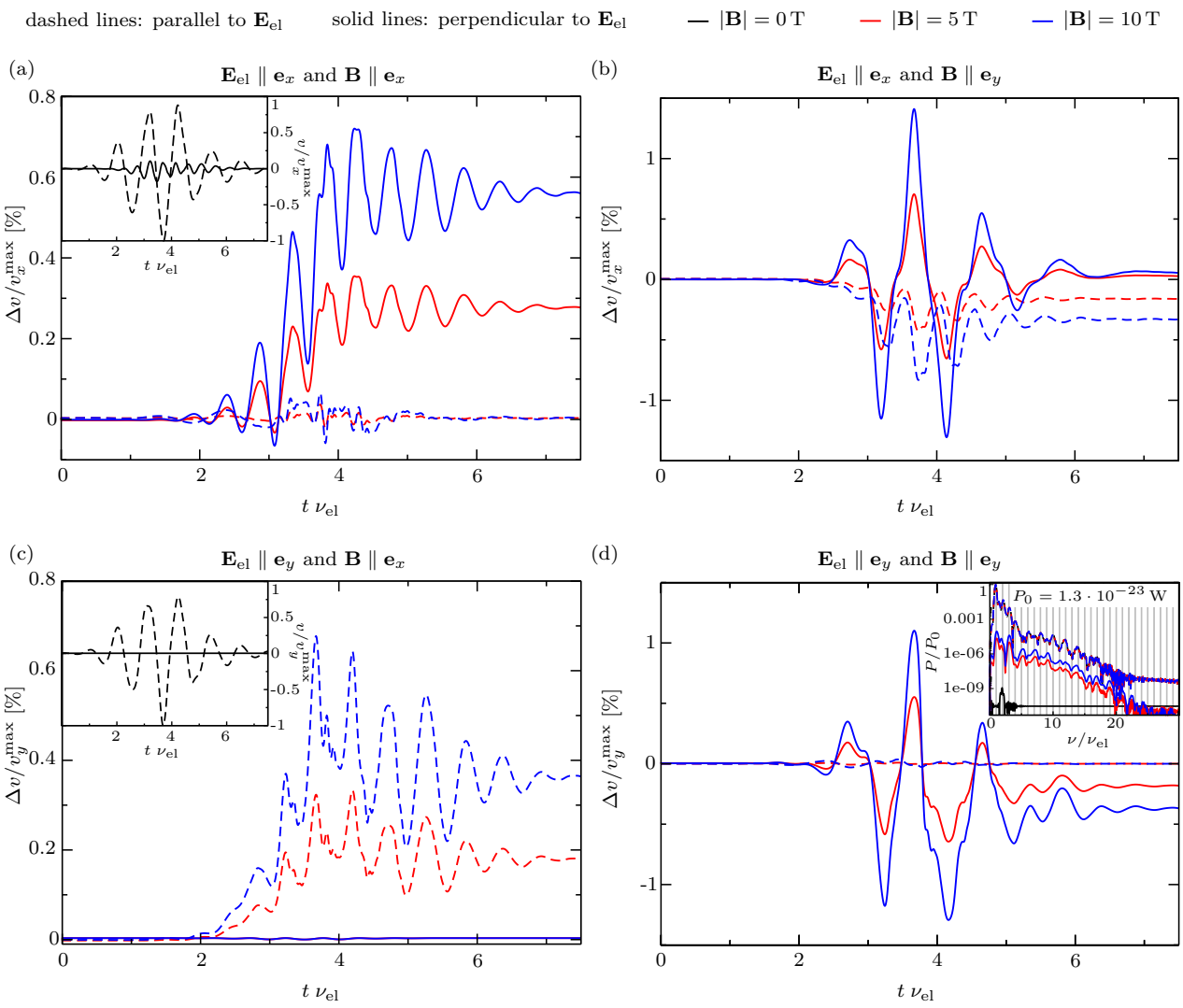

Fig. 7.1: Effects of an in-plane magnetic field on the dynamics of Bi_2Te_3 surface states driven by short laser pulses. The insets of panel (a) and (c) depict the respective reference velocity for $|\mathbf{B}| = 0$. The four panels display the differences Δv of the resulting velocities as compared to this reference velocity for the different possible configurations of the electric field $\mathbf{E}_{\mathrm{el}}$ and the magnetic field $\mathbf{B}$. All data has been rescaled with the maximal parallel velocities $v_x^{\max} = |-0.089\,57\,\text{Å}\,\text{fs}^{-1}|$ and $v_y^{\max} = |-0.098\,05\,\text{Å}\,\text{fs}^{-1}|$, respectively. The dashed curves correspond to the velocity parallel to $\mathbf{E}_{\mathrm{el}}$, whereas the solid lines represent the velocity component perpendicular to $\mathbf{E}_{\mathrm{el}}$. Overall, the changes induced by the magnetic field are at least two orders of magnitude smaller than the total velocity. Nevertheless, we find a distinctly different behavior for the two magnetic field configurations which is most likely related to the fact that the Bi_2Te_3 surface states are still topologically protected for $\mathbf{B} \parallel \mathbf{e}_x$ whereas a gap is opened in the spectrum for $\mathbf{B} \parallel \mathbf{e}_y$. For the configuration in panel (d) we find the most significant magnetic-field effect on the emitted HHs. The resulting spectrum is shown in the inset and confirms that emission with perpendicular polarization arises with increasing magnetic-field strength. However, since the power P of the perpendicular emission does not exceed the parallel one, experimental observation is difficult.*

* Data contributed by Alexander Riedel [240].

orders of magnitude smaller than the associated total velocity. Within the investigated parameter range, these variations scale linearly with the magnetic field strength $|\mathbf{B}|$, as extracted by Riedel in his work. Interestingly, the characteristics of the deviations differ for the two magnetic field configurations. For $\mathbf{B} \parallel \mathbf{e}_x$, Δv is larger for v_y and its value is mainly positive. This property does not rotate with the electric field, therefore parallel and perpendicular velocity component switch between panels (a) and (c) of Fig. 7.1. For $\mathbf{B} \parallel \mathbf{e}_y$ on the other hand, it is always the velocity component perpendicular to the electric field pulse for which the variations Δv are largest and instead of being mainly positive, Δv oscillates around zero. This different behavior is most likely related to the fact that the topological protection stays intact for $\mathbf{B} \parallel \mathbf{e}_x$ and is destroyed for $\mathbf{B} \parallel \mathbf{e}_y$. In the first case, the magnetic field merely distorts the energy bands. Since this change mainly affects the intraband velocities, the changes induced in the electron velocities are independent of the direction of the applied driving. In the second case however, a band gap is opened and thus the overall geometrical properties of the Hamiltonian change. At least in first-order approximation in the electric field strength, compare Eq. (2.59), these properties imprint on the velocity component perpendicular to the driving field, which is in agreement with our observations.

We also find characteristics of the velocity variation Δv that depend on the electric field direction. For $\mathbf{E}_{\mathrm{el}} \parallel \mathbf{e}_x$ both velocity components are affected by the in-plane magnetic field, whereas for $\mathbf{E}_{\mathrm{el}} \parallel \mathbf{e}_y$ the changes in the velocity component parallel to the applied magnetic field are negligibly small in comparison to those in the velocity component perpendicular to the magnetic field. This is most probably related to the differences between driving along the $\overline{\Gamma\mathrm{M}}$ and $\overline{\Gamma\mathrm{K}}$ direction that we discussed in Sec. 6.4 and that are already present without an additional magnetic field. Then, the threefold symmetric Berry curvature of the surface states is symmetric around the $\overline{\Gamma\mathrm{K}}$ axis and antisymmetric with respect to the $\overline{\Gamma\mathrm{M}}$ axis, which leads to a vanishing perpendicular velocity component for driving along $\overline{\Gamma\mathrm{M}}$. Accordingly, for the configuration in panel (c) the effects of the in-plane magnetic field on the perpendicular velocity are approximately zero since for $\mathbf{B} \parallel \mathbf{e}_x$ the geometric properties of the Hamiltonian remain the same. For $\mathbf{B} \parallel \mathbf{e}_y$ however, the mirror symmetry of the Bi_2Te_3 crystal is broken and the gap opening in the surface states gives rise to a non-zero perpendicular velocity even for driving along $\overline{\Gamma\mathrm{M}}$. Still, we are not sure about the reason why in this configuration the parallel velocity is only slightly affected by the magnetic field. For a deeper analysis of the electron dynamics with respect to the different bandstructures and Berry curvatures induced by the magnetic fields, we refer the reader to Riedel's thesis [240].

Apart from the inset in Fig. 7.1(d) we omit presenting the corresponding HHs spectra here. Since the effects of the in-plane magnetic field on the velocities are relatively small, they do not significantly affect the emitted HHs. We expect the largest influence for the field configuration in panel (d), since then the perpendicular velocity is zero for $|\mathbf{B}| = 0$ but arises with increasing magnetic field. Therefore, the magnetic-field effect is not buried within the dynamics of the system that are independent of the magnetic field. Indeed, the HHs spectrum shows an increasing power P emitted with polarization perpendicular to the electric field that scales with the magnetic field strength. Nevertheless, the amplitude of the spectrum is below the one of the parallel emission at all frequencies and therefore – at least for the parameters studied here – the effect is probably not observable in experiment. However, other Hamiltonian and pulse parameters could be investigated in future research in order to find parameters with more promising prospects.

In conclusion, together with Alexander Riedel we found effects of a constant, in-plane magnetic field on the dynamics of electrons in TI surface states with hexagonal warping. Despite the small amplitude of these effects with respect to the total dynamics, the velocity variations Δv potentially contain fingerprints of the dual topological character of TIs from the Bi_2Te_3 family and reflect the distinct symmetries of the system along $\overline{\Gamma M}$ and $\overline{\Gamma K}$ direction. Nevertheless, the small amplitude most likely prevents experimental observation at least within the explored parameter regime.

7.3. Bi_2Te_3 surface states in a constant, out-of-plane magnetic field

Having studied the effects of constant, in-plane magnetic fields in Sec. 7.2, we now turn towards magnetic fields that are perpendicular to the illuminated Bi_2Te_3 surface, i.e. $\mathbf{B} \parallel \mathbf{e}_z$. In this configuration, the magnetic field does not only couple to the system via a Zeeman term but also induces an orbital effect. In order to disentangle the two contributions, in the following we consider the Zeeman and orbital coupling separately. Unfortunately, up to now numerical issues arise when we try to combine orbital effects and the surface Hamiltonian (2.21) with hexagonal warping within our TQT simulations. Therefore, we only consider the full Hamiltonian (2.21) in Sec. 7.3.1 and employ the simple Dirac cone as a model system for obtaining first results with an orbital magnetic field in Sec. 7.3.2.

7.3.1. Influence of Zeeman splitting

As discussed in Sec. 7.2, in an effective model the strength of the Zeeman coupling is described by an effective g factor. For out-of-plane magnetic fields, this g factor has been calculated as $g^z_{\text{eff}} = 13$ for the Bi_2Te_3 surface Hamiltonian (2.21) [87]. Accordingly, neglecting the orbital contribution of the magnetic field, the total effective Hamiltonian reads

$$\hat{\mathcal{H}}(\mathbf{k}) = D(k_x^2+k_y^2)\mathbb{1}+A(k_y\sigma_x-k_x\sigma_y)+2R(k_x^3-3k_xk_y^2)\sigma_z+\frac{1}{2}g^z_{\text{eff}}\mu_{\text{B}}B_z\sigma_z, \quad (7.2)$$

with the Bohr magneton μ_{B} and the magnetic field strength $B_z = |\mathbf{B}\cdot\mathbf{e}_z|$ along the z direction. Like the in-plane field $\mathbf{B} \parallel \mathbf{e}_y$, the out-of-plane field $\mathbf{B} \parallel \mathbf{e}_z$ breaks the mirror symmetry of the Bi_2Te_3 crystal. This lifts the topological protection of the surface states and their spectrum becomes gapped [251].

In his work, Riedel found that the gap induced by an out-of-plane magnetic field has a stronger effect on the electron dynamics driven by an external laser pulse than the gap opened by an in-plane field pointing along the y direction [240]. In Fig. 7.2 we display the results he obtained for $\mathbf{B} \parallel \mathbf{e}_z$ with the simulation parameters summarized in Sec. 7.2. Panel (a) depicts the case where the electric field pulse is applied along the $\overline{\Gamma\text{K}}$ direction of the crystal and panel (b) the case with electric driving along the $\overline{\Gamma\text{M}}$ direction. Since here the magnetic field has a resolvable impact on the generated harmonics, we show the frequency spectra in the main graphs and the magnetic-field dependent changes Δv of the velocities in the insets. We normalize the spectra to the first order P_0 of the parallel emission and the velocities to the respective maximal parallel velocity $v^{\text{max}}_{x/y}$. In order to discriminate between contributions parallel and perpendicular to the polarization of $\mathbf{E}_{\text{el}}$, we dashed the lines corresponding to the parallel components.

As stated by Riedel, the variations Δv in the velocities are at least one order of magnitude larger than for the in-plane magnetic fields. Nevertheless, the temporal shape is similar to what we observe for $\mathbf{B} \parallel \mathbf{e}_y$, which supports our hypothesis that this shape originates from the broken topological protection and the thereby opened band gap. For both electric field configurations, the magnetic field has a stronger impact on the velocity component, and therefore HH emission, perpendicular to the polarization direction of the laser pulse. For $|\mathbf{B}| = 0$, perpendicular emission is suppressed when the laser pulse is polarized along the $\overline{\Gamma\text{M}}$ direction, compare Sec. 6.4. With increasing out-of-plane magnetic field however, such a spectral component emerges, as shown in Fig. 7.2(b).

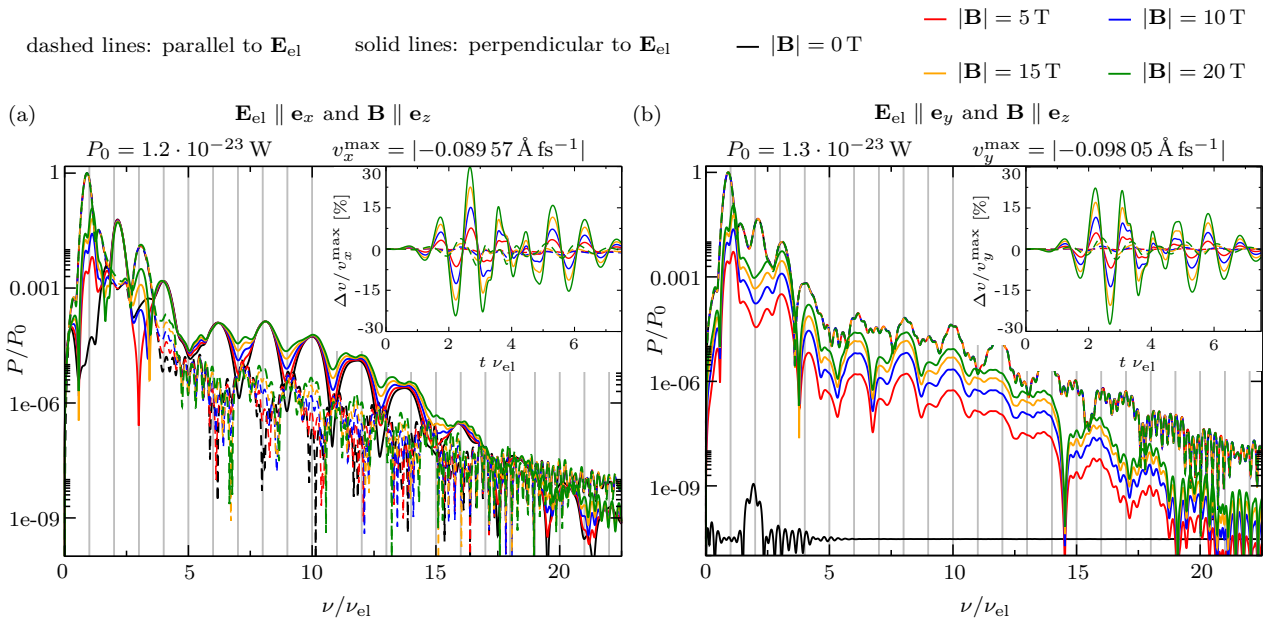

Fig. 7.2: Effects of an out-of-plane magnetic field on the dynamics of Bi_2Te_3 surface electrons driven by short laser pulses polarized along the (a) $\overline{\Gamma K}$ and (b) $\overline{\Gamma M}$ direction of the crystal. The insets depict the differences Δv of the resulting velocities as compared to the respective reference velocity for $|\mathbf{B}| = 0$ shown in Fig. 7.1. This data is rescaled with the corresponding maximal parallel velocities $v_{x/y}^{\max}$, whereas the HHs spectra are normalized to the first-order parallel emission P_0. The dashed curves constitute the component parallel to $\mathbf{E}_{\mathrm{el}}$, whereas the solid lines represent the perpendicular contribution. The changes induced by the magnetic field are at least one order of magnitude larger than for the in-plane magnetic field investigated in Fig. 7.1. Still, the temporal shape of Δv matches our observations for $\mathbf{B} \parallel \mathbf{e}_y$, which is in line with the fact that both magnetic-field configurations lift the topological protection and open a gap in the surface spectrum. For both polarizations of the laser pulse, the additional magnetic field mainly affects the perpendicular velocity and spectral component. For driving along $\overline{\Gamma K}$, panel (a), odd-order harmonics with perpendicular polarization emerge with increasing field strength $|\mathbf{B}|$, whereas for driving along $\overline{\Gamma M}$, panel (b), both odd and even orders only arise in the perpendicular spectrum when a magnetic field $|\mathbf{B}| > 0$ is applied.*

* Data contributed by Alexander Riedel [240].

At low-order harmonics, this perpendicular emission lies at odd-order frequencies, as expected for a gapped Dirac system. For HHs on the contrary, the perpendicular emission consists of both odd and even orders, whereby the amplitude of the even orders mainly exceeds the one of the odd orders. This indicates that the magnetic field also gives rise to signatures of the threefold symmetric Berry curvature in the HHs generated for driving along the $\overline{\Gamma M}$ axis. Nevertheless, even for $|\mathbf{B}| = 20\,\mathrm{T}$, the perpendicular spectrum is buried beneath the parallel one, which makes experimental observation difficult – at least for the parameters discussed here. Still, further investigation of the scaling of the spectra, e.g. with the applied electric-field strength or the warping parameter, could reveal system configurations where experimental detection is possible.

For driving along the $\overline{\Gamma K}$ direction, on the contrary, a spectral component with polarization perpendicular to the incoming laser beam is already present without an applied magnetic field. Since the magnetic field opens a band gap, it induces the additional emission of odd-order harmonics in the perpendicular component. The resulting spectrum plotted in Fig. 7.2(a) can be considered as an overlap of the emission from the hexagonally warped Bi_2Te_3 surface and the gapped Dirac cone we studied in Sec. 6.5. At low harmonic orders, these odd orders are buried below the parallel emission, at high-order harmonics they mainly appear as a decrease of the dents between the even-order harmonics of the perpendicular spectrum. For the system parameters studied by Riedel, these changes in the dents should in principle appear in measurements since the perpendicular emission exceeds the parallel one for $\nu/\nu_{\mathrm{el}} \geq 4$.

We extend the results Riedel obtained for driving along the $\overline{\Gamma K}$ direction by performing simulations for the model Hamiltonian (7.2) with the prefactors given in Ref. [87], i.e. the system introduced in Sec. 2.1.2 and extensively studied in Chap. 6 without a magnetic field. We apply an electric field with pulse shape (6.9) and peak strength $E_{\mathrm{el}} = 0.5\,\mathrm{MV\,cm^{-1}}$ and evaluate the resulting dynamics within the k-mask (6.12) with $k_{x,\mathrm{cut}} = 0.13\,\mathrm{\AA}^{-1}$. Our primary interest is to see how the emitted harmonics depend on the warping parameter R and the magnetic field $\mathbf{B}$.

In panels (a) and (b) of Fig. 7.3, we contrast the HH emission for $|\mathbf{B}| = 0$ and $|\mathbf{B}| = 10\,\mathrm{T}$ for warping parameters from $R = 0$ to $R = 25.6614\,\mathrm{eV\,\AA}^3$, where the highest value is the one computed for the Bi_2Te_3 surface states in Ref. [87]. The most prominent change induced by the non-zero magnetic field is a shift of the peak positions in the emission with polarization perpendicular to the electric pulse E_{el}, as highlighted in the close ups of the plateaus of the spectra[1]. Without magnetic field and for warping $R = 0$, our model system is a simple Dirac cone and, thus, the perpendicular emission is approximately zero. Increasing the warping parameter R leads to an enhancement of the emitted power P, but the peak positions are independent of R. With a non-zero magnetic field, however, for $R = 0$ the model system represents a gapped Dirac cone. Therefore, the perpendicular emission is non-zero but at odd-order harmonics, compare Sec. 6.5. As a consequence, the emitted power does not only grow with the warping parameter R, but the peak positions also shift from odd to even orders. We marked this continuous change in the zoom on the plateau in panel (b).

[1]Note that for better visibility we omit the parallel emission in these insets.

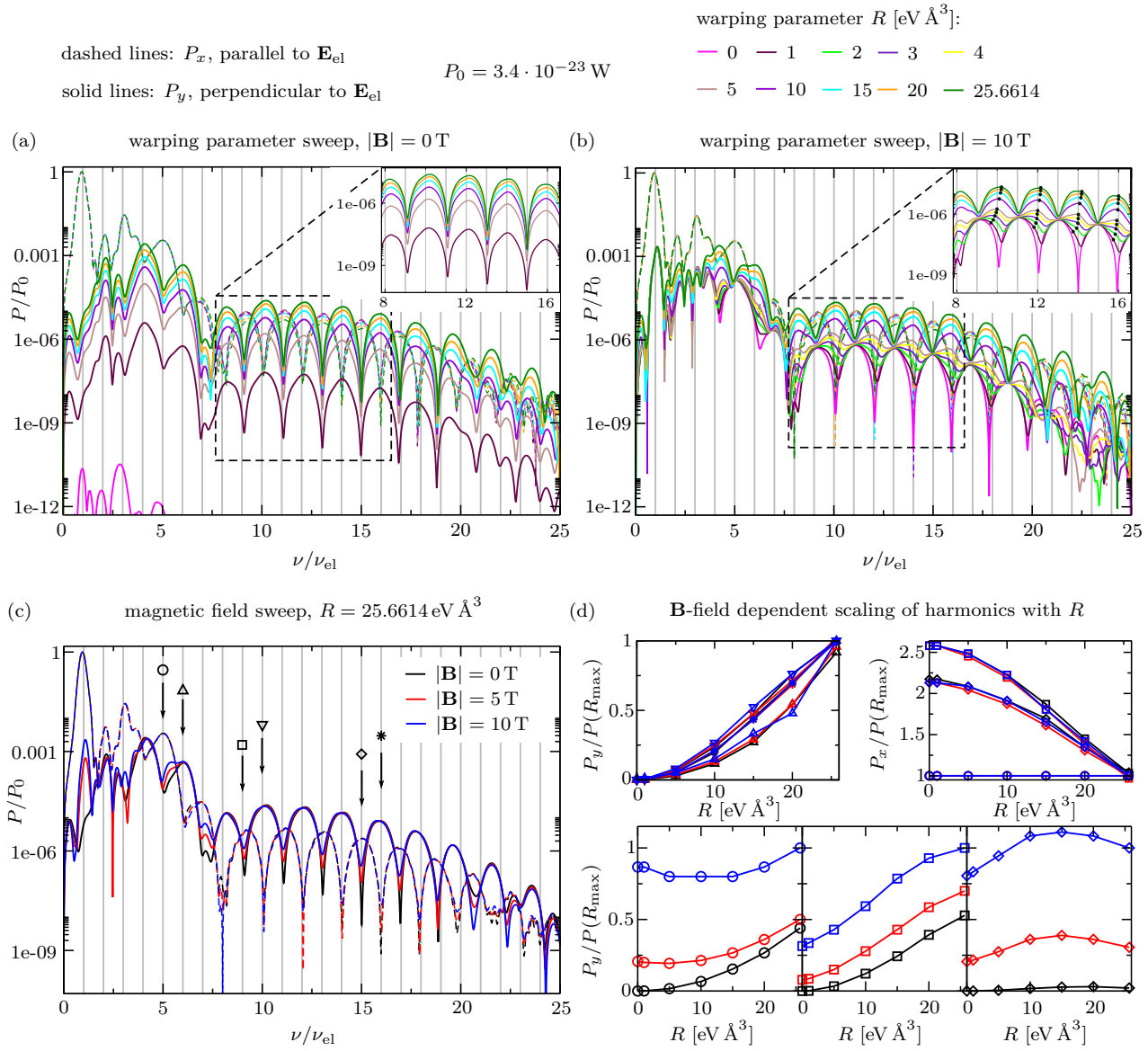

Fig. 7.3: Interaction of magnetic field and hexagonal warping in the generation of HHs for driving along $\overline{\Gamma\mathrm{K}}$. Panels (a) and (b) contrast the influence of an increasing hexagonal warping with and without an additional Zeeman field. The close ups highlight the evolution of the perpendicular emission within the plateau of the spectrum. While for $|\mathbf{B}| = 0\,\mathrm{T}$ the emitted power simply grows with the warping parameter, for $|\mathbf{B}| = 10\,\mathrm{T}$ the peaks also shift from odd to even orders. These spectra combine the properties of a gapped Dirac cone and the hexagonally warped surface states and the warping parameter R determines which contribution dominates. In panel (c) we fix the warping and change the magnetic field, revealing that then the spectra mainly differ in the dents between the even-order peaks of the perpendicular emission. In panel (d) we explore the scaling of different harmonic orders with the warping parameter R for the magnetic fields compared in panel (c). We rescale the extracted data with the power $P(R_{\mathrm{max}})$ of the respective harmonic for $R = R_{\mathrm{max}} = 25.6614\,\mathrm{eV\,Å}^3$ and $|\mathbf{B}| = 10\,\mathrm{T}$. The different marks indicate the corresponding harmonic order. This analysis shows that the magnetic-field effects are strongest at the odd orders of the perpendicular emission.

In experiment, the warping parameter is a material dependent quantity that cannot be tuned. In Fig. 7.3 (c) we keep the warping parameter fixed to $25.6614\,\mathrm{eV\,\AA}^3$ and plot the spectra for three different magnetic field strengths. Like for the system parameters of Riedel shown in Fig. 7.2(a), the magnetic field leads to the emergence of odd-order harmonics that mainly appear as reduced dents between the even-order peaks, but for our warping R these features are buried below the parallel emission. The depth of these dents is determined by the perpendicularly polarized even-order harmonics emitted from the system without warping, as shown in the warping sweep in Fig. 7.3(b). Overall, these findings again highlight that the spectra we observe when an additional out-of-plane magnetic field is applied can be considered as a combination of HHG from a hexagonally warped and a gapped Dirac system.

In order to quantify how different harmonics scale with the magnetic field and the warping parameter, we extract the respective power P at six exemplary harmonic orders, two within the first intensity fall off, two at the onset, and two at the cut off of the plateau[2]. Thereby, we always take one odd and one even order, as marked in Fig. 7.3(c). For comparability, we rescaled all points with the power $P(R_{\mathrm{max}})$ of the spectrum obtained for $R = 25.6614\,\mathrm{eV\,\AA}^3$ and $|\mathbf{B}| = 10\,\mathrm{T}$. The different colors denote the corresponding magnetic field strength and the marks indicate the respective harmonic order as shown in the spectrum in Fig. 7.3(c). In the upper left panel of Fig. 7.3(d), we consider the scaling of even-order harmonics in the emission perpendicular to the driving field. We find that their power increases with the warping R, but the curves are similar for all harmonic orders and magnetic field strengths. In the odd-order harmonics of the parallel emission, see the upper right panel of Fig. 7.3(d), the situation is more complex. For $\nu/\nu_{\mathrm{el}} = 5$, i.e. at the intensity fall-off at the lowest-order harmonics, the emitted power is independent of both the magnetic field and the warping. Within the plateau however, see $\nu/\nu_{\mathrm{el}} = 9$ and $\nu/\nu_{\mathrm{el}} = 15$, the emitted power decreases when the warping grows stronger, but is still independent of the magnetic field. This different behavior once more indicates that the two spectral regions are generated in different areas of momentum space. As discussed in Sec. 6.7, the low-order harmonics originate from states close to the Dirac point, where the linear Dirac dispersion dominates over the hexagonal warping. Therefore, the emitted harmonics are independent of the warping parameter R. The plateau, on the other hand, is determined by emission from states farther away from the Dirac point and thus strongly affected by changes of the warping parameter. One might ask, why these features do not appear in the perpendicular emission. As we have

[2]Since the peaks are not always exactly located at integer multiples of the driving frequency, we do not compare the maxima of the peaks but the amplitude P of the spectra at fixed frequency values.

seen in Chaps. 5 and 6, the perpendicular spectrum is strongly dependent on the Berry curvature of the system and not only on the band dispersion. Unlike the energy bands, the Berry curvature is shaped by the hexagonal warping at all momenta, compare Fig. 5.3. Accordingly, the perpendicular spectra scale with the warping parameter at all harmonic orders. This difference also explains why the power of the perpendicular emission increases with the warping, whereas the power of the plateau in the parallel spectrum decreases. The Berry curvature grows with the warping, while the strong nonlinearity of the Dirac dispersion gets reduced by the higher-order momentum term in the Hamiltonian.

In the lower row of Fig. 7.3(d), we analyze the magnetic-field and hexagonal-warping dependency of the odd-order harmonics with polarization perpendicular to the laser pulse. Only in these powers, which in most cases appear as dents instead of peaks in the spectrum, we find a strong influence of both $\mathbf{B}$ and R on the scaling. As discussed previously, this perpendicular emission at odd orders is a signature of the gap opened by the magnetic field. In terms of the Berry curvature, this gap opening induces a competition between the Berry curvature of a gapped Dirac cone and of the hexagonally warped surface states, see Fig. 5.3 for reference. For the gapped cone, one obtains only odd harmonics with perpendicular polarization and for the surface states only even orders, as observed in Sec. 6.5. In the combined case resulting from the Zeeman coupling, we find that the power emitted at odd orders grows with the magnetic field strength, as expected for an increasing gap size within the Berry-curvature interpretation. Additionally, we notice a different dependency on the warping parameter for each analyzed harmonic, which in the meantime is independent of the magnetic-field strength. Currently, we are not sure how to interpret this scaling with the warping parameter. Nevertheless, the picture of competing Berry curvatures explains the shift from odd to even harmonics in the perpendicular emission for a fixed magnetic field and increasing warping parameter, as discussed in Fig. 7.3(b). As long as the gapped cone dominates, the peaks lie at odd-order harmonics. With increasing influence of the hexagonal warping term, the peaks continuously shift towards even orders, but the contribution of the gapped cone is still present and limits the dents between two neighboring peaks. For the system parameters from Ref. [87] studied here, the discussed features are buried below the parallel emission, but in Riedel's system configuration they exceed the parallel spectral component, see Fig. 7.2(a). Therefore, further investigation for realistic material parameters could reveal a setup where experimental observation of this out-of-plane Zeeman effect is possible.

7.3.2. Including orbital effects

So far we have only considered the Zeeman effect induced by an out-of-plane magnetic field $\mathbf{B} \parallel \mathbf{e}_z$, see Sec. 7.3.1. In the following, we present first studies on the corresponding orbital contribution. The orbital magnetic-field effect is introduced into the effective Hamiltonian by minimal coupling, i.e. the substitution $\mathbf{k} \to \mathbf{k} + \frac{e}{\hbar}\mathbf{A}(\mathbf{r})$. Thereby, the vector potential $\mathbf{A}(\mathbf{r})$ describing the magnetic field $\mathbf{B}$ has to fulfill

$$\mathbf{B} = \nabla_{\mathbf{r}} \times \mathbf{A}(\mathbf{r}) \tag{7.3}$$

and for $\mathbf{B} \parallel \mathbf{e}_z$ can be written as $\mathbf{A}(\mathbf{r}) = (A_x(\mathbf{r}), A_y(\mathbf{r}), 0)$. In simulations using TQT the orbital effect can either be introduced by hand when defining the system's Hamiltonian or by using a TQT-internal method. The latter option is especially favorable for models with nonlinear momentum contributions, since then a definition by hand requires caution with commutators between the position and momentum operator. The TQT routine circumvents these commutators by applying subsequent gauge transformations on the vector potential $\mathbf{A}(\mathbf{r})$, see Sec. 3.4 for details.

Even though we employ the TQT-internal function for our calculations, it is important to know how the minimal coupling changes the Hamiltonian. For the TI surface states, the model (2.21) with orbital coupling reads

$$\begin{aligned}\hat{\mathcal{H}}(\mathbf{k},\mathbf{r}) =& D\left[\left(k_x + \frac{e}{\hbar}A_x(\mathbf{r})\right)^2 + \left(k_y + \frac{e}{\hbar}A_y(\mathbf{r})\right)^2\right]\mathbb{1} \\ &+ A\left[\left(k_y + \frac{e}{\hbar}A_y(\mathbf{r})\right)\sigma_x - \left(k_x + \frac{e}{\hbar}A_x(\mathbf{r})\right)\sigma_y\right] \\ &+ 2R\left[\left(k_x + \frac{e}{\hbar}A_x(\mathbf{r})\right)^3 - 3\left(k_x + \frac{e}{\hbar}A_x(\mathbf{r})\right)\left(k_y + \frac{e}{\hbar}A_y(\mathbf{r})\right)^2\right]\sigma_z.\end{aligned} \tag{7.4}$$

The terms of second and third order in momentum give rise to products of k_x, k_y and the components $A_x(\mathbf{r})$, $A_y(\mathbf{r})$ of the vector potential. Since the velocity operator is defined as $\hat{\mathbf{v}} = \frac{1}{\hbar}\nabla_{\mathbf{k}}\hat{\mathcal{H}}(\mathbf{k},\mathbf{r})$, it is modified by these mixed terms and obtains a spatial dependence through $\mathbf{A}(\mathbf{r})$. Currently, we have not implemented the necessary numerical routines to treat such a spatially dependent velocity operator in TQT. On top of that, we encounter problems with the stability of our simulations when including the hexagonal warping term and the orbital coupling simultaneously. Resolving these issues will be a task for the future. Within this work, we omit the PHS breaking and the

hexagonal warping and only study the orbital effects for the simple Dirac cone

$$\hat{\mathcal{H}}(\mathbf{k},\mathbf{r}) = A\left[k_y\sigma_x - k_x\sigma_y + \frac{e}{\hbar}\left(A_y(\mathbf{r})\sigma_x - A_x(\mathbf{r})\sigma_y\right)\right]. \tag{7.5}$$

Then, the velocity operator reduces to

$$\hat{\mathbf{v}} = \frac{A}{\hbar}\begin{pmatrix}-\sigma_y\\ \sigma_x\end{pmatrix}. \tag{7.6}$$

Generally, the equations of motion of a state restricted to one band n and driven by an electric field $\mathbf{E}_{\mathrm{el}}$ and a magnetic field $\mathbf{B}$ are given by

$$\frac{\mathrm{d}\mathbf{r}}{\mathrm{d}t} = \frac{1}{\hbar}\nabla_{\mathbf{k}}E_n(\mathbf{k}) + \frac{\mathrm{d}\mathbf{k}}{\mathrm{d}t}\times\boldsymbol{\Omega}_n(\mathbf{k}) \tag{7.7}$$

in real space and by

$$\hbar\frac{\mathrm{d}\mathbf{k}}{\mathrm{d}t} = -e\mathbf{E}_{\mathrm{el}} - e\frac{\mathrm{d}\mathbf{r}}{\mathrm{d}t}\times\mathbf{B} \tag{7.8}$$

in momentum space [252]. For a Dirac dispersion $E_n(\mathbf{k}) = n\,A|\mathbf{k}|$, with band label $n = \pm$, the Berry curvature $\boldsymbol{\Omega}_n$ is zero. In this case, solving Eqs. (7.7) and (7.8) for $\mathbf{E}_{\mathrm{el}} = 0$ leads to a circular motion of the states, see e.g. Krückl's thesis for details [182]. In momentum space, these circles are described by

$$\mathbf{k}(t) = |\mathbf{k}_i|\begin{pmatrix}\cos(\omega_{\mathrm{c}}t + \theta_{\mathbf{k}})\\ \sin(\omega_{\mathrm{c}}t + \theta_{\mathbf{k}})\end{pmatrix}, \tag{7.9}$$

where $\omega_{\mathrm{c}} = AeB/(\hbar^2|\mathbf{k}_i|)$ is the cyclotron frequency and $\mathbf{k}_i = |\mathbf{k}_i|\exp(\mathrm{i}\theta_{\mathbf{k}})$ is the initial momentum of the state. When additionally applying the electric field pulse (5.10), these circles are deformed by the drift of the states caused by the electric field.

Here, we aim at studying how the emitted HHs are affected by the orbital coupling of the magnetic field. To this end, we use the Fermi sea method as introduced in Chap. 6 with the static k-mask (6.12). We set the electric peak strength to $E_{\mathrm{el}} = 0.5\,\mathrm{MV\,cm^{-1}}$ and find convergence for $k_{x,\mathrm{cut}} = 0.13\,\mathrm{Å}^{-1}$. Due to the circular motion induced by the orbital magnetic field, we increase the grid size in y direction to $N_y = 2048$ and reduce the time step to $\delta t = 0.05\,\mathrm{fs}$ for a stable propagation in TQT. The other simulation parameters are set as listed in App. A.10. We restrict ourselves to comparably small fields, $|\mathbf{B}| \leq 0.1\,\mathrm{T}$, since we observe that the k-mask is not fully covered by the wave packet at all times, whereby the issue grows with the magnetic field strength. Due to this problem, the results discussed in the following are preliminary.

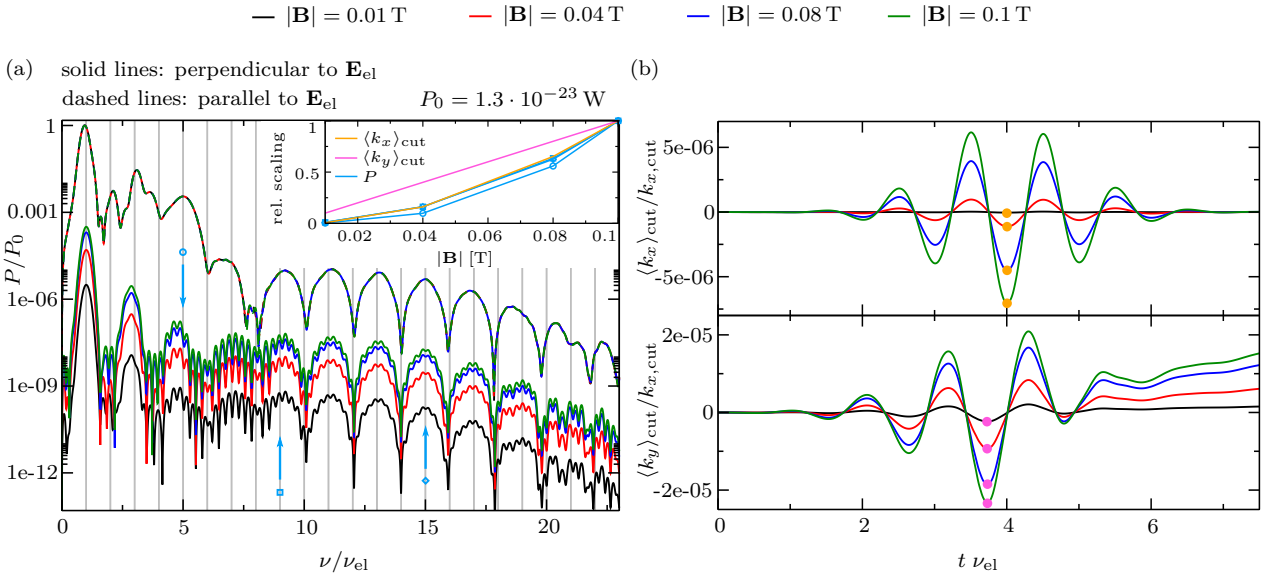

Fig. 7.4: Effect of an orbital magnetic field on HHG from a Dirac cone. (a) HHs spectra for different magnetic field strengths $|\mathbf{B}|$. The emission parallel to the driving laser's polarization is independent of the magnetic field, but a perpendicular component emerges with increasing $|\mathbf{B}|$. (b) Momentum-space center of mass $\langle k_{x/y} \rangle_{cut}$ of the wave packet within the k-mask. Ideally, these curves would be at least eight orders of magnitude smaller than the k-mask boundary $k_{x,cut}$, see App. A.8. Here, we find results that are only five to six orders of magnitude smaller. Since these deviations grow with the magnetic field strength, we restrict our studies to comparably small values of $|\mathbf{B}|$. In order to determine whether the imperfections of the k-mask coverage have an influence on the computed HHs, in the inset in panel (a) the magnetic-field scaling of the marked harmonic orders is compared to the dependency of the maxima of $\langle k_{x/y} \rangle_{cut}$ on $|\mathbf{B}|$. For comparability, all curves are plotted relative to their value at $|\mathbf{B}| = 0.1$ T. Since for $\langle k_y \rangle_{cut}$ the scaling differs from the one of $\langle k_x \rangle_{cut}$ and the power P of the harmonics, we conclude that the observed orbital effect is physical and not just a result of the numerical issues with the k-mask. Still, this has to be confirmed by additional simulations with wave packets with larger $|\mathbf{k}_{lim}|$ in the future.

In Fig. 7.4(a), we compare the HHs spectra for different magnetic field strengths $|\mathbf{B}|$ obtained for an initial wave packet with envelope as defined in Eq. (6.10) and $|\mathbf{k}_{lim}| = 0.22\,\text{Å}^{-1}$. The parallel emission is not affected by the orbital effect, whereas the perpendicular emission increases with $|\mathbf{B}|$. Since without magnetic field the perpendicular emission from a pure Dirac system is zero, this emerging spectral component is a consequence from additional phases the states acquire due to the circular motion induced by the orbital field. Presumably, this phase is the Berry phase, $\gamma_\pm = \pm\pi$, a state picks up when enclosing the Dirac point on its trajectory in momentum space [253]. However, this interpretation has to be verified in future studies. As no hexagonal warping is present in our model system, these perpendicular HHs lie at odd-order multiples of the driving frequency. In the inset of panel (a), we analyze how the odd harmonic orders we already investigated for the Zeeman field in Fig. 7.3 scale with the orbital magnetic field. Thereby, we normalize all curves

to their respective value for $|\mathbf{B}| = 0.1\,\mathrm{T}$ and find a nonlinear dependency on $|\mathbf{B}|$ that is similar for all considered harmonics.

Due to the circular motion in momentum space, the k-mask is not perfectly covered by the propagated wave packet at all times. In Fig. 7.4(b), we show the momentum-space center of mass $\langle k_{x/y}\rangle_{\mathrm{cut}}$ of the wave packet within the k-mask. We find an oscillatory deviation from zero that is five to six orders of magnitude smaller than the limit $k_{x,\mathrm{cut}}$ of the k-mask and grows with the applied field strength $|\mathbf{B}|$. For a reference, in App. A.8 we check the coverage of the k-mask for a wave packet without external magnetic fields. There, we observe that, for a fully covered k-mask, $\langle k_{x/y}\rangle_{\mathrm{cut}}$ is eight orders of magnitude smaller than $k_{x,\mathrm{cut}}$, whereas imbalances at the borders of the k-mask at the peaks of the electric pulse lead to spikes that are only three orders of magnitude smaller than $k_{x,\mathrm{cut}}$. The deviations we obtain with the orbital magnetic field lie in between the two cases and thus might not affect the computed dynamics. To gain a first intuition whether the observed features in the HHs spectra in Fig. 7.4(a) are actually a physical consequence of the orbital magnetic field, and not only a result from the numerical issue of the temporarily unbalanced occupation of the k-mask, we extract the scaling or the highest peak of $\langle k_{x/y}\rangle_{\mathrm{cut}}$ and include it in the inset of Fig. 7.4(a). This comparison reveals that $\langle k_x\rangle_{\mathrm{cut}}$ has indeed the same magnetic-field dependence as the power of the different harmonics, but $\langle k_y\rangle_{\mathrm{cut}}$ shows a linear increase with $|\mathbf{B}|$. Since we only observe an influence of the orbital effect on the perpendicular emission, we assume that the emerging spectrum is physical. Nevertheless, the simulations should be repeated for a wave packet with larger $|\mathbf{k}_{\mathrm{lim}}|$ in the future to confirm this assumption.

In conclusion, we find first fingerprints of an orbital magnetic field effect on HHG from a simple Dirac system. Even though the presented data is preliminary, it strongly indicates that the orbital coupling gives rise to HHs with polarization perpendicular to the driving laser pulse. We assume that these additional spectral features arise due to the Berry phase of $\pm\pi$ that states acquire when circling the Dirac point during the motion induced by the orbital magnetic field. In future studies, the wave-packet definition has to be varied in order to confirm these observations. Additionally, our numerical routine has to be extended such that also systems with higher-order momentum contributions, like the hexagonal warping of the Bi_2Te_3 surface states (7.4), can be simulated. The final step is to combine the Zeeman and the orbital effect in order to obtain a complete picture of the influence of perpendicular magnetic fields on HHG from TI surface states.

7.4. Outlook: Including the pulse as an electromagnetic wave

Within this thesis, we have approximated the laser pulse as a purely electric wave of the form (5.10) and disregarded the magnetic contribution. Generally, the electric field $\mathbf{E}_{\mathrm{el}}(\mathbf{r},t)$ and magnetic field $\mathbf{B}(\mathbf{r},t)$ are described by a vector potential $\mathbf{A}(\mathbf{r},t)$ and a scalar potential $\phi_{\mathrm{el}}(\mathbf{r},t)$ as

$$\begin{aligned}\mathbf{E}_{\mathrm{el}}(\mathbf{r},t) &= -\frac{\partial \mathbf{A}(\mathbf{r},t)}{\partial t} - \nabla_{\mathbf{r}}\phi_{\mathrm{el}}(\mathbf{r},t),\\ \mathbf{B}(\mathbf{r},t) &= \nabla_{\mathbf{r}} \times \mathbf{A}(\mathbf{r},t).\end{aligned} \tag{7.10}$$

For an exact representation of a focused, few-cycle laser pulse, defining these potentials in line with Maxwell's equations becomes challenging. We recommend using the closed analytical form presented in Ref. [254] for such pulses, if a full description is necessary. However, oftentimes the scales of the investigated system allow for simplifications of the pulse form. Since this work has been motivated by the HHG experiment on Bi_2Te_3 in Ref. [81], among others, we take the laser pulse employed there for reference. In the experiment, a Gaussian laser beam was focused to a spot of about $60\,\mu$m full width at half maximum on the Bi_2Te_3 crystal, see Fig. 7.5(a) for a sketch. Our simulations are confined to a numerical grid representing a system with less than $2.5\,\mu$m width[3], however. Thus, in the real space area covered by the wave packet propagated in these simulations, the Gaussian shape of the laser spot is negligible and we consider a pulse with infinite extension on the 2D surface instead. Choosing the gauge $\phi_{\mathrm{el}}(\mathbf{r},t) = 0$ and $\mathbf{A}(\mathbf{r},t) = (A_x(\mathbf{r},t), 0, 0)$, we define the pulse based on the vector potential

$$A_x(\mathbf{r},t) = -\frac{E_{\mathrm{el}}}{\omega}\,\exp\left(-\frac{t^2}{2\Delta t^2}\right)\cos\left(\frac{n_{\mathrm{r}}\omega}{c}\left(y\cos\theta - z\sin\theta\right) + \omega t\right), \tag{7.11}$$

where $\mathbf{r} = (x,y,z)$ describes the propagation of the wave, θ is the angle of incidence on the 2D surface, n_{r} the refractive index, $\omega = 2\pi\nu_{\mathrm{el}}$ the pulse frequency, and c the speed of light. The corresponding system geometry is sketched in Fig. 7.5(b). Using Eq. (7.10), we obtain the fields

$$\begin{aligned}\mathbf{E}_{\mathrm{el}}(\mathbf{r},t) =& E_{\mathrm{el}}\,\exp\left(-\frac{t^2}{2\Delta t^2}\right)\sin\left(\frac{n_{\mathrm{r}}\omega}{c}\left(y\cos\theta - z\sin\theta\right) - \omega t\right)\mathbf{e}_x\\ &+ \frac{E_{\mathrm{el}}t}{\omega\Delta t^2}\exp\left(-\frac{t^2}{2\Delta t^2}\right)\cos\left(\frac{n_{\mathrm{r}}\omega}{c}\left(y\cos\theta - z\sin\theta\right) + \omega t\right)\mathbf{e}_x\end{aligned} \tag{7.12}$$

[3] As shown in App. A.10, the largest grid we use in TQT has 4096 points with a spacing of 6 Å.

and

$$\mathbf{B}(\mathbf{r},t) = -\frac{E_{\mathrm{el}} n_{\mathrm{r}}}{c} \exp\left(-\frac{t^2}{2\Delta t^2}\right) \sin\left(\frac{n_{\mathrm{r}}\omega}{c}\left(y\cos\theta - z\sin\theta\right) + \omega t\right) \begin{pmatrix} 0 \\ \sin\theta \\ \cos\theta \end{pmatrix}. \tag{7.13}$$

Since our simulations are restricted to a 2D plane, we set $z = 0$. Neglecting the second term of $\mathbf{E}_{\mathrm{el}}(\mathbf{r},t)$ in Eq. (7.12), we find the relation $|\mathbf{B}| = \frac{n_{\mathrm{r}}}{c}|\mathbf{E}_{\mathrm{el}}|$ between the amplitudes of the two waves. By additionally assuming the approximation $y = 0$ is justified, we retrieve the electric field (5.10), employed for the HH simulations shown throughout this thesis, from Eq. (7.12). We compare the wave forms of the pulses (5.10) and (7.12) for $y = z = 0$ in Fig. 7.5(c). The contribution of the second term of Eq. (7.12) is about one order of magnitude smaller than the peak amplitude of the total pulse. Thus, the additional term mainly affects the initial and final oscillation cycles, where the overall amplitude is comparable to the one of this term. We conclude that the pulse definition (5.10) is a good approximation as long as magnetic field effects are neglected and $y = z = 0$. Concerning the validity of the approximation $y = 0$, further investigation is necessary. For the pulse frequency $\nu_{\mathrm{el}} = 25\,\mathrm{THz}$ and the refractive index $n_{\mathrm{r}} = 10$ of Bi_2Te_3, we obtain a wave length $\lambda = c/(n_{\mathrm{r}}\nu_{\mathrm{el}}) \approx 1.3\,\mu\mathrm{m}$, which is of the same order of magnitude as our system in TQT. However, the relevance of the y dependence is determined by the extent of the propagated wave packet in real space, which is a quantity we have not paid particular attention to so far.

In principle, it is possible to implement the fields (7.12) and (7.13) in TQT via minimal coupling of the vector potential (7.11). As long as the spatial dependence in y is considered, this minimal coupling induces the orbital effect of the z component[4] of $\mathbf{B}(\mathbf{r},t)$. The Zeeman effects have to be added by hand using the magnetic field (7.13), as described in Secs. 7.2 and 7.3.1. But, as discussed in Sec. 7.3.2, the spatial dependence of the velocity operator resulting from higher-order momentum contributions in the system Hamiltonian in combination with the vector potential (7.11) cannot be treated by the algorithm yet. Moreover, here $\mathbf{A}(\mathbf{r},t)$ also contains a time dependence which we cannot add to the currently defined velocity operator neither. The only option to gain first insights into the wave-packet dynamics for the full pulse would be to omit the k-mask and to use the COM observable instead, see Sec. 3.5 for an introduction.

The spatial inhomogeneity of the fields (7.12) and (7.13) also gives rise to the

[4]Note that without the y dependence, the magnetic wave would be zero, compare Eq. (7.10). Then, the minimal coupling is only another option for applying the electric field $\mathbf{E}_{\mathrm{el}}(t)$.

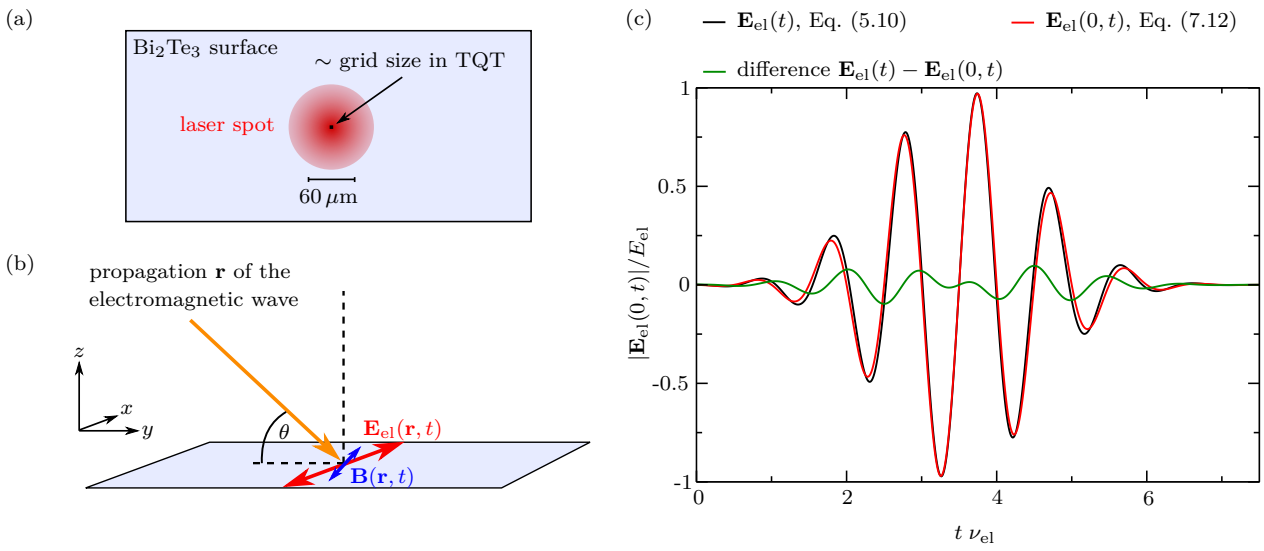

Fig. 7.5: Sketch of (a) the laser spot from the experiment [81] and (b) the corresponding field directions. Since the size of our numerical grid is small in comparison to the laser spot, we assume a homogeneous field distribution in our model. The fields are aligned such that the electric field polarization lies in the Bi_2Te_3 surface plane and the magnetic wave has a component in the sample as well as perpendicular to it, depending on the chosen angle of incidence θ. (c) Comparison of the definition (5.10) for the electric wave employed throughout this work and the electric field (7.12) derived from the vector potential (7.11). Due to the additional spatial dependence, the potential (7.11) also contains the magnetic component (7.13) of the light field. In this derivation, the electric field obtains a second term, compare Eq. (7.12). The amplitude of this term is one order of magnitude smaller than the peak strength of the total pulse and mainly affects the onset and the last oscillations of the pulse. Thus, we conclude that the definition (5.10) used throughout this work is a good approximation as long as magnetic-field effects are neglected.

question of where to set the origin of the coordinate system with respect to the initial position of the propagated wave packet. One solution for this problem is to average over various configurations of the system in real space. The *Lanczos Source propagator* we introduced in Sec. 3.3 offers another possibility to resolve this issue. With this propagator, plane waves instead of wave packets can be considered as initial states with the restriction that the applied time-dependent potentials are localized in real space. The basic idea of the algorithm is to split the time evolution of the system in a trivial and a non-trivial part, in order to circumvent numerical issues caused by the plane wave extending over the full numerical grid. This splitting is achieved by interpreting the localized potential as a source term that generates a wave packet out of the plane wave. The wave packet undergoes the non-trivial time evolution caused by the potential, while the time evolution of the plane wave is simply defined by the time-independent system. In App. A.12 we show our testing of this new propagator using a 1D Fabry-Perot system and a comparison with TKWANT. As discussed in App. A.12.4, by integration over the observables calculated for all relevant plane waves, the Fermi sea can be taken into account, similar

to the k-mask approach we introduced for wave packets in Chap. 6. Note that in this context, *relevant* refers to all momenta that would lie within the k-mask when using the wave-packet approach, compare Sec. 6.3.3. For the Lanczos Source propagator, instead of the vector potential (7.11), a pulse description that additionally takes the spot size in real space into account has to be derived based on Ref. [254]. Then, the requirement of a localized potential is naturally fulfilled. Employing this new propagator to study HHG with an exact definition of a focused, few-cycle laser pulse is a promising task for future research.

8. Conclusion

Throughout this thesis we studied the dynamics of Dirac electrons under different types of driving by employing wave-packet-based approaches. To conclude our investigations, in the following we briefly summarize our main findings and give an outlook on interesting questions for future research.

We started our work considering time-periodic driving protocols (Chap. 4). Then, the electron motion can be understood within the framework of an effective Floquet quasi bandstructure. We showed that electrons perform Bloch-like oscillations when they are moved through Floquet bands which are (quasi)periodic in momentum space by an additional static electric field. Due to this analogy, we dubbed the phenomenon *Floquet oscillations* [74]. From the viewpoint of the static system's bandstructure, Floquet oscillations can also be interpreted as consecutive electron transitions at (multi-)photon resonances of the driving field with the local energy gap. Thereby, the inverse proportionality of the Floquet oscillation's frequency to the driving frequency can be explained. For our demonstration, we focused on Dirac-like dispersions, which are found e.g. in graphene, TIs, and cold atoms in artificial honeycomb lattices. We investigated two driving schemes that couple the branches of the Dirac cone and thus lead to the formation of (quasi)periodic Floquet bands in a certain range of momentum space. We obtained the resulting Floquet oscillations by propagating wave packets by numerically solving the time-dependent Schrödinger equation and by computing the wave-packet dynamics using Floquet theory. In real space, the oscillations feature an amplitude modulation that resembles the Floquet bands, thus offering an experimental tool for mapping out Floquet bandstructures. Moreover, Floquet oscillations are modified by Zitterbewegung and we found first indications that they contain traces of the Floquet band's Berry curvature. We also explored the experimental feasibility of Floquet oscillations in graphene and concluded that, by correct tuning of the parameters, experimental realization should be possible. Overall, our studies provide a link between the intuitive time-dependent picture and the Floquet framework. The potential of using Floquet oscillations for studying the Berry curvature of the Floquet system

and for the experimental detection of Zitterbewegung could be investigated in future research. Additionally, a generalization of the concept to other bandstructures could be considered in order to identify further platforms for experimental realization. In principle, by taking small frequencies in comparison to the bandwidth and a driving mechanism that efficiently couples the bands, an arbitrary bandstructure can be transformed to (quasi)periodic Floquet bands. However, suitable parameters have to be found such that the Floquet oscillation's period T_F is smaller than the scattering time τ_s of the electrons in the system. Otherwise, experimental detection of the Floquet oscillations is not possible.

For the remainder of the presented work (Chaps. 5 - 7), we switched from periodic driving to ultrashort laser pulses. Those studies were initially motivated by the experimental observation of HHG from the surface states of the 3D TI Bi_2Te_3. In a collaboration with several theoretical and experimental groups, we were able to demonstrate that the emitted harmonics are governed by the Dirac-like dispersion of the surface states. On top of that, the measurements confirmed that the polarization of the different harmonic orders contains fingerprints of the system's Berry curvature, as already predicted in earlier works [85]. The results of our joined efforts are published in Ref. [81]. Despite providing an intriguing insight into the nonlinear dynamics of topologically protected surface states, the experimental findings also raised further questions about the occurring processes. In this thesis we displayed a more detailed analysis of the dynamics of the TI surface electrons under strong and short laser pulses, focusing on the quantum processes influencing the HHG.

First, we investigated the motion of single test charges, that we modeled as narrow wave packets in momentum space, in Chap. 5. Thereby we compared four Dirac-based Hamiltonians with different Berry curvatures: a simple Dirac cone, a gapped Dirac cone and a higher-order momentum expansion of the Bi_2Te_3 surface Hamiltonian which includes a hexagonal warping term. For the latter we contrasted two different parameter sets from the literature [81, 87]. Our studies of the resulting velocity expectation values for both constant fields and short pulses confirmed the imprint of the Berry curvature especially on the velocity component perpendicular to the polarization of the incoming radiation. By varying the pulse strength and the initial momentum of the wave packets we explored different transition regimes following the classification of Heide et al. [173]. Thus, we could affirm that the threefold symmetric Berry curvature imposed by the hexagonal warping is crucial to recreate the experimentally observed polarization pattern of the HHs spectrum. Our findings also highlight the great diversity of the dynamics and transition processes occurring when

the Bi_2Te_3 surface interacts with a strong laser pulse. In an experiment at the current state of the art it is not possible to only select a particular part of these processes. Instead, the recorded HHs spectra contain the emission resulting from the interference of all electron dynamics driven within the bands. Accordingly, computing spectra from the velocities of only a few test charges is insufficient when looking for the interpretation of experimental data. Therefore, in Chap. 6, we developed a novel method to simulate HHG from a full Fermi sea using a wave-packet approach and effective model Hamiltonians without band bottom. To avoid spurious contributions due to the finite wave packet, we introduced a k-mask in which the velocities were evaluated. This k-mask also constitutes the only kind of dephasing entering our ansatz since it neglects everything outside of its momentum area. Overall, our Fermi sea approach is complementary to investigating HHG using the semiconductor Bloch equations without dephasing [95]. Nevertheless, being based on wave packets, it offers a more intuitive and illustrative insight into the system's dynamics. Our studies of the influence of the k-mask shape and the Fermi energy on the resulting HHs spectra revealed that the low-order harmonics and their fine structure are mainly contributed by states close to the Dirac point, whereas the high-order harmonics of the plateau are affected by states experiencing larger local energy gaps. This momentum dependence indicates the necessity of introducing momentum-dependent dephasing in future HHs calculations to improve the agreement between theoretical and experimental data. Additionally, we could show that our novel method allows for the qualitative investigation of HHG in Dirac systems and significantly increases the quality of the resulting HHs spectra as compared to calculations without a k-mask or for single test charges only.

An advantage of the presented approach over the semiconductor Bloch equations is that one can integrate spatially dependent potentials into the algorithm. This enables taking the full electro*magnetic* wave of the laser pulse into account. In Chap. 7 we presented first results on how magnetic field effects influence HHG in effective Dirac systems. Thereby, we focused on constant magnetic fields for simplicity. The Zeeman coupling of a magnetic field opens band gaps in the energy dispersion and thus can modify the Berry curvature and therefore also the HHs spectrum. The orbital effects of an out-of-plane magnetic field induce a cyclic motion of the states in momentum space, potentially leading to fingerprints of a Berry phase that is picked up when the Dirac point is enclosed in the electron trajectory. This phase effect appears to only affect the HH emission perpendicular to the driving field. Unfortunately, so far it is not possible to include the hexagonal warping terms and orbital effects into the simulation simultaneously. Therefore, further development of our numerical

method and a deeper analysis is required to draw final conclusions on how static magnetic fields imprint on HHs spectra from Bi_2Te_3 surface states. To fully explore the influence of magnetic fields and especially of the magnetic component of the laser pulse on HHG in TI surface states, not only constant but also time-dependent magnetic fields have to be investigated. Due to the relatively large refractive index ($n_\mathrm{r} \approx 10$) of Bi_2Te_3, the magnetic component of the light field can reach peak strengths of $|\mathbf{B}| = \frac{n_\mathrm{r}}{c}|\mathbf{E}_\mathrm{el}| \approx 10\,\mathrm{T}$ for an electric peak field of $|\mathbf{E}_\mathrm{el}| \approx 3\,\mathrm{MV\,cm^{-1}}$, which is the order of magnitude applied in the experiment [81]. Whether the resulting HHs spectra contain fingerprints of the magnetic component or are unaffected by it, has to be determined in future studies. For such studies, the strong real-space localization of the wave packet representing the Fermi sea may become problematic. It is still unclear, whether this localization leads to spurious effects when considering potentials with an inhomogeneous spatial dependence such as the vector potential describing the orbital coupling of a magnetic wave. To investigate this, one might have to switch from wave packets to plane waves that are localized in momentum space but cover the full real space. The Lanczos Source propagator we implemented in TQT is capable to treat such plane waves in a setup with time-dependent and spatially localized potentials. In future studies, it can be applied to extend our understanding of the interaction of TI surface states with electromagnetic waves.

But even leaving the magnetic field aside again, further analysis of HHG from TI surface states is required. As already mentioned, our results indicate that a better understanding of dephasing mechanisms and their momentum dependence is necessary in order to improve the agreement between experimental data and theoretical predictions. Additionally, the interplay of intraband and interband effects in the process of HHG is still not completely clear. Since these effects are also affected differently by the dephasing mechanisms, other methods based on e.g. the semiconductor Bloch equations are better suited to perform a deeper analysis in that direction.

In order to obtain a new perspective on HHG, one could also consider using approaches based on the Floquet formalism. For continuous radiation, such methods have already been established [255, 256] and even allowed for obtaining analytical results [257]. With a newly proposed Floquet group theory, selection rules for the generated harmonics and their respective polarization have been derived [258]. A recent experiment demonstrated that the formation of Floquet bands does not require time-periodic driving but already sets in after one oscillation cycle of a laser pulse. By employing time-resolved ARPES measurements, Ito et al. recorded the build-up of the Floquet band's population

as well as the intraband motion of the excited electrons in the surface states of Bi_2Te_3 [259]. They used a similar laser pulse as for the observation of HHG from said surface states presented in Ref. [81] and discussed throughout this work. Hence, Floquet theory could also extend our understanding of HHG from TI surface states and pulsed systems in general. During our work on this thesis we assisted first studies of Yuriko Baba which aimed at a theoretical modeling of the build-up of Floquet bands and their population in Dirac systems using the so-called $t - t'$ formulation [260, 261]. In future research, these investigations could be extended in order to calculate HHs spectra and to gain deeper insights into the occurring quantum processes from the perspective of a Floquet framework.

In conclusion, our work established new insights into the interaction of Dirac systems with strong, time-dependent potentials. We proposed the concept of Floquet oscillations for time-periodic driving as well as investigated HHG from Dirac-like states. Additionally, we devised a novel method for calculating HHG from a Fermi sea based on the propagation of wave packets. Our studies pave the way for a better understanding of the physical interpretation of Floquet theory and the quantum processes leading to the generation of HHs in strongly driven solids.

A. Appendix

A.1. Calculation of the velocity matrix elements

In this section we give a more detailed derivation of the matrix elements of the velocity operator $\hat{\mathbf{v}} = \frac{\mathrm{i}}{\hbar}\left[\hat{\mathcal{H}}(\mathbf{k}), \hat{\mathbf{r}}\right]$ in the basis of the eigenstates $|\varphi_{\mathbf{k},\pm}\rangle$ of $\hat{\mathcal{H}}(\mathbf{k})$. The position operator represented in momentum space is $\hat{\mathbf{r}} = \mathrm{i}\nabla_{\mathbf{k}}$. We start with the diagonal entry $\mathbf{v}_{\mathbf{k}}^{++}$,

$$\begin{aligned}
\mathbf{v}_{\mathbf{k}}^{++} =& \langle\varphi_{\mathbf{k},+}|\hat{\mathbf{v}}|\varphi_{\mathbf{k},+}\rangle = \frac{\mathrm{i}}{\hbar}\left\langle\varphi_{\mathbf{k},+}\left|\left[\hat{\mathcal{H}}(\mathbf{k}), \hat{\mathbf{r}}\right]\right|\varphi_{\mathbf{k},+}\right\rangle \\
=& \frac{\mathrm{i}}{\hbar}\left\{\left\langle\varphi_{\mathbf{k},+}\left|\hat{\mathcal{H}}(\mathbf{k})\,\hat{\mathbf{r}}\right|\varphi_{\mathbf{k},+}\right\rangle - \left\langle\varphi_{\mathbf{k},+}\left|\hat{\mathbf{r}}\,\hat{\mathcal{H}}(\mathbf{k})\right|\varphi_{\mathbf{k},+}\right\rangle\right\} \\
=& \frac{\mathrm{i}}{\hbar}\left\{E_+(\mathbf{k})\left\langle\varphi_{\mathbf{k},+}\left|\hat{\mathbf{r}}\right|\varphi_{\mathbf{k},+}\right\rangle - \left\langle\varphi_{\mathbf{k},+}\left|\hat{\mathbf{r}}\right|\varphi_{\mathbf{k},+}\right\rangle E_+(\mathbf{k})\right\} \\
=& -\frac{1}{\hbar}\left\{E_+(\mathbf{k})\left\langle\varphi_{\mathbf{k},+}\left|\nabla_{\mathbf{k}}\right|\varphi_{\mathbf{k},+}\right\rangle - \left\langle\varphi_{\mathbf{k},+}\left|\left(\nabla_{\mathbf{k}}\right|\varphi_{\mathbf{k},+}\right\rangle\right) E_+(\mathbf{k})\right. \\
& \left. - \left\langle\varphi_{\mathbf{k},+}\right|\left.\varphi_{\mathbf{k},+}\right\rangle\left(\nabla_{\mathbf{k}} E_+(\mathbf{k})\right)\right\} \\
=& \frac{1}{\hbar}\nabla_{\mathbf{k}} E_+(\mathbf{k}).
\end{aligned} \tag{A.1}$$

The component $\mathbf{v}_{\mathbf{k}}^{--}$ for the lower band can be computed analogously,

$$\mathbf{v}_{\mathbf{k}}^{--} = \langle\varphi_{\mathbf{k},-}|\hat{\mathbf{v}}|\varphi_{\mathbf{k},-}\rangle = \frac{1}{\hbar}\nabla_{\mathbf{k}} E_-(\mathbf{k}). \tag{A.2}$$

For the off-diagonal entries, the first steps are similar. We begin with $\mathbf{v}_{\mathbf{k}}^{+-}$,

$$\begin{aligned}
\mathbf{v}_{\mathbf{k}}^{+-} =& \langle\varphi_{\mathbf{k},+}|\hat{\mathbf{v}}|\varphi_{\mathbf{k},-}\rangle = \frac{\mathrm{i}}{\hbar}\left\{E_+(\mathbf{k})\left\langle\varphi_{\mathbf{k},+}\left|\hat{\mathbf{r}}\right|\varphi_{\mathbf{k},-}\right\rangle - \left\langle\varphi_{\mathbf{k},+}\left|\hat{\mathbf{r}}\right|\varphi_{\mathbf{k},-}\right\rangle E_-(\mathbf{k})\right\} \\
=& -\frac{1}{\hbar}\left\{E_+(\mathbf{k})\left\langle\varphi_{\mathbf{k},+}\left|\nabla_{\mathbf{k}}\right|\varphi_{\mathbf{k},-}\right\rangle - \left\langle\varphi_{\mathbf{k},+}\left|\left(\nabla_{\mathbf{k}}\right|\varphi_{\mathbf{k},-}\right\rangle\right) E_-(\mathbf{k})\right. \\
& \left. - \left\langle\varphi_{\mathbf{k},+}\right|\left.\varphi_{\mathbf{k},-}\right\rangle\left(\nabla_{\mathbf{k}} E_-(\mathbf{k})\right)\right\} \\
=& \frac{1}{\hbar}\left[E_-(\mathbf{k}) - E_+(\mathbf{k})\right]\left\langle\varphi_{\mathbf{k},+}\left|\nabla_{\mathbf{k}}\right|\varphi_{\mathbf{k},-}\right\rangle.
\end{aligned} \tag{A.3}$$

Using definition (2.36) for the interband or transition matrix element $\boldsymbol{\mathcal{A}}_{+-}(\mathbf{k})$, we can rewrite Eq. (A.3) as

$$\mathbf{v}_{\mathbf{k}}^{+-} = \frac{\mathrm{i}}{\hbar}\left[E_+(\mathbf{k}) - E_-(\mathbf{k})\right]\boldsymbol{\mathcal{A}}_{+-}(\mathbf{k}). \tag{A.4}$$

The derivation of $\mathbf{v}_{\mathbf{k}}^{-+}$ is again analogous,

$$\mathbf{v}_{\mathbf{k}}^{-+} = \langle\varphi_{\mathbf{k},-}|\hat{\mathbf{v}}|\varphi_{\mathbf{k},+}\rangle = \frac{\mathrm{i}}{\hbar}\left[E_-(\mathbf{k}) - E_+(\mathbf{k})\right]\boldsymbol{\mathcal{A}}_{-+}(\mathbf{k}). \tag{A.5}$$

From the hermiticity of the velocity operator $\hat{\mathbf{v}}$ it follows that

$$\boldsymbol{\mathcal{A}}_{+-}(\mathbf{k}) = \boldsymbol{\mathcal{A}}_{-+}^{*}(\mathbf{k}). \tag{A.6}$$

When directly evaluating the commutator, one finds that the velocity operator can also be expressed as

$$\hat{\mathbf{v}} = \frac{\mathrm{i}}{\hbar}\left[\hat{\mathcal{H}}(\mathbf{k}), \hat{\mathbf{r}}\right] = \frac{1}{\hbar}\nabla_{\mathbf{k}}\hat{\mathcal{H}}(\mathbf{k}). \tag{A.7}$$

Thus, by combining Eqs. (A.4) and (A.7) one obtains the relation

$$\boldsymbol{\mathcal{A}}_{+-}(\mathbf{k}) = -\mathrm{i}\frac{\langle\varphi_{\mathbf{k},+}|\nabla_{\mathbf{k}}\hat{\mathcal{H}}(\mathbf{k})|\varphi_{\mathbf{k},-}\rangle}{\left[E_+(\mathbf{k}) - E_-(\mathbf{k})\right]}, \tag{A.8}$$

and $\boldsymbol{\mathcal{A}}_{-+}(\mathbf{k})$ analogously. With this, the link between Berry curvature as summation over eigenstates, see Eq. (2.37), and from the interband matrix element, see Eq. (2.38), becomes apparent.

A.2. Further data on Floquet oscillations in periodically gapped Dirac systems

In this section we show some additional data for the Floquet oscillations achieved in Dirac systems with periodically opened mass gap. The main results are discussed in Sec. 4.4.2 in the main text.

In the left panel of Fig. A.1 the velocity curves of Fig. 4.3(a) are plotted again. The right panel is a zoom into the region marked by the red rectangle. This segment of the velocity contains all the small deviations between TQT and Floquet results discussed in Sec. 4.4.2. One example where the rectangular Zitterbewegung is not well reproduced in the Floquet approach is marked by

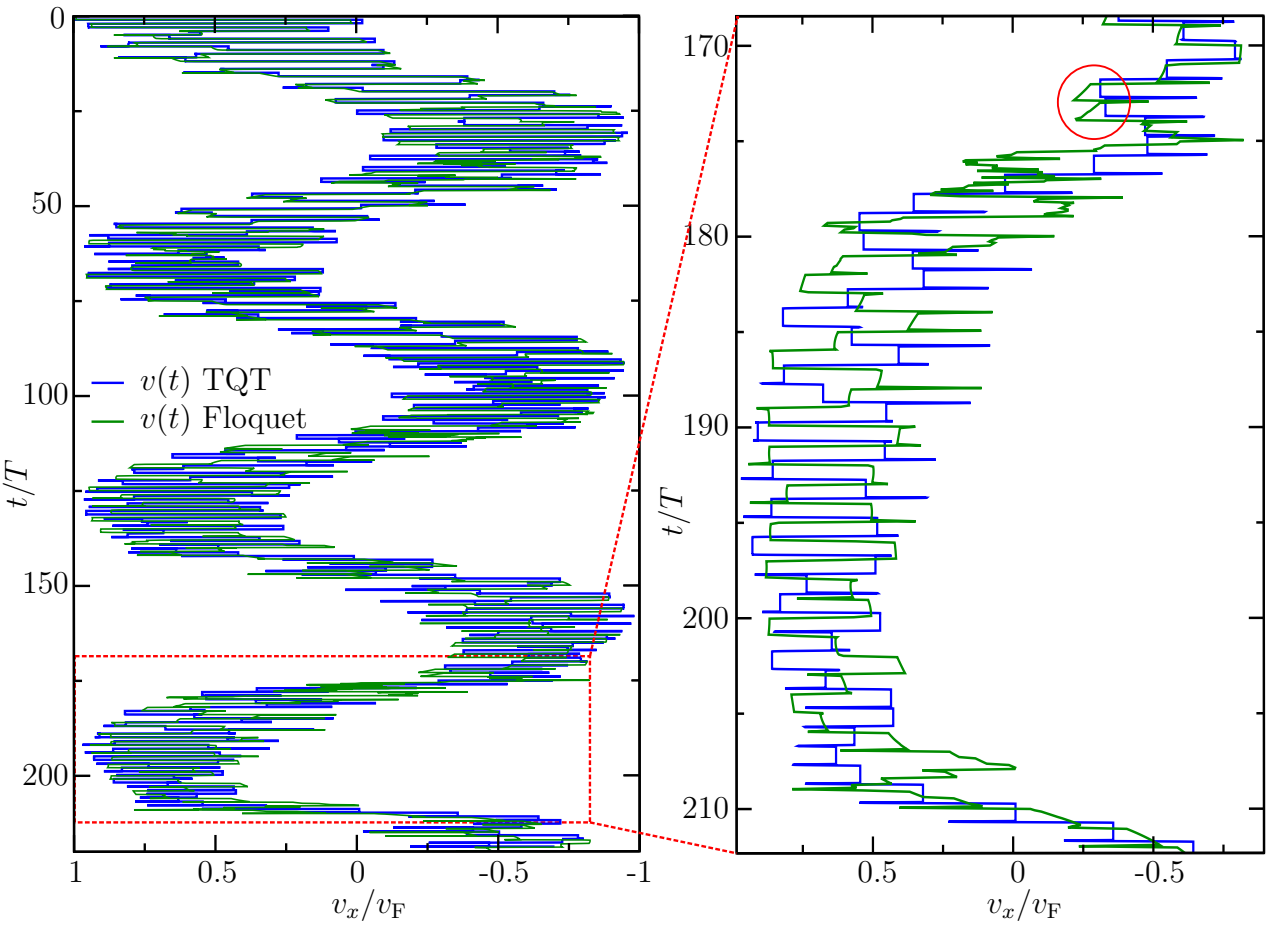

Fig. A.1: Velocity of an electron in a periodically gapped Dirac system undergoing Floquet oscillations. The left panel shows the same velocities as Fig. 4.3(a) in the main text. The right panel is a zoom into the section marked by the red rectangle in the left panel. It contains all deviations between Floquet and TQT results discussed in Sec. 4.4.2, namely bad approximation of the rectangular Zitterbewegung (marked by the red circle), a phase shift of π between the resulting Zitterbewegung and a small time shift between both curves.

the red circle. Throughout most of the curve displayed in the zoomed graph, a phase shift of π between the Zitterbewegung computed with TQT and Floquet is present. The small time shift between both results is also apparent and best visible whenever the Zitterbewegung switches amplitude.

To check whether the deviations in the Zitterbewegung originate from the truncation of the Floquet matrix at $n, m = \pm 100$, we repeated the calculation for different values of n, m. The results for the position expectation value in Fig. A.2(a) agree rather well for all values of n, m. Only the small wiggly motion stemming from Zitterbewegung has different phases depending on the truncation of the Floquet matrix. Those phase deviations are much more pronounced in the velocity, see Fig. A.2(b). For better visibility we only show the zoomed region already discussed in Fig. A.1. Since the results for $n, m = \pm 100$ and $n, m = \pm 500$ are rather similar and taking smaller Floquet

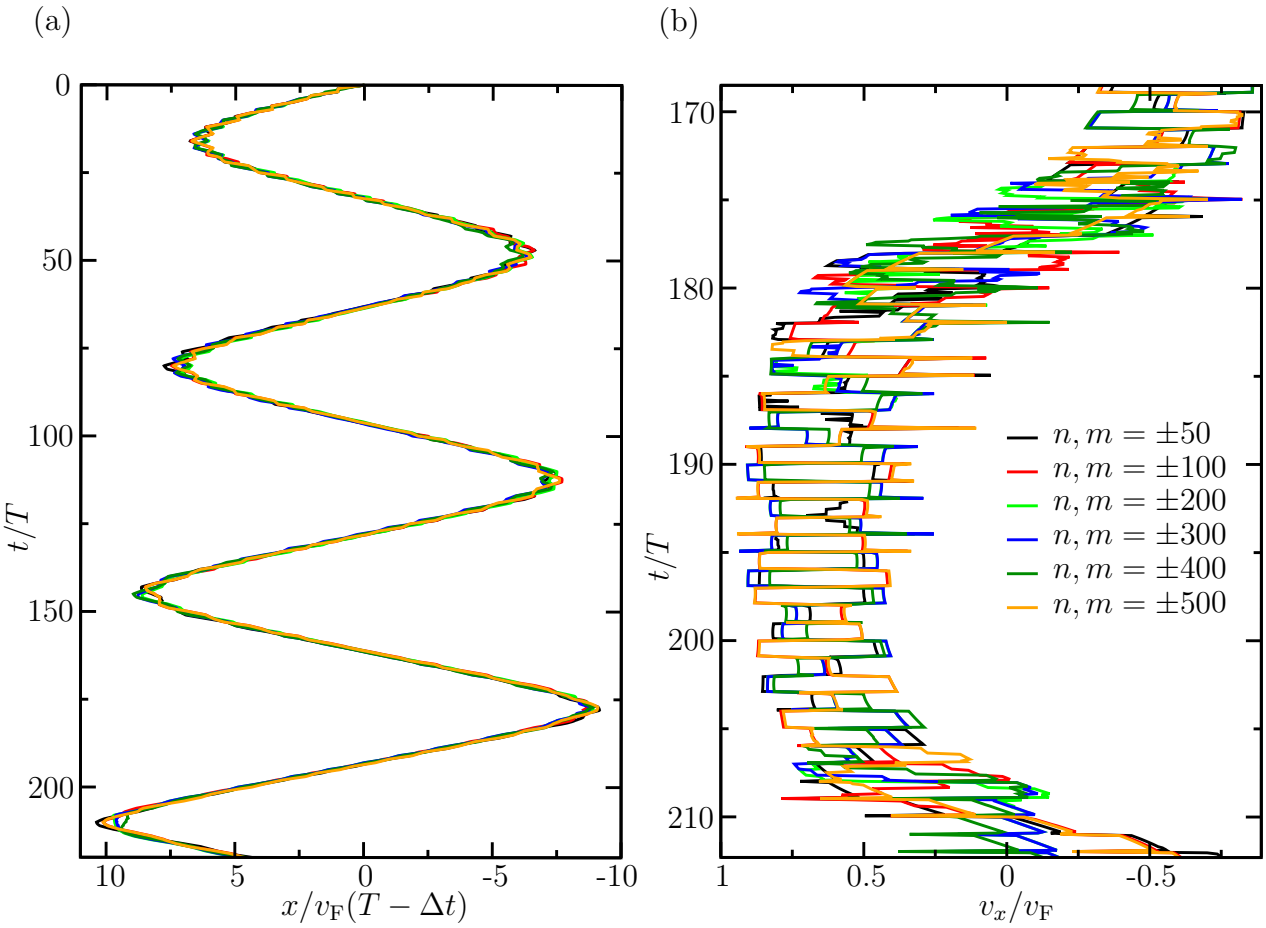

Fig. A.2: Floquet oscillations of an electron for different sizes n, m of the Floquet matrix. (a) Position expectation value. Only the phase of the small wiggly motion on top of the Floquet oscillations differs for different n, m. (b) Zoom into the velocity expectation value as in Fig. A.1. The different phases of the Zitterbewegung are much more pronounced in the velocity. Since the results for $n, m = \pm 100$ and $n, m = \pm 500$ are rather similar, we settled for the former to reduce numerical costs. Also, in comparison with TQT those are the values with best agreement during the total propagation time.

matrices saves numerical costs, we chose $n, m = \pm 100$ for the data shown in the main text. Also, considering the agreement with TQT over the full propagation time as in Fig. A.1, $n, m = \pm 100$ and $n, m = \pm 500$ show the best results.

As discussed in Sec. 4.4.2, for longer propagation times the gaps between the Floquet bands become too small for Floquet oscillations to occur. We studied this regime in Ref. [123], so we do not want to repeat the discussion here. For completeness however, in Fig. A.3 we show the position computed with TQT for longer propagation times. After roughly four cycles of Floquet oscillations the gaps between the Floquet bands become too small and transitions between the Floquet bands begin to dominate the dynamics. Then, Floquet oscillations cannot be observed anymore.

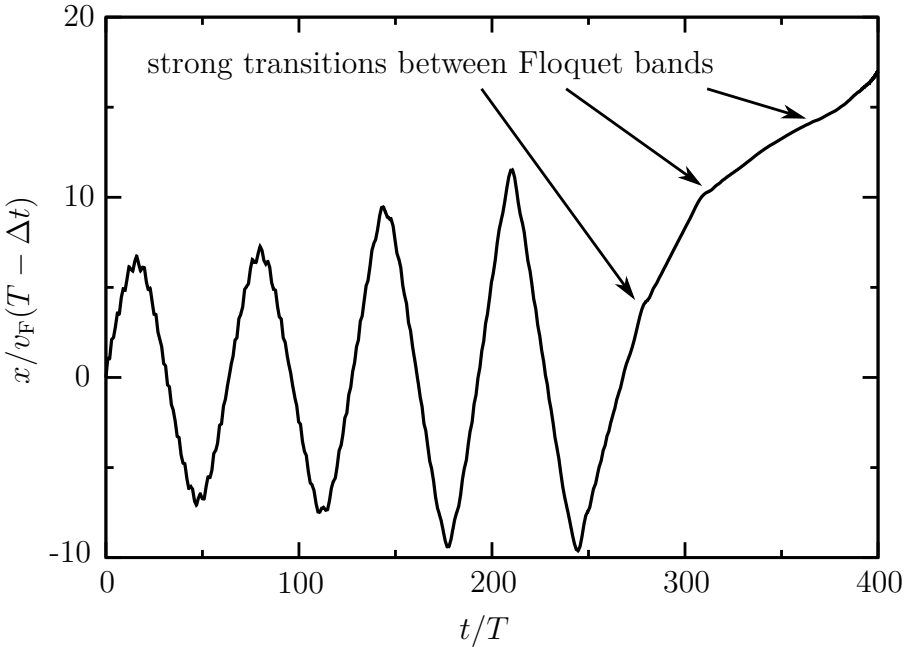

Fig. A.3: Position expectation value of an electron propagated for a longer time using TQT. When the electron reaches a region where the gaps between the Floquet bands become rather small, transitions start to dominate the dynamics and Floquet oscillations cannot be observed anymore. The curve shown here is just an extension of the one in Fig. 4.3(a).

A.3. Treating circularly polarized light in TQT

Currently, it is not possible to treat systems depending on more than one time-dependent function with TQT. Circularly polarized light however is described by the vector potential

$$\mathbf{A}(t) = A \begin{pmatrix} \cos(\omega t) \\ \sin(\omega t) \end{pmatrix} \tag{A.9}$$

and thus contains two time-dependent functions, $\cos(\omega t)$ and $\sin(\omega t)$. To circumvent this issue, we use a gauge transformation,

$$\begin{aligned} \mathbf{A}'(t) &= \mathbf{A}(t) + \nabla\Lambda(\mathbf{r}, t), \\ \phi'(\mathbf{r}, t) &= \phi(\mathbf{r}, t) - \frac{\partial}{\partial t}\Lambda(\mathbf{r}, t). \end{aligned} \tag{A.10}$$

By choosing the function

$$\Lambda(\mathbf{r}, t) = -A\cos(\omega t)x, \tag{A.11}$$

we obtain the potentials

$$\begin{aligned} \mathbf{A}'(t) &= A \begin{pmatrix} 0 \\ \sin(\omega t) \end{pmatrix}, \\ \phi'(\mathbf{r}, t) &= -A\omega \sin(\omega t)x, \end{aligned} \tag{A.12}$$

reducing the problem to one time-dependent function.

A.4. Fitted Bi_2Te_3 surface Hamiltonian in TQT

TQT can only process Hamiltonians that are given as polynomials of the momentum $\mathbf{k} = (k_x, k_y)$. Therefore, it is not possible to work with the fitted Hamiltonian $\hat{\mathcal{H}}_\mathrm{f}(\mathbf{k})$ introduced in Sec. 5.2 when using TQT. To get around this problem, we apply an expansion to the momentum-dependent prefactors $B_\mathrm{f}(\mathbf{k})$ and $R_\mathrm{f}(\mathbf{k})$ defined in Eq. (5.2) and write them as

$$\begin{aligned} D_\mathrm{f}^\mathrm{e}(\mathbf{k}) =& D_1 + D_2 k^2 + D_3 k^4 + D_4 k^6 + D_5 k^8 + D_6 k^{10} + D_7 k^{12} + D_8 k^{14} + D_9 k^{16}, \\ R_\mathrm{f}^\mathrm{e}(\mathbf{k}) =& R_1 + R_2 k^2 + R_3 k^4 + R_4 k^6 + R_5 k^8 + R_6 k^{10} + R_7 k^{12} + R_8 k^{14} + R_9 k^{16} \\ &+ R_{10} k^{18}, \end{aligned} \tag{A.13}$$

where $k = |\mathbf{k}| = \sqrt{k_x^2 + k_y^2}$. With these polynomials, the rotational symmetry of the prefactors is preserved and they again do not change the symmetry properties of the Hamiltonian $\hat{\mathcal{H}}_\mathrm{f}(\mathbf{k})$.

Using the plot program *xmgrace* [262] we fit the bandstructure resulting from the expanded prefactors $D_\mathrm{f}^\mathrm{e}(\mathbf{k})$ and $R_\mathrm{f}^\mathrm{e}(\mathbf{k})$, Eq. (A.13), to the bands obtained from the full prefactors, Eq. (5.2). For simplicity we restrict ourselves to 1D plots and only fit along the high-symmetry axes $\overline{\Gamma\mathrm{K}}$ and $\overline{\Gamma\mathrm{M}}$, where $k_y = 0$ and $k_x = 0$, respectively. To achieve good agreement, we additionally have to limit the fitting region to $k_{x,y} \lesssim 0.4\,\text{Å}^{-1}$. The resulting parameters are given in Tab. A.1.

In Fig. A.4 we compare the bands from DFT, the Hamiltonian $\hat{\mathcal{H}}_\mathrm{f}(\mathbf{k})$ from Sec. 5.2 and the results for the expanded prefactors (A.13) along $\overline{\Gamma\mathrm{K}}$ and $\overline{\Gamma\mathrm{M}}$ direction. Within the fitting window, the bands from our expanded prefactors match nicely with the bands of $\hat{\mathcal{H}}_\mathrm{f}(\mathbf{k})$ with the full prefactors. Additionally, the bands from DFT agree reasonably well with those of the model Hamiltonian $\hat{\mathcal{H}}_\mathrm{f}(\mathbf{k})$ with and without the expanded prefactors. Outside the fitting window, i.e. for $k_{x,y} > 0.4\,\text{Å}^{-1}$ however, the bands from our expansion strongly diverge. This divergence leads to numerical issues within TQT. For stable calculations, the grid in momentum space has to be defined such that the diverging regions are not included. Hence, we can only use the fitted Hamiltonian $\hat{\mathcal{H}}_\mathrm{f}(\mathbf{k})$ for problems for which this limited grid is sufficient. Another disadvantage of

D_f^e		R_f^e	
D_1	$18.3218\,\mathrm{eV}$	R_1	$-34.4034\,\mathrm{eV}$
D_2	$-656.14\,\mathrm{eV\,Å}$	R_2	$-38.7236\,\mathrm{eV\,Å}$
D_3	$1.371\,36\cdot10^4\,\mathrm{eV\,Å}^2$	R_3	$2.684\,27\cdot10^4\,\mathrm{eV\,Å}^2$
D_4	$-1.714\,04\cdot10^5\,\mathrm{eV\,Å}^3$	R_4	$-6.588\,21\cdot10^5\,\mathrm{eV\,Å}^3$
D_5	$1.317\,46\cdot10^6\,\mathrm{eV\,Å}^4$	R_5	$8.201\,46\cdot10^6\,\mathrm{eV\,Å}^4$
D_6	$-6.268\,11\cdot10^6\,\mathrm{eV\,Å}^5$	R_6	$-6.178\,08\cdot10^7\,\mathrm{eV\,Å}^5$
D_7	$1.796\,39\cdot10^7\,\mathrm{eV\,Å}^6$	R_7	$2.927\,66\cdot10^8\,\mathrm{eV\,Å}^6$
D_8	$-2.838\,46\cdot10^7\,\mathrm{eV\,Å}^7$	R_8	$-8.549\,06\cdot10^8\,\mathrm{eV\,Å}^7$
D_9	$1.898\,08\cdot10^7\,\mathrm{eV\,Å}^8$	R_9	$1.407\,21\cdot10^9\,\mathrm{eV\,Å}^8$
		R_{10}	$-9.997\,85\cdot10^8\,\mathrm{eV\,Å}^9$

Tab. A.1: Parameters of the expanded prefactors (A.13).

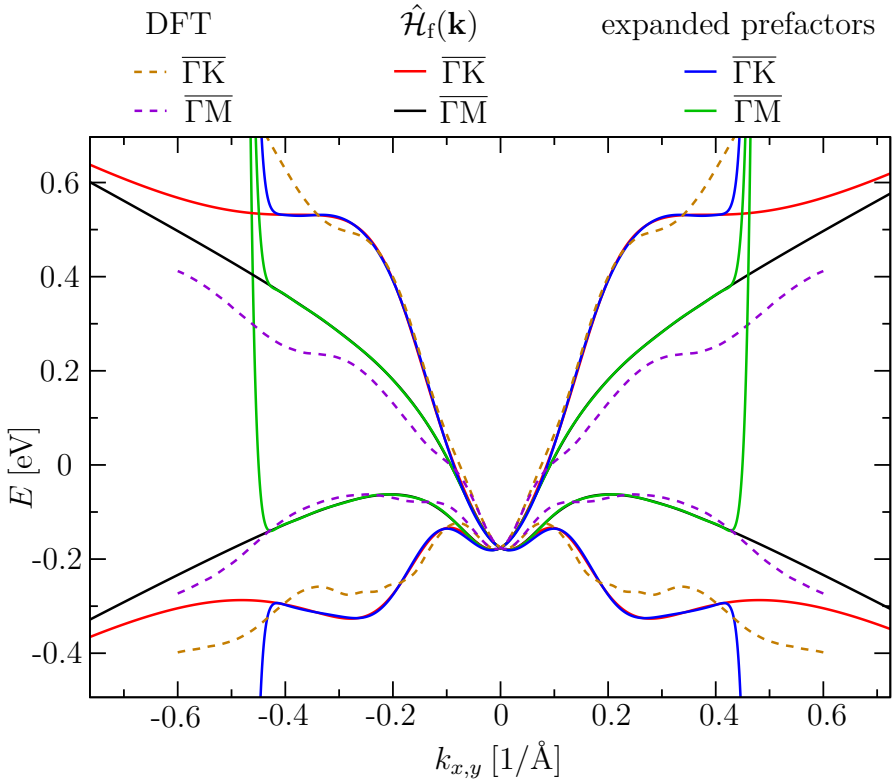

Fig. A.4: Bandstructure of Bi_2Te_3 from DFT, for the Hamiltonian $\hat{\mathcal{H}}_\mathrm{f}(\mathbf{k})$ from Sec. 5.2 and for the expanded prefactors from Eq. (A.13) along the high-symmetry axes $\overline{\Gamma\mathrm{K}}$ and $\overline{\Gamma\mathrm{M}}$. Within the fitting window, good agreement is achieved. Since the fitting region was limited to $k_{x,y} \lesssim 0.4\,\mathrm{Å}^{-1}$, the bands for the expanded prefactors diverge for $k_{x,y} > 0.4\,\mathrm{Å}^{-1}$.

the expanded prefactors is that each summand is treated separately in TQT, see Sec. 3.1. The large number of summands increases the RAM usage and computation time and thus makes calculations with the fitted Hamiltonian $\hat{\mathcal{H}}_\mathrm{f}(\mathbf{k})$ less efficient than with the literature surface Hamiltonian $\hat{\mathcal{H}}_\mathrm{s}(\mathbf{k})$. Hence, we refrain from using the fitted Hamiltonian $\hat{\mathcal{H}}_\mathrm{f}(\mathbf{k})$ after verifying that the simple model $\hat{\mathcal{H}}_\mathrm{s}(\mathbf{k})$ leads to qualitatively correct results.

A.5. Velocity operator for the fitted Bi_2Te_3 surface model

The velocity operator $\hat{\mathbf{v}}_\mathrm{f}$ for the fitted Hamiltonian $\hat{\mathcal{H}}_\mathrm{f}(\mathbf{k})$, that was introduced as a more realistic model for the Bi_2Te_3 surface states in Sec. 5.2, reads

$$\begin{aligned}\hat{\mathbf{v}}_\mathrm{f} = \frac{1}{\hbar}\Bigg[&2D_\mathrm{f}(\mathbf{k})\begin{pmatrix}k_x\\k_y\end{pmatrix}\mathbb{1} + \left(\nabla_\mathbf{k} D_\mathrm{f}(\mathbf{k})\right)\left(k_x^2+k_y^2\right)\mathbb{1} + A_\mathrm{f}\begin{pmatrix}-\sigma_y\\\sigma_x\end{pmatrix}\\ &+ 6R_\mathrm{f}(\mathbf{k})\begin{pmatrix}k_x^2-k_y^2\\-2k_xk_y\end{pmatrix}\sigma_z + 2\left(\nabla_\mathbf{k} R_\mathrm{f}(\mathbf{k})\right)\left(k_x^3-3k_xk_y^2\right)\sigma_z\Bigg].\end{aligned} \tag{A.14}$$

Since all terms containing only the unit matrix $\mathbb{1}$ drop from the commutator $\left[\hat{\mathbf{v}}_\mathrm{f}, \hat{\mathcal{H}}_\mathrm{f}(\mathbf{k})\right]$, only the prefactor $R_\mathrm{f}(\mathbf{k})$ plays a role there. The commutator gives

$$\begin{aligned}\left[\hat{\mathbf{v}}_\mathrm{f}, \hat{\mathcal{H}}_\mathrm{f}(\mathbf{k})\right] = \frac{2\mathrm{i}A_\mathrm{f}}{\hbar}\Bigg[&A_\mathrm{f}\begin{pmatrix}k_y\\-k_x\end{pmatrix}\sigma_z - 2R_\mathrm{f}(\mathbf{k})\left(k_x^3-3k_xk_y^2\right)\begin{pmatrix}\sigma_x\\\sigma_y\end{pmatrix}\\ &+ 6R_\mathrm{f}(\mathbf{k})\left(k_y\sigma_y + k_x\sigma_x\right)\begin{pmatrix}k_x^2-k_y^2\\-2k_xk_y\end{pmatrix}\\ &+ 2\left(\nabla_\mathbf{k} R_\mathrm{f}(\mathbf{k})\right)\left(k_x^3-3k_xk_y^2\right)\left(k_y\sigma_y + k_x\sigma_x\right)\Bigg].\end{aligned} \tag{A.15}$$

As $R_\mathrm{f}(\mathbf{k})$ only depends on the absolute value $k = |\mathbf{k}|$ of the momentum, the additional term acts equally on both vector components of the commutator. Like for $\hat{\mathcal{H}}_\mathrm{s}(\mathbf{k})$, for $k_x = 0$ Zitterbewegung can only arise in v_x, whereas the latter is possible for any $\mathbf{k} \neq (0,0)$.

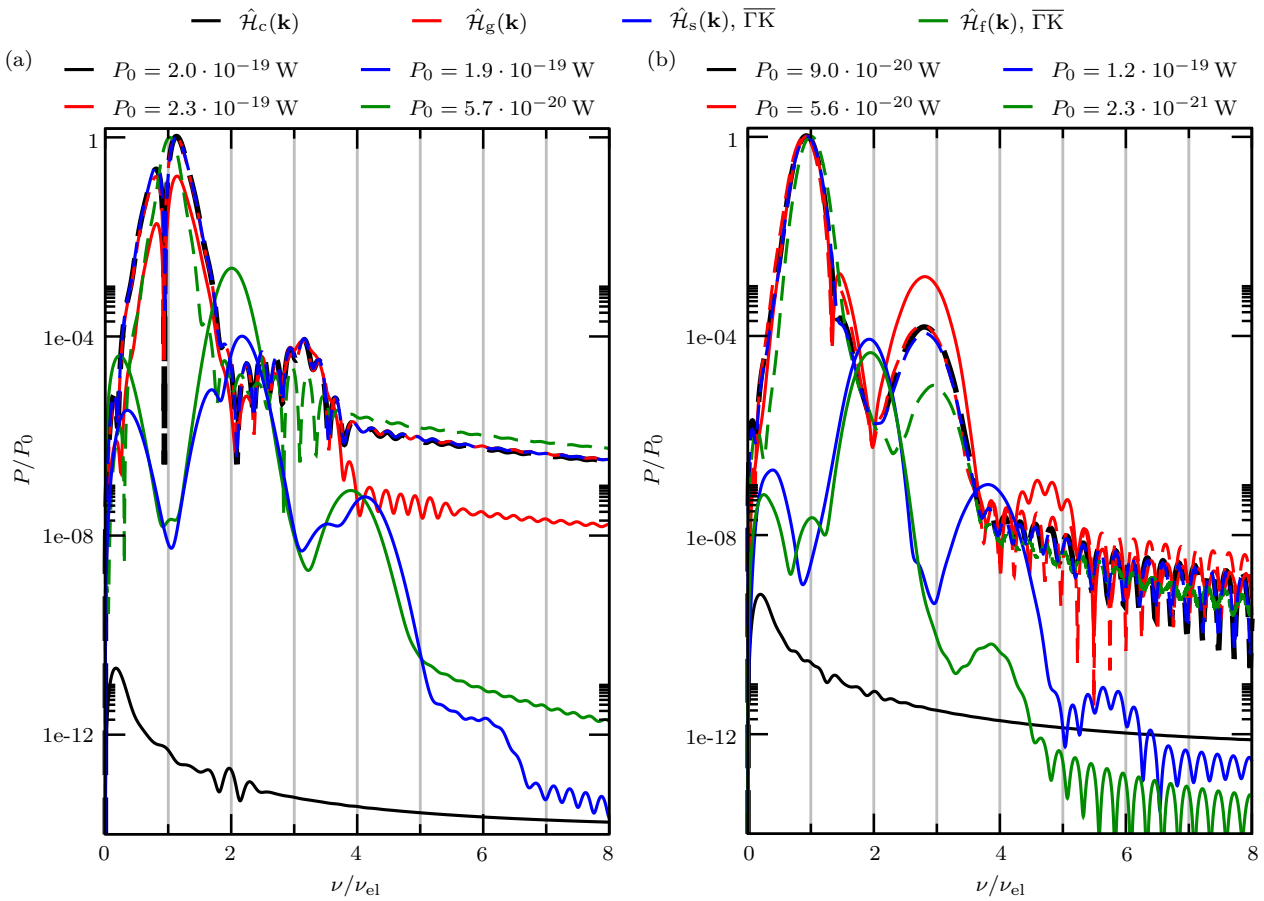

Fig. A.5: HHs spectrum of the test charges in the (a) Rabi and (b) nonimpulsive Landau-Zener regime. The respective velocities are plotted in Figs. 5.7 and 5.8. To distinguish parallel and orthogonal emission, we dashed the spectra belonging to P_x. As in the adiabatic case, see Sec. 5.5.1, the orthogonal emission P_y is zero for the Dirac cone $\hat{\mathcal{H}}_c(\mathbf{k})$, at odd orders for the gapped cone $\hat{\mathcal{H}}_g(\mathbf{k})$, and shifts to even orders for the Hamiltonians with hexagonal warping $\hat{\mathcal{H}}_{s/f}(\mathbf{k})$. We normalized the power P with $P_0 = P_x(2\pi\nu_{el})$ for each system.

A.6. Spectra for resonant and nonimpulsive Landau-Zener regime

In Sec. 5.5.1 we discuss how the Berry curvature of the underlying model system imprints on the emitted HHs spectrum based on the velocities of two test charges in the adiabatic regime, see Sec. 5.4.1 for the latter. Applying the same field strength, $E_{el} = 0.1\,\mathrm{MV\,cm^{-1}}$, we also studied the resonant (Sec. 5.4.2) and nonimpulsive Landau-Zener regime (Sec. 5.4.3) by simply varying the initial momenta $\mathbf{k}_i$ of the test charges. For completeness, the corresponding spectra for these two regimes are shown in Fig. A.5. As in Sec. 5.5.1 in the main text, the dashed lines show the emission P_x parallel to the driving field, whereas the solid lines show the emission P_y perpendicular to it. All spectra are renormalized with their respective first peak of the parallel

component, $P_0 = P_x(2\pi\nu_{\mathrm{el}})$. Qualitatively, we observe the same features as in the adiabatic regime. The parallel spectrum contains the first and the third harmonic for all systems, whereas the perpendicular emission depends on the Berry curvature of the model system.

Additionally we find that the relative amplitude P/P_0 of the perpendicular emission P_y of the gapped cone[1] $\hat{\mathcal{H}}_{\mathrm{g}}(\mathbf{k})$ increases with decreasing initial momentum $\mathbf{k}_i$. In the adiabatic regime it was about four orders of magnitude smaller than the parallel emission P_x, whereas in the resonant regime both components are comparable and in the nonimpulsive Landau-Zener regime the perpendicular third harmonic even exceeds the parallel one and a fifth harmonic emerges[2]. This coincides with the fact that for the gapped cone the Berry curvature is largest at the Dirac point and decreases with increasing $\mathbf{k}$, see Eq. (5.3) for reference. Concerning the relative amplitudes of the perpendicular emission P_y in the warped systems $\hat{\mathcal{H}}_{\mathrm{s}}(\mathbf{k})$ and $\hat{\mathcal{H}}_{\mathrm{f}}(\mathbf{k})$ we find a variation depending on the initial momentum but cannot extrapolate a clear trend.

Furthermore, in the resonant regime, Fig. A.5(a), the peak of the first harmonic is split for all model systems. This is probably due to an interference of the resonance peak of the system with the harmonic since they have the same frequency. In the nonimpulsive Landau-Zener regime the initial momenta $\mathbf{k}_i$ are smaller than for the resonant regime in all systems, thus the resonance frequency is smaller than the driving frequency ν_{el} and no resonance peak appears.

A.7. From Fermi sea to single-particle states

This section is based on the derivations presented in Ref. [263], Chap. IV, Sec. 4.

For non-interacting fermions the wave function for M particles can generally be defined as

$$\Psi(1,\ldots,M) = \frac{1}{\sqrt{M!}} \sum_P (-1)^P \hat{\mathcal{P}} \phi_{\alpha_1}(1) \ldots \phi_{\alpha_M}(M), \tag{A.16}$$

[1] Note that this also applies to the ungapped cone $\hat{\mathcal{H}}_{\mathrm{c}}(\mathbf{k})$. There we interpret the result as an increasing noise level when approaching the Dirac point.

[2] Remember that in the adiabatic regime we use $\mathbf{k}_i = (0, \pm 0.1)\text{Å}^{-1}$, in the resonant regime $\mathbf{k}_i = (0, \pm 0.015)\text{Å}^{-1}$ and in the nonimpulsive Landau-Zener regime $\mathbf{k}_i = (0, \pm 0.007)\text{Å}^{-1}$.

where the sum runs over all $M!$ possible permutations P. An even (odd) number of permutations obtains a positive (negative) sign, $\hat{\mathcal{P}}$ is the permutation operator, and $\phi_{\alpha_i}(i)$ are the single-particle wave functions for the i-th electron. If two electrons i and j occupy the same state, i.e. $\phi_{\alpha_i}(i) = \phi_{\alpha_j}(j)$, $\Psi(1,\ldots,M) = 0$ due to the Pauli exclusion principle. The different summands of $\Psi(1,\ldots,M)$ are orthogonal with respect to each other and $\phi^*_{\alpha_i}(i)\phi_{\alpha_j}(j) = \delta_{i,j}$.

We now compute observables for such a state $\Psi(1,\ldots,M)$. Let $\hat{\mathcal{O}}$ be an arbitrary single-particle operator, then

$$\begin{aligned}\langle\hat{\mathcal{O}}\rangle =& \frac{1}{M!}\left[\sum_P (-1)^P \hat{\mathcal{P}}\phi^*_{\alpha_1}(1)\ldots\phi^*_{\alpha_M}(M)\right] \times \\ & \times \sum_{\alpha_i} O_{\alpha_i,\alpha_i}\left[\sum_{P'}(-1)^{P'}\hat{\mathcal{P}}'\phi_{\alpha_1}(1)\ldots\phi_{\alpha_M}(M)\right] \\ =& \sum_{\alpha_i}\phi^*_{\alpha_i}(i)\; O_{\alpha_i,\alpha_i}\;\phi_{\alpha_i}(i).\end{aligned} \tag{A.17}$$

All permutations give the same result due to the single-particle nature of $\hat{\mathcal{O}}$, so they just cancel the $\frac{1}{M!}$. Additionally, since the summands in $\Psi(1,\ldots,M)$ are orthogonal with respect to each other, only the same permutations on left and right side of the operator give non-vanishing terms. The $\phi_{\alpha_i}(i)$ not affected by O_{α_i,α_i} disappear due to their orthonormality. Thus, the observable reduces to a calculation depending on the single-particle wave functions $\phi_{\alpha_i}(i)$.

As a next step, we include the time dependency of the single-particle wave functions $\phi_{\alpha_i}(i) \to \phi_{\alpha_i}(i,t)$. Since the time evolution considered throughout this work is unitary, the orthonormality condition still holds, i.e. $\phi^*_{\alpha_i}(i,t)\phi_{\alpha_j}(j,t') = \delta_{i,j}\delta_{t,t'}$, and we can generalize

$$\langle\hat{\mathcal{O}}\rangle(t) = \sum_{\alpha_i}\phi^*_{\alpha_i}(i,t)\; O_{\alpha_i,\alpha_i}\;\phi_{\alpha_i}(i,t). \tag{A.18}$$

Note that α_i labels the initial parameters of the state $\phi_{\alpha_i}(i,t)$. For our work, $\alpha_i = (\mathbf{k}_i, s_i)$ consists of the momentum $\mathbf{k}_i$ and band index $s_i = \pm$ of electron i and

$$\phi_{\alpha_i}(i) = \delta(\mathbf{k} - \mathbf{k}_i)\varphi_{s_i}(\mathbf{k}_i), \tag{A.19}$$

with the spinor $\varphi_{s_i}(\mathbf{k}_i)$. Then, the $\phi_{\alpha_i}(i)$ are orthonormal,

$$\int \mathrm{d}\mathbf{k}\;\delta(\mathbf{k}-\mathbf{k}_i)\varphi^*_{s_i}(\mathbf{k}_i)\;\delta(\mathbf{k}-\mathbf{k}_j)\varphi_{s_j}(\mathbf{k}_j) = \delta_{\mathbf{k}_i,\mathbf{k}_j}\delta_{s_i,s_j}. \tag{A.20}$$

During the time evolution, the state $\phi_{\alpha_i}(i,t)$ may move around in momentum space and/or switch between bands, but due to the unitarity of the evolution,

the states stay orthonormal with respect to each other. In consequence, Eq. (A.18) for the computation of observables still holds.

We can conclude that it is sufficient to calculate the time evolution of the initially occupied single-particle states in order to obtain observables including Pauli blocking. Since all operators of interest are diagonal in $\mathbf{k}$, to reduce computational effort we can combine all initially occupied states $\phi_{\mathbf{k}_i,s_i}(i,0)$ of one band s_i to a wave packet and propagate them simultaneously. This leads us to the initial wave packets

$$\Psi_{\pm}(\mathbf{k},0) = \frac{1}{\sqrt{N}}\, g_{\pm}(\mathbf{k})\varphi_{\pm}(\mathbf{k}) \tag{A.21}$$

discussed in Sec. 6.2 in the main text. The limitation to initial wave packets only containing states from one band s_i is necessary however due to e.g. the velocity operator containing off-diagonal terms in the basis of the eigenstates $\varphi_{\pm}(\mathbf{k})$. Thus, unphysical interference between single-particle states $\phi_{\mathbf{k}_i,s_i}(i,0)$ and $\phi_{\mathbf{k}_j,s_j}(j,0)$ with $\mathbf{k}_i = \mathbf{k}_j$ but $s_i \neq s_j$ are avoided when calculating observables. This is discussed in more detail in the main text.

A.8. Benchmarking wave-packet versus k-mask size

A fast and simple way to check whether the momentum area within the k-mask is covered by the wave packet $\Psi_{-}(\mathbf{k},t)$ at all times t is to compute the COM of $\Psi_{-}(\mathbf{k},t)$ within the k-mask, i.e. $\langle k_x(t)\rangle_{\mathrm{cut}}$ introduced in Sec. 3.5. Since the wave packet $\Psi_{-}(\mathbf{k},t)$ and the k-mask $f(\mathbf{k})$ are centered around the Dirac point $\mathbf{k} = (0,0)$, $\langle k_x(t)\rangle_{\mathrm{cut}} \approx 0$ as long as the evaluated region is completely filled. As demonstrated in Fig. A.6, when defining $f(\mathbf{k})$ by Eq. (6.12) and taking $k_{x,\mathrm{cut}} = 0.16\,\text{Å}^{-1}$ for the system specified in Sec. 6.3.1, the condition $\langle k_x(t)\rangle_{\mathrm{cut}} \approx 0$ is met. Even though a remainder of the dynamics is resolved, it is about eight orders of magnitude smaller than the k-mask boundary $k_{x,\mathrm{cut}}$. For $k_{x,\mathrm{cut}} = 0.17\,\text{Å}^{-1}$ however, we find that at times of maximal excursion of the wave packet in momentum space the edges of the k-mask are not covered by $\Psi_{-}(\mathbf{k},t)$ anymore. This issue is indicated by the spikes in $\langle k_x(t)\rangle_{\mathrm{cut}}$ that lead to a change in sign and are only three orders of magnitude smaller than $k_{x,\mathrm{cut}}$. Within this work, we only consider k-masks that show a similar behavior as the data presented for $k_{x,\mathrm{cut}} = 0.16\,\text{Å}^{-1}$. Data with spikes similar to those

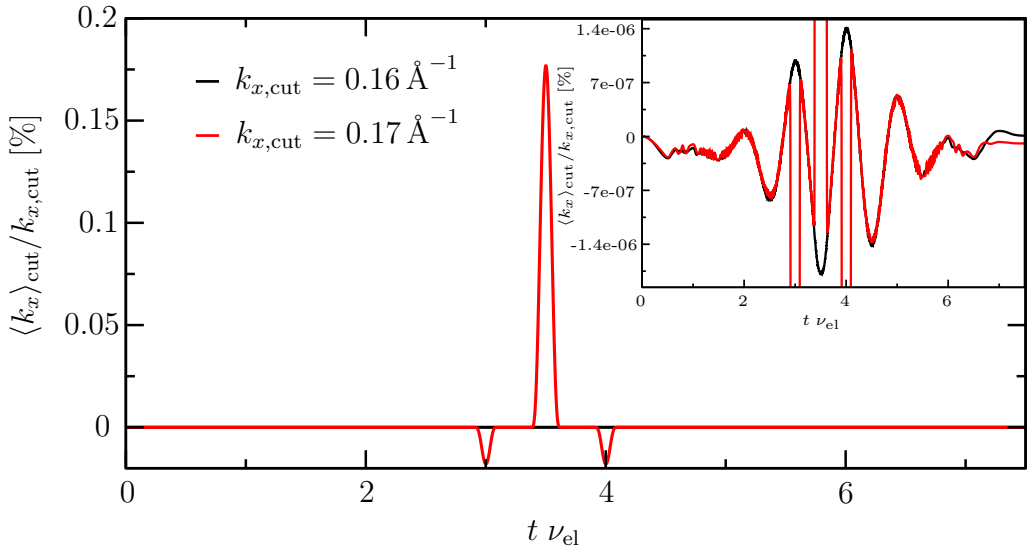

Fig. A.6: COM $\langle k_x(t) \rangle_{\mathrm{cut}}$ of $\Psi_-(\mathbf{k}, t)$ evaluated for two k-masks with $k_{x,\mathrm{cut}} = 0.16\,\text{Å}^{-1}$ and $k_{x,\mathrm{cut}} = 0.17\,\text{Å}^{-1}$, respectively. The inset is a zoom-in on the graphs. For $k_{x,\mathrm{cut}} = 0.16\,\text{Å}^{-1}$ the COM is approximately zero and the k-mask region is covered by the wave packet $\Psi_-(\mathbf{k}, t)$ at all times t. For $k_{x,\mathrm{cut}} = 0.17\,\text{Å}^{-1}$ however, at the times of maximal excursion in momentum space the edges of the k-mask are not covered by $\Psi_-(\mathbf{k}, t)$ anymore, resulting in spikes of the expectation value $\langle k_x(t) \rangle_{\mathrm{cut}}$.

for $k_{x,\mathrm{cut}} = 0.17\,\text{Å}^{-1}$ or larger is discarded or recomputed for a wave packet $\Psi_-(\mathbf{k}, t)$ with larger bound $|\mathbf{k}_{\mathrm{lim}}|$.

A.9. Effects of velocity-data processing on high-harmonics spectra

As sketched in Sec. 2.3.3, we take several steps to process the raw velocity data from our numerical simulations before calculating the corresponding HHs spectra. Oftentimes in literature, this processing is realized by multiplying the time-dependent data with a window function [172]. Within this work, we use the free software *xmgrace* [262] to compute the discrete Fourier transform of the velocity. This program also offers various window functions, of which the *Hanning window* is the most suitable for our purpose. However, in order to have full control over the data processing, we devised our own routine instead of using the build-in function. In this section we sketch our routine and explore its effects on the resulting HHs spectrum. For this purpose we use the velocity data $\mathbf{v}_-^{\mathrm{cut}}(t)$ obtained for our standard k-mask with $k_{x,\mathrm{cut}} = 0.13\,\text{Å}^{-1}$ in the setup described in Sec. 6.3. In Fig. A.7(a) we compare the processed data to the raw data. As shown in Fig. A.7(b), we achieve spectra that have a

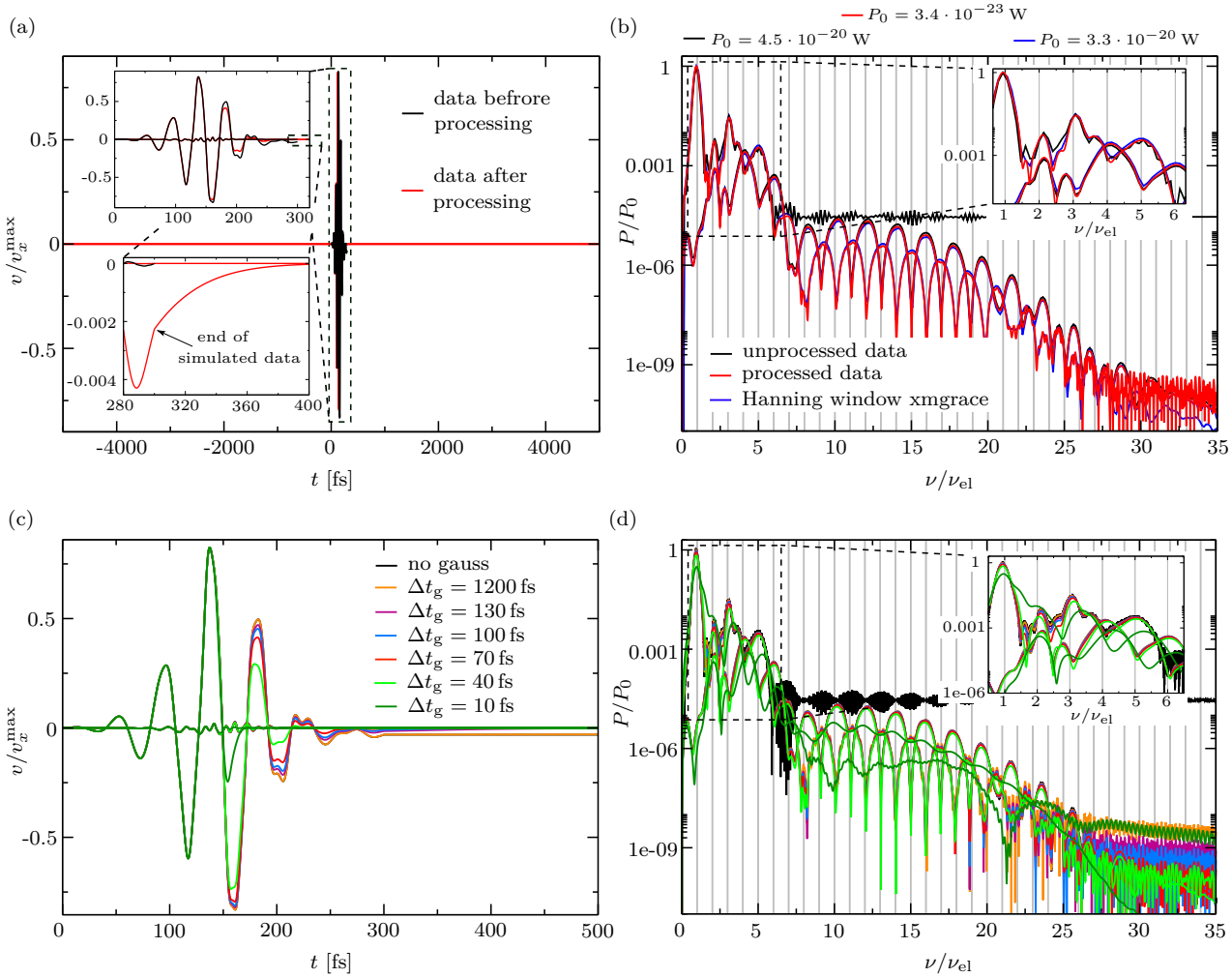

Fig. A.7: Comparison of different data processing for HH-spectra computation. The velocities are rescaled to their maximal intraband velocity before processing, $v_x^{\max} = |-0.182\,56\,\text{Å}\,\text{fs}^{-1}|$. (a) Time-resolved velocity data before and after our standard processing. The insets show zooms on the data without zero padding and on the transition from numerical data to zero padding with Gaussian decay. (b) HHs spectra of unprocessed and processed data compared to the Hanning window function of *xmgrace*. Without processing, the HHs of the parallel emission cannot be resolved. Our evaluation method adds small wiggles to the peaks with $\nu/\nu_{\mathrm{el}} \geq 20$ and reduces the order of magnitude of the spectrum by a factor of three, but qualitatively it is in good agreement with the Hanning window. (c) Excerpt of the velocity data and (d) corresponding HHs spectra with Gaussian decays of different widths Δt_{g}. The effects of the width is negligible as long as it is not damping most of the dynamics, compare $\Delta t_{\mathrm{g}} = 10\,\text{fs}$. Apart from that, only the wiggles on top of the highest-order peaks increase in amplitude with increasing Δt_{g}. When no Gaussian is applied, the spectra are similar to those of the unprocessed data, only with faster oscillations in the noise of the parallel spectrum. The power spectrum is normalized to the first harmonic peak for $\Delta t_{\mathrm{g}} = 70\,\text{fs}$ with $P_0 = 3.4 \cdot 10^{-23}\,\text{W}$.

significantly lower noise level in the parallel emission than the spectra of the raw data. Additionally, our spectra are similar to those computed with the Hanning window of *xmgrace*, only the overall order of magnitude is reduced by a factor of three.

First, we interpolate the velocity data such that its time step is reduced to $\delta t = 0.02\,\mathrm{fs}$ from the original time step of the TQT simulation. This assures that all data has the same time resolution before the Fourier transform is applied even though the time steps of the original TQT simulations might differ[3]. Since the time step is related to the frequency resolution of the discrete Fourier transform, it is advisable to adjust it beforehand. Then, we damp the second half of the signal with a Gaussian-shaped decay,

$$\mathbf{v}(t) \to \mathbf{v}(t)\ \exp\left[-\frac{(t-t_0)^2}{2\Delta t_\mathrm{g}}\right]\quad \text{, for } t \geq t_0, \tag{A.22}$$

where t_0 is the center of the applied light pulse, compare Eq. (6.9). The purpose of this damping is to reduce the signal to its initial, constant value after a finite time, thus decreasing the noise level of the HH spectrum. From a physical perspective, the Gaussian decay mimics dephasing on a very basic level, since it assures that all dynamics decay within a finite time but without distinguishing the underlying scattering and decoherence mechanisms. In Fig. A.7(c) we compare the velocity data multiplied with Gaussians of different width Δt_g. For the spectra shown in this work, we use $t_0 = 140\,\mathrm{fs}$ and $\Delta t_\mathrm{g} = t_0/2$. However, as demonstrated in Fig. A.7(d), the exact value of Δt_g is almost irrelevant. The only exception is that t_g must not be so short that it dampens out almost all dynamics of the second pulse half, as $t_\mathrm{g} = 10\,\mathrm{fs}$ here. On the other hand, even a Gaussian of width $\Delta t_\mathrm{g} = 30\Delta t$, where $\Delta t = 40\,\mathrm{fs}$ is the width of the electric field pulse (6.9), has the desired effect of decreasing the noise level. Lastly, we pad the velocity data with zeros before and after the actual dynamics to further increase the quality and resolution of the spectrum, similar to the effect of a Hanning window. Within this work, we choose the padding such that the total data set extends from $-5000\,\mathrm{fs}$ to $5000\,\mathrm{fs}$ with a time step of $\delta t = 0.02\,\mathrm{fs}$. Since the TQT simulation ends at $t = 300\,\mathrm{fs}$ and the signal usually has not fully decayed to zero by then even with the Gaussian damping (A.22), the zero padding after the pulse is actually defined by the tail of the Gaussian,

$$\mathbf{v}(t) = \mathbf{v}(t = 300\,\mathrm{fs})\ \exp\left[-\frac{(t-t_0)^2}{2\Delta t_\mathrm{g}}\right]\quad \text{, for } t \geq 300\,\mathrm{fs}, \tag{A.23}$$

[3]Note that for the simulation we always try to take the largest time step possible to decrease computation time while still obtaining a numerically stable propagation. Accordingly, the time step increases with decreasing field strength for the HH calculations.

E_{el} [MV/cm]	$N_x \times N_y$	δx [Å]	δy [Å]	δt [fs]	$\lvert\mathbf{k}_{\mathrm{lim}}\rvert$ [Å^{-1}]	$k_{x,\mathrm{cut}}$ [Å^{-1}]
0.1	2048×1024	6	10	0.5	0.15	0.05
0.2	2048×1024	6	10	0.2	0.15	0.07
0.3	2048×1024	6	10	0.2	0.15	0.09
0.4	2048×1024	6	10	0.1	0.22	0.11
0.5	2048×1024	6	10	0.1	0.22	0.13
0.6	4096×4096	6	6	0.03	0.35	0.15
0.7	4096×4096	6	6	0.03	0.35	0.17
0.8	4096×4096	6	6	0.03	0.35	0.19
0.9	4096×4096	6	6	0.03	0.35	0.21
1.0	4096×4096	6	6	0.03	0.35	0.21

Tab. A.2: Parameters of the Fermi sea simulations for different field strengths.

with $\mathbf{v}(t = 300\,\mathrm{fs})$ being the last data point from the TQT simulation. This procedure leads to a small bend in the time-resolved data as shown in the inset of Fig. A.7(a).

A.10. Peak-field dependent simulation parameters for the Fermi sea method

In Chap. 6 we evaluate HHG from a Fermi sea of Bi_2Te_3 surface states. Most of our simulations focus on a peak field $E_{\mathrm{el}} = 0.5\,\mathrm{MV\,cm^{-1}}$, but in Sec. 6.6 we also investigate how the results depend on the field strength E_{el}. In Tab. A.2 we summarize the parameters we used for our TQT simulations, including the outer limit $|\mathbf{k}_{\mathrm{lim}}|$ of the wave packet as defined in Eq. (6.10) and the boundary $k_{x,\mathrm{cut}}$ of the k-mask for which we achieved convergence as discussed in Sec. 6.3.3. Note that we optimized the parameters for $E_{\mathrm{el}} = 0.1, 0.3, 0.5$, and $1.0\,\mathrm{MV\,cm^{-1}}$ to shorten the computational time. For the other field strengths we simply used the parameters such that the calculations are stable and the wave packets are sufficiently large to cover all relevant transitions, but the computational time could be reduced by fine tuning of the wave-packet and grid size as well as the time step δt.

E_{el} [MV/cm]	P_0 [W]	P_9/P_0	P_{10}/P_0	P_{14}/P_0	P_{15}/P_0
0.1	$2.1 \cdot 10^{-24}$	$3.0 \cdot 10^{-7}$	$5.8 \cdot 10^{-10}$	$6.5 \cdot 10^{-13}$	–
0.2	$9.9 \cdot 10^{-24}$	$2.0 \cdot 10^{-5}$	$1.1 \cdot 10^{-6}$	$6.1 \cdot 10^{-9}$	–
0.3	$3.2 \cdot 10^{-23}$	$3.0 \cdot 10^{-5}$	$1.6 \cdot 10^{-5}$	$3.7 \cdot 10^{-7}$	$1.9 \cdot 10^{-7}$
0.4	$1.6 \cdot 10^{-23}$	$1.6 \cdot 10^{-5}$	$2.9 \cdot 10^{-5}$	$7.7 \cdot 10^{-6}$	$2.2 \cdot 10^{-6}$
0.5	$3.4 \cdot 10^{-23}$	$4.0 \cdot 10^{-6}$	$2.9 \cdot 10^{-5}$	$1.5 \cdot 10^{-5}$	$2.4 \cdot 10^{-6}$
0.6	$9.2 \cdot 10^{-24}$	$3.2 \cdot 10^{-6}$	$1.6 \cdot 10^{-5}$	$1.5 \cdot 10^{-5}$	$1.3 \cdot 10^{-6}$
0.7	$1.5 \cdot 10^{-23}$	$2.6 \cdot 10^{-5}$	$4.6 \cdot 10^{-5}$	$9.2 \cdot 10^{-6}$	$4.7 \cdot 10^{-7}$
0.8	$2.2 \cdot 10^{-23}$	$1.5 \cdot 10^{-4}$	$2.7 \cdot 10^{-4}$	$6.6 \cdot 10^{-6}$	$2.4 \cdot 10^{-7}$
0.9	$3.1 \cdot 10^{-23}$	$4.4 \cdot 10^{-4}$	$9.0 \cdot 10^{-4}$	$4.3 \cdot 10^{-6}$	$1.7 \cdot 10^{-7}$
1.0	$4.6 \cdot 10^{-23}$	$8.3 \cdot 10^{-4}$	$3.4 \cdot 10^{-3}$	$3.9 \cdot 10^{-5}$	$6.1 \cdot 10^{-7}$

Tab. A.3: High-harmonic powers of the Fermi sea simulations for different field strengths.

Table A.3 contains the powers P_0 of the first harmonic of the HHs spectra for the different field strengths. We use these values to normalize the results shown in Fig. 6.12 in the main text. Additionally, in Tab. A.3 we summarize the normalized powers of the harmonic orders 9, 10, 14, and 15 as plotted in the inset of Fig. 6.12(a). Note that the values are rounded to one digit since the readout is not precise as it is difficult to determine the exact maximum of the harmonic peaks. Nevertheless, the data allows for deducing a trend for the scaling of the harmonic peaks with the field strength.

A.11. Velocity renormalization for Fermi energy sweeps

In Sec. 6.7 we study the influence of the Fermi energy E_{F} on the HHs emitted from the Bi_2Te_3 surface states. For computing the total velocity $\mathbf{v}(t) = \mathbf{v}_+(t) + \mathbf{v}_-^{\mathrm{cut}}(t)$ of the Fermi sea for $E_{\mathrm{F}} > 0$, we have to make $\mathbf{v}_+(t)$ and $\mathbf{v}_-^{\mathrm{cut}}(t)$ comparable. In order to compensate for the different sizes of the propagated wave packets $\Psi_\pm(\mathbf{k}, t)$, we renormalize $\mathbf{v}_+(t)$ with the norm N_+ of $\Psi_+(\mathbf{k}, t)$ and then divide it by the norm $N_-^{\mathrm{cut}}(E_{\mathrm{F}} = 0)$ of $\Psi_-(\mathbf{k}, t)$ inside the

k_F [Å^{-1}]	N_+	N_-^cut	$N_-^\mathrm{cut}(E_\mathrm{F}=0)$
0.02	4008	170 867	174 878
0.04	16 027	158 843	174 878
0.06	36 092	138 733	174 878
0.08	64 309	110 205	174 878

Tab. A.4: Norms of the different wave packets employed for calculating HHG from Bi_2Te_3 surface states for different Fermi energies E_F. The Fermi energies are defined by the Fermi wave vector $\mathbf{k}_\mathrm{F} = (k_\mathrm{F}, 0)$ on the k_x axis as $E_\mathrm{F} = E_\pm(\mathbf{k}_\mathrm{F})$, where "+" describes a positive and "−" a negative Fermi energy. N_+ denotes the norm for the case $E_\mathrm{F} > 0$, whereas N_-^cut is the norm inside the k-mask for $E_\mathrm{F} < 0$. The reference norm for $E_\mathrm{F} = 0$ is $N_-^\mathrm{cut}(E_\mathrm{F} = 0)$.

k-mask[4]. This gives the total velocity

$$\mathbf{v}(t) = \frac{N_+}{N_-^\mathrm{cut}(E_\mathrm{F}=0)}\mathbf{v}_+(t) + \mathbf{v}_-^\mathrm{cut}(t). \tag{A.24}$$

Since for all explored cases with $E_\mathrm{F} > 0$ we can use the same wave packet $\Psi_-(\mathbf{k}, 0)$, this renormalization of $\mathbf{v}_+(t)$ also ensures the comparability of the total velocities $\mathbf{v}(t)$ for different positive Fermi energies. To achieve this comparability for the negative Fermi energies as well, we also rescale the corresponding velocities $\mathbf{v}_-^\mathrm{cut}(t)$ for $E_\mathrm{F} < 0$. We thus multiply $\mathbf{v}_-^\mathrm{cut}(t)$ with their respective norm $N_-^\mathrm{cut}(E_\mathrm{F})$ inside the k-mask and then divide the result by the norm[5] $N_-^\mathrm{cut}(E_\mathrm{F} = 0)$ of the wave packet propagated for $E_\mathrm{F} = 0$. In Tab. A.4 we summarize the different values relevant for this renormalization. We define the Fermi energy E_F by the Fermi wave vector $\mathbf{k}_\mathrm{F} = (k_\mathrm{F}, 0)$ on the k_x axis as $E_\mathrm{F} = E_\pm(\mathbf{k}_\mathrm{F})$, where "+" describes a positive and "−" a negative Fermi energy. Then, we can write the norm N_+ for the case $E_\mathrm{F} > 0$ and the norm N_-^cut inside the k-mask for $E_\mathrm{F} < 0$ in one row. In the end, all data sets are normalized relative to the wave packet propagated for $E_\mathrm{F} = 0$, which also constitutes $\Psi_-(\mathbf{k}, t)$ for the calculations with positive Fermi energy. Its norm is denoted as $N_-^\mathrm{cut}(E_\mathrm{F} = 0)$.

[4]We denote the norm like the one for $E_\mathrm{F} = 0$ here since the wave packets $\Psi_-(\mathbf{k}, t)$ are the same for both cases.

[5]This norm is equal to the one for $\Psi_-(\mathbf{k}, t)$ in the case of positive Fermi energy.

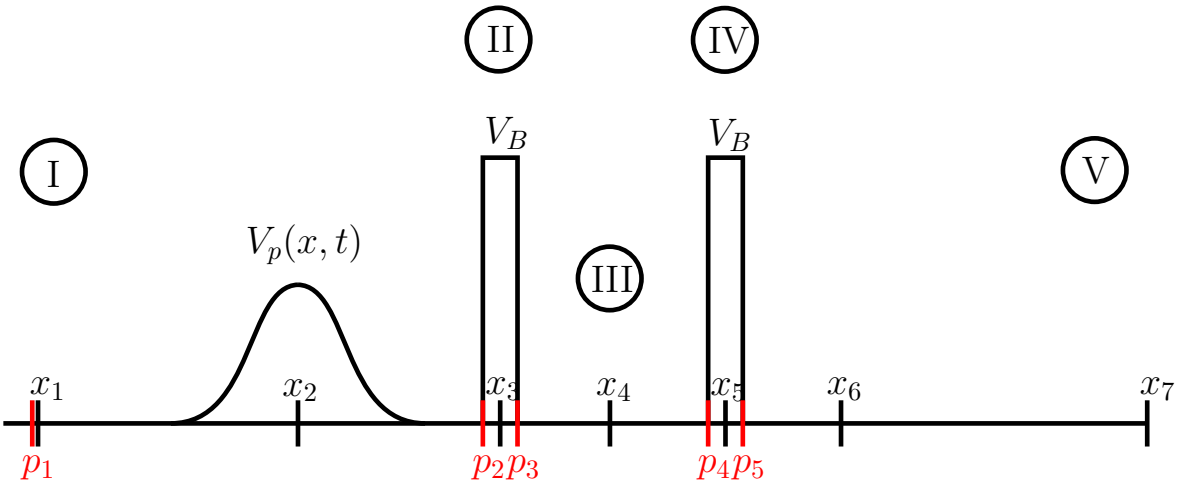

Fig. A.8: Sketch of the simulated Fabry-Perot system with applied pulse $V_p(t)$. The ansatz for the scattering state in TQT is split into the regions I-V. The time dependent local density of the total state $\Psi_n(x,t)$ at initial energy E_n is measured at the points 1-7. The height of the barriers is given by V_B and their width by $d = 3a_0$. The length of the cavity is $l = 70a_0$. The points p_1 - p_5 marked in red refer to the origin of the wave functions for transport from left to right. The points x_1 - x_7 indicate where we compare the local densities computed in TQT and Tkwant.

A.12. Testing the Lanczos Source propagator

A.12.1. Constructing the test system in TQT and Tkwant

In order to test the Lanczos Source propagator, we employ the Fabry-Perot setup studied in Ref. [264] using Tkwant. In collaboration with Geneviève Fleury from CEA-Saclay we set up the 1D Fabry-Perot system in Tkwant and adapt the tight-binding system to a continuum model. The latter we implement in TQT. For the sake of simplicity, we choose the lattice constant $a_0 = 1$ in both programs and thus all spatial coordinates are equal. A sketch of the system is shown in Fig. A.8. We set the width d of the barriers of height V_B to $d = 3a_0$ and the length l of the cavity to $l = 70a_0$.

The tight-binding Hamiltonian in Tkwant is

$$H_0 = -\gamma \sum_i c_i^\dagger c_{i+1} + \sum_i (2\gamma + V_i)\, c_i^\dagger c_i, \tag{A.25}$$

where $\gamma = 1$ is the nearest neighbor hopping (and unit of energy), 2γ the uniform onsite potential and V_i an additional potential defining the barriers V_B around x_3 and x_5. For all other lattice sites i, $V_i = 0$ and the eigenenergies are

$$E(k) = 2\gamma(1 - \cos(ka_0)). \tag{A.26}$$

To achieve a similar bandstructure (at least for low energies) in TQT we take the Hamiltonian

$$H_0 = \gamma k^2 + V_B(x), \tag{A.27}$$

where $\gamma = \hbar$ since the TQT algorithm scales all energies with $\hbar$, and $V_B(x) = V_B$ at the same lattice sites as in the TKWANT system and $V_B(x) = 0$ otherwise. For $V_B(x) = 0$ we get the eigenenergies

$$E(k) = \gamma k^2. \tag{A.28}$$

When comparing the results for TQT and TKWANT we have to keep in mind that the systems are only equivalent for small energies.

The pulse $V_p(x,t)$ which excites a wave packet $\psi_n(x,t)$ from the plane wave $\varphi_n(x)$ is defined as

$$V_p(x,t) = V_p \exp\left(-4\log(2)\frac{(t-3\tau_p)^2}{\tau_p^2}\right)\exp\left(-\frac{(x-x_2)^2}{2\Delta x^2}\right), \tag{A.29}$$

with $\tau_p/\hbar = 10/\gamma$, $x_2 = -50a_0$ and $\Delta x = 10a_0$ both in TQT and TKWANT.

A.12.2. Computing the scattering states for TQT

TKWANT uses KWANT [186] routines to calculate the scattering states of the static system which are then used as basis for the Fermi sea calculations. In TQT we either have to use wave-packet-based approaches already implemented by Krückl or to analytically define the scattering states. For the Fabry-Perot system we go for the analytical solution. We separate our system into five regions labeled by I-V in Fig. A.8 and make the plane wave ansatz

$$\begin{aligned}
\varphi_I(x) &= a\exp\left(\mathrm{i}k(x-p_1)\right) + b\exp\left(-\mathrm{i}k(x-p_1)\right),\\
\varphi_{II}(x) &= c\exp\left(\mathrm{i}\kappa(x-p_2)\right) + d\exp\left(-\mathrm{i}\kappa(x-p_2)\right),\\
\varphi_{III}(x) &= e\exp\left(\mathrm{i}k(x-p_3)\right) + f\exp\left(-\mathrm{i}k(x-p_3)\right),\\
\varphi_{IV}(x) &= g\exp\left(\mathrm{i}\kappa(x-p_4)\right) + h\exp\left(-\mathrm{i}\kappa(x-p_4)\right),\\
\varphi_V(x) &= j\exp\left(\mathrm{i}k(x-p_5)\right) + m\exp\left(-\mathrm{i}k(x-p_5)\right).
\end{aligned} \tag{A.30}$$

The origins p_1 - p_5 are marked in red in Fig. A.8. When considering transport from the left to the right side of the system – which is equivalent to the transmission from left to right lead in TKWANT – we can choose a freely and set $m = 0$. Comparison to the TKWANT scattering states suggests to use $a = -1$. The initial energy E_n of the static state defines $k = \sqrt{E_n/\gamma}$ and

$\kappa = \sqrt{(E_n - V_B)/\gamma}$. The origin $p_1 = -110a_0 - a_0/2$ is given by the left edge of the scattering region in TKWANT. The other parameters are defined by the barrier positions $p_2 = 0 - a_0/2$, $p_3 = p_2 + d$, $p_4 = p_3 + l$, $p_5 = p_4 + d$. The shift by $a_0/2$ is necessary since in TKWANT all potentials effectively begin in the middle of two lattice sites. The points p_2, p_3, p_4 and p_5 also mark the positions where we have to match the wave functions of the neighboring regions. They have to fulfill

$$\varphi_A(p_i) = \varphi_{A-1}(p_i) \text{ and } \varphi'_A(p_i) = \varphi'_{A-1}(p_i), \tag{A.31}$$

where $A \in [II, III, IV, V]$ and $p_i \in [p_2, p_3, p_4, p_5]$. We use the matching conditions to compute the prefactors b, c, d, e, f, g, h and j in *Mathematica* [239].

Our final goal is to compute observables for a band filled up to the Fermi energy E_F. For this we also need the scattering states for transport from the right to the left side of the system, i. e. the equivalent of transmission from right to left lead in TKWANT. Since for this case we plug in negative values for k, we set $j = -1$ and $b = 0$. To be consistent with the phases in TKWANT, we have to shift $\varphi_V(x)$ such that its origin lies at the right edge of the scattering region in TKWANT, meaning $p_5 \to p_5 + 110a_0$. Note that the matching conditions and the ansatz for the wave functions in other regions remain the same for both directions.

A.12.3. Comparison of the TQT and Tkwant results for a single k-mode

For comparing our TQT results to those from TKWANT and thus verifying that our Lanczos Source propagator works, we run tests for different pulse strengths V_p and barrier heights V_B. As initial energy we choose $E_n = 0.00747759\gamma$. The observable we compare is the local density $|\Psi(x_i, t)|^2 = |\exp(-\mathrm{i}E_n t)(\psi(x_i, t) + \varphi_0(x_i))|^2 = |\psi(x_i, t) + \varphi_0(x_i)|^2$, where $\varphi_0(x)$ is the scattering state constructed in Sec. A.12.2 and $\psi(x, t)$ the time dependent state computed by the Lanczos Source propagator. In TKWANT we obtain the same quantity by evaluating the implemented density operator for a one-body scattering state with initial energy E_n. For the points x_i we choose the positions marked in Fig. A.8, namely $x_1 = -110a_0$, $x_2 = -50a_0$, $x_3 = 1a_0$, $x_4 = 38a_0$, $x_5 = 74a_0$, $x_6 = 86a_0$ and $x_7 = 186a_0$.

We expect the best agreement for small energies E_n, relatively weak barriers

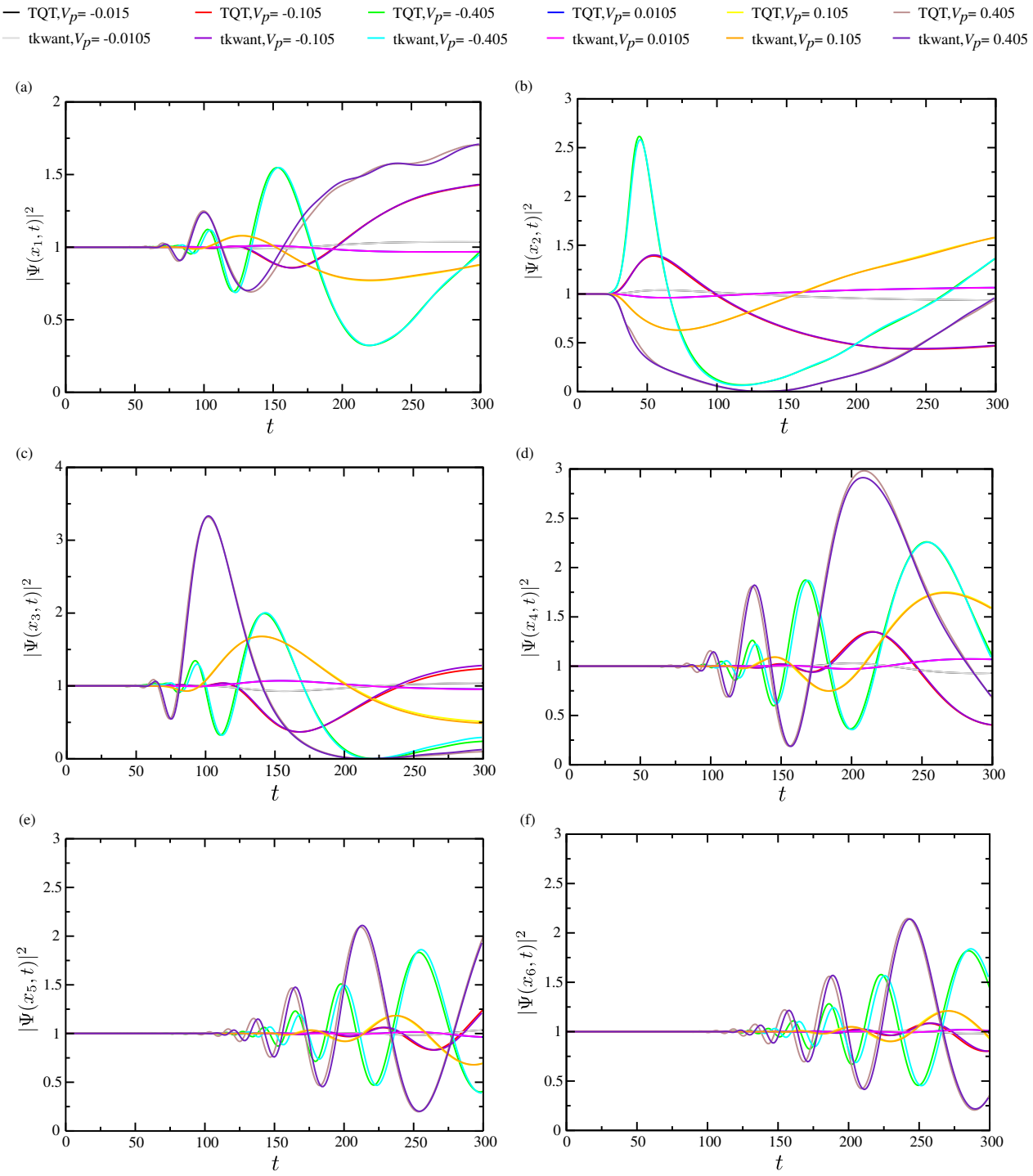

Fig. A.9: Comparison between TQT and TKWANT results for $V_B = 0.01\gamma$ and different strengths of V_p. Besides a phase shift that appears after the first barrier, the results show good agreement.

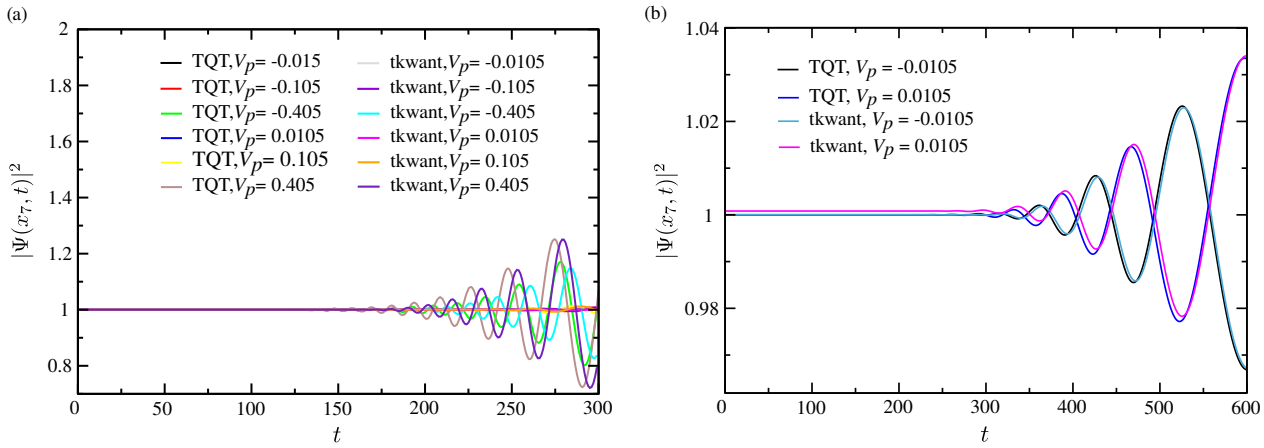

Fig. A.10: Comparison between TQT and TKWANT results for $V_B = 0.01\gamma$ at x_7 for (a) all pulse strengths V_p and short propagation times and (b) $V_p = \pm 0.0105$ and long propagation times.

V_B and small pulse strength V_p since the band structures are only in good agreement up to certain values of k. This is confirmed by first results shown in Fig. A.9. The results for the left and inside of the first barrier, see panels (a), (b), and (c), agree almost perfectly for all pulse strengths V_p. Then, in panels (d), (e), and (f), at least for the larger pulse strengths, some phase shift starts to enter. This shift is most probably a result of the dispersion inside the barrier and seems to only appear at the beginning of the signal. Since at position x_7 we only record the beginning of the signal when calculating up to $t = 300$, we repeat the calculations for larger propagation times. In Fig. A.10(a) we show the results for all pulse strengths for the shorter propagation times and in Fig. A.10(b) we illustrate the longer propagation times for the smallest pulse strength V_p since there the agreement should be best. Indeed, the results agree quite nicely which suggests that our Lanczos Source propagator is working.

A.12.4. Comparison of the TQT and Tkwant results for a Fermi sea

Our last step in testing the Lanczos Source propagator is to take the results for single k modes and to integrate over them as derived in App. A.7 in order to compute observables for a Fermi sea. For direct comparison with TKWANT, we have to adjust the formulation to the notation used in the TKWANT source code. There, the expectation value of an operator $\hat{\mathcal{O}}$ for a Fermi sea is defined as

$$\langle\hat{\mathcal{O}}\rangle(t) = \sum_\alpha \int \frac{\mathrm{d}E}{2\pi} f_\alpha(E) \langle\Psi_{\alpha E}(t)|\hat{\mathcal{O}}|\psi_{\alpha E}(t)\rangle, \tag{A.32}$$

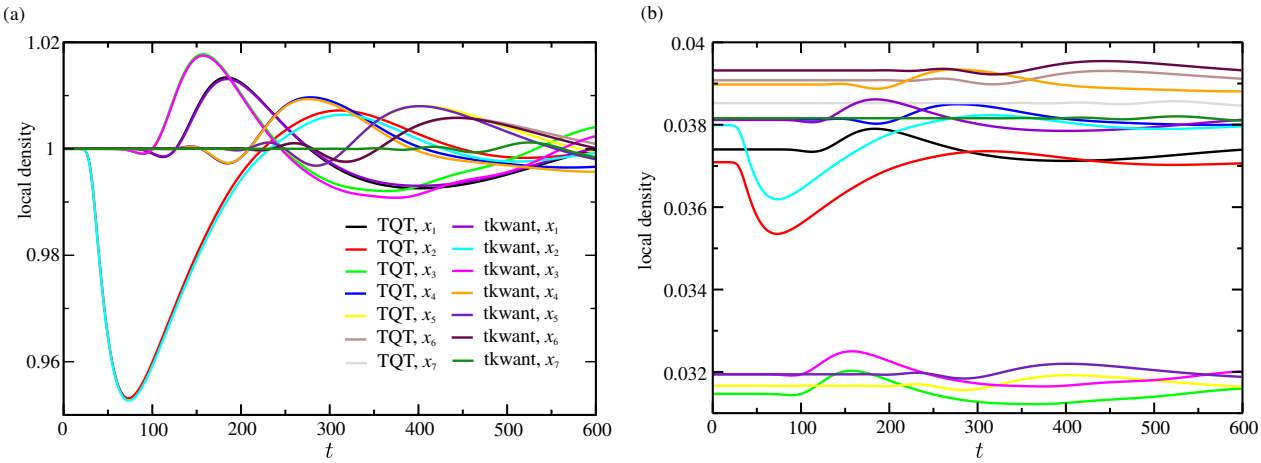

Fig. A.11: Comparison between TQT and TKWANT results for $V_B = 0.01\gamma$, $V_p = 0.0105$, integrated from $k_0 = \pm 0.0001/a_0$ to $k_n = \pm 0.1201/a_0$ using a Gauss-Kronrod scheme of order $m = 21$. In panel (a) the results are all rescaled to 1 whereas in panel (b) the normalization of the states in TQT is compensated by multiplying the results by the grid size. Due to the smaller scale of the resulting plot, mismatches are resolved more clearly than in the comparison in panel (a). However, the overall good agreement shows that the Lanczos Source propagator and the Gauss-Kronrod integration scheme are working.

where α labels the incoming channel, E the initial energy of the mode, and $f_\alpha(E)$ is the Fermi function of the lead associated with α. To translate this to TQT, we have to move from an energy-dependent description to a momentum-dependent one. Since our energy dispersion is parabolic, every energy E is connected to two k values with opposite sign. To rewrite the integral from energy to k space, we have to substitute $\int \mathrm{d}E \to \int 2\gamma k \, \mathrm{d}k$. Note that according to our definition of the scattering states in App. A.12.2, the positive (negative) k value corresponds to transport from left (right) to right (left) lead and thus is equivalent to the sum over leads α in Eq. (A.32). In TQT, we hence calculate the observable $\langle\hat{\mathcal{O}}\rangle(t)$ as

$$\langle\hat{\mathcal{O}}\rangle(t) = \int_{-k_F}^{0} \frac{2\gamma k}{2\pi} \langle\Psi_k(t)|\hat{\mathcal{O}}|\Psi_k(t)\rangle \, \mathrm{d}k + \int_{0}^{k_F} \frac{2\gamma k}{2\pi} \langle\Psi_k(t)|\hat{\mathcal{O}}|\Psi_k(t)\rangle \, \mathrm{d}k, \quad \text{(A.33)}$$

where we insert the Fermi distribution function $f_\alpha(E)$ for $T = 0$ in the following. Since in TKWANT the scattering states are normalized with respect to their velocity, we have to divide our TQT results $|\Psi_k(t)\rangle$ by $\sqrt{\frac{\mathrm{d}E}{\mathrm{d}k}} = \sqrt{2\gamma k}$ before performing the integral. Additionally, TQT normalizes the states with respect to the grid, which defines the scaling factor $N_x \cdot N_y$, where N_x and N_y are the number of TQT grid points in x and y direction, respectively, between the observables in TQT and TKWANT.

To perform the integration in a numerically efficient way, we subdivide the integral region into n intervals and use the Gauss-Kronrod method from TKWANT on each interval to choose the k modes k_j we want to sample over

and to obtain weights w_j for each point. It is then sufficient to compute the time evolution for the modes k_j and the integral can be approximated as

$$\int_{k_0}^{k_n} f(k)\,\mathrm{d}k = \sum_{i=0}^{n-1} \int_{k_i}^{k_{i+1}} f(k)\,\mathrm{d}k \approx \sum_{i=0}^{n-1} \sum_{k_i \le k_j < k_{i+1}} f(k_j) w_j, \tag{A.34}$$

where $k_n = k_F$. First, we have to check our results for convergence. Conveniently, the Gauss-Kronrod routine of TKWANT directly delivers the weights for the expansion of order m and $2m + 1$. If the results are the same for both orders, convergence is achieved. For the Fabry-Perot system we obtain convergence for $m = 21$ per interval and $n = 4$ intervals, integrating from $k_0 = \pm 0.0001/a_0$ to $k_n = \pm 0.1201/a_0$ and taking the parameters $V_p = 0.0105$ and $V_B = 0.01\gamma$, which already showed good agreement with TKWANT for the single k mode evaluation in Sec. A.12.3. For this specific case, we have to run TQT for 344 k modes. We choose $k_0 = \pm 0.0001/a_0$ as lower boundary of the integral to avoid numerical issues with the band bottom. For the time-independent case cross checking with *Mathematica* showed that this gives approximately the same results for the density as integrating from $k_0 = 0$ to k_n. The results are shown in Fig. A.11. In panel (a) we rescaled all final results to one for better comparability. In panel (b) we did the rescaling as supposed by the different normalizations, i.e. by simply multiplying the TQT results by the grid size. The qualitative agreement is good in both cases. Note that in the second case the scaling is small as compared to panel (a) such that even a small mismatch is resolved. Nonetheless, we are content with the agreement we achieved and are convinced that our Lanczos Source propagator as well as the Gauss-Kronrod integration scheme are working.

Bibliography

[1] C. B. Boyer, *The rainbow: From myth to mathematics* (T. Yoseloff, 1959).

[2] K. Hentschel, *Mapping the spectrum: Techniques of visual representation in research and teaching* (Oxford University Press, 2002).

[3] G. Kirchhoff, "Über die Fraunhofer'schen Linien", Ber. Akad. Wiss. Berlin, 662–665 (1859).

[4] J. C. Maxwell, "VIII. a dynamical theory of the electromagnetic field", Phil. Trans. R. Soc. **155**, 459–512 (1865).

[5] M. Planck, "Ueber das Gesetz der Energieverteilung im Normalspectrum", Ann. Phys. **309**, 553–563 (1901).

[6] A. Einstein, "Über einen die Erzeugung und Verwandlung des Lichtes betreffenden heuristischen Gesichtspunkt", Ann. Phys. **322**, 132–148 (1905).

[7] A. Einstein, "Zur Quantentheorie der Strahlung", Phys. Z. **18**, 121–128 (1917).

[8] J. P. Gordon, H. J. Zeiger, and C. H. Townes, "Molecular microwave oscillator and new hyperfine structure in the microwave spectrum of NH3", Phys. Rev. **95**, 282 (1954).

[9] T. H. Maiman, "Stimulated optical radiation in ruby", Nature **187**, 493–494 (1960).

[10] J. M. Dudley, "Light, Lasers, and the Nobel Prize", Adv. Photonics **2**, 050501 (2020).

[11] The Nobel Commitee for Physics, "For experimental methods that generate attosecond pulses of light for the study of electron dynamics in matter", Scientific Background (2023).

[12] M. Ferray, A. L'Huillier, X. F. Li, L. A. Lompre, G. Mainfray, and C. Manus, "Multiple-harmonic conversion of 1064 nm radiation in rare gases", J. Phys. B: At. Mol. Opt. Phys. **21**, L31 (1988).

[13] T. W. Hänsch, "A proposed sub-femtosecond pulse synthesizer using separate phase-locked laser oscillators", Opt. Commun. **80**, 71–75 (1990).

[14] G. Farkas and C. Tóth, "Proposal for attosecond light pulse generation using laser induced multiple-harmonic conversion processes in rare gases", Phys. Lett. A **168**, 447–450 (1992).

[15] S. E. Harris, J. J. Macklin, and T. W. Hänsch, "Atomic scale temporal structure inherent to high-order harmonic generation", Opt. Commun. **100**, 487–490 (1993).

[16] A. L'Huillier, K. J. Schafer, and K. C. Kulander, "Theoretical aspects of intense field harmonic generation", J. Phys. B: At. Mol. Opt. Phys. **24**, 3315 (1991).

[17] K. J. Schafer, B. Yang, L. F. Dimauro, and K. C. Kulander, "Above threshold ionization beyond the high harmonic cutoff", Phys. Rev. Lett. **70**, 1599 (1993).

[18] P. B. Corkum, "Plasma perspective on strong field multiphoton ionization", Phys. Rev. Lett. **71**, 1994 (1993).

[19] M. Lewenstein, P. Balcou, M. Y. Ivanov, A. L'Huillier, and P. B. Corkum, "Theory of high-harmonic generation by low-frequency laser fields", Phys. Rev. A **49**, 2117 (1994).

[20] M. Bellini, C. Lyngå, A. Tozzi, M. B. Gaarde, T. W. Hänsch, A. L'Huillier, and C. G. Wahlström, "Temporal coherence of ultrashort high-order harmonic pulses", Phys. Rev. Lett. **81**, 297 (1998).

[21] J. M. Schins, P. Breger, P. Agostini, R. C. Constantinescu, H. G. Muller, G. Grillon, A. Antonetti, and A. Mysyrowicz, "Observation of laser-assisted Auger decay in argon", Phys. Rev. Lett. **73**, 2180 (1994).

[22] M. Hentschel, R. Kienberger, C. Spielmann, G. A. Reider, N. Milosevic, T. Brabec, P. Corkum, U. Heinzmann, M. Drescher, and F. Krausz, "Attosecond metrology", Nature **414**, 509–513 (2001).

[23] P. M. Paul, E. S. Toma, P. Breger, G. Mullot, F. Augé, P. Balcou, H. G. Muller, and P. Agostini, "Observation of a train of attosecond pulses from high harmonic generation", Science **292**, 1689–1692 (2001).

[24] G. Floquet, "Sur les équations différentielles linéaires à coefficients périodiques", Ann. Sci. Éc. Norm. Supér. **12**, 47–88 (1883).

[25] J. H. Shirley, "Solution of the Schrödinger equation with a Hamiltonian periodic in time", Phys. Rev. **138**, B979 (1965).

[26] Y. B. Zel'dovich, "The quasienergy of a quantum-mechanical system subjected to a periodic action", Sov. Phys. JETP **24**, 1006 (1967).

[27] H. Sambe, "Steady states and quasienergies of a quantum-mechanical system in an oscillating field", Phys. Rev. A **7**, 2203 (1973).

[28] S. I. Chu and D. A. Telnov, "Beyond the Floquet theorem: Generalized Floquet formalisms and quasienergy methods for atomic and molecular multiphoton processes in intense laser fields", Phys. Rep. **390**, 1–131 (2004).

[29] N. Tzoar and J. I. Gersten, "Theory of electronic band structure in intense laser fields", Phys. Rev. B **12**, 1132 (1975).

[30] M. Z. Hasan and C. L. Kane, "Colloquium: Topological insulators", Rev. Mod. Phys. **82**, 3045 (2010).

[31] X. L. Qi and S. C. Zhang, "Topological insulators and superconductors", Rev. Mod. Phys. **83**, 1057 (2011).

[32] A. H. Castro Neto, F. Guinea, N. M. R. Peres, K. S. Novoselov, and A. K. Geim, "The electronic properties of graphene", Rev. Mod. Phys. **81**, 109 (2009).

[33] N. P. Armitage, E. J. Mele, and A. Vishwanath, "Weyl and Dirac semimetals in three-dimensional solids", Rev. Mod. Phys. **90**, 015001 (2018).

[34] B. Yan and C. Felser, "Topological materials: Weyl semimetals", Annu. Rev. Condens. Matter Phys. **8**, 337–354 (2017).

[35] M. Imada, A. Fujimori, and Y. Tokura, "Metal-insulator transitions", Rev. Mod. Phys. **70**, 1039 (1998).

[36] T. Oka and S. Kitamura, "Floquet engineering of quantum materials", Annu. Rev. Condens. Matter Phys. **10**, 387–408 (2019).

[37] K. von Klitzing, G. Dorda, and M. Pepper, "New method for high-accuracy determination of the fine-structure constant based on quantized Hall resistance", Phys. Rev. Lett. **45**, 494 (1980).

[38] D. C. Tsui, H. L. Stormer, and A. C. Gossard, "Two-dimensional magnetotransport in the extreme quantum limit", Phys. Rev. Lett. **48**, 1559 (1982).

[39] C. L. Kane and E. J. Mele, "Z2 topological order and the quantum spin hall effect", Phys. Rev. Lett. **95**, 146802 (2005).

[40] B. A. Bernevig, T. L. Hughes, and S.-C. Zhang, "Quantum spin Hall effect and topological phase transition in HgTe quantum wells", Science **314**, 1757–1761 (2006).

[41] M. König, S. Wiedmann, C. Brüne, A. Roth, H. Buhmann, L. W. Molenkamp, X.-L. Qi, and S.-C. Zhang, "Quantum spin Hall insulator state in HgTe quantum wells", Science **318**, 766–770 (2007).

[42] Y. Xia, D. Qian, D. Hsieh, L. Wray, A. Pal, H. Lin, A. Bansil, D. Grauer, Y. S. Hor, R. J. Cava, and M. Z. Hasan, "Observation of a large-gap topological-insulator class with a single Dirac cone on the surface", Nat. Phys. **5**, 398–402 (2009).

[43] Y. L. Chen, J. G. Analytis, J. H. Chu, Z. K. Liu, S. K. Mo, X. L. Qi, H. J. Zhang, P. H. Lu, X. Dai, Z. Fang, S. C. Zhang, I. R. Fisher, Z. Hussain, and Z. X. Shen, "Experimental realization of a three-dimensional topological insulator, Bi2Te3", Science **325**, 178–181 (2009).

[44] D. Hsieh, Y. Xia, D. Qian, L. Wray, F. Meier, J. H. Dil, J. Osterwalder, L. Patthey, A. V. Fedorov, H. Lin, A. Bansil, D. Grauer, Y. S. Hor, R. J. Cava, and M. Z. Hasan, "Observation of time-reversal-protected single-Dirac-cone topological-insulator states in Bi2Te3 and Sb2Te3", Phys. Rev. Lett. **103**, 146401 (2009).

[45] D. A. Kozlov, Z. D. Kvon, E. B. Olshanetsky, N. N. Mikhailov, S. A. Dvoretsky, and D. Weiss, "Transport properties of a 3D topological insulator based on a strained high-mobility HgTe film", Phys. Rev. Lett. **112**, 196801 (2014).

[46] F. D. M. Haldane, "Model for a quantum Hall effect without Landau levels: Condensed-matter realization of the "parity anomaly"", Phys. Rev. Lett. **61**, 2015 (1988).

[47] F. D. M. Haldane, "Nobel lecture: Topological quantum matter", Rev. Mod. Phys. **89**, 040502 (2017).

[48] T. Jungwirth, Q. Niu, and A. H. MacDonald, "Anomalous Hall effect in ferromagnetic semiconductors", Phys. Rev. Lett. **88**, 207208 (2002).

[49] N. Nagaosa, J. Sinova, S. Onoda, A. H. Macdonald, and N. P. Ong, "Anomalous Hall effect", Rev. Mod. Phys. **82**, 1538 (2010).

[50] R. Peierls, "Quelques propriétés typiques des corps solides", Annales de l'I. H. P. **5**, 177–222 (1935).

[51] L. Landau, "On the theory of phase transitions", Phys. Z. Sowjetunion **11**, 19–32 (1937).

[52] K. S. Novoselov, A. K. Geim, S. V. Morozov, D. Jiang, Y. Zhang, S. V. Dubonos, I. V. Grigorieva, and A. A. Firsov, "Electric field effect in atomically thin carbon films", Science **306**, 666–669 (2004).

[53] J. C. Meyer, A. K. Geim, M. I. Katsnelson, K. S. Novoselov, T. J. Booth, and S. Roth, "The structure of suspended graphene sheets", Nature **446**, 60–63 (2007).

[54] T. Oka and H. Aoki, "Photovoltaic Hall effect in graphene", Phys. Rev. B **79**, 081406(R) (2009).

[55] J. W. McIver, B. Schulte, F. U. Stein, T. Matsuyama, G. Jotzu, G. Meier, and A. Cavalleri, "Light-induced anomalous Hall effect in graphene", Nat. Phys. **16**, 38–41 (2020).

[56] N. H. Lindner, G. Refael, and V. Galitski, "Floquet topological insulator in semiconductor quantum wells", Nat. Phys. **7**, 490–495 (2011).

[57] T. Kitagawa, M. A. Broome, A. Fedrizzi, M. S. Rudner, E. Berg, I. Kassal, A. Aspuru-Guzik, E. Demler, and A. G. White, "Observation of topologically protected bound states in photonic quantum walks", Nat. Commun. **3**, 882 (2012).

[58] W. Hu, J. C. Pillay, K. Wu, M. Pasek, P. P. Shum, and Y. D. Chong, "Measurement of a topological edge invariant in a microwave network", Phys. Rev. X **5**, 011012 (2015).

[59] L. J. Maczewsky, J. M. Zeuner, S. Nolte, and A. Szameit, "Observation of photonic anomalous Floquet topological insulators", Nat. Commun. **8**, 13756 (2017).

[60] S. Mukherjee, A. Spracklen, M. Valiente, E. Andersson, P. Öhberg, N. Goldman, and R. R. Thomson, "Experimental observation of anomalous topological edge modes in a slowly driven photonic lattice", Nat. Commun. **8**, 13918 (2017).

[61] A. D'Errico, F. Cardano, M. Maffei, A. Dauphin, R. Barboza, C. Esposito, B. Piccirillo, M. Lewenstein, P. Massignan, and L. Marrucci, "Two-dimensional topological quantum walks in the momentum space of structured light", Optica **7**, 108 (2020).

[62] Y. G. Peng, C. Z. Qin, D. G. Zhao, Y. X. Shen, X. Y. Xu, M. Bao, H. Jia, and X. F. Zhu, "Experimental demonstration of anomalous Floquet topological insulator for sound", Nat. Commun. **7**, 13368 (2016).

[63] K. Wintersperger, C. Braun, F. N. Ünal, A. Eckardt, M. D. Liberto, N. Goldman, I. Bloch, and M. Aidelsburger, "Realization of an anomalous Floquet topological system with ultracold atoms", Nat. Phys. **16**, 1058–1063 (2020).

[64] F. N. Ünal, B. Seradjeh, and A. Eckardt, "How to directly measure Floquet topological invariants in optical lattices", Phys. Rev. Lett. **122**, 253601 (2019).

[65] M. S. Rudner, N. H. Lindner, E. Berg, and M. Levin, "Anomalous edge states and the bulk-edge correspondence for periodically driven two-dimensional systems", Phys. Rev. X **3**, 031005 (2013).

[66] T. Kitagawa, E. Berg, M. Rudner, and E. Demler, "Topological characterization of periodically driven quantum systems", Phys. Rev. B **82**, 235114 (2010).

[67] A. P. Schnyder, S. Ryu, A. Furusaki, and A. W. Ludwig, "Classification of topological insulators and superconductors in three spatial dimensions", Phys. Rev. B **78**, 195125 (2008).

[68] G. G. Pyrialakos, J. Beck, M. Heinrich, L. J. Maczewsky, N. V. Kantartzis, M. Khajavikhan, A. Szameit, and D. N. Christodoulides, "Bimorphic Floquet topological insulators", Nat. Mater. **21**, 634–639 (2022).

[69] M. Wackerl, "Transport in periodically driven systems", PhD thesis, University of Regensburg, Germany (2020).

[70] F. Bloch, "Über die Quantenmechanik der Elektronen in Kristallgittern", Z. Phys. **52**, 555–600 (1929).

[71] C. Zener, "A theory of the electrical breakdown of solid dielectrics", Proc. R. Soc. Lond. A **145**, 523–529 (1934).

[72] A. Wacker, "Semiconductor superlattices: a model system for nonlinear transport", Phys. Rep. **357**, 1–111 (2002).

[73] S. Arlinghaus and M. Holthaus, "Generalized acceleration theorem for spatiotemporal Bloch waves", Phys. Rev. B **84**, 054301 (2011).

[74] V. Junk, P. Reck, C. Gorini, and K. Richter, "Floquet oscillations in periodically driven Dirac systems", Phys. Rev. B **101**, 134302 (2020).

[75] B. Hamdou, J. Gooth, A. Dorn, E. Pippel, and K. Nielsch, "Surface state dominated transport in topological insulator Bi2Te3 nanowires", Appl. Phys. Lett. **103**, 193107 (2013).

[76] J. Dufouleur, L. Veyrat, A. Teichgräber, S. Neuhaus, C. Nowka, S. Hampel, J. Cayssol, J. Schumann, B. Eichler, O. G. Schmidt, B. Büchner, and R. Giraud, "Quasiballistic transport of Dirac fermions in a Bi2Se3 nanowire", Phys. Rev. Lett. **110**, 186806 (2013).

[77] L. A. Jauregui, M. T. Pettes, L. P. Rokhinson, L. Shi, and Y. P. Chen, "Magnetic field-induced helical mode and topological transitions in a topological insulator nanoribbon", Nat. Nanotechnol. **11**, 345–351 (2016).

[78] L. Fu and C. L. Kane, "Topological insulators with inversion symmetry", Phys. Rev. B **76**, 045302 (2007).

[79] D. Hsieh, D. Qian, L. Wray, Y. Xia, Y. S. Hor, R. J. Cava, and M. Z. Hasan, "A topological Dirac insulator in a quantum spin Hall phase", Nature **452**, 970–974 (2008).

[80] J. Reimann, S. Schlauderer, C. P. Schmid, F. Langer, S. Baierl, K. A. Kokh, O. E. Tereshchenko, A. Kimura, C. Lange, J. Güdde, U. Höfer, and R. Huber, "Subcycle observation of lightwave-driven Dirac currents in a topological surface band", Nature **562**, 396–400 (2018).

[81] C. P. Schmid, L. Weigl, P. Grössing, V. Junk, C. Gorini, S. Schlauderer, S. Ito, M. Meierhofer, N. Hofmann, D. Afanasiev, J. Crewse, K. A. Kokh, O. E. Tereshchenko, J. Güdde, F. Evers, J. Wilhelm, K. Richter, U. Höfer, and R. Huber, "Tunable non-integer high-harmonic generation in a topological insulator", Nature **593**, 385–390 (2021).

[82] N. Yoshikawa, T. Tamaya, and K. Tanaka, "Optics: high-harmonic generation in graphene enhanced by elliptically polarized light excitation", Science **356**, 736–738 (2017).

[83] H. A. Hafez, S. Kovalev, J. C. Deinert, Z. Mics, B. Green, N. Awari, M. Chen, S. Germanskiy, U. Lehnert, J. Teichert, Z. Wang, K. J. Tielrooij, Z. Liu, Z. Chen, A. Narita, K. Müllen, M. Bonn, M. Gensch, and D. Turchinovich, "Extremely efficient terahertz high-harmonic generation in graphene by hot Dirac fermions", Nature **561**, 507–511 (2018).

[84] B. Cheng, N. Kanda, T. N. Ikeda, T. Matsuda, P. Xia, T. Schumann, S. Stemmer, J. Itatani, N. P. Armitage, and R. Matsunaga, "Efficient terahertz harmonic generation with coherent acceleration of electrons in the Dirac semimetal Cd3As2", Phys. Rev. Lett. **124**, 117402 (2020).

[85] R. E. Silva, Jiménez-Galán, B. Amorim, O. Smirnova, and M. Ivanov, "Topological strong-field physics on sub-laser-cycle timescale", Nat. Photon. **13**, 849–854 (2019).

[86] H. Zhang, C. X. Liu, X. L. Qi, X. Dai, Z. Fang, and S. C. Zhang, "Topological insulators in Bi2Se3, Bi2Te3 and Sb2Te3 with a single Dirac cone on the surface", Nat. Phys. **5**, 438–442 (2009).

[87] C.-X. Liu, X.-L. Qi, H. Zhang, X. Dai, Z. Fang, and S.-C. Zhang, "Model Hamiltonian for topological insulators", Phys. Rev. B **82**, 045122 (2010).

[88] L. Fu, "Hexagonal warping effects in the surface states of the topological insulator Bi2Te3", Phys. Rev. Lett. **103**, 266801 (2009).

[89] D. Baykusheva, A. Chacón, D. Kim, D. E. Kim, D. A. Reis, and S. Ghimire, "Strong-field physics in three-dimensional topological insulators", Phys. Rev. A **103**, 023101 (2021).

[90] D. Baykusheva, A. Chacón, J. Lu, T. P. Bailey, J. A. Sobota, H. Soifer, P. S. Kirchmann, C. Rotundu, C. Uher, T. F. Heinz, D. A. Reis, and S. Ghimire, "All-optical probe of three-dimensional topological insulators based on high-harmonic generation by circularly polarized laser fields", Nano Lett. **21**, 8970–8978 (2021).

[91] C. Heide, Y. Kobayashi, D. R. Baykusheva, D. Jain, J. A. Sobota, M. Hashimoto, P. S. Kirchmann, S. Oh, T. F. Heinz, D. A. Reis, and S. Ghimire, "Probing topological phase transitions using high-harmonic generation", Nat. Photon. **16**, 620–624 (2022).

[92] O. Neufeld, N. Tancogne-Dejean, H. Hübener, U. D. Giovannini, and A. Rubio, "Are there universal signatures of topological phases in high harmonic generation? Probably not", Phys. Rev. X **13**, 031011 (2023).

[93] C. Yu, S. Jiang, and R. Lu, "High order harmonic generation in solids: a review on recent numerical methods", Adv. Phys.: X **4**, 1562982 (2019).

[94] E. Goulielmakis and T. Brabec, "High harmonic generation in condensed matter", Nat. Photon. **16**, 411–421 (2022).

[95] M. Kira and S. W. Koch, *Semiconductor quantum optics* (Cambridge University Press, 2011).

[96] E. Runge and E. K. Gross, "Density-functional theory for time-dependent systems", Phys. Rev. Lett. **52**, 997 (1984).

[97] E. Coccia and E. Luppi, "Time-dependent ab initio approaches for high-harmonic generation spectroscopy", J. Phys.: Condens. Matter **34**, 073001 (2022).

[98] L. Plaja and L. Roso-Franco, "High-order harmonic generation in a crystalline solid", Phys. Rev. B **45**, 8334 (1992).

[99] Z. Guan, X. X. Zhou, and X. B. Bian, "High-order-harmonic generation from periodic potentials driven by few-cycle laser pulses", Phys. Rev. A **93**, 033852 (2016).

[100] X. Liu, X. Zhu, P. Lan, X. Zhang, D. Wang, Q. Zhang, and P. Lu, "Time-dependent population imaging for high-order-harmonic generation in solids", Phys. Rev. A **95**, 063419 (2017).

[101] X. Q. Wang, Y. Xu, X. H. Huang, and X. B. Bian, "Interference between inter- and intraband currents in high-order harmonic generation in solids", Phys. Rev. A **98**, 023427 (2018).

[102] J. Li, S. Fu, H. Wang, X. Zhang, B. Ding, B. Hu, and H. Du, "Limitations of the single-active-electron approximation in quantum simulations of solid high-order harmonic generation", Phys. Rev. A **98**, 043409 (2018).

[103] J. N. Domrzalski, T. E. Stevens, R. M. V. Ginhoven, al -, S. A. Policastro, R. M. Anderson, C. M. Hangarter, M. Korbman, S. Y. Kruchinin, and V. S. Yakovlev, "Quantum beats in the polarization response of a dielectric to intense few-cycle laser pulses", New J. Phys. **15**, 013006 (2013).

[104] T. Ikemachi, Y. Shinohara, T. Sato, J. Yumoto, M. Kuwata-Gonokami, and K. L. Ishikawa, "Trajectory analysis of high-order-harmonic generation from periodic crystals", Phys. Rev. A **95**, 043416 (2017).

[105] J. Z. Jin, X. R. Xiao, H. Liang, M. X. Wang, S. G. Chen, Q. Gong, and L. Y. Peng, "High-order harmonic generation from a two-dimensional band structure", Phys. Rev. A **97**, 043420 (2018).

[106] J. M. Luttinger and W. Kohn, "Motion of electrons and holes in perturbed periodic fields", Phys. Rev. **97**, 869 (1955).

[107] J. Wilhelm, P. Grössing, A. Seith, J. Crewse, M. Nitsch, L. Weigl, C. Schmid, and F. Evers, "Semiconductor Bloch-equations formalism: Derivation and application to high-harmonic generation from Dirac fermions", Phys. Rev. B **103**, 125419 (2021).

[108] M. Graml, M. Nitsch, A. Seith, F. Evers, and J. Wilhelm, "Influence of chirp and carrier-envelope phase on noninteger high-harmonic generation", Phys. Rev. B **107**, 054305 (2023).

[109] H. B. Nielsen and M. Ninomiya, "A no-go theorem for regularizing chiral fermions", Phys. Lett. B **105**, 219–223 (1981).

[110] H. B. Nielsen and M. Ninomiya, "Absence of neutrinos on a lattice: (i). Proof by homotopy theory", Nucl. Phys. B **185**, 20–40 (1981).

[111] H. B. Nielsen and M. Ninomiya, "Absence of neutrinos on a lattice: (II). Intuitive topological proof", Nucl. Phys. B **193**, 173–194 (1981).

[112] L. Tarruell, D. Greif, T. Uehlinger, G. Jotzu, and T. Esslinger, "Creating, moving and merging Dirac points with a Fermi gas in a tunable honeycomb lattice", Nature **483**, 302–305 (2012).

[113] G. Weick, C. Woollacott, W. L. Barnes, O. Hess, and E. Mariani, "Dirac-like plasmons in honeycomb lattices of metallic nanoparticles", Phys. Rev. Lett. **110**, 106801 (2013).

[114] T. Jacqmin, I. Carusotto, I. Sagnes, M. Abbarchi, D. D. Solnyshkov, G. Malpuech, E. Galopin, A. Lemaître, J. Bloch, and A. Amo, "Direct observation of Dirac cones and a flatband in a honeycomb lattice for polaritons", Phys. Rev. Lett. **112**, 116402 (2014).

[115] P. R. Wallace, "The band theory of graphite", Phys. Rev. **71**, 622 (1947).

[116] G. W. Semenoff, "Condensed-matter simulation of a three-dimensional anomaly", Phys. Rev. Lett. **53**, 2449 (1984).

[117] K. S. Novoselov, A. K. Geim, S. V. Morozov, D. Jiang, M. I. Katsnelson, I. V. Grigorieva, S. V. Dubonos, and A. A. Firsov, "Two-dimensional gas of massless Dirac fermions in graphene", Nature **438**, 197–200 (2005).

[118] K. von Klitzing, "The quantized Hall effect", Rev. Mod. Phys. **58**, 519 (1986).

[119] O. Klein, "Die Reflexion von Elektronen an einem Potentialsprung nach der relativistischen Dynamik von Dirac", Z. Phys. **53**, 157–165 (1929).

[120] M. I. Katsnelson, K. S. Novoselov, and A. K. Geim, "Chiral tunnelling and the Klein paradox in graphene", Nat. Phys. **2**, 620–625 (2006).

[121] A. F. Young and P. Kim, "Quantum interference and Klein tunnelling in graphene heterojunctions", Nat. Phys. **5**, 222–226 (2009).

[122] K.-I. Sasaki and R. Saito, "Pseudospin and deformation-induced gauge field in graphene", Prog. Theo. Phys. Supp. **176**, 253–278 (2008).

[123] V. Junk, "Dynamics of wave packets in periodically driven Dirac systems", Master's thesis, University of Regensburg, Germany (2018).

[124] M. I. Katsnelson, *Graphene: Carbon in two dimensions* (Cambridge University Press, 2012).

[125] C. Zener and J. E. Lennard-Jones, "The general proof of certain fundamental equations in the theory of metallic conduction", Proc. R. Soc. Lond. A **144**, 101–117 (1934).

[126] P. Reck, "Quantum echoes and revivals in two-band systems and Bose-Einstein condensates", PhD thesis, University of Regensburg, Germany (2018).

[127] M. O. Goerbig, "Electronic properties of graphene in a strong magnetic field", Rev. Mod. Phys. **83**, 1193 (2011).

[128] C. Brüne, C. X. Liu, E. G. Novik, E. M. Hankiewicz, H. Buhmann, Y. L. Chen, X. L. Qi, Z. X. Shen, S. C. Zhang, and L. W. Molenkamp, "Quantum Hall effect from the topological surface states of strained bulk HgTe", Phys. Rev. Lett. **106**, 126803 (2011).

[129] C. Y. Zhu, S. H. Zheng, H. J. Duan, M. X. Deng, and R. Q. Wang, "Double Andreev reflections at surface states of the topological insulators with hexagonal warping", Front. Phys. **15**, 23602 (2020).

[130] R. S. Akzyanov and A. L. Rakhmanov, "Surface charge conductivity of a topological insulator in a magnetic field: The effect of hexagonal warping", Phys. Rev. B **97**, 075421 (2018).

[131] R. S. Akzyanov and A. L. Rakhmanov, "Bulk and surface spin conductivity in topological insulators with hexagonal warping", Phys. Rev. B **99**, 045436 (2019).

[132] T. Choudhari and N. Deo, "Effect of hexagonal warping of the Fermi surface on the thermoelectric properties of a topological insulator irradiated with linearly polarized radiation", Phys. Rev. B **100**, 035303 (2019).

[133] Z. Li and J. P. Carbotte, "Hexagonal warping on optical conductivity of surface states in topological insulator Bi2Te3", Phys. Rev. B **87**, 155416 (2013).

[134] G. Tkachov, *Topological insulators : the physics of spin helicity in quantum transport* (Jenny Stanford Publishing, 2016).

[135] M. V. Berry, "Quantual phase factors accompanying adiabatic changes", Proc. R. Soc. Lond. A **392**, 45–57 (1984).

[136] B. Simon, "Holonomy, the quantum adiabatic theorem, and Berry's phase", Phys. Rev. Lett. **51**, 2167 (1983).

[137] S.-S. Chern and J. Simons, "Characteristic forms and geometric invariants", Ann. Math. **99**, 48–69 (1974).

[138] D. J. Thouless, M. Kohmoto, M. P. Nightingale, and M. den Nijs, "Quantized Hall conductance in a two-dimensional periodic potential", Phys. Rev. Lett. **49**, 405 (1982).

[139] M. C. Chang and Q. Niu, "Berry phase, hyperorbits, and the Hofstadter spectrum", Phys. Rev. Lett. **75**, 1348 (1995).

[140] R. Resta, "Theory of the electric polarization in crystals", Ferroelectrics **136**, 51–55 (1992).

[141] R. D. King-Smith and D. Vanderbilt, "Theory of polarization of crystalline solids", Phys. Rev. B **47**, 1651(R) (1993).

[142] T. Thonhauser, D. Ceresoli, D. Vanderbilt, and R. Resta, "Orbital magnetization in periodic insulators", Phys. Rev. Lett. **95**, 137205 (2005).

[143] D. Xiao, J. Shi, and Q. Niu, "Berry phase correction to electron density of states in solids", Phys. Rev. Lett. **95**, 137204 (2005).

[144] D. Xiao, M. C. Chang, and Q. Niu, "Berry phase effects on electronic properties", Rev. Mod. Phys. **82**, 1959 (2010).

[145] A. Chacón, D. Kim, W. Zhu, S. P. Kelly, A. Dauphin, E. Pisanty, A. S. Maxwell, A. Picón, M. F. Ciappina, D. E. Kim, C. Ticknor, A. Saxena, and M. Lewenstein, "Circular dichroism in higher-order harmonic generation: Heralding topological phases and transitions in Chern insulators", Phys. Rev. B **102**, 134115 (2020).

[146] E. Schrödinger, *Ueber die kraeftefreie Bewegung in der relativistischen Quantenmechanik* (Akademie der Wissenschaften in Kommission bei W. de Gruyter u. Company, 1930).

[147] K. Huang, "On the zitterbewegung of the Dirac electron", Am. J. Phys. **20**, 479–484 (1952).

[148] L. Ferrari and G. Russo, "Nonrelativistic zitterbewegung in two-band systems", Phys. Rev. B **42**, 7454 (1990).

[149] J. Schliemann, D. Loss, and R. M. Westervelt, "Zitterbewegung of electronic wave packets in III-V zinc-blende semiconductor quantum wells", Phys. Rev. Lett. **94**, 206801 (2005).

[150] W. Zawadzki, "One-dimensional semirelativity for electrons in carbon nanotubes", Phys. Rev. B **74**, 205439 (2006).

[151] T. M. Rusin and W. Zawadzki, "Zitterbewegung of electrons in graphene in a magnetic field", Phys. Rev. B **78**, 1–9 (2008).

[152] M. I. Katsnelson, "Zitterbewegung, chirality, and minimal conductivity in graphene", Eur. Phys. J. B **51**, 157–160 (2006).

[153] P. Reck, C. Gorini, and K. Richter, "Steering zitterbewegung in driven Dirac systems: From persistent modes to echoes", Phys. Rev. B **101**, 094306 (2020).

[154] L. K. Shi, S. C. Zhang, and K. Chang, "Anomalous electron trajectory in topological insulators", Phys. Rev. B **87**, 161115(R) (2013).

[155] R. Gerritsma, G. Kirchmair, F. Zähringer, E. Solano, R. Blatt, and C. F. Roos, "Quantum simulation of the Dirac equation", Nature **463**, 68–71 (2010).

[156] C. Qu, C. Hamner, M. Gong, C. Zhang, and P. Engels, "Observation of zitterbewegung in a spin-orbit-coupled Bose-Einstein condensate", Phys. Rev. A **88**, 021604(R) (2013).

[157] L. J. Leblanc, M. C. Beeler, K. Jiménez-García, A. R. Perry, S. Sugawa, R. A. Williams, and I. B. Spielman, "Direct observation of zitterbewegung in a bose–einstein condensate", New J. Phys. **15**, 073011 (2013).

[158] I. Stepanov, M. Ersfeld, A. V. Poshakinskiy, M. Lepsa, E. L. Ivchenko, S. A. Tarasenko, and B. Beschoten, "Coherent electron zitterbewegung", Preprint (2016) 10.48550/arxiv.1612.06190.

[159] W. Zawadzki and T. M. Rusin, "Zitterbewegung (trembling motion) of electrons in semiconductors: a review", J. Phys.: Condens. Matter **23**, 143201 (2011).

[160] C. Aversa and J. E. Sipe, "Nonlinear optical susceptibilities of semiconductors: Results with a length-gauge analysis", Phys. Rev. B **52**, 14636 (1995).

[161] Y. C. Han and L. B. Madsen, "Comparison between length and velocity gauges in quantum simulations of high-order harmonic generation", Phys. Rev. A **81**, 063430 (2010).

[162] G. B. Ventura, D. J. Passos, J. M. L. D. Santos, J. M. V. P. Lopes, and N. M. Peres, "Gauge covariances and nonlinear optical responses", Phys. Rev. B **96**, 035431 (2017).

[163] M. Ebner, "Carrier dynamics in Dirac systems induced by strong light pulses", Master's thesis, University of Regensburg, Germany (2022).

[164] R. Karplus and J. M. Luttinger, "Hall effect in ferromagnetics", Phys. Rev. **95**, 1154 (1954).

[165] D. Shin, S. A. Sato, H. Hübener, U. D. Giovannini, J. Kim, N. Park, and A. Rubio, "Unraveling materials Berry curvature and Chern numbers from real-time evolution of Bloch states", PNAS **116**, 4135–4140 (2019).

[166] M. Göppert-Mayer, "Über Elementarakte mit zwei Quantensprüngen", Ann. Phys. **401**, 273–294 (1931).

[167] P. A. Franken, A. E. Hill, C. W. Peters, and G. Weinreich, "Generation of optical harmonics", Phys. Rev. Lett. **7**, 118 (1961).

[168] O. Schubert, M. Hohenleutner, F. Langer, B. Urbanek, C. Lange, U. Huttner, D. Golde, T. Meier, M. Kira, S. W. Koch, and R. Huber, "Sub-cycle control of terahertz high-harmonic generation by dynamical Bloch oscillations", Nat. Photon. **8**, 119–123 (2014).

[169] M. Hohenleutner, F. Langer, O. Schubert, M. Knorr, U. Huttner, S. W. Koch, M. Kira, and R. Huber, "Real-time observation of interfering crystal electrons in high-harmonic generation", Nature **523**, 572–575 (2015).

[170] T. T. Luu and H. J. Wörner, "Measurement of the Berry curvature of solids using high-harmonic spectroscopy", Nat. Commun. **9**, 916 (2018).

[171] J. D. Jackson, *Classical electrodynamics*, 2nd edition (Wiley, 1975).

[172] L. Yue and M. B. Gaarde, "Introduction to theory of high-harmonic generation in solids: tutorial", JOSA B **39**, 535–555 (2022).

[173] C. Heide, T. Boolakee, T. Higuchi, and P. Hommelhoff, "Adiabaticity parameters for the categorization of light-matter interaction: from weak to strong driving", Phys. Rev. A **104**, 023103 (2021).

[174] L. V. Keldysh, "Ionization in the field of a strong electromagnetic wave", J. Exp. Theor. Phys. **20**, 1307–1314 (1965).

[175] L. D. Landau, "A theory of energy transfer on collisions", Phys. Z. Sowjetunion **1**, 88 (1932).

[176] C. Zener, "Non-adiabatic crossing of energy levels", Proc. R. Soc. Lond. A **137**, 696–702 (1932).

[177] L. D. Landau, "On the theory of transfer of energy at collisions II", Phys. Z. Sowjetunion **2**, 118 (1932).

[178] E. K. G. Stückelberg, "Theorie der unelastischen Stösse zwischen Atomen", Helv. Phys. Acta **5**, 369–422 (1932).

[179] B. M. Breid, D. Witthaut, and H. J. Korsch, "Bloch-Zener oscillations", New J. Phys. **8**, 110 (2006).

[180] V. Krückl and K. Richter, "Bloch-Zener oscillations in graphene and topological insulators", Phys. Rev. B **85**, 115433 (2012).

[181] S. N. Shevchenko, S. Ashhab, and F. Nori, "Landau-Zener-Stückelberg interferometry", Phys. Rep. **492**, 1–30 (2010).

[182] V. Krückl, "Wave packets in mesoscopic systems: From time-dependent dynamics to transport phenomena in graphene and topological insulators", PhD thesis, University of Regensburg, Germany (2013).

[183] L. Susskind, "Lattice fermions", Phys. Rev. D **16**, 3031 (1977).

[184] R. Stacey, "Eliminating lattice fermion doubling", Phys. Rev. D **26**, 468 (1982).

[185] R. Kozlovsky, "Magnetotransport in 3D topological insulator nanowires", PhD thesis, University of Regensburg, Germany (2020).

[186] C. W. Groth, M. Wimmer, A. R. Akhmerov, and X. Waintal, "Kwant: a software package for quantum transport", New J. Phys. **16**, 063065 (2014).

[187] T. Kloss, J. Weston, B. Gaury, B. Rossignol, C. Groth, and X. Waintal, "Tkwant: a software package for time-dependent quantum transport", New J. Phys. **23**, 023025 (2021).

[188] B. Messias de Resende, F. C. de Lima, R. H. Miwa, E. Vernek, and G. J. Ferreira, "Confinement and fermion doubling problem in dirac-like hamiltonians", Phys. Rev. B **96**, 161113(R) (2017).

[189] J. W. Cooley and J. W. Tukey, "An algorithm for the machine calculation of complex Fourier series", Math. Comp. **19**, 297–301 (1965).

[190] P. A. M. Dirac, *The principles of quantum mechanics* (Clarendon Press, 1930).

[191] H. Tal-Ezer and R. Kosloff, "An accurate and efficient scheme for propagating the time dependent Schrödinger equation", J. Chem. Phys. **81**, 3967–3971 (1998).

[192] G. Faber, "Über polynomische Entwickelungen", Math. Ann. **57**, 389–408 (1903).

[193] W. Huisinga, L. Pesce, R. Kosloff, and P. Saalfrank, "Faber and Newton polynomial integrators for open-system density matrix propagation", J. Chem. Phys. **110**, 5538–5547 (1999).

[194] C. Lanczos, "An iteration method for the solution of the eigenvalue problem of linear differential and integral operators", J. Res. Natl. Bur. Stand. **45**, 255 (1950).

[195] T. J. Park and J. C. Light, "Unitary quantum time evolution by iterative Lanczos reduction", J. Chem. Phys. **85**, 5870–5876 (1986).

[196] W. E. Arnoldi, "The principle of minimized iterations in the solution of the matrix eigenvalue problem", Quart. Appl. Math. **9**, 17–29 (1951).

[197] J. Weston and X. Waintal, "Linear-scaling source-sink algorithm for simulating time-resolved quantum transport and superconductivity", Phys. Rev. B **93**, 134506 (2016).

[198] W. S. Dunbar and A. D. Woodbury, "Application of the Lanczos Algorithm to the solution of the groundwater flow equation", Water Resour. Res. **25**, 551–558 (1989).

[199] S. Kling, T. Salger, C. Grossert, and M. Weitz, "Atomic Bloch-Zener oscillations and Stückelberg interferometry in optical lattices", Phys. Rev. Lett. **105**, 215301 (2010).

[200] A. Zenesini, D. Ciampini, O. Morsch, and E. Arimondo, "Observation of Stückelberg oscillations in accelerated optical lattices", Phys. Rev. A **82**, 065601 (2010).

[201] J. Feldmann, K. Leo, J. Shah, D. A. Miller, J. E. Cunningham, T. Meier, G. V. Plessen, A. Schulze, P. Thomas, and S. Schmitt-Rink, "Optical investigation of Bloch oscillations in a semiconductor superlattice", Phys. Rev. B **46**, 7252(R) (1992).

[202] C. Waschke, H. G. Roskos, R. Schwedler, K. Leo, H. Kurz, and K. Köhler, "Coherent submillimeter-wave emission from Bloch oscillations in a semiconductor superlattice", Phys. Rev. Lett. **70**, 3319 (1993).

[203] A. A. Ignatov, E. Schomburg, K. F. Renk, W. Schatz, J. F. Palmier, and F. Mollot, "Response of a Bloch oscillator to a THz-field", Ann. Phys. **506**, 137–144 (1994).

[204] M. B. Dahan, E. Peik, J. Reichel, Y. Castin, and C. Salomon, "Bloch oscillations of atoms in an optical potential", Phys. Rev. Lett. **76**, 4508 (1996).

[205] S. R. Wilkinson, C. F. Bharucha, K. W. Madison, Q. Niu, and M. G. Raizen, "Observation of atomic Wannier-Stark ladders in an accelerating optical potential", Phys. Rev. Lett. **76**, 4512 (1996).

[206] T. Pertsch, P. Dannberg, W. Elflein, A. Bräuer, and F. Lederer, "Optical Bloch oscillations in temperature tuned waveguide arrays", Phys. Rev. Lett. **83**, 4752 (1999).

[207] R. Morandotti, U. Peschel, J. S. Aitchison, H. S. Eisenberg, and Y. Silberberg, "Experimental observation of linear and nonlinear optical Bloch oscillations", Phys. Rev. Lett. **83**, 4756 (1999).

[208] H. Sanchis-Alepuz, Y. A. Kosevich, and J. Sánchez-Dehesa, "Acoustic analogue of electronic Bloch oscillations and resonant Zener tunneling in ultrasonic superlattices", Phys. Rev. Lett. **98**, 134301 (2007).

[209] C. J. Fujiwara, K. Singh, Z. A. Geiger, R. Senaratne, S. V. Rajagopal, M. Lipatov, and D. M. Weld, "Transport in Floquet-Bloch bands", Phys. Rev. Lett. **122**, 010402 (2019).

[210] A. Alberti, V. V. Ivanov, G. M. Tino, and G. Ferrari, "Engineering the quantum transport of atomic wavefunctions over macroscopic distances", Nat. Phys. **5**, 547–550 (2009).

[211] E. Haller, R. Hart, M. J. Mark, J. G. Danzl, L. Reichsöllner, and H.-C. Nägerl, "Inducing transport in a dissipation-free lattice with Super Bloch oscillations", Phys. Rev. Lett. **104**, 200403 (2010).

[212] K. Kudo and T. S. Monteiro, "Theoretical analysis of super-Bloch oscillations", Phys. Rev. A **83**, 053627 (2011).

[213] D. M. Gangardt and A. Kamenev, "Bloch oscillations in a one-dimensional spinor gas", Phys. Rev. Lett. **102**, 070402 (2009).

[214] F. Meinert, M. Knap, E. Kirilov, K. Jag-Lauber, M. B. Zvonarev, E. Demler, and H. C. Nägerl, "Bloch oscillations in the absence of a lattice", Science **356**, 945–948 (2017).

[215] L. Yuan and S. Fan, "Bloch oscillation and unidirectional translation of frequency in a dynamically modulated ring resonator", Optica **3**, 1014–1018 (2016).

[216] M. S. Rudner and N. H. Lindner, "Band structure engineering and non-equilibrium dynamics in Floquet topological insulators", Nat. Rev. Phys. **2**, 229–244 (2020).

[217] M. S. Rudner and N. H. Lindner, "The Floquet engineer's handbook", Preprint (2020) 10.48550/arxiv.2003.08252.

[218] C. Weitenberg and J. Simonet, "Tailoring quantum gases by Floquet engineering", Nat. Phys. **17**, 1342–1348 (2021).

[219] M. Holthaus, "Floquet engineering with quasienergy bands of periodically driven optical lattices", J. Phys. B: At. Mol. Opt. Phys. **49**, 013001 (2015).

[220] U. de Giovannini and H. Hübener, "Floquet analysis of excitations in materials", J. Phys. Mater. **3**, 012001 (2020).

[221] M. Laumer, "Velocity of Dirac fermions in a Floquet system", Bachelor's thesis, University of Regensburg, Germany (2022).

[222] H. P. Breuer and M. Holthaus, "Quantum phases and Landau-Zener transitions in oscillating fields", Phys. Lett. A **140**, 507–512 (1989).

[223] Y. I. Rodionov, K. I. Kugel, and F. Nori, "Floquet spectrum and driven conductance in Dirac materials: Effects of Landau-Zener-Stückelberg-Majorana interferometry", Phys. Rev. B **94**, 195108 (2016).

[224] P. Reck, C. Gorini, A. Goussev, V. Krueckl, M. Fink, and K. Richter, "Dirac quantum time mirror", Phys. Rev. B **95**, 165421 (2017).

[225] O. V. Kibis, "Metal-insulator transition in graphene induced by circularly polarized photons", Phys. Rev. B **81**, 165433 (2010).

[226] Y. Zhou and M. W. Wu, "Optical response of graphene under intense terahertz fields", Phys. Rev. B **83**, 245436 (2011).

[227] S. E. Savel'ev and A. S. Alexandrov, "Massless Dirac fermions in a laser field as a counterpart of graphene superlattices", Phys. Rev. B **84**, 035428 (2011).

[228] J. Atteia, J. H. Bardarson, and J. Cayssol, "Ballistic transport through irradiated graphene", Phys. Rev. B **96**, 245404 (2017).

[229] H. K. Kelardeh, V. Apalkov, and M. I. Stockman, "Attosecond strong-field interferometry in graphene: Chirality, singularity, and Berry phase", Phys. Rev. B **93**, 155434 (2016).

[230] P. Delplace, Á. Gómez-León, and G. Platero, "Merging of Dirac points and Floquet topological transitions in ac-driven graphene", Phys. Rev. B **88**, 245422 (2013).

[231] G. Usaj, P. M. Perez-Piskunow, L. E. F. Foa Torres, and C. A. Balseiro, "Irradiated graphene as a tunable Floquet topological insulator", Phys. Rev. B **90**, 115423 (2014).

[232] P. M. Perez-Piskunow, L. E. F. Foa Torres, and G. Usaj, "Hierarchy of Floquet gaps and edge states for driven honeycomb lattices", Phys. Rev. A **91**, 043625 (2015).

[233] L. Wang, I. Meric, P. Y. Huang, Q. Gao, Y. Gao, H. Tran, T. Taniguchi, K. Watanabe, L. M. Campos, D. A. Muller, J. Guo, P. Kim, J. Hone, K. L. Shepard, and C. R. Dean, "One-dimensional electrical contact to a two-dimensional material", Science **342**, 614–617 (2013).

[234] A. I. Berdyugin, S. G. Xu, F. M. Pellegrino, R. K. Kumar, A. Principi, I. Torre, M. B. Shalom, T. Taniguchi, K. Watanabe, I. V. Grigorieva, M. Polini, A. K. Geim, and D. A. Bandurin, "Measuring hall viscosity of graphene's electron fluid", Science **364**, 162–165 (2019).

[235] T. Kitagawa, T. Oka, A. Brataas, L. Fu, and E. Demler, "Transport properties of nonequilibrium systems under the application of light: Photoinduced quantum Hall insulators without Landau levels", Phys. Rev. B **84**, 235108 (2011).

[236] L. E. F. Torres, P. M. Perez-Piskunow, C. A. Balseiro, and G. Usaj, "Multiterminal conductance of a floquet topological insulator", Phys. Rev. Lett. **113**, 266801 (2014).

[237] F. Giorgianni, E. Chiadroni, A. Rovere, M. Cestelli-Guidi, A. Perucchi, M. Bellaveglia, M. Castellano, D. D. Giovenale, G. D. Pirro, M. Ferrario, R. Pompili, C. Vaccarezza, F. Villa, A. Cianchi, A. Mostacci, M. Petrarca, M. Brahlek, N. Koirala, S. Oh, and S. Lupi, "Strong nonlinear terahertz response induced by Dirac surface states in Bi2Se3 topological insulator", Nat. Commun. **7**, 11421 (2016).

[238] H. Liu, Y. Li, Y. S. You, S. Ghimire, T. F. Heinz, and D. A. Reis, "High-harmonic generation from an atomically thin semiconductor", Nat. Phys. **13**, 262–265 (2017).

[239] Wolfram Research, Inc., *Mathematica, Version 10.3*, Champaign, IL (2015).

[240] A. Riedel, "Magnetic field effects on light-driven topological insulator surface states", Master's thesis, University of Regensburg, Germany (2023).

[241] R. E. Silva, F. Martín, and M. Ivanov, "High harmonic generation in crystals using maximally localized Wannier functions", Phys. Rev. B **100**, 195201 (2019).

[242] H. Rubinsztein-Dunlop, A. Forbes, M. V. Berry, M. R. Dennis, D. L. Andrews, M. Mansuripur, C. Denz, C. Alpmann, P. Banzer, T. Bauer, E. Karimi, L. Marrucci, M. Padgett, M. Ritsch-Marte, N. M. Litchinitser, N. P. Bigelow, C. Rosales-Guzmán, A. Belmonte, J. P. Torres, T. W. Neely, M. Baker, R. Gordon, A. B. Stilgoe, J. Romero, A. G. White, R. Fickler, A. E. Willner, G. Xie, B. McMorran, and A. M. Weiner, "Roadmap on structured light", J. Opt. **19**, 013001 (2016).

[243] A. Seith, F. Evers, and J. Wilhelm, "Giant DC residual current generated by subcycle laser pulses", Preprint (2024) `10.48550/arXiv.2402.01490`.

[244] Y. Tang and A. E. Cohen, "Optical chirality and its interaction with matter", Phys. Rev. Lett. **104**, 163901 (2010).

[245] X. Zhang, T. Wu, X. Zhang, and R. Wang, "Strongly enhanced Raman optical activity in molecules by magnetic response of nanoparticles", J. Phys. Chem. C **120**, 14795–14804 (2016).

[246] A. Manjavacas, R. Fenollosa, I. Rodriguez, M. C. Jiménez, M. A. Miranda, and F. Meseguer, "Magnetic light and forbidden photochemistry: the case of singlet oxygen", J. Mater. Chem. C **5**, 11824–11831 (2017).

[247] T. H. Taminiau, S. Karaveli, N. F. V. Hulst, and R. Zia, "Quantifying the magnetic nature of light emission", Nat. Commun. **3**, 979 (2012).

[248] A. Junck, G. Refael, and F. V. Oppen, "Photocurrent response of topological insulator surface states", Phys. Rev. B **88**, 075144 (2013).

[249] L. M. Roth, B. Lax, and S. Zwerdling, "Theory of optical magneto-absorption effects in semiconductors", Phys. Rev. **114**, 90 (1959).

[250] R. Winkler, *Spin-orbit coupling effects in two-dimensional electron and hole systems* (Springer Berlin, Heidelberg, 2003).

[251] T. Rauch, M. Flieger, J. Henk, I. Mertig, and A. Ernst, "Dual topological character of chalcogenides: Theory for Bi2Te3", Phys. Rev. Lett. **112**, 016802 (2014).

[252] G. Sundaram and Q. Niu, "Wave-packet dynamics in slowly perturbed crystals: Gradient corrections and Berry-phase effects", Phys. Rev. B **59**, 14915 (1999).

[253] Z. Yuanbo, T. Yan-Wen, S. H. L., and K. Philip, "Experimental observation of the quantum Hall effect and Berry's phase in graphene", Nature **438**, 201–204 (2005).

[254] D. an der Brügge and A. Pukhov, "Ultrashort focused electromagnetic pulses", Phys. Rev. E **79**, 016603 (2009).

[255] F. H. Faisal and J. Z. Kamiński, "Floquet-Bloch theory of high-harmonic generation in periodic structures", Phys. Rev. A **56**, 748 (1997).

[256] F. H. Faisal, J. Z. Kamiski, and E. Saczuk, "Photoemission and high-order harmonic generation from solid surfaces in intense laser fields", Phys. Rev. A **72**, 023412 (2005).

[257] T. N. Ikeda, K. Chinzei, and H. Tsunetsugu, "Floquet-theoretical formulation and analysis of high-order harmonic generation in solids", Phys. Rev. A **98**, 063426 (2018).

[258] O. Neufeld, D. Podolsky, and O. Cohen, "Floquet group theory and its application to selection rules in harmonic generation", Nat. Commun. **10**, 405 (2019).

[259] S. Ito, M. Schüler, M. Meierhofer, S. Schlauderer, J. Freudenstein, J. Reimann, D. Afanasiev, K. A. Kokh, O. E. Tereshchenko, J. Güdde, M. A. Sentef, U. Höfer, and R. Huber, "Build-up and dephasing of Floquet–Bloch bands on subcycle timescales", Nature **616**, 696–701 (2023).

[260] Y. Baba, "Quantum transport in Dirac materials under external fields and disorder", PhD thesis, Universidad Complutense de Madrid, Spain (2023).

[261] K. Drese and M. Holthaus, "Floquet theory for short laser pulses", Eur. Phys. J. D **5**, 119–134 (1999).

[262] P. J. Turner, *Xmgrace, Version 5.1.25*, Center for Coastal and Land-Margin Research, Oregon Graduate Institute of Science and Technology, Beaverton, OR (2005).

[263] G. Grosso and G. P. Parravicini, *Solid state physics* (Academic Press, 2000).

[264] B. Gaury and X. Waintal, "Dynamical control of interference using voltage pulses in the quantum regime", Nat. Commun. **5**, 3844 (2014).

List of publications

[74] V. Junk, P. Reck, C. Gorini, K. Richter, "Floquet oscillations in periodically driven Dirac systems", Phys. Rev. B **101**, 134302 (2020).

[81] C. P. Schmid, L. Weigl, P. Grössing, V. Junk, C. Gorini, S. Schlauderer, S. Ito, M. Meierhofer, N. Hofmann, D. Afanasiev, J. Crewse, K. A. Kokh, O. E. Tereshchenko, J. Güdde, F. Evers, J. Wilhelm, K. Richter, U. Höfer, and R. Huber, "Tunable non-integer high-harmonic generation in a topological insulator", Nature **593**, 385-390 (2021).

List of Figures

Acknowledgments

In this last paragraph, I want to express my gratitude to all people who supported me and my work during the last years.

I thank Klaus Richter for making this project possible. He encouraged me to delve into the theory of time-dependent phenomena in my master's thesis, and gave me the opportunity to stay and dive deeper into this research field for my PhD. He was always there to provide creative input when I was stuck on a problem but also trusted me in finding my own solutions. In addition to his scientific counsel, he was always mindful and created a very enjoyable working atmosphere.

Moreover, I want to thank everyone with whom I collaborated over the last years. I start with Phillipp Reck, who supervised my master's thesis and thereby provided me with the foundation for working on my PhD project. His introduction into the field and especially the handling of TQT saved me from many hardships. Next, I want to thank Cosimo Gorini for the various fruitful discussions and for teaching me to focus on the positive aspects of having identified a mistake. In Wolfgang Hogger I found a companion to debate our joint research topics and he enriched this project with his perspective on the ongoing physics. Even more importantly, he helped me in keeping up my spirit in stressful times. Special thanks also go to him, Angelika Knothe, and Michael Barth for their great efforts in proof reading this thesis. I also want to mention the numerous students I was able to supervise in the course of this project. Their work was a valuable contribution and I greatly enjoyed all collaborations. The master's students Mario Ebner and Alexander Riedel played an important role in the development of the Fermi sea approach for wave packets and in understanding magnetic-field effects on HHG. The bachelor's students Johanna Meier, Martin Steinau, and Michael Laumer helped me extend my understanding of Floquet systems, and Malin Horstmann and Lukas Beringer introduced me to the twists of Klein tunneling in moiré superlattices. Lastly, I want to thank all members of the chair for the great lunch and coffee breaks, dinners, and excursions, as well as the

multifaceted conversations that made working in this group a real pleasure.

I appreciate having participated in the collaboration initiated by Rupert Huber to interpret the experimentally observed HH emission from Bi_2Te_3. This project inspired the wave-packet analysis I developed in this thesis. I especially want to thank Christoph Schmid and Leonard Weigl for the insights into the results from the lab and for the various discussions on the experimental parameters and their implications for theoretical modeling. From the theory side, Patrick Grössing was a great coworker, and I really enjoyed our regular Zoom meetings, where we debated physics and fought the sometimes lonely working atmosphere during the pandemic.

I acknowledge funding by the Deutsche Forschungsgemeinschaft through the SFB 1277, project A07. The SFB created a fruitful research environment and encouraged exchange with other groups. The softskill seminars organized by the IRTG were a valuable complement to my scientific education.

Last but not least, I thank my partner Martin, my family, and my friends – in particular my weekly running companion Annka and the P56 gang Jan, Stefan, Jakob, and Beril – for their support over the last years and for their understanding of my limited time resources during the last weeks of completing this dissertation. I know that bearing my moods was challenging sometimes – especially for Martin, who had to share a home with me – but still you were always there for me and ready to provide me with the kind of encouragement I needed at that moment.